Dissertation

submitted to the

Combined Faculties of the Natural Sciences and Mathematics

of the Ruberto-Carola-University of Heidelberg. Germany

for the degree of

Doctor of Natural Sciences

Put forward by

Terese Thidemann Hansen

born in: Nyborg, Denmark

Oral examination: November 4, 2015

An observational study of metal-poor stars

Acknowledgements

Abstract

The outer atmosphere of the first generation of low-mass stars retain to a great extent the original composition of the interstellar medium at the time and place of their birth. Hence the earliest phases of Galactical chemical evolution and nucleosynthesis can be investigated by means of studying the old, metal-poor stars. A minority of these stars exhibit dramatic enhancements in their abundances of heavy neutron-capture elements and/or of carbon. The key question for Galactic chemical evolution models is whether these peculiarities reflect the composition of the natal clouds, or if they are due to later (post-birth) mass transfer of chemically processed material from a binary companion. If the latter is the case, these stars should all be members of binary systems.

This thesis presents high-resolution elemental-abundance analysis for a sample of 23 very metal-poor (VMP; [Fe/H] < -2.0) stars, 12 of which are extremely metal-poor (EMP; [Fe/H] < -3.0), and 4 of which are ultra metal-poor (UMP; [Fe/H] < -4.0). The results of radial velocity monitoring of 17 r-process enhanced stars (r-I and r-II stars), 24 CEMP-no stars, 18 CEMP-s and four CEMP-r/s stars, are also presented.

The stars, for which the abundance analysis were performed, were targeted to explore differences in the abundance ratios of Li, C, N, O, the α-elements, the iron-peak elements, and a number of neutron-capture elements. These are elements that constrain the possible astrophysical sites of element production. This sample has substantially increased the number of known carbon-enhanced metal-poor (CEMP) and nitrogen-enhanced metal-poor (NEMP) stars. The sample of stars include eight that are considered "normal" metal-poor stars, six CEMP-no stars, five CEMP-s stars, two CEMP-r stars, and two CEMP-r/s stars. One of the CEMP-r stars and one of the CEMP-r/s stars are possible NEMP stars. Lithium is detected for three of the six CEMP-no stars, all of which are Li-depleted with respect to the Li plateau for metal-poor dwarfs found by Spite & Spite. This suggests that whatever site(s) produced C either do not completely destroy lithium, or that Li has been astrated by early-generation stars and mixed with primordial Li in the gas that formed the stars observed at present. Carbon and nitrogen abundances for the CEMP stars reveal, for the majority, that a small degree of mixing has happened in their progenitor stars ([C/N] > 0). However, signs of a larger degree of mixing ([C/N] < 0) is found in some CEMP-no stars, but these stars are only found at the lowest metalicities ([Fe/H] < -3.4). CEMP-no stars with large enhancements in Na, Mg, and Al are also only found below this metallicity. This sample confirms the existence of two separate bands in the absolute carbon abundances

of CEMP stars, as suggested by Spite et al. The derived abundances for the α-elements and iron-peak elements of the stars are similar to those found in previous large samples of metal-poor stars. Finally evidence for a "floor" in the absolute Ba abundances of CEMP-no stars at $A(\mathrm{Ba}) \sim -2.0$ is also presented.

Binary frequencies of 18%, 17%, and 75% are found for the r-process enhanced, CEMP-no and CEMP-s stars, respectively. These results show that the nucleosynthetic processes, responsible for the strong carbon excess in the CEMP-no stars, and the r-process element enhancement in the r-I and r-II stars, are unrelated to their binary population. Instead, the element excess was imprinted on the natal molecular clouds of these stars by an external, distant source. The high frequency of binary stars found for the CEMP-s stars however, demonstrate that the peculiar abundance pattern of these stars is coupled to the binary nature of the stars.

Zusammenfasshung

Die äußere Atmosphäre der ersten Generation von massearmen Sternen bewahrt zu einem Großteil die urspüngliche Zusammensetzung des Interstellaren Mediums. Daher läßt sich die Frühphase der Galaktischen chemischen Entwicklung und Nukleosynthese anhand von metallarmen Sternen gut untersuchen. Eine Minderheit dieser Sterne zeigt dramatische Anreicherungen in schweren Neutroneneinfangselementen und/oder Kohlenstoff. Die grundlegende Frage für chemische Entwicklungsmodelle ist, ob diese Besonderheiten die ursprüngliche Zusammensetzung der Geburtswolken reflektiert oder durch späteren Massetransfer von chemisch angereichertem Material eine Begleiters in einem Doppelstern verursacht wurde. Der zweite Fall würde nahelegen, daß all solche Sterne Mitglieder von Doppelsternsystemen sein sollten.

In dieser Arbeit werden hochaufgelöste Häufigkeitsanalysen von 23 sehr metallarmen Sternen (VMP; [Fe/H] < -2.0) präsentiert, von denen 12 extrem metallarm sind und vier ultra-metallarm (UMP; [Fe/H] < -4.0). Außerdem werden lang angelegte Radialgeschwindigkeitsmessungen von 17 Sternen mit erhöhten Häufigkeiten an r-Prozeß-elementen (r-I und r-II Sterne) diskutiert, sowie 24 CEMP-no, 28 CEMP-s und 4 CEMP-r/s Sterne.

Die Sterne, für die Häufigkeitsanalysen durchgeführt wurden, wurden ursprünglich ausgesucht, um Unterschiede in der Verteilung von Li, C, N, O, den α- und Eisenpeak-Elementen und einer Vielzahl von Neutroneneinfangselementen zu untersuchen – eben solche, mit denen sich mögliche astrophysikalische Orte der Elementproduktion einschränken lassen. Die Gruppe der hier untersuchten Sterne hat die Anzahl der bekannten metallarmen Sterne mit starker Kohlenstoffanreicherung ("Carbon-enhanced metal-poor"; CEMP) und Stickstoffanreicherung ("Nitrogen-enhanced metal-poor"; CEMP) signifikant erhöht. Unser Sample enthält acht "normale" metallarme Sterne, sechs sogenannte CEMP-no Sterne, fünf CEMP-s Sterne, zwei CEMP-r Sterne und zwei CEMP-r/s Sterne. Einer der CEMP-r und einer der CEMP-r/s Sterne sind möglicherweise auch stark mit Stickstoff angereichert.

In dreien von sechs CEMP-no Sternen konnte Lithium detektiert werden; in allen lag die Lithiumhäufigkeit unter dem kanonischen Plateau, das von Spite & Spite für metallarme Sterne gefunden wurde. Was auch immer für ein Szenario die Überhäufigkeit an Kohlenstoff produziert scheint also nicht vollständig vorhandenes Lithium zu zerstören. Auch möglich ist, daß sich Lithium aus einer früheren Generation an Sternen mit primordialem Lithium aus dem Gas vermischt hat, aus dem sich die heute beobachteten Sterne gebildet haben.

Die C- und N-Häufigkeiten der CEMP Sterne zeigen größtenteils, daß ein gewisser Grad an Durchmischung in den Vorgängersternen passiert sein muss (so daß [C/N]>0). Es gibt jedoch Anzeichen für stärkere Mischungsprozesse ([C/N]<0) in einigen CEMP-no Sternen, wenn auch diese Sterne nur bei niedrigsten Metallizitäten unterhalb von [Fe/H]< −3.4 auftauchen. Ebenso finden sich CEMP-no Sterne mit starken Anreicherungen von Na, Mg und Al auch nur bei diesen niedrigen Metallizitäten. Unser Sample bestätigt das Vorkommen von zwei deutlich getrennten "Bändern" in der absoluten Kohlenstoffhäufigkeit von CEMP Sternen, wie von Spite vorgeschlagen wurde. Die α- und Eisenpeakhäufigkeiten ähneln stark denen von anderen großen Samples von metallarmen Sternen. Letztlich präsentiert diese Arbeit auch Anzeichen für eine Untergrenze in der absoluten Barium-Häufigkeit von CEMP-no Sternen, dessen Wert bei ca. $A(\mathrm{Ba}) \sim −2.0$ liegt.

Der Anteil von Doppelsternen an den r-Prozeß, CEMP-no und CEMP-s Sternen liegt bei 18%, 17% bzw. 75%. Dieses Ergebnis zeigt, daß die Nukleosyntheseprozesse, die für die starke Anreicherung mit Kohlenstoff in den CEMP-no Sternen und den überhäufigkeiten von r-Prozeß-Elementen in den r-I und r-II Sternen verantwortlich sind, nichts mit deren Vorkommen in Doppelsternen zu tun hat. Stattdessen müssen diese Überschüsse bereits der ursprünglichen Gaswolke durch einen anderen externen Mechanismus aufgeprägt worden sein. Auf der anderen Seite demonstriert der hohe Anteil von Doppelsternen an den CEMP-s Sternen, daß die besonderen Elementverteilungen dieser Sterne an dessen Doppelsternnatur gekoppelt ist.

Contents

x

List of Figures

List of Tables

C H A P T E R 1

Introduction

The stellar atmospheres of the first generations of low-mass ($M \leq 0.8\ M_\odot$) stars are believed be fossil records of the chemical composition of the nearly pristine gas of the interstellar medium (ISM) at the time and place of their birth. Whether these stars formed happened in dwarf galaxies or in the Milky Way Galaxy, these stars represent the first star formation in the given systems. Thus by detailed investigation of their abundance patterns and other properties, we can constrain the events in the early Universe that led to low mass star formation and the nucleosynthesis taking place at the earliest times. At these early times, the two light elements carbon and lithium play a major role in cosmological studies, as well as in our understanding of early star formation. In addition, the production site(s) of the elements beyond the iron peak remains a major unanswered question.

1.1 The early Universe

The first stars and galaxies are assumed to form in the Universe at redshift $z \sim 20-30$, about 100 - 200 Myrs after the Big Bang. The build-up of structure in the Universe follows the Cold Dark Matter hierarchical cluster paradigm, first proposed by White & Rees (1978), where small dark matter halos merge into larger ones. These contain gas reservoirs from which the first stars and galaxies form. The evolution of galaxies is a continuous process, from the formation of a galaxy in the central halo, through accretion from large-scale filaments, and smaller haloes containing dwarf galaxies.

The first stars are predicted to have formed in dark matter mini-haloes of mass $\sim 10^6 M_\odot$ (Couchman & Rees 1986). Due to the lack of metals at this time in the Universe, cooling could only happen via atomic or molecular hydrogen. Since this type of cooling is less efficient, it is commonly assumed that the first stars to form in the Universe were very massive. These massive stars lived short lives which ended in supernova (SN) explosions, where by they enriched the interstellar medium (ISM) in elements heavier than H and He. Subsequent stellar populations have continuously enriched the ISM all the way till today.

When the first metals entered the ISM, the first low-mass stars could form, although the exact transition between high and low-mass stars formation is still debated (Klessen et al. 2012). Two formation channels have been proposed for the formation of the first low-mass stars: Cooling via fine-structure lines of C II and O II or dust cooling (Frebel et al. 2007b; Klessen et al. 2012). Later on, when the ISM becomes more enriched, the gas clouds can cool efficiently via metal lines.

1.2 Metal-poor stars

The metallicity of stars (and the Universe) is conventionally tracked by their iron content. Metal-poor stars are defined as stars with [Fe/H][1] < -1.0. The most metal-poor of these stars are the first low-mass stars to form in the Universe.

A number of surveys have been initiated to search for metal-poor stars since the discovery of these in the 1950's (for a review, see Beers & Christlieb (2005)). Among the first large surveys was the HK objective-prism survey of Beers, Preston and Shectman (Beers et al. 1985), later the Hamburg/ESO Survey (HES) of Christlieb and colleagues (Christlieb et al. 2008) returned a total of 20271 metal-poor star candidates (Christlieb et al. 2008). More recent surveys include the SEGUE 1+2 (Sloan Extension for Galactic Understanding and Exploration) extension of Sloan Digital Sky Survey (SDSS), a photometric and spectroscopic survey of the northern hemisphere. The Radial Velocity Experiment Spectroscopic (RAVE) Survey, with the object of measuring radial velocities and stellar atmosphere parameters for up to one million stars. Although this survey is not targeted on finding metal-poor stars, several candidates have already been found (V. Placco private communication). Also the Skymapper survey of the southern hemisphere and the Large Sky Area Multi-Object Spectroscopic Telescope (LAMOST) have returned numerous metal-poor candidates (Jacobson et al. 2015; Li et al. 2015), along with the Turn-Off PrimOrdial Stars (TOPoS) Survey, selecting EMP candidates from SDSS for intermediate or high resolution followup (Caffau et al. 2013b).

The majority of metal-poor stars are found in the inner- and outer halos of the Milky Way, the inner halo having a mean metallicity of [Fe/H] ~ -1.6 and the outer halo beyond R ~ 15 kpc having a mean metallicity of [Fe/H] ~ -2.2. The inner halo is believed to have formed formed in-situ with the Galaxy, while the outer halo is mainly build up via accretion of smaller stellar systems orbiting the Galaxy (Carollo et al. 2012).

Following the nomenclature of Beers & Christlieb (2005), the metal-poor stars can be divided into sub classes according to metallicity, listed in Table 1.1. Besides metallicity, the metal-poor stars can also be characterized by other signatures, as described in more detail in section 1.3 below. A small portion of them are enhanced in neutron-capture elements. These are termed r, s or r/s stars, according to the nature of the neutron-capture elements seen in their spectra. A larger group, about 20%, are enhanced in carbon, the so-called carbon-enhanced metal-poor (CEMP) stars. Some of the CEMP stars also show signatures of neutron-capture elements in their spectra, by which they can be divided into further sub-classes. Each of these sub-classes appear to be associated with different element production

---

[1]$[\mathrm{X/H}] = \log \left(\frac{N(\mathrm{X})}{N(\mathrm{H})} \right)_* - \log \left(\frac{N(\mathrm{X})}{N(\mathrm{H})} \right)_\odot$, where $N(\mathrm{X})$ is the number density of atoms of the element X.

[Fe/H]	Term	Acronym
< -1	Metal-poor	MP
< -2	Very metal-poor	VMP
< -3	Extremely metal-poor	EMP
< -4	Ultra metal-poor	UMP
< -5	Hyper metal-poor	HMP
< -6	Mega metal-poor	MMP

Table 1.1: Classification of metal-poor stars according to their metallicity.

histories. Thus the study of these stars provides insight into the variety of astrophysical sites in the early Galaxy that were primarily responsible for their origin.

1.3 Different classes of metal-poor stars

1.3.1 Normal metal-poor star

Normal metal-poor (NMP) stars are stars with [Fe/H] < -1.0 and no significant over abundance of any element or group of elements. Yong et al. (2013) has argued that such a group of "normal" metal-poor stars exists, which share a general abundance pattern without large over abundances of any elements. The majority of metal-poor stars known are NMP. These stars are believed to be enriched by core collapse SN in the early Universe and later by stellar winds from asymptotic giant branch (AGB) stars.

1.3.2 CEMP stars

The class of carbon-enhanced metal-poor stars, was originally defined by Beers & Christlieb (2005) as metal-poor stars with [C/Fe] $\geq +1.0$. This has been redefined by Aoki et al. (2007) to be stars with

$$[\text{C/Fe}] \quad \geq \quad +0.7, \quad \text{for stars with} \quad \log(L/L_\odot) \leq 2.3 \tag{1.1}$$
$$[\text{C/Fe}] \quad \geq \quad +3.0 - \log(L/L_\odot), \quad \text{for stars with} \quad \log(L/L_\odot) > 2.3 \tag{1.2}$$

based on C abundances in a large sample of C-rich stars and as a consequence of the changes in the surface abundances of stars during their evolution. The value of 0.7 is used in most contemporary work. The different sub-classes of CEMP stars are described below.

CEMP-no stars

The CEMP-no stars are carbon-enhanced stars which do not show enhancements in neutron-capture elements. They are defined by the following abundance signatures: [Fe/H] < -1.0, [C/Fe] > 0.7, and [Ba/Fe] < 0.0.

It has been shown that at extremely low metallicity, [Fe/H] < -3.0, the CEMP-no stars are the dominant sub-class of the CEMP stars (Aoki et al. 2007). The CEMP-no stars are predominantly found in the outer halo of the Milky Way (Carollo et al. 2014).

Different progenitors have been suggested for the CEMP-no stars, such as pollution by faint SNe that experienced extensive mixing and fallback during their explosions (Umeda & Nomoto 2003, 2005; Tominaga et al. 2007, 2014; Ito et al. 2009, 2013; Nomoto et al. 2013), winds from massive, rapidly rotating, mega metal-poor ([Fe/H] < -6.0) stars, so-called "spinstars" (Hirschi & et al. 2006; Meynet et al. 2006; Hirschi 2007; Meynet et al. 2010; Cescutti et al. 2013), or mass transfer from an AGB companion star (Suda et al. 2004; Masseron et al. 2010).

The CEMP-no stars are of special importance, as the preponderance of evidence points to their being associated with elemental-abundance patterns that were produced by the very first generation of massive stars (see discussion in section 8.1.6). Thus they potentially provide a unique probe of the first mass function in the early Universe, along with providing information on the nucleosynthesis and properties of the first stars.

The initial mass function (IMF, $\xi(M)$) of the first stars can not be observationally constrained, as those stars no longer exists. The only ways to constrain the IMF for those stars, is to analyze the imprints, that generations of stars has put on subsequent generations of stars, and from theoretical simulations of star formation in the early universe. Heger & Woosley (2010) computed a set of models for the evolution of metal-free stars in the mass range 10-100$M_\odot$, and calculated the yields for the SN explosions of these stars for various explosion energies and degrees of mixing and fallback. By using a Salpeter IMF ($\xi(M) = \xi_0 M^{-2.35}$) for the given mass range, for their first stars sample, they found general agreement between the SN yields and the element abundance patterns found in the sample of metal-poor stars from Cayrel et al. (2004).

CEMP-s stars

Contrary to the CEMP-no stars, the CEMP-s stars exhibit large over-abundances of elements produced in the slow (s-) neutron-capture process, as well as carbon. They are defined by the following abundance ratios: [Fe/H] < -0.7, [C/Fe] > 0.7, [Ba/Fe] > 1.0, and [Ba/Eu] < 0.5. The latter, to ensure it is a pure or almost pure s-process signature, which is seen in the stars (see section 1.4.5). The CEMP-s stars are the most commonly observed sub-class of CEMP stars; around 80% of the CEMP stars exhibit s-process-element enhancements (Aoki et al. 2007). These stars are mostly found in the inner halo (Carollo et al. 2014).

The favored scenario for the formation of CEMP-s stars is mass transfer of carbon- and s-process-enhanced material from the envelope of an AGB star to its (presently observed) binary companion (e.g., Herwig 2005; Sneden et al. 2008). Radial-velocity data support this picture. Lucatello et al. (2005) argued that the multiple-epoch observations of CEMP-s stars, available at the time, were consistent with essentially all CEMP-s stars being members of binary systems. They found that 68% of their 19 sample stars exhibited radial-velocity variation. From Monte Carlo simulations using a distribution of orbital parameters, they find a detection frequency of $\sim$36%, when assuming a true binary fraction 100%. This is well below the 68% binary frequency, they detect for their 19 sample stars, leading them to conclude that all stars of this type are part of binary systems.

CEMP-r stars

CEMP-r stars are enhanced in carbon and elements produced in the rapid (r-) neutron-capture process and have [Fe/H] < -1, [C/Fe] > 0.7, and [Eu/Fe] > 1.0. The first star to be discovered of this type was CS 22892$-$052, called "Sneden's star", which is also classified as an r-II star (see below). Prior to this thesis only three stars of this type had been discovered (Roederer et al. 2014c). No formation scenarios, accounting for both the carbon and r-process excess seen in these stars, have been suggested.

CEMP-r/s stars

The CEMP-r/s stars show enhancements in elements produced both in the s- and r-process. They are defined by the following abundance ratios: [Fe/H] < -1, [C/Fe] > 0.7, and $0.0 <$ [Ba/Eu] < 0.5. About 15 of these objects are presently known (Aoki et al. 2002d; Barbuy et al. 2005; Masseron et al. 2010).

Several formation scenarios for these stars were discussed by Jonsell et al. (2006) (and references there in). Among these, that a binary system formed from an r-process enriched (by SN) cloud, the more massive part then evolve to the AGB phase and polluted the surface of the low-mass companion with carbon and s-process material via mass transfer. A more extreme version is the formation of a binary system from a non-enriched cloud, the more massive star evolves to the AGB phase, transfers C and s-process enriched material to its low-mass companion, where after it becomes a white dwarf. At this point, mass is transferred from the low-mass companion back to the white dwarf until the Chandrasekhar mass is reached, and the white dwarf explodes in a SN, enriching the low-mass companion in r-process material.

1.3.3 NEMP stars

The NEMP stars are Nitrogen-Enhanced Metal-Poor stars. Stars with [N/Fe] $> +0.5$ and [C/N] < -0.5 are, according to Johnson et al. (2007), classified as NEMP. These stars are the result of mass transfer from an intermediate-mass AGB star which has undergone hot bottom burning, and thereby produced large amounts of nitrogen. At present, no confirmed NEMP stars exists. Four stars has been suggested to be NEMP stars, based on their abundance pattern. These are CS 30322$-$023, CS 22949$-$037, HE 1031$-$0020, and CS 29528$-$041 (Johnson et al. 2007), but radial-velocity monitoring of the stars is needed, to determine their binary status and possibly confirm their NEMP classification.

1.3.4 r-I and r-II stars

A small fraction ($\sim 3\%$) of the extremely metal-poor stars are strongly enhanced in r-process elements, usually revealed by a large europium abundance. These are the r-I ($0.3 \leq$ [Eu/Fe] ≤ 0.0, [Ba/Fe] < 0.0) and r-II ([Eu/Fe] > 1.0, [Ba/Fe] < 0.0) stars. CS 22892$-$052 is the prototype of the r-II stars. It has [Fe/H] $= -3.1$, and is enriched in r-process elements by 1.7 dex. This star is also carbon-enhanced (see above section 1.3.2) and it has been the subject of many studies (e.g., Sneden et al. (1996, 2000); Cowan & Sneden (2006)). The r-II stars are found only in a narrow metallicity range around [Fe/H] ~ -3, whereas the r-I stars

are found over a wider range of metallicities (Barklem et al. 2005). It has been proposed that these stars are the result of mass transfer in a binary system (Qian & Wasserburg 2001).

1.4 Element formation and abundance signatures

In recent years, high-resolution spectroscopic analyses of samples of stars with metallicities significantly below Solar have grown to the point that one can begin to establish the general behaviors of elemental abundance ratios associated with production by the first few generations of stars to form the Galaxy (for a recent review see, e.g., Frebel & Norris (2015)). These "statistical" samples are particularly valuable when the data is analysed in a self-consistent manner (e.g. Yong et al. 2013). Then comparisons of derived abundance ratios are not plagued by the scatter introduced from the different assumptions and procedures used by individual researchers, which can be sufficiently large as to obscure important details. This section will go through the different elements detected in metal-poor stars; how these elements are formed and the abundance signatures of them detected in metal-poor stars.

1.4.1 Lithium

Formation

Lithium is produced in very small amounts during Standard Big Bang Nucleosynthesis (BBN). $A(\mathrm{Li})^2_{\mathrm{BBN}}$ can be calculated using the accurate baryon density obtained from the *Wilkinson Mirowave Anisotropy Probe* (Spergel et al. 2007; Hinshaw et al. 2013) and *Planck* (Collaboration 2013) combined with standard BBN models, resulting in $A(\mathrm{Li})_{\mathrm{BBN}} = 2.69 \pm 0.04$ (Coc et al. 2013). Further production of Li can happen by spallation of heavier nuclei by energetic cosmic rays, or in AGB stars via the Cameron–Fowler mechanism, where $^7\mathrm{Be}$ created at the bottom of the convective envelope $(^3\mathrm{He}(\alpha,\gamma)^7\mathrm{Be})$, travels to cooler regions and captures an electron $(^7\mathrm{Be}(e,\nu)^7\mathrm{Li})$ (Sackmann & Boothroyd 1992). The last two production sites requires an evolved Universe, with cosmic rays and AGB stars, to contribute to the Li abundance in the Universe. In the early metal-poor Universe only Li produced in the Big Bang Nucleosynthesis is present.

Li burns at low temperatures (T $= 2.5 \times 10^6$ K), this means it is easily destroyed in stars with deep convective envelopes, where the surface Li is brought down to regions hot enough for Li burning, thus depleting the Li abundance at the surface of the star.

Signatures

Spite & Spite (1982) detected similar Li abundances ($A(\mathrm{Li}) = 2.05$) for a sample of metal-poor dwarfs (T$_{\mathrm{eff}} = 5700 - 6250$ K), independent of metallicity in the range $-2.4 \leq$ [Fe/H] ≤ -1.4, now referred to as the Spite Plateau. This Li abundance is believed to reflect the BBN Li production, but is significantly below what is found from the microwave background radiation. When moving to lower metallicities, Sbordone et al. (2010) reported

---

$^2 A(\mathrm{Li}) = \log(N(\mathrm{Li})/N(\mathrm{H})) + 12$, see section 2.1.7 for further information.
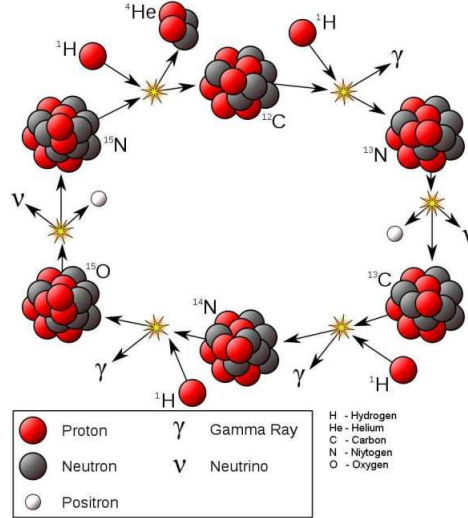
Figure 1.1: Overview of the Carbon-Nitrogen-Oxygen cycle fusing four protons using C, N, and O isotopes as catalyst (Figure from www.whillyard.com).

on a melt down of the Li plateau, suggesting some depletion of Li in the early Universe. Recently Mucciarelli et al. (2014) measured the Li abundance of lower red giant branch stars in the globular cluster M54, and found values similar to the Spite Plateau, concluding that the missing Li problem is universal.

Lithium abundances have not been explored widely in CEMP stars, but a compilation of the literature data plus additional new data was done by Masseron et al. (2012), who report on the Li abundances or upper limits of 44 CEMP stars (including all sub-classes no, s, r, r/s). They find a very large spread in the Li abundances of CEMP stars, but specifically for the CEMP-no stars, no stars are found with a Li abundance above that of the Spite Plateau.

1.4.2 Carbon, nitrogen and oxygen

Formation

Stars of all masses produce carbon, nitrogen and oxygen, either expelled from the star in winds, or during the final SN explosion.

Carbon is created in triple α reactions; $3\,^4\mathrm{He}(,\gamma)^{12}\mathrm{C}$ during He burning. Oxygen, among other elements, is created via successive α captures on $^{12}\mathrm{C}$. Nitrogen can be produced as a result of H burning via the CNO cycle shown in Figure 1.1, which has the following reaction chain:

$$^{12}\mathrm{C}(^1\mathrm{H},\gamma)^{13}\mathrm{N}(e^+,\nu_e)^{13}\mathrm{C}(^1\mathrm{H},\gamma)^{14}\mathrm{N}(^1\mathrm{H},\gamma)^{15}\mathrm{O}(e^+,\nu_e)^{15}\mathrm{N}(^1\mathrm{H},^4\mathrm{He})^{12}\mathrm{C}. \tag{1.3}$$
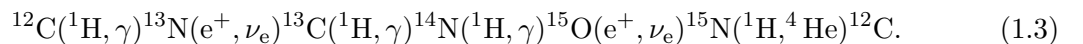
The reaction $^{14}\mathrm{N}(^1\mathrm{H},\gamma)^{15}\mathrm{O}$ has the smallest probability, hence the CNO cycle effectively converts $^{12}\mathrm{C}$ to $^{14}\mathrm{N}$. Running of the CNO cycle also result in a lowering of the $^{12}\mathrm{C}/^{13}\mathrm{C}$

ratio, which becomes a powerful diagnostic of the level of CN processing. The equilibrium value of the carbon ratio reached in the CNO cycle is $^{12}C/^{13}C \sim 4$.

In low- and intermediate mass stars ($M \sim 1 - 8 M_\odot$), the C, N and O can be mixed to the surface of the star during dredge-up episodes, most prominently during the third dredge up (TDU) episodes in the AGB phase, where the elements are also expelled from the star in stellar winds. Evolved low- and intermediate mass stars will thus show a decrease of the surface C abundance, but an increase of the surface N abundance, as C from the surface is mixed down to H burning layers, where it is converted to N via the CNO cycle, which is then brought to the surface. The derived abundances of C and N in evolved stars will as such not reflect the chemical composition of the ISM from which the star formed, but processes in the star itself. For un-evolved stars however, the C and N abundances can be used to access the level of mixing that has happened in the progenitors of the stars.

In the early Universe, two external sources of C, N an O have been proposed:
The first are the spinstars, i.e., fast rotating massive stars at very low metallicity (Meynet et al. 2006; Hirschi 2007). Due to the lack of C at low metallicity, these stars start burning H via the pp chains, but this is not efficient enough to stop the gravitational collapse of the star. The star will therefore continue to contract, until it reaches temperatures in the core where triple α reactions can create C. With this C the star can start burning H via the CNO cycle, and it stops contracting.

These massive, almost metal-free stars in the early Universe have been found to rotate very fast, close to break-up velocities (Maeder & Meynet 2001). The rotation induces a shear mixing[3], which mixes the elements between the different burning zones (He and H), continuously feeding the burning zones with new fuel (Maeder & Meynet 2001). Models of these stars predict them to produce large amounts of C, N and O (Meynet et al. 2006). Also, the $^{12}C/^{13}C$ ratio is predicted to be low (30-300) due to the large degree of CN processing by the CNO cycle (Chiappini et al. 2008).

Another possible source of large amounts of C, N and O in the early Universe are the so-called mixing and fallback SN (Umeda & Nomoto 2002). In the mixing and fallback models, during the explosion, a reverse shock is formed when the core hits the surrounding He and H envelopes. This reverse shock decelerates the expansion of the core. At the interfaces between the different burning regions H/He, He/C+O and O/Si, Rayleigh Taylor instabilities[4] are induced by this slow down of the core expansion (Ebisuzaki et al. 1989; Arnett et al. 1989). This results in mixing between the layers. Secondly the reverse shock can also make matter fall back on the remnant (Kifonidis et al. 2000).

Umeda & Nomoto (2002) show that the following two steps always happen to some extent in a SN explosion: 1) burned material mixes uniformly in a zone between an initial mass cut and the top of the incomplete Si burning zone; 2) the mixed material below a final mass cut falls back on the remnant. This means more of the light elements are expelled into the ISM, whereas the heavy elements fall back on the remnant. An example of yields for mixing and fallback SN models from Umeda & Nomoto (2005) are shown in Figure 1.2. Here the yields for four SN with same mass and metallicity (50 $M_\odot$ and $Z = 10^{-4}$), but varying exploding energies, and degrees of mixing and fallback, are compared with the

---

[3]Shear mixing is mixing occurring when two neighboring fluid layers have different velocities.

[4]Rayleigh Taylor instabilities are instabilities forming at the interface between two fluids with different density, when the lighter one pushes the heavier one.
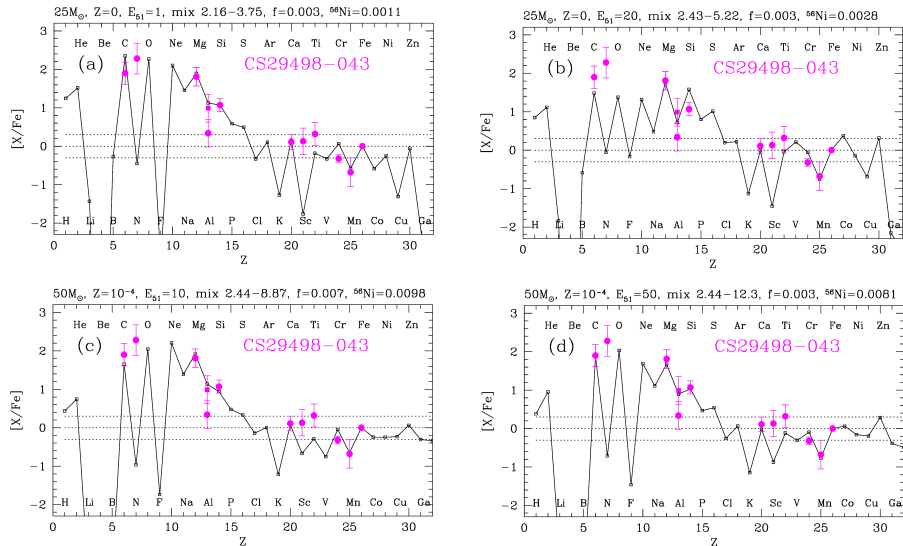
Figure 1.2: Yields from mixing and fallback SN models from Umeda & Nomoto (2005) compared to the abundance pattern of the CEMP-no star CS 29498−043. The different panels show yields for different values of explosion energy,and mixing and fallback for a model with a mass of 50 M$_\odot$ and metallicity Z = 10^{-4} ([Fe/H] = 2.3).

abundance pattern of the CEMP-no star CS 29498−043, highlighting the large production of carbon in this type of SN.

Signatures

Spite et al. (2005) found a large (>2 dex) scatter in the carbon and nitrogen abundances in their sample of metal-poor stars. They separated the stars into a mixed ([N/Fe] > 0.5) and an un-mixed ([N/Fe] < 0.5) group, where the mixed where more evolved stars, showing evidence of CN processing in the surface abundances of C and N (i.e. a decrease in C and increase in N, as described above). The mixed stars also showed strong Li depletion. The two groups of stars can be seen in Figure 1.3; dots represent the unmixed stars with low N, and open circles the mixed stars with higher N abundances. This result emphasize that when determining the C and N abundances of stars, the evolutionary status of the star need to be taken into account. Placco et al. (2014c) developed a method to correct for this evolutionary effect on the abundances. This is described in greater detail in section 4.4.1.

A large fraction, ∼20% of stars with [Fe/H] ≤ −2 have been found to be enhanced in carbon (Beers & Christlieb 2005). These CEMP stars were originally identified among the metal-poor stars discovered a quarter-century ago by the HK survey of Beers, Preston, & Shectman (Beers et al. 1985, 1992), and supplemented by numerous surveys since. Recent studies, such as Carollo et al. (2012), Lee et al. (2013), Cohen et al. (2013) and Norris et al. (2013b) confirm that CEMP stars constitute a large fraction of the most metal-poor stars known. A strong increase in the fraction of CEMP stars is also found with decreasing metallicity, from ∼ 3% at [Fe/H] < −1 to ∼ 75% at [Fe/H] < −4 (Marsteller et al. 2005; Lucatello et al. 2006; Lee et al. 2013; Placco et al. 2014c). However, Cohen et al. (2013)
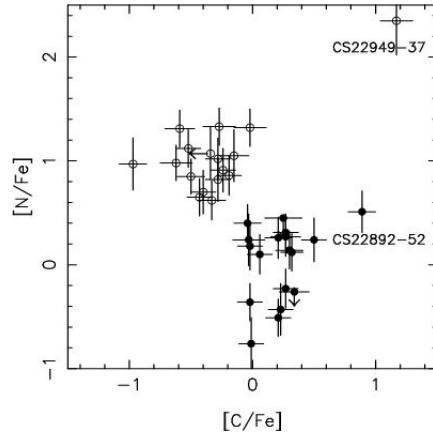
Figure 1.3: [N/Fe] vs [C/Fe] for the sample of 35 extremely metal-poor giants from Spite et al. (2005). The plot clearly shows a group of unmixed stars (dots) and group of mixed stars (open circles).

note that the CEMP stars are overrepresented in their sample, due to a selection effect in the algorithm of Beers et al. (1998), used to select metal-poor candidates from the HES survey. The algorithm underestimated [Fe/H] in carbon enhanced stars, thus an unreal large fraction of metal-poor candidates selected with this algorithm was C-rich (Cohen et al. 2005).

Recently, Spite et al. (2013) examined the carbon abundances of dwarfs and turnoff stars, in which mixing has not altered the carbon abundance at the surface. They suggest the presence of two plateaus of the carbon abundances, one for [Fe/H] > -3.0 at $A(C) \sim$ 8.25, and one for [Fe/H] < -3.4 at $A(C) \sim 6.8$. They point to the low number of stars observed with [Fe/H] < -3.4, and highlight the difficulty of observing carbon in warmer, unmixed stars. As a result, they could not conclude if the lower plateau is just an upper limit on the detections, or an actual plateau. The work of Bonifacio et al. (2015) has confirmed the existence of two carbon plateaus, or bands, in the carbon abundances of CEMP stars. The interpretation of these two bands is that stars on the higher C-band has gained their carbon abundance from an external source (mass transfer in binary system). Where as stars on the lower C-band, was born with their large C abundance (Spite et al. 2013).

1.4.3 Light and α elements

Formation

The light and α elements includes; sodium (Na), magnesium (Mg), aluminum (Al), silicon (Si), calcium (Ca), and titanium (Ti), all produced in massive stars (M $> 8M_\odot$) during hydrostatic carbon and neon burning, and during complete and incomplete silicon burning, in some cases explosive. Na and Al are also produced in the Ne-Na and Mg-Al cycles, that operate alongside the CNO cycle in H burning regions, when the temperature is high $(40 - 70 \times 10^6 \text{K})$. At low metallicities, the stars are hotter and denser than their metal-rich counterparts, meaning that these cycles are active in spinstars (Meynet et al. 2010). Na and Mg are also expected to be produced in low-metallicity AGB stars (Gallino et al. 2006),
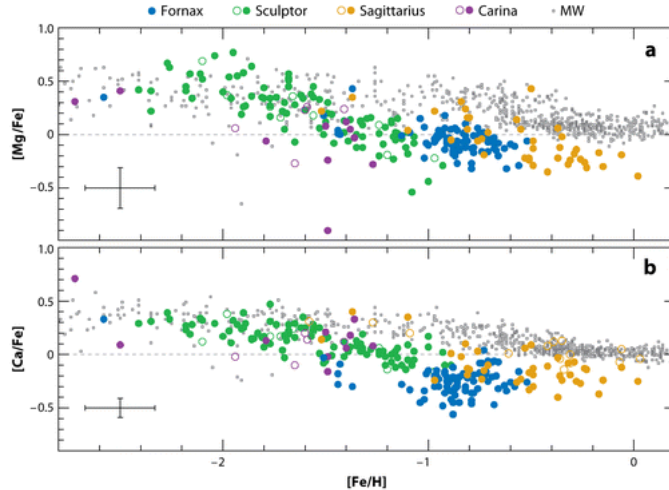
Figure 1.4: Mg (top) and Ca (bottom) abundances as function of metallicity for stars in the Milky Way (grey points) and stars in dwarf galaxies (coloured point). Clearly showing the different onset time for the Ia SN in the different galaxies (Tolstoy et al. 2009).

where there is a large production of ^{22}Ne from ^{14}N. During the thermal pulses, neutron- and α-capture on ^{22}Ne creates ^{23}N, and ^{25,26}Mg respectively, that are dredged up to the surface in the TDU episodes, and expelled to the ISM via stellar winds.

Signatures

Calcium and titanium are so-called α-elements. For these, several abundance analysis studies have found a small over-abundance in metal-poor stars, along with very small scatter ($\sim$0.1 dex) in the abudances (Cayrel et al. 2004; Yong et al. 2013). This very uniform level of $[\alpha/\text{Fe}] \sim 0.4$, over a vide range of metallicities, is interpreted as the signature of core-collapse SN in the early Universe. It is found up to the metallicity where type Ia SNe, that mainly yield C, O and Fe, start to explode, increasing the iron content in the Universe, and hence lowering the α to Fe abundance ratio. This transition in the $[\alpha/\text{Fe}]$ at the onset of the Ia SN is the so-called knee in the α abundances, which trace the star formation rate of the galaxy and its ability to build up chemical elements (Tinsley 1979). A slowly enriched galaxy will have the α knee at low [Fe/H], whereas a fast enriched galaxy will have the knee at a higher [Fe/H] ratio. This is clearly shown in Figure 1.4 taken from Tolstoy et al. (2009), where Mg and Ca abundances are plotted as function of metallicity for stars in the Milky Way and different dwarf galaxies.

The abundances of Na, Mg, Al and Si are found to be greatly enhanced, as much as 2-3 dex, in some CEMP stars, and in general show a larger scatter than the alpha elements in these stars, in some cases increasing with decreasing metallicity (Norris et al. 2013b). In the NMP stars Mg and Si follow the picture of the other alpha elements, where as the abundances of Na and Al show a larger scatter $\sim$0.2 dex (Cayrel et al. 2004; Yong et al. 2013).

It should be noted that Cohen et al. (2013) found a small sub-group, $\sim$10% of Ca deficint stars in their sample of NMP stars. Also Caffau et al. (2013a) have found evidence of a group

of α-poor stars, suggested to be the metal-poor counterpart, of the low-α halo population found by Nissen & Schuster (2010) in the metallicity range $-1.6 < [\text{Fe/H}] < -0.4$

1.4.4   Iron group elements

Formation

The iron group elements are cromiun (Cr), manganese (Mg), iron (Fe), cobalt (Co), nickel (Ni) and zink (Zi), all produced in massive stars during complete or incomplete silicon burning, and in SN explosions.

Signatures

Cayrel et al. (2004) investigated the abundances of the iron-peak elements in metal-poor stars. Their results are shown in Figure 1.5. Inspection of the differnt panels in Figure 1.5 reveal the following trends for the iron group element abundances in metal-poor stars: [Cr/Fe] show a decreasing trend with decreasing metallicity, Mn show no trend with metallicity but is found to be deficient with respect to iron, [Co/Fe] show a slight increasing trend with decreasing metallicity, [Ni/Fe] show a mean value close to zero, independent of metallicity, and [Zn/Fe] increases with decreasing metallicity. However, the lines of some of these elements are strongly affected by Non Local Thermodynamic Equillibrium (NLTE) effects[5]. The trend in [Cr/Fe] disappears when correcting for NLTE effects (Bergemann & Cescutti 2010b), whereas the trend found for Co seems to be enhanced by NLTE effects (Bergemann et al. 2010a). Regardles of possible NLTE effects, what is striking, is the very small scatter found in the derived abundances of most of the iron peak elements (Cayrel et al. 2004; Yong et al. 2013; Roederer et al. 2014b). As low as 0.05 dex for [Cr/Fe] was found by Cayrel et al. (2004), who interprets this as a signature that the abundances are the result of a burst of enrichment events or promptly mixing of the ISM after an event.

1.4.5   Neutron-capture elements

Formation

Most elements beyond the iron peak are produced by neutron capture, where a neutron is absorbed by a nucleus. Adding neutrons to an element usually takes it away from stability, and it will eventually decay via beta decay ($n \to p + e^-$). Neutron captures can happen either in the (slow) s-process, where the neutron capture timescale is shorter than the beta decay timescale, or the (rapid) r-process, where consequtive neutron captures happen, taking the element far away from stability, before beta decays happen (Burbidge et al. 1957; Sneden et al. 2008). The paths of the s- and r-process, along with their indivudual production of elements, are illustrated in Figure 1.6. Each of the processes produce about half of the heavy elements. Elements with the most stable configuration of neutrons, so-called magic neutron numbers, have very low neutron-capture cross-section and acts as bottlenecks in the reaction chain. This results in peaks in the s-process abundance pattern. Similar peaks are seen in the r-process abundance patterns produced by decay of unstable nuclei with

---

[5]The concept of NLTE is explored further in section 2.1.8.
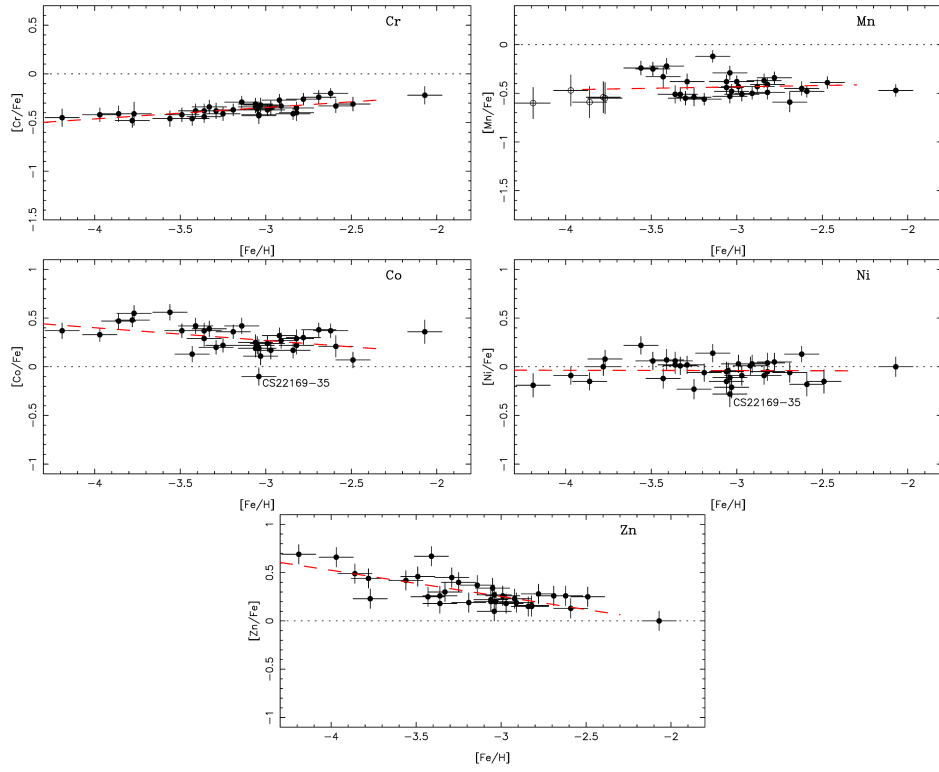
Figure 1.5: Derived abundances for the iron-peak elements as function of metallicity from Cayrel et al. (2004). All elements show very little scatter in the derived abundances. The different elements show different trends with metallicity, but some trends may be due to NLTE effects.
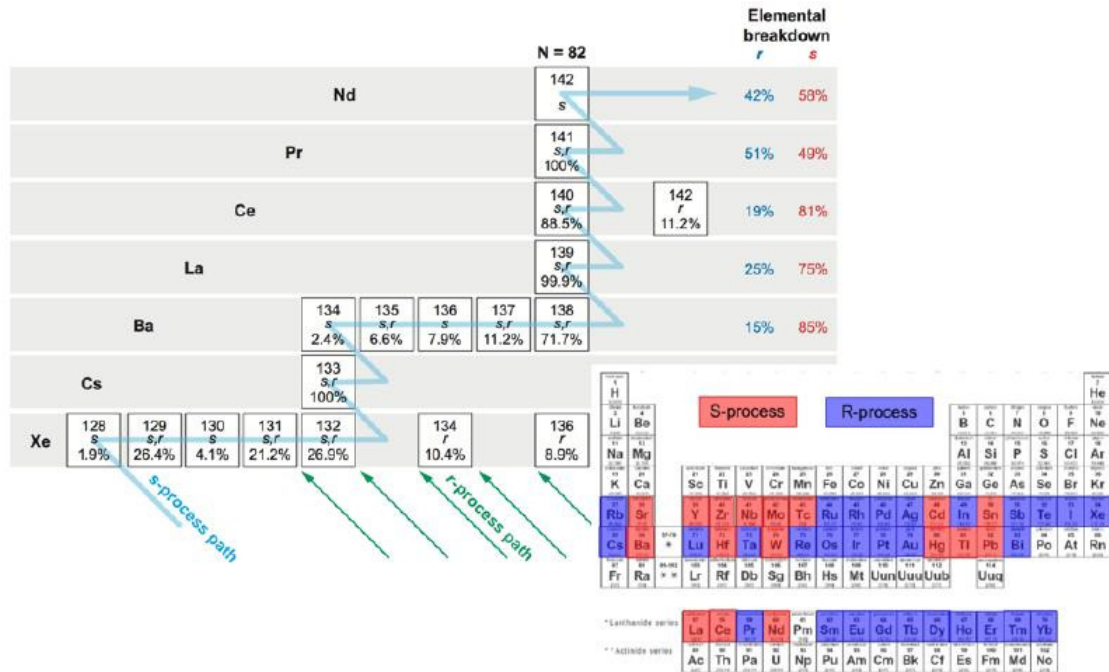
Figure 1.6: Path of s- and r-process, along with element production by the two processes (Sneden et al. 2008)

magic numbers. The s-process has the following peaks; first: Sr, Y, Zr, Second: Ba, La, Ce and third: Pb, Bi. For the r-process the peaks are; first: Se, Br, Kr, second: Te, I, Xe and third: Os, Ir, Pt. The Solar system abundance pattern, including the s- and r-process is shown in Figure 1.7.

s-process The s-process has a main component, happening in low-mass stars, and a weak component taking place in massive stars.

In low-mass stars, the s-process takes place during the thermal pulse AGB phase. The star here consist of a C-O core and two alternate burning H and He shells and consequitive TDU episodes happen. During a TDU, the convective H envelope reaches down to the He intershell region, which is rich in ^{12}C. Protons penetrate the He intershell and capture on the ^{12}C (^{12}C(^{12}C(p,γ)^{13}N($\beta\nu$)^{13}C), creating what is called a ^{13}C pocket. This pocket is compressed and heated, till at some point the reaction ^{13}C(α,n)^{16}O happens. This process creates a steady neutron flux over a period of $\sim$10,000 years, facilitating the s-process. The s-process elements created are mixed to the surface at the next TDU episode, and the cycle continues. From the surface they are expelled to the ISM via stellar winds (Busso et al. 1999; Käppeler et al. 2011).

A second, weaker, neutron source in low-mass stars is the reaction: ^{22}Ne(α,n)^{25}Mg. Here, primary ^{12}C is mixed with the envelope during TDU. In the H shell it is converted to ^{14}N via the CNO cycle, this then is converted into ^{22}Ne via ^{14}N(α,γ)^{18}F($\beta^+\nu$)^{22}Ne in the He shell. At the base of the thermal pulse, the Ne-Mg reaction happens, creating a small neutron flux. Alternatively, neutrons can also capture on the newly-synthesized ^{22}Ne, forming heavier elements up to iron, and thereafter s-process elements (Gallino et al. 2006).
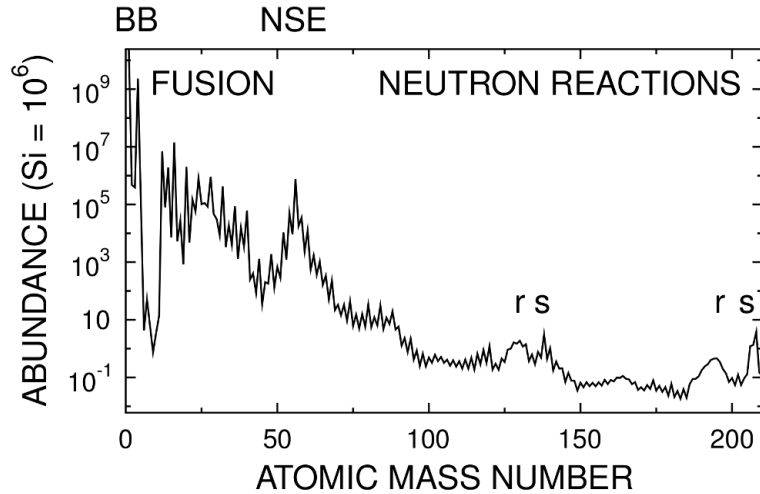
Figure 1.7: Solar system abundance pattern with s- and r-process abundance peaks (Reifarth et al. 2014).

The production of ^{22}Ne is important in low-metallicity ([Fe/H] < -2) AGB stars, because larger amounts of ^{12}C are mixed with the envelope at each TDU episode (Bisterzo et al. 2010).

The distribution of elements produced in the main s-process is quite different for high and low metallicity environments, due to the lack of seed nuclei at low metallicity. This results in more neutron-captures per seed nucleus at low metallicity, giving an abundance pattern where third peak elements, such as Pb, will dominate (Bisterzo et al. 2010).

In massive stars, the reaction ^{22}Ne(α,n)^{25}Mg acts as the neutron source. This happens during the convective He core burning, and in the subsequent convective shell C burning. ^{22}Ne is produced from the ^{14}N left over from the H burning via the CNO cycle, in the reaction given above (Käppeler et al. 2011). The synthesized elements are expelled during the SN explosion, where the ejected C shell carries the unchanged s-process signature of the previous burning phases with it (Pignatari et al. 2008).

The weak s-process in massive stars is a secondary process, as the neutron source ^{22}Ne is produced from secondary elements, and the seed nuclei are secondary. This means the efficiency of this process decreases with decreasing metallicity. However, rotation is predicted to have a large impact on the efficiency of the weak s-process (Pignatari et al. 2008). As described above, large amounts of ^{14}N are produced in the rotating massive spinstars, when ^{12}C from the convective He core is mixed into the convective H shell, where the CNO cycle operates. Parts of the ^{14}N are mixed back down into the He core, and ^{22}Ne is produced via the reaction given above. Close to the He exhaustion, the Ne-Mg reaction is activated, facilitating the s-process (Pignatari et al. 2008). Generally, the light s-process elements (Sr, Y, Zr) are produced in the s-process in spinstars, with [Sr/Ba] > 0; only in extreme cases does the production run all the way through to Pb (Frischknecht et al. 2012). The amount of s-process elements formed is highly dependent on the amount of ^{22}Ne created,

hence on the level of rotation induced mixing, but also on the efficency of so-called neutron poisons, such as ^{16}O. ^{16}O can capture a neutron via the reaction ^{16}O(n,γ)^{17}O, the ^{17}O then reacts further, either via ^{17}O(γ,n)^{20}Ne, recycling the neutron, or via ^{17}O(α,γ)^{21}Ne loosing the neutron. The rate of these two reactions is very uncertain, and hence also their effect on the efficiency of the weak s-process in spinstars (Frischknecht et al. 2012).

Due to the life times of low-mass stars before they reach the AGB phase ($\sim$1 Gyr), the main s-process can not have contributed to the neutron-capture element abundances in the early Universe. The onset of the contribution from the main s-process is seen at [Fe/H] ~ -2.5 (François et al. 2007). The weak s-process may have operated already in the very first stars and may have contributed to the abundances in the early Universe, though with some uncertainty on the efficiency as a result of unknown neutron poison effects and the lack of seed nuclei at low metallicity (Pignatari et al. 2008; Frischknecht et al. 2012).

r-process Contrary to the s-process, the location of the r-process is poorly constrained. It is believed to happen during the core collapse SN explosions of massive stars, possibly in the high entropy, neutrino-driven wind expelled from the newly formed neutron star (Meyer et al. 1992; Woosley et al. 1994; Arcones & Montes 2011), or in jets created in the explosion (Winteler et al. 2012). Another promising site are neutron star mergers. These are very extreme environments, where the heavy elements far from stability are quickly created. The heavy elements will fission and neutron capture will happen again on the fission products. Multiple of these fission cycles create very robust r-process pattern from these events (Freiburghaus et al. 1999; Goriely et al. 2011).

Signatures

The neutron-capture elements strontium (Sr) and barium (Ba) are those that are most easily measured in low-metallicity stars, unless the star shows enhancements in neutron-capture elements such as the CEMP-s, -r, and -r/s stars, or the r-I and r-II stars. Several abundance analysis works have found a scatter of several dex in the abundances of these two elements for the NMP stars, pointing to the existence of more than one formation site/process (François et al. 2007; Hansen et al. 2012, 2013; Yong et al. 2013).

Aoki et al. (2002d) studied a sample of eight CEMP-s stars and found a large spread in the abundances of s-process elements detected in these stars. They find large over-abundances (1-3 dex) for most of the s-process elements in all stars, and in particular Pb is detected in seven of the eight stars, all with [Pb/Fe] > 1.6. Similarly Cohen et al. (2006) also detects large amounts of Pb in the CEMP-s stars in their sample. More recently, Placco et al. (2013) reported on the discovery of two new CEMP-s stars, for which they compare their derived abundances with literature data. Generally larger over-abundances, $\sim$2 dex, are derived for the heavy s-process elements, Ba and La, while over-abundances of $\sim$1 dex is generally found for the lighter s-process elements, such as Sr, Zr, and Y. For all a spread of several dex are found in the derived abundances. Finally, in line with the results from Aoki et al. (2002d) and Cohen et al. (2006), Placco et al. (2013) also find that their stars are enhanced in Pb by 3 - 4 dex.

Studies of the r-process enhanced stars (both CEMP and non C enhanced) have shown the abundance patterns for the heavy neutron-capture elements ($56 \lesssim \mathcal{Z} \lesssim 77$) is similar in these stars and scales with the Solar system r-process pattern (Sneden et al. (2008) and

references there in). For the lighter r-process elements ($\mathcal{Z} < 56$), a larger spread is seen in the abundances. It has been proposed that a second, weak r-process is responsible for the formation of the light r-process elements (Travaglio et al. 2004; Montes et al. 2007; Hansen & Primas 2011).

1.5 Sources of halo stars

The Milky Way galaxy continuously accrete smaller systems orbiting around it, such as dwarf galaxies and clusters. Thus the stars found in the halo may not have been formed in the Galaxy but rather in these smaller systems. The study of the abundance signatures of stars in these systems is an important tool to identify stars lost from these systems to the Milky Way halo. A brief introduction to the abundance signatures found for stars in dwarf galaxies and globular clusters is given below.

1.5.1 Dwarf galaxies

The term dwarf galaxy covers a wide range of low mass, low luminosity galaxies. Such as, the ultra-faint dwarfs with $10^3 <L_\odot< 10^5$, and the classical dwarfs with $10^5 <L_\odot< 10^8$. Kirby et al. (2008) was the first to discover extremely metal-poor stars in dwarf galaxies. These authors found 15 stars with [Fe/H] < -3 in 7 ultra faint dwarfs. Later more stars have been detected also in other types of dwarf galaxies (see Frebel & Norris (2015), and references therein). In general the metal-poor stars in dwarf galaxies have the same chemical signatures as what is found for metal-poor stars in the Milky Way halo. Carbon-enhanced stars have been identified in the ultra faint but not yet in the dwarf spheroidal (dSph) galaxies (Frebel & Norris 2015). In the ultra-faint dwarf galaxies no stars are found with [Fe/H] > -1.5 which is interpreted as some truncation of the chemical evolution in these. Also the α-knee is generally placed at low metallicities in the dSphs, which is a signature that these systems has experienced a slower chemical enrichment. Sr and Ba have been detected in a number of dwarf galaxy stars. In the ultra-faint dwarfs very low abundances are found for these elements compared to halo stars of same metallicity, this effect is less pronounced in the classical dwarfs (Frebel & Norris 2015).

1.5.2 Globular clusters

Globular clusters (GC) are dense systems of stars, some of which may be as old as the Universe. They have been subject to intense investigation, as they presumably are excellent examples of simple stellar populations; large samples of stars with same age and chemical composition. However, these investigation have shown that GC are not the simple stellar systems once thought. Several chemical peculiarities have been detected in these systems. Large variations have been found in the C, N, O, Na and Al abundances of GCs. Clusters with high N are found to have low C or vice versa, varying from cluster to cluster with many showing a bimordial distribution of CN strength. Additionally the Na, Al and Mg abundances are correlated with the CN band strength in metal-poor clusters (Kraft 1994; Smith 1987). Pilachowski (1989) and Drake et al. (1992) suggested that the Na and O abundances were anticorreleted in the clusters M13 and M4 respectively. Later this signature has been

found in many GCs (Gratton et al. 2004). A clear correlation of Na and Al abundances is also observed in several clusters (Ivans et al. 2001) along with a Mg-Al anticorrelation (Kraft et al. 1997), though less prominent in the most metal-poor objects (Gratton et al. 2004). The behavior of the α and iron-peak elements in GC are found to be similar to field stars of the same metallicity. Also the neutron-capture element abundances (Ba and Eu) from GC stars follow that of the field stars (Gratton et al. 2004).

1.6   Binary stars

Since VMP and EMP halo stars probe the earliest epochs of chemical evolution in the Galaxy, their elemental abundance patterns reflect the products of the primary heavy-element synthesis and enrichment processes in the early Galaxy. However, as described above, significant samples of chemically peculiar stars have been identified, in particular among the VMP and EMP stars. Because anomalies affecting a single element or group of elements must be produced by a small number of nucleosynthesis events (including possible single events), the chemically peculiar stars provide the opportunity to characterize the progenitors and enrichment processes that produced the abundance patterns in the long-lived metal-poor stars seen today.

However, in the more metal-rich Population I and II stars, some chemical anomalies are known to be due to evolution in a close binary system (e.g., Ba and CH stars; McClure et al. (1980); McClure (1984); R.D. & A.W. (1990)), in which a higher-mass binary companion has evolved to the AGB stage. Through processes involving Roche-lobe overflow and/or wind accretion, the higher-mass star is expected to have contaminated the envelope of its surviving companion with any elements that formed during its final evolutionary stages. This mechanism could explain the presence of elements produced in the early Universe by stars more massive than $\sim$0.7 M$_\odot$ (i.e., with main-sequence lifetimes less than the Hubble time), but does of course require the presence of a binary companion, which by now is presumably a white dwarf or neutron star.

Hence, for the chemically peculiar VMP and EMP stars, a crucial first step is to establish whether any such putative binary companions actually exist, and to determine their main orbital parameters (i.e., period, semi-major axis, and eccentricity). This requires radial-velocity monitoring of adequate precision and duration for a sufficiently large sample of stars. High spectroscopic resolution ($R \lesssim 30,000$) allows one to determine radial velocities efficiently by cross-correlating even a relatively low-S/N spectrum with an appropriate template, while long-term thermal and mechanical stability of the spectrograph employed is needed in order detect variations with amplitudes below 1 km s^{-1}.

The radial-velocity monitoring of r-process enhanced stars, CEMP-no, and CEMP-s and CEMP-r/s is described in chapters 5, 6 and 7 respectively.

1.7 This thesis

The aim of this thesis is to combine the results of detailed abundance analysis with radial velocity monitoring of metal-poor stars, in order to constrain the sequence of events leading to the formation of the different types of stars described above. The abundance analysis have been carried out for a sample of 24 stars, containing a mixture of the different sub-groups. While samples containing four different sub-classes of metal-poor stars been monitored for radial-velocity variations, namely 24 CEMP-no stars, 18 CEMP-s, and 4 CEMP-r/s stars, and 17 r-I + r-II stars. There is no overlap of stars between the different samples. The thesis is organized as follows: Chapter 2 presents the different methods used for the analysis, Chapters 3 and 4 present the results of the abundance analysis, while Chapters 5, 6 and 7 present the results of the radial-velocity monitoring of r-process enhanced stars, CEMP-no stars, and CEMP-s and CEMP-r/s stars, respectively. These results are discussed in Chapter 8 and finally a outlook is given in Chapter 9.

CHAPTER 2

Methods

The two main tools I have used, for the work presented in this thesis, are abundance analysis and determination of a stars binarity from radial-velocity monitoring. Below the two methods are described, with the tool sets needed for the individual analyses.

2.1 Abundance analysis

To derive abundances of different elements from their absorption lines in the observed stellar spectrum, i.e. converting the integrated area of the absorption lines to abundances, the following input described in detail below is needed: a model atmosphere of the star, computed from knowledge of the stellar parameters; effective temperature (T_{eff}), gravity ($\log g$), metallicity ([Fe/H]), and microturbulence (ξ); along with the stellar model atmosphere a line list with information of the atomic and molecular line transitions is needed.

2.1.1 The stellar atmosphere

The gas in stellar atmospheres consist mainly of hydrogen (X$\sim$74%) and helium (Y$\sim$24%). The heavy elements (Z) make up only a small fraction ($< 2\%$) of the total mass per volume for Sun-like stars. The velocity field of the particles in the gas is governed by the Maxwell-Boltzmann distribution, given by:

$$f(v) = (4\pi \frac{m}{2\pi kT})^{3/2} \exp(-\frac{mv^2}{2kT})v^2 \tag{2.1}$$

where m is the gas particle mass, k is the Boltzmann constant and T is the temperature of the gas. The pressure in the gas is a combination of the particle pressure and the radiation pressure. From an abundance analysis point of view we are mostly interested in the transport of light (energy) through the stellar atmosphere and to our telescopes. From this light we can determine the composition of the star and its intensity. The specific

intensity I_λ is defined as:

$$I_\lambda = \frac{E_\lambda d\lambda}{d\lambda dt dA \cos\theta d\omega}.$$ (2.2)

and gives the amount of energy in a given wavelength range which flows from the star per time through a given surface area in a given direction. As the light travels through the atmosphere some of this will be scattered and some will absorbed and (re-) emitted. The degree to which these processes happen is described by the absorption coefficient κ and the emission coefficient j. The ratio between these two at a given wavelength (or frequency) is described by the source function, $S_\lambda = j_\lambda/\kappa_\lambda$. The absorption coefficient and the density (ρ) of the gas determine the mean free path of the photons. This is conveniently described by the optical depth parameter, τ, which is defined as:

$$d\tau_\lambda = -\kappa_\lambda \rho ds$$ (2.3)

where s is the distance traveled by the photon. A high optical depth, $\tau >> 1$ corresponds to an optically thick gas, where the mean free path of the photons is short. On the other hand a low optical depth, $\tau << 1$ corresponds to an optically thin gas. When observing a star in a given wavelength we see through the surface layers down to $\tau_\lambda \sim 1$. At the top of the atmosphere we have $\tau_\lambda \sim 0$, as the photons essentially travel un-hindered from this point to the observer.

There is a net transport of radiation moving outwards in the star as a result of the drop in radiative pressure with increasing distance from the center, due to the decreasing temperature. This transportation is described by the radiative transfer equation:

$$-\frac{1}{\kappa_\lambda \rho}\frac{dI_\lambda}{dS} = I_\lambda - S_\lambda.$$ (2.4)

In addition to radiative transport convective energy transport can also take place. The convective energy transport happens when gas elements, that are hotter, and lighter than the surrounding gas, rise and more heavy, and cool elements sink. Radiative energy transport is the dominant form of energy transport in the stellar photosphere. But some stars have convective envelopes that reach all the way up to the bottom of the photosphere and here convective energy transport plays a role.

2.1.2   Model atmospheres

To derive elemental abundances from a stellar spectrum we construct a model atmosphere of the star. The model atmosphere describes the relation between the temperature, electron pressure, absorption coefficient and density of the gas at different optical depths.

A number of assumptions are usually made when calculating 1D model atmospheres:

- The atmosphere is assumed to be one dimensional (1D) and plane parallel, so the physical properties only depend on one space coordinate, the vertical optical depth.

- Hydrostatic equilibrium

- Structure like granulation and star spots is neglected and no magnetic fields are included

- Local Thermodynamic Equilibrium (LTE)

Assuming thermodynamic equilibrium means that the gas and radiation in the star are in equilibrium, i.e. every process happens at the same rate as its inverse. This is of course not true for the entire star, as there is a net transport of energy from the center to the surface. What is used is then a local thermal equilibrium. In LTE it is assumed that the average distance traveled by the particles and photons is much smaller than the distance over which the temperature changes. In this approximation one physical temperature can be ascribed to a given depth. The temperature dependence on depth is found by assuming radiative equilibrium. When assuming the star is in radiative equilibrium, all energy created in the center reaches the surface, and there are no extra sinks or sources of energy. The pressure dependence on the depth is derived by assuming ionization equilibrium. In models where LTE is assumed the source function is that of a black body, namely the Planck function, $B_\lambda(T) = \frac{2hc^2/\lambda^5}{e^{hc/\lambda kT}-1}$. Convection in 1D LTE models is treated with the so-called mixing length theory, describing the length an element of gas will move before mixing with the surroundings. The assumption of LTE is a good approximation for the deeper layers of the star, where the energy transport is dominated by collisions in the gas. In the outer layers of the star, where radiative energy transport is dominate, the assumption breaks down.

2.1.3 Stellar parameters

To construct the model atmosphere we need a set of stellar parameters describing the star. The determination of stellar parameters is a crucial step in the abundance analysis procedure. Several methods can be used to derive the parameters. For stars with available high-resolution, high signal-to-noise spectra, where multiple Fe I and Fe II lines can be detected, the parameters can easily be determined spectroscopicly. However, in metal-poor stars, Fe lines are less abundant and other methods may be used.

Spectroscopic determination of $T_{\rm eff}$ is done by using the fact that at a higher temperature more of a given element will be exited or ionised. Furthermore, any given cool star can only have one abundance of a given element, representative of the surface composition. We can therefor use the excitation equilibrium to determine the temperature, ensuring that the abundance of a given element (usually iron) is independent of the excitation potential of individual lines of this element. To get a reliable temperature, iron lines covering a large range in excitation energies are needed. With only a few iron lines detected in the metal-poor stars analysed in this thesis, getting reliable temperatures from excitation equilibrium was not possible. The temperatures for the stars analyzed in chapter 3 and 4 are therefore derived by fitting spectrophotometric (wide spectral range) observations of the stars with synthetic spectra. The model atmospheres used for this are described in more detail in section 4.2 in chapter 4. For some stars we did not have spectrophotometric observations. For these stars the temperatures are determined from photometry, using an empirical relation between the photometric color (e.g., $V - K$) of a star and its temperature and metallicity (see section 4.2).

The gravities of the stars are determined from isochrones. Isochrones are evolutionary tracks of stars with a given age and metallicity. A certain temperature corresponds to a given point in the stellar evolution, and, as such, also to a specific gravity. Around the

main sequence turnoff, one temperature can correspond to two gravities, depending on how evolved the star is, i.e. just before or after the turnoff (see Figure 4.1 in chapter 4), here other ways for determining the gravity must be employed. Alternative methods for gravity determination include enforcing ionisation equilibrium or fitting of gravity sensitive spectral lines, as described in section 4.2 and 2.1.7.

The metallicity is determined from equivalent width measurements (see below) of Fe I lines. Fe I lines can be affected by non-LTE (NLTE) effects (see section 2.1.8), whereas Fe II lines are not. It is therefor better to use Fe II lines when determining the metallicity of the star. However, this is often not an option in metal-poor stars, where only a few or no Fe II lines can be found. The fourth stellar parameter, the microturbulence is caused by small (less than the mean free path of photons) turbulent elements in the photosphere. The term is added in 1D stellar atmosphere to additionally broaden the absorption lines, and compensate for the lack of convection that 3D model can reproduce more accurate. The microturbulence is usually found by removing any slope in a plot of abundances as function of reduced equivalent widths of Fe I lines. This ensures that all Fe I lines, independent of strength, give one consistent abundance value. The stellar parameters all depend on each other, i.e., a change in one will alter the value of the others. Therefore the parameter determination is an iterative process.

2.1.4 Continuum and line formation

There are several sources of opacity in the stellar atmospheres, which are responsible for the formation of continuum and absorptions lines in the stellar spectra.

The main source of continuum formation in cool stars are the bound-free transitions of H^- i.e. photoionization of H^-. The extra electron in H^- is bound with only 0.754 eV, corresponding to a photon with wavelength 1640 nm, hence all photons with wavelengths shorter than this (higher energy) can ionize the H^- atom. In warmer stars (A type), photoionization of neutral hydrogen (H I) is the main continuum source.

Spectral lines are formed from bound-bound transitions where an electron moves from one state to another in an atom or ion, creating an absorption line at the wavelength corresponding to the energy difference between the two states. The opacity in the stellar atmosphere is highest in the center of the lines (highest number of absorbers) and decreases in the wings, meaning that the core of the lines are formed in the upper, cooler layers of the star whereas the wings are formed in deeper, hotter layers.

The absorption lines are broadened by several different effects. First the natural broadening, which arises from then fact, that the energy of a given state can not have a precise value due to the Heisenbergs uncertainty principle, $\Delta E \Delta t \sim h/2\pi$. The effect of natural broadening is given by:

$$\Delta \lambda_E = \frac{\lambda^2}{2\pi c} \Gamma_{ik} \tag{2.5}$$

where Γ_{ik} is the damping coefficient. Secondly, the lines are broadened due to the thermal motions of the atoms in the gas, this is the Doppler broadening. As mentioned above the velocity field of the gas is described by the Maxwell-Boltzmann distribution. This distribution gives a most probable velocity, $v = \sqrt{2kT/m}$ of the individual gas particles.

Additionally there may also be a bulk motion of larger volumes of the gas, for example in stars with convective envelopes. Assuming these turbulent velocities follow the Maxwell-Boltzmann distribution with a most probable velocity of v_{mic}, we can combine these two gas velocities with the Doppler effect, to find the following Doppler broadening:

$$\Delta\lambda_D = \frac{2\lambda_0}{c}\sqrt{\frac{2kT\ln 2}{m}}. \tag{2.6}$$

A third effect broadening the spectral lines is particle collisions in the gas also called pressure broadening. When an absorbing atom collides with another atom or ion, the energy levels are distorted. The effect of this depends on the collision cross-section σ, particle density n, and the temperature of the gas, and is given by:

$$\Delta\lambda = \frac{\lambda^2}{2\pi c}n\sigma\sqrt{\frac{2kT}{m}} \tag{2.7}$$

The pressure and natural broadening have Lorentz profiles whereas the Doppler broadening has a Gaussian profile. A convolution of these two is a so-called Voigt profile, which is often used to fit spectral lines. In the central regions of the line the Doppler broadening dominates, but when moving to the wings of the line the pressure and natural broadening takes over.

2.1.5 Level populations

To determine the abundance of a given element, we need to relate the strength/intensity of the observed absorption line with the column density of atoms in the state that gives rise to the absorption line. Under the assumption of LTE, this is done using the Saha and Boltzmann equations. The Saha equation describes the number ratio of ionized N_{i+1} to neutral N_i atoms of a given species with ionization energy χ_i, at a given temperature, and is given by:

$$\frac{N_{i+1}}{N_i} = \frac{2Z_{i+1}}{n_e Z_i}\left(\frac{2\pi m_e kT}{h^2}\right)^{3/2}e^{-\chi_i/kT} \tag{2.8}$$

where n_e is the electron density, m_e is the electron mass, h is the Planck constant, and Z_{i+1} and Z_i are the partition functions. The partition functions are the sum of the possible energy states of the atom. For a given energy level with energy E_n and statistical weight g_n the partition function is defined as:

$$Z = \sum_{n=1}^{\infty} g_n e^{-(E_n - E_1)/kT}. \tag{2.9}$$

The statistical weights reflects the energy degeneracy of the states. The number of states with energy E_n is given by $g_n = 2n^2$. The two possible spins of the electron is reflected in the factor of 2 in front of the partition function in the Saha equation. The Boltzmann equation gives the ratio of populations in two energy levels, n and m, with the excitation energies x_n and x_m, of a given species, and is given by:

$$\frac{N_n}{N_m} = \frac{g_n}{g_m}e^{(x_n - x_m)/kT} \tag{2.10}$$
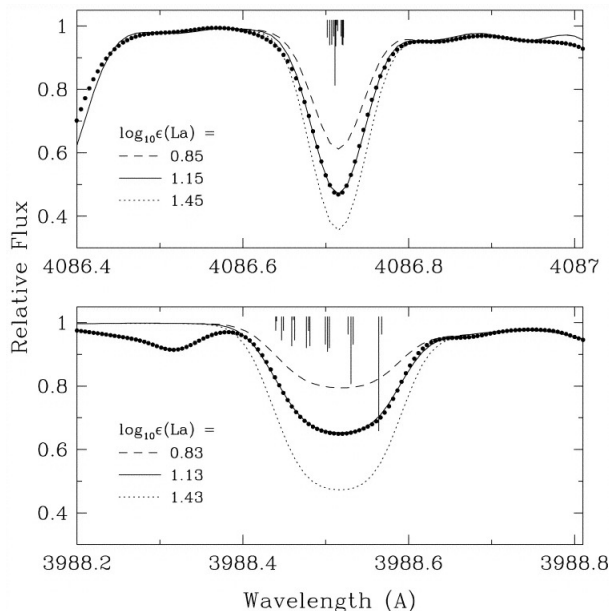
Figure 2.1: Figure from Lawler et al. (2001) showing the synthetic spectra of two La lines. The hyperfine structure is shown as vertical lines. The line shown in the top panel has a compact hyperfine structure, while the line in the bottom panel has a broader hyperfine patter.

2.1.6 Line list

Finally, a line list with information of the atomic and molecular transitions is needed. The line list contains the wavelength, excitation energy, oscillator strength (f), and damping coefficients for a given atomic transition. For molecular transitions the line list also gives the dissociation energy of the molecule. The oscillator strength combined with the statistical weight describes the probability of a given transition, combining the probabilities of the possible transition types; spontaneous emission, photo-absorption and stimulated emission. The damping coefficients depend on the temperature of the star. For cool stars, the Van der Waals broadening is dominant. This broadening arise from interactions between neutral particles. All lines are affected by this. In hotter stars, the Stark effect from electric interaction from ions and electrons also plays a role.

Some lines are affected by hyperfine structure and isotopic shifts, which needs to be accounted for in the line list. The hyperfine structure is a splitting of lines of odd $\mathcal{Z}$ elements due to interaction between the nuclear spin and the angular momentum of the nucleus. This effect broadens the lines as shown for two lines of La in Figure 2.1. Isotopic shifts happen for elements, where there are contributions from more than one isotope of the given element. For Ba for example the five isotopes: ^{134}Ba, ^{135}Ba, ^{136}Ba, ^{137}Ba, ^{138}Ba all contribute to the absorptions lines in stars. Each of these isotopes have a different mass shifting the wavelength of the combined line.
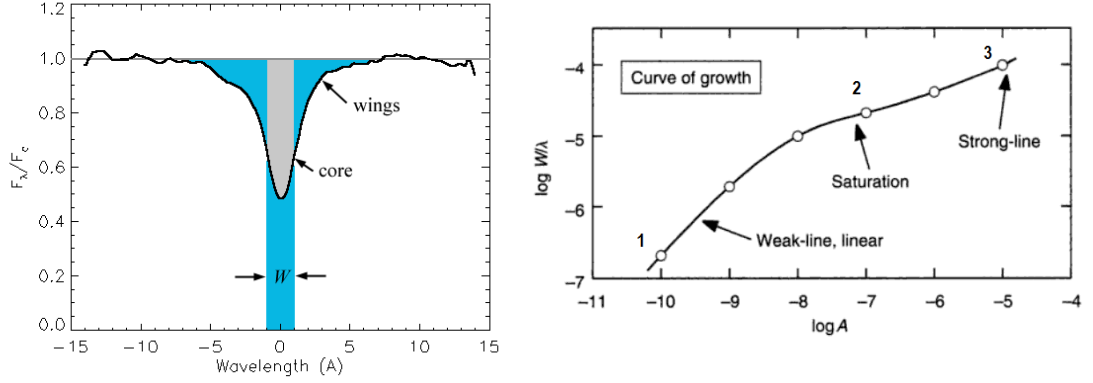
Figure 2.2: Equivalent with of a spectral line (left) and the curve of growth (right) (C. Hansen priv. comm.)

2.1.7 Final abundances

With all of the above in place, we can measure the abundances of a given element or molecule by measuring the intensity features in the stellar spectrum with respect to the continuum. For single un-blended atomic lines, the abundance can be obtained from the Equivalent Width (EW) of the lines, which can be measured by fitting either a Gaussian profile (weak lines), a Lorentz profile (strong lines) or a combination (Voigt profile) to the lines.

The EW of a spectral line is defined as the width of an rectangle with an area equal to the area covered by the spectra line:

$$EW = \int_{-\infty}^{+\infty} \frac{F_{cont} - F_\lambda}{F_{cont}} d\lambda \tag{2.11}$$

where F_{cont} and F_λ are the continuum and line flux respectively. The EW is related to the abundance, via the following equation:

$$\log(EW) = \log C + \log(N_A) + \log(gf\lambda) - \theta_x \chi - \log(\kappa_\nu) \tag{2.12}$$

where C is a constant specific for the star and the particular quantum transition, N_A is the number of atoms of element A relative to the number of hydrogen atoms, g is the statistical weight of the transition, f is the oscillator strength, $\theta_x = 5040/T$, χ is the excitation potential, and κ_ν is the continuum absorption coefficient. The relation between the EW and the number of absorbers is also described by the curve of growth, which is a log-log plot of the line strength as function of number of absorbers. For weak lines the abundance grows linearly with the EW (EW$\propto N_a$). At some point the absorption line becomes saturated, while the wings continue to grow. Adding more absorbers will not linearly increase the abundance (flat middle part, EW$\propto \ln(N_a)^{1/2}$), with growing abundance from here the wings will continue to grow deeper (EW$\propto N_a^{1/2}$). The equivalent with of a spectra line and a curve of growth is shown in Figure 2.2

Alternatively, a spectrum synthesis of multiple absorption lines can be performed. This gives the option to include blended lines and molecular bands in the abundance analysis.
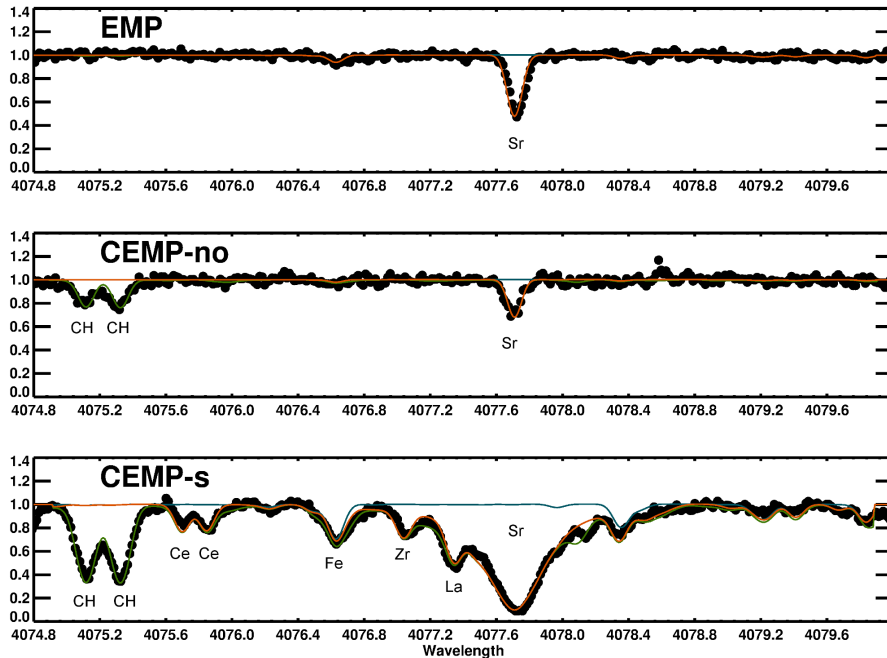
Figure 2.3: Observed and synthetic spectrum the Sr II line at 4077 Å of an EMP (top), CEMP-no (middle) and CEMP-*s* (bottom) star. Blue line fits only Fe lines, brown fits Fe and Sr, and all lines are included in the green line fit.

For some stars, like the CEMP stars, many of the spectral features are blends of several atomic and molecular lines, making spectrum synthesis the best option for deriving the stellar abundances. An example of this is shown in Figure 2.3, where synthesis of the same spectral region in an EMP, CEMP-no, and CEMP-*s* star is shown. For the CEMP-*s* star, clearly abundances should only be derived by synthesis. The abundances derived in this work are all derived from spectral synthesis using the program MOOG (see section 4.3).

The resultant stellar element abundances are usually given on a logarithmic scale relative to the Solar abundance. This is the square bracket notation, given by:

$$[\text{A/B}] = \log\left(\frac{\text{N(A)}}{\text{N(B)}}\right)_* - \log\left(\frac{\text{N(A)}}{\text{N(B)}}\right)_\odot \tag{2.13}$$

where N(A) and N(B) are column number densities of elements A and B, in the star (*) and in the Sun ($\odot$), respectively. The column number densities are given per 10^{12} hydrogen atoms. Abundances can also be given on an absolute scale:

$$\log\epsilon(\text{A}) = \log(\text{N(A)/N(H)}) - 12 \tag{2.14}$$

where $\log\epsilon(H) = 12$ per definition.

Changes in the stellar parameters of the star naturally give rise to changes in the abundance derived for a given element (see eqn. 2.12). As can be seen above both the Saha and Boltzmann equations (2.8, 2.10) depends on the temperature of the gas. The actual

change in the abundance depends on the temperature regime. For the stars analysed in the thesis, with 4800 K < T_{eff} < 6900 K, a change in t_{eff} of 100 K resulted in abundance changes of < 0.1 dex, for the single atomic lines. However, for the abundances derived from molecular bands changes of ∼0.2 dex where found. Owing to formation of molecules in the outer parts of the stellar atmosphere, their abundances are highly temperature sensitive and grow with decreasing temperature. Changes in the gravity of the star changes the pressure of the gas, which effects the ionisation equilibrium and absorption coefficient, and thereby the abundances of pressure sensitive lines (e.g. ions). The strongest effect of this if seen in abundances derived from strong lines with pressure broadened wing, such as Mg I and the Ca II H and K lines. Changes in microturbulence, generally have little effect on abundances derived form weak lines. However, for strong and saturated lines the microturbulence has an effect. Increasing the value of ξ will decrease, and in some cases de-saturate, the abundance derived from the line.

2.1.8   NLTE and 3D

The model atmosphere assumptions of 1D and LTE are not always good approximations. For example, observations of the surface of the Sun clearly show granulation features. Also in hot, low-density atmospheres of giant stars the rate of photon absorption is larger than the collision rate, which means that the assumption of LTE breaks down here. The departure from LTE and 1D will in some cases result in an offset in the derived abundances. As described above, in LTE the level population are determined from the Saha and Boltzmann equations (2.8, 2.10). When computing stellar atmospheres in NLTE the rate equations are solved simultaneously with the transfer equation. The line opacity also changes, which means the source function changes, resulting in a change of the linestrenghts. The departure from LTE results in a number of different effects such as resonance scattering and overionisation. Resonance scattering happens when $J_\nu < B_\nu$, where J_ν is the mean intensity. This is when the outwards photon loss is so large that scattering dominates over absorption. In this case lines becomes stronger in NLTE. Overionisation happens in the opposite situation when $J_\nu > B_\nu$. Here the rate of photoionisation is underestimated in LTE, i.e. an LTE analysis will underestimate the abundances from these lines. In Solar type stars the Fe I lines are affected by overionisation, and since these are often used for the parameter determination of the star, the NLTE effects also change the parameters. Lind et al. (2012) and Bergemann et al. (2012) found that abundance corrections due to NLTE effects often increase with decreasing metallicity, increasing effective temperature and decreasing gravity. The stellar parameters are of course only affected if they are derived directly from the iron lines.

One of the major differences between 1D and 3D model atmospheres is the temperature gradient. The temperature in the outer layers of the atmosphere can differ by 1000 K or more between 3D and 1D models (Asplund 2005). This arises because the 3D models takes into account the cooling of the atmosphere happening when radiation leaves the star. Such large temperature changes obviously also have a large effect on the line shapes and derived abundances.

Dedicated work has been carried out to determine the NLTE and 3D abundances corrections, which needs to be performed to abundances derived under the assumptions of 1D

and LTE (e.g. Asplund (2005); Mashonkina et al. (2007); Bergemann et al. (2012); Collet et al. (2007)). However, for most of this work only one of the effects (either 3D or NLTE) is taken into account. It was shown by Hansen et al. (2013) that for Sr the two effects cancel each other, so the abundances derived using both 3D and NLTE calculations were equal to the ones derived under the assumption of 1D and LTE. Similar studies needs to be carefully conducted to probe the necessity of applying 3D, NLTE corrections to the elements under study.

2.2 Binary Stars

Binary stars can be detected in a number of ways, depending on the distance to the stars and the inclination of the system towards the observer. The binaries detected in this project are spectroscopic binaries discovered from shifts of the spectral lines as the stars move around the orbit.

2.2.1 Radial velocity determination

The determination of the radial-velocity of the star from the stellar spectrum is done by cross-correlating the observed spectrum with an optimized template.

The cross-correlation function is given by:

$$c(x) = \int_{-\infty}^{\infty} f(k)g(k-x)dx \tag{2.15}$$

where $c(x)$ is the convolution of two functions (spectra), the target spectrum $f(k)$ and the template spectrum $g(k)$. The integral of the product of $f(k)$ and $g(k)$ is calculated for a range of values x. This gives a value for how well the two functions match at any given x, when one spectrum is shifted past the other. The cross-correlation function will then peak when the line patterns of the two spectra lie precisely on top of each other. This happens when $x = \ln(1 + v/c)$, where v is the relative velocity between the two spectra. In practice the cross correlation is done in Fourier space; this is easy because a convolution in x space simply becomes a multiplication in Fourier space. For this project, different template spectra was used for the cross-correlation dependent on the nature of the object star and the quality of the observed spectrum. The different template spectra are described in detail in section 5.3.

2.2.2 Orbital solution

The motion of the stars around their common center of mass is described by Kepler's third law:

$$P^2 = \frac{4\pi^2 a^3}{M} \tag{2.16}$$

where $M = M_1 + M_2$ is the total mass of the system, a is the semi major axis and P is the period.

The binary system is characterized by a set of orbital parameters. These are listed in Table 2.1, and shown in Figure 2.4. From the measured orbital parameters, the mass

function, giving the relation between the stellar masses, the inclination angle, period and K_1 can be computed:

$$f(m) = \frac{M_2^3 \sin^3 i}{(M_1 + M_2)} = 1.3061 \cdot 10^{-7}(1 - e^2)^{3/2} K_1^3 P M_\odot. \tag{2.17}$$

Usually, both the stellar masses and the inclination angle of the system is unknown, so when calculating the mass function, assumptions for the values of these are made. For the binary systems detected in this work, details are described in section 5.4.3.

Mass can be transferred from one star in a binary system to the other, either via Roche-lobe or wind mass transfer or a combination of both. The different types of mass transfer are described in section 7.4.

Symbol	Description
i	Inclination angle, the position of the orbital plane in space with respect to reference plane.
ω	Orientation of longest axis of elliptical orbit within orbital plane.
a	Semi major axis.
e	Eccentricity.
P	Period.
K_1	Radial velocity amplitude for primary star
K_2	Radial velocity amplitude for secondary star
γ	Radial velocity of center of mass.
T	Time of ephemeris.

Table 2.1: Orbital parameters for binary system
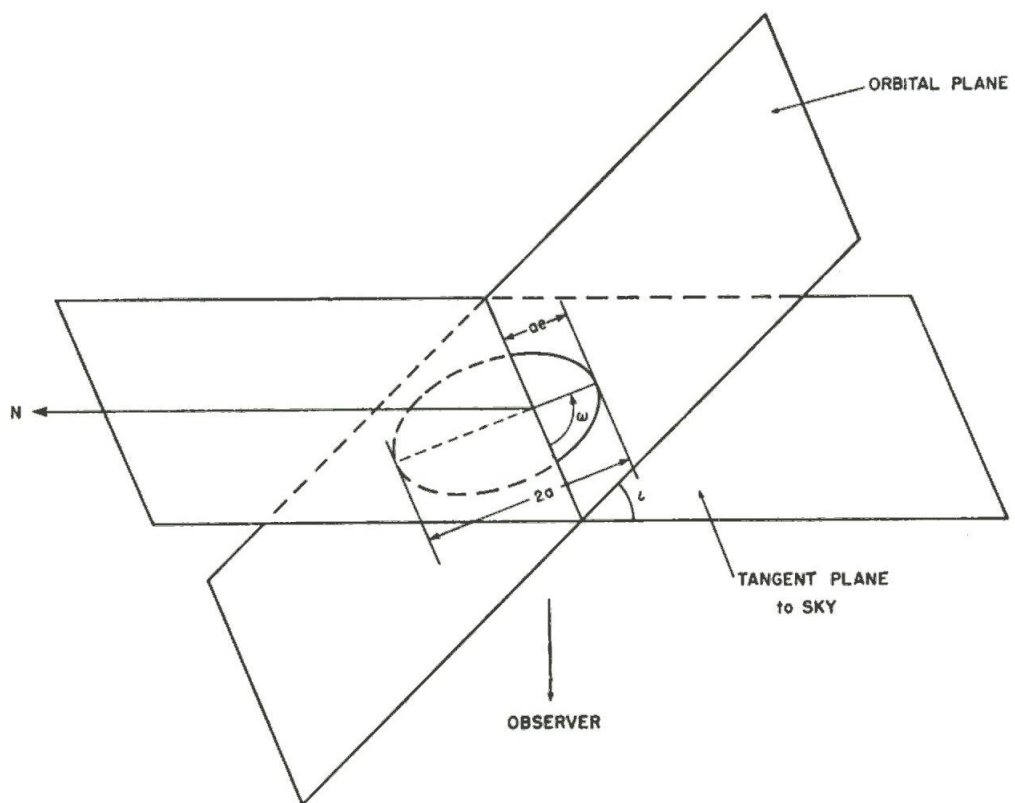
Figure 2.4: Parameters characterizing a binary system (Hilditch 2001)

CHAPTER 3

Exploring the origin of lithium, carbon, strontium and barium with four new ultra metal-poor stars

This chapter is taken from the paper "Exploring the origin of lithium, carbon, strontium and barium with four new ultra metal-poor stars", describing the abundance analysis and results of four ultra metal-poor stars. The paper was published in The Astrophysical Journal, volume 787, page 162, with the following author list: T. Hansen, C. J. Hansen, N. Christlieb, D. Yong, M. S. Bessel, A. E. Garcia Perez, T. C. Beers, V. M. Placco, A. Frebel, J. E. Norris & M. Asplund. M. S. Bessell has derived spectrophotometric temperatures for the sample stars. The remaining analyses presented in this paper is work of the author of this thesis; all co-authors have commented on the manuscript.

3.1   Observations and data analysis

The four stars presented in this paper are part of a larger sample of metal-poor candidates selected from the Hamburg/ESO survey, followed-up with medium-resolution spectroscopy on a variety of $2-4$ m class telescopes, then observed at high spectral resolution with Very Large Telescope (VLT)/UVES (Dekker et al. 2000). The complete sample will be presented in Paper II of this series, along with a detailed description of the observations, data reduction procedure, parameter determination, and abundance analysis. Here, only the key points of the techniques employed are listed.

Figure 3.1 shows the medium-resolution spectra of the program stars. It is possible to see features such as the Ca II K line, H_β, H_γ, and H_δ, as well as the CH and CN molecular carbon bands for HE 1310$-$0536. Both the Southern Astrophysical Research (SOAR) 4.1 m and KPNO/Mayall 4 m data have a wavelength coverage of 3550–5500 Å, with a resolving power of $R \sim 1500$ and signal-to-noise ratios of S/N$\sim$ 30 per pixel at 4000 Å. For the ESO 3.6 m data, the resolving power and signal-to-noise were similar to the SOAR 4.1 m and Mayall
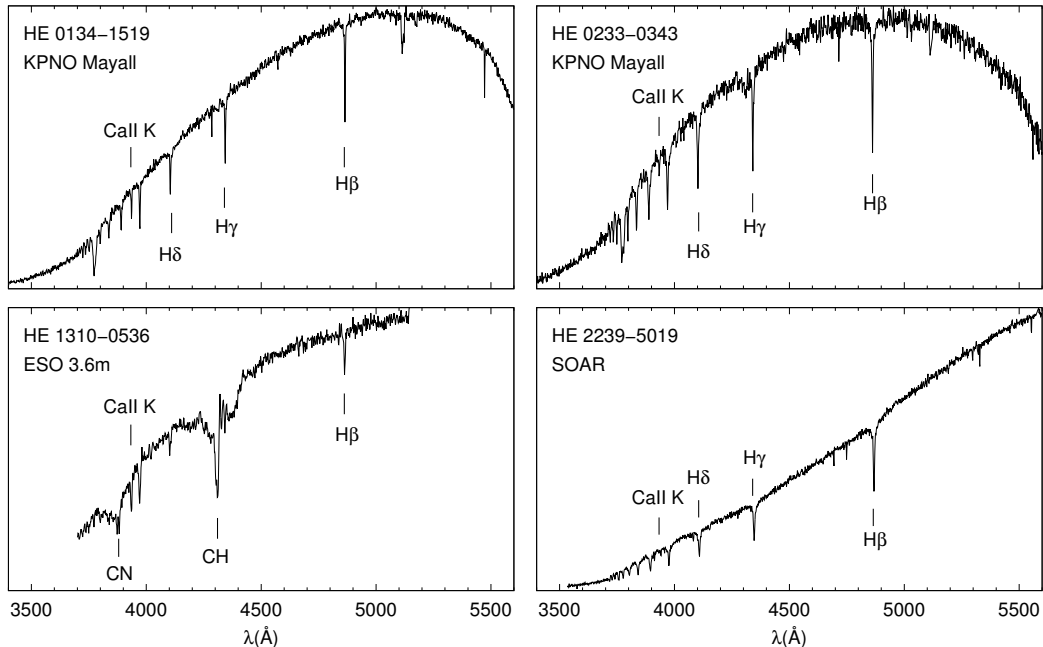
Figure 3.1: Medium-resolution spectra of our four program stars. The locations of the Ca II K line, H_β, H_γ, and H_δ lines are shown. For HE 1310−0536, the CH and CN molecular carbon bands are clearly visible.

4 m data, but the wavelength range is narrower, covering the interval 3700–5100 Å.

Medium-resolution spectra obtained with the Wide Field Spectrograph (WiFeS; Dopita et al. 2007) on the Australian National University 2.3 m Telescope at Siding Spring Observatory were used for the temperature determination.

The high-resolution data was obtained during the nights of 2005 November 17 and 20, and 2006 April 17. The data cover a wavelength range from 3100 Å to 9500 Å, with a resolving power of $R \sim 45000$. The spectra were reduced using the UVES reduction pipeline, version 4.9.8. Radial-velocity shifts, co-addition of the spectra, and continuum normalization were all performed using IRAF[1]. The average S/N of the reduced spectra is S/N ~ 10, ~ 30, and ~ 55 pixel^{-1} at 3400 Å, 4000 Å, and 6700 Å, respectively.

3.1.1 Stellar parameters

The stellar atmospheric parameters were determined by standard techniques, generally following the steps outlined in Yong et al. (2013). Effective temperatures were determined by fitting the spectrophotometric observations with model atmosphere fluxes (Bessell 2007; Norris et al. 2013a). LTE model atmosphere fluxes from the MARCS grid (Gustafsson et al. 2008), with $[\alpha/Fe] = +0.4$, were used for the model fitting. Estimates of surface gravity were determined from the Y^2 isochrones (Demarque et al. 2004), assuming an age

---

[1]IRAF is distributed by the National Astronomy Observatory, Inc., under cooperative agreement with the National Science Foundation.

of 10 Gyr and an α-element enhancement of $[\alpha/\text{Fe}] = +0.3$. These isochrones only extend down to $[\text{Fe/H}] = -3.5$; therefore, a linear extrapolation down to $[\text{Fe/H}] = -4.7$ has been used to obtain the surface-gravity estimates for our four stars. The average difference between the listed surface gravities, where the actual $[\text{Fe/H}]$ values have been used, and the surface gravity obtained using the $[\text{Fe/H}] = -3.5$ isochrone, is rather small (on the order of 0.07 dex). Metallicities were determined from equivalent-width measurements of the Fe I lines. Non-LTE (NLTE) effects might be present in the Fe I lines, which can affect the derived metallicity (Lind et al. 2012), but no Fe II lines were detected in any of the four program stars. The measured Fe abundance may also be subject to uncertainties from three-dimensional (3D) effects. Collet et al. (2006) report a 3D correction of ~ -0.2 dex for the Fe abundance for two of the most metal-poor stars known (HE 0107-5240 and HE 1327$-$2326), both of which have temperatures and gravities that are comparable, within the combined error bars, to those of the stars presented in this paper. A better basis for comparison, at the same metallicity as our program stars, is clearly desirable. Bergemann et al. (2012) found, however, that departures from LTE will likely partly compensate such 3D LTE effects, leaving a smaller net effect. Our stars have several Fe I lines in common with the study of Bergemann et al. (2012). A full 3D NLTE study is clearly warranted, but beyond the scope of the present study.

The microturbulent velocity was computed in the usual way, by forcing the abundances from Fe I lines to show no trend with reduced equivalent width, $\log(W_\lambda/\lambda)$. For HE 0233$-$0343, too few Fe I lines were present to determine the microturbulent velocity in this way, so a fixed valued of $\xi = 2$ km s^{-1} was used for this star.

For the warmer stars, HE 0233$-$0343 and HE 2239$-$5019, two possible solutions for the surface gravity were found. Several tests were made to settle on the listed values, both consistent with subgiant, rather than dwarf, classifications. This aspect will be explored further in Paper II of this series. The final stellar parameters and their associated uncertainties are listed in Table 3.1.

3.1.2 Abundance analysis

The abundance analysis has been carried out by synthesizing individual spectral lines with the 2011 version of MOOG (Sneden 1973), which includes a proper treatment of continuum scattering (Sobeck et al. 2011). A set of α-enhanced ATLAS9 models (Castelli & Kurucz 2003) have been used, along with interpolation software tested in Allende Prieto et al. (2004), which produces models with the required stellar parameters (e.g., Reddy et al. 2003; Allende Prieto et al. 2004). For HE 0233$-$0343, the metallicity in the model atmosphere was $[\text{m/H}] = -4.5$, which differs by 0.18 dex from the metallicity of the star. This difference is within the uncertainty of the derived $[\text{Fe/H}]$ of the star and given the small difference, we expect no change in any of the abundances when using a model with $[\text{m/H}] = -4.7$.

The *Gaia*/ESO line list version 3 has been used (Heiter et al., in preparation). Atomic data from VALD (Kupka et al. 2000) were adopted for lines not included in that line list. Hyperfine splitting was taken into account for lines of Sc, Mn, and Co, using the data from Kurucz (1995). For Ba and Li, both hyperfine splitting and isotope shifts are present, and data from McWilliam (1998) and Asplund et al. (2006) were included, respectively. The molecular information for CH, CN, and NH was kindly provided from T. Masseron (private

Table 3.1: Stellar parameters and derived abundances for the UMP stars

	HE 0134−1519	HE 0233−0343	HE 1310−0536	HE 2239−5019
R.A.	01 37 05.4	02 36 29.7	13 13 31.2	22 42 26.9
Decl.	−15 04 24	−03 30 06	−05 52 13	−50 04 01
V^a	14.47	15.43	14.35	15.85
$B - V^a$	0.50	0.34	0.71	0.39
$J - K^a$	0.43	0.30	0.64	0.40
Radial velocity (km s^{-1})	244	64	113	370
Parameters				
T_{eff} (±100 K)	5500	6100	5000	6100
$\log g$ (±0.3 dex)	3.2	3.4	1.9	3.5
[Fe/H] (±0.2 dex)	−4.0	−4.7	−4.2	−4.2
ξ (±0.3 km s^{-1})	1.5	2.0	2.2	1.8
Abundances				
A(Li)	+1.27 (0.19)	+1.77 (0.18)	< +0.80 ...	< +1.70 ...
[Fe/H]	−3.98 (0.30)	−4.68 (0.30)	−4.15 (0.30)	−4.15 (0.30)
[C/Fe]	+1.00 (0.26)	+3.48 (0.24)	+2.36 (0.23)	< +1.70 ...
[N/Fe]	< +1.00 ...	< +2.80 ...	+3.20 (0.37)	< +2.70 ...
[Na/Fe]	−0.24 (0.15)	< +0.50 ...	+0.19 (0.14)	< −0.30 ...
[Mg/Fe]	+0.25 (0.14)	+0.59 (0.15)	+0.42 (0.16)	+0.45 (0.15)
[Al/Fe]	−0.38 (0.20)	< +0.03 ...	−0.39 (0.21)	−0.57 (0.21)
[Si/Fe]	+0.05 (0.16)	+0.37 (0.15)	< +0.25 ...	+0.06 (0.15)
[Ca/Fe]	+0.10 (0.13)	+0.34 (0.15)	0.00 (0.20)	+0.23 (0.15)
[Sc/Fe]	−0.10 (0.18)	< +0.20 ...	−0.23 (0.16)	+0.26 (0.16)
[Ti/Fe]	+0.11 (0.21)	+0.18 (0.17)	+0.35 (0.18)	+0.37 (0.17)
[Cr/Fe]	−0.22 (0.18)	< +0.50 ...	−0.49 (0.26)	0.00 (0.17)
[Mn/Fe]	−1.19 (0.19)	< −0.10 ...	−1.40 (0.20)	< −0.60 ...
[Co/Fe]	+0.25 (0.18)	< +1.60 ...	+0.10 (0.16)	< +0.70 ...
[Ni/Fe]	+0.19 (0.19)	< +0.90 ...	−0.12 (0.20)	+0.24 (0.17)
[Sr/Fe]	−0.30 (0.19)	+0.32 (0.19)	−1.08 (0.14)	< −0.60 ...
[Ba/Fe]	< −0.50 ...	< +0.80 ...	−0.50 (0.15)	< +0.00 ...

a) Beers et al. (2007a)

communication)

The derived elemental abundances, along with propagated uncertainties arising from the effects of uncertain stellar parameters, continuum placement, and line information, are listed in Table 3.1. The adopted solar abundances are from Asplund et al. (2009). All listed abundances are derived under one-dimentional (1D) and LTE assumptions. NLTE effects will be explored in Paper II.

3.2 Results

3.2.1 Radial velocity

Two of the stars listed in Table 3.1, HE 0134−1519 and HE 2239−5019, exhibit quite high radial velocities, 244 km s^{-1} and 370 km s^{-1}, respectively. The uncertainty of the

listed radial velocities is on the order of ~ 1 km s^{-1}. Such high velocities may suggest membership in the proposed outer-halo population of the Milky Way (Carollo et al. 2007, 2010; Beers et al. 2012). A kinematic analysis of the full space motions of our complete program sample, including the four stars reported on here, will be presented in Paper II of this series. In this context, it is interesting that Carollo et al. (2014) present tentative evidence that the CEMP-s and CEMP-no stars may well be associated with progenitors that belong, in different proportion, to the suggested inner- and outer-halo populations of the Milky Way.

3.2.2 Elemental abundances

Our analysis has produced abundance estimates, or upper limits, for 17 elements – Li, C, N, Na, Mg, Al, Si, Ca, Sc, Ti, Cr, Mn, Fe, Co, Ni, Sr, and Ba. We describe these analyses in detail in the subsections below.

Lithium

We derived lithium abundances from synthesis of the Li I 6707.8 Å doublet. Lithium is detected for two of our program stars–HE 0134$-$1519, with $A(\text{Li}) = 1.27$[2], and HE 0233$-$0343, with $A(\text{Li}) = 1.77$. Figure 3.2 shows the spectral region around the Li line for two of our stars (top: HE 0134$-$1519, and bottom: HE 0233$-$0343), together with three synthetic spectra computed with $A(\text{Li}) = 1.46$, 1.27, and 1.08, respectively, for HE 0134$-$1519, and $A(\text{Li}) = 1.95$, 1.77, and 1.59, respectively, for HE 0233$-$0343. HE 0233$-$0343 is the second most metal-poor star with a detected lithium line, as lithium was also detected in the most metal-poor star known, SMSS J031300.36-670839.3 with [Fe/H] < -7, recently discovered by Keller et al. (2014) ($A(\text{Li}) = 0.7$). Li is not detected for the two remaining program stars; we computed upper limits of $A(\text{Li}) < 0.8$ and $A(\text{Li}) < 1.70$ for HE 1310$-$0536 and HE 2239$-$5019, respectively. The very low upper limit detected in HE 1310$-$0536 is expected, as this star is sufficiently evolved that it has undergone first dredge up. Its convective zone likely extends down to layers in the atmosphere where lithium has been destroyed by nuclear burning.

Figure 3.3 displays the Li abundance for our two CEMP-no stars with Li detections, as a function of their luminosity, following Figure 16 of Masseron et al. (2012). Luminosities have been determined in the same way as in Masseron et al. (2012), assuming $M = 0.8 M_\odot$. For comparison, we also plot the CEMP-no stars of their sample. The solid line marks the division between Li-normal (above) and Li-depleted (below) stars. The line is computed from the Li abundance of non-CEMP stars with luminosities in the range $-0.2 < \log(L/L_\odot) < 2.1$. The line follows the Spite Li plateau for dwarf stars, then exhibits a linear decline in the Li abundances of giants, where the Li is expected to be gradually depleted due to convective burning episodes (see Masseron et al. 2012, for details). Stars outside the above range in luminosity are expected to have destroyed all their Li. Note that HE 1310$-$0536, with $\log(L/L_\odot) = 2.11$, falls ounecessitytside that range. Our two Li detections both lie above the Li-normal line, but with lithium abundances below the Spite plateau. Hence, Li has been depleted in these stars, consistent with the result found by

---

[2]$A(\text{Li})$ is defined in the usual manner, $A(\text{Li}) = \log(N(\text{Li})/N(\text{H})) + 12$.
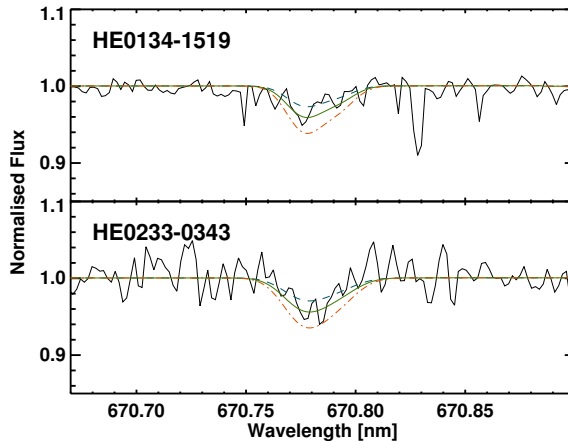
Figure 3.2: Li line fit for HE 0134−1519 (top) A(Li) = 1.46, 1.27, and 1.08 (blue dashed line, solid green line, and red dot-dashed line, respectively) and HE 0233−0343 (bottom) A(Li) = 1.95, 1.77, and 1.59 (blue dashed line, solid green line, and red dot-dashed line, respectively). The blue dashed and red dot-dashed lines correspond to A(Li)$\pm\sigma$(Li), respectively, as listed in Table 3.1.

Masseron et al. (2012), that the CEMP-no class *only* contains Li-depleted stars, even at these low metallicities.

Carbon

Three of our four program stars, HE 0134−1519, HE 0233−0343, and HE 1310−0536, are carbon enhanced, with [C/Fe] $\geq$ +0.7. They exhibit no enhancements in their neutron-capture elements ([Ba/Fe] $\leq$ 0.0; Beers & Christlieb 2005), and are considered CEMP-no stars. Technically, the status of HE 0233−0343 cannot be confirmed, as only an upper limit for the Ba abundance of [Ba/Fe] $<$ +0.8 is found. Considering that the great majority of CEMP stars with [Fe/H] $<$ −3 are CEMP-no stars (Aoki et al. 2010), and the fact that there are no known CEMP-s stars with [Fe/H] $<$ −3.5, there is a high likelihood that HE 0233−0343 also belongs to the CEMP-no class. The last of the four stars, HE 2239−5019, shows no clear carbon enhancement; we compute an upper limit of [C/Fe] $<$ +1.7 for this star. With no carbon detected, this star is a potential candidate to be in the same class as SDSS J102915+172927, the only star with [Fe/H] $<$ −4.5 found not to be carbon enhanced (Caffau et al. 2011).

Figure 3.4 shows the spectral range including the CH G band for SDSS J102915+172927, HE 2239−5019, and HE 0233−0343. HE 0233−0343 has similar stellar parameters as HE 2239−5019, but it is more iron poor and carbon enhanced. Similar to SDSS J102915+172927, no CH features are visible in HE 2239−5019. However, the noise level in the spectrum of HE 2239−5019 is quite high, resulting in a high derived upper limit on the carbon abundance, so it cannot be ruled out as being a CEMP star.

Since three out of the four stars are carbon enhanced, the oxygen and nitrogen abun-
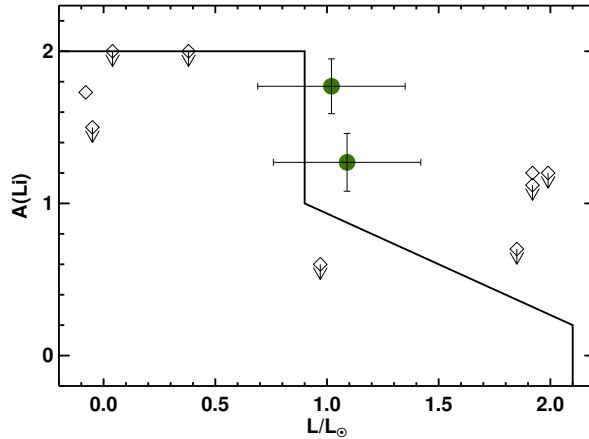
Figure 3.3: LTE lithium abundances, A(Li), as a function of luminosity, for HE 0134−1519 and HE 0233−0343 (green circles), along with the CEMP-no stars of Masseron et al. (2012) (black diamonds). Upper limits are indicated by arrows. The solid line indicates the division between Li-normal (above) and Li-depleted (below) stars.

dances are also of interest. Nitrogen was detected in only one star, HE 1310−0536, where the abundance listed in Table 3.1 is derived from synthesis of the CN band at 3883 Å. For the remaining three stars, upper limits are derived from synthesis of the NH band at 3360 Å. Previous studies, such as Sivarani et al. (2006) and Norris et al. (2013b), have found a correlation of [N/Fe] with [C/Fe] for CEMP stars. The N abundance and upper limits that we derive support this correlation. Oxygen was not detected in any of our program stars, and the noise levels in the spectra were too high to compute a meaningful upper limit on its abundance.

Light elements and neutron-capture elements

Since the stars in this sample have been analyzed in a similar manner as those of Yong et al. (2013), the two samples are directly comparable. In the top panel of Figure 3.5, the mean [α/Fe] (taken to be the mean of [Mg/Fe], [Ca/Fe], and [Ti/Fe]) abundance ratios of our four stars is compared to those of Yong et al. (2013). Their sample includes some of the most metal-poor stars known to date (HE 0107−5240: Christlieb et al. (2002); HE 1327−2326: Frebel et al. (2005); and HE 0557−4840: Norris et al. (2007). A small over-abundance of the [α/Fe] ratio is seen in the four new stars, consistent with the existing picture of the α-element abundances in metal-poor stars, reflecting the enrichment from core–collapse SNe in the early universe. Norris et al. (2013b) found that 50% of their CEMP stars are more enhanced in the light elements Na, Mg, Al, and Si, compared to other (C-normal) EMP stars with similar stellar parameters. Among our program stars, HE 0233−0343 exhibits higher abundances of these elements relative to the rest of the sample. However, none of our stars show over-abundances of these elements as large as those found for some CEMP stars in the sample of Norris et al. (2013b). The observed abundances for Al and Mn in
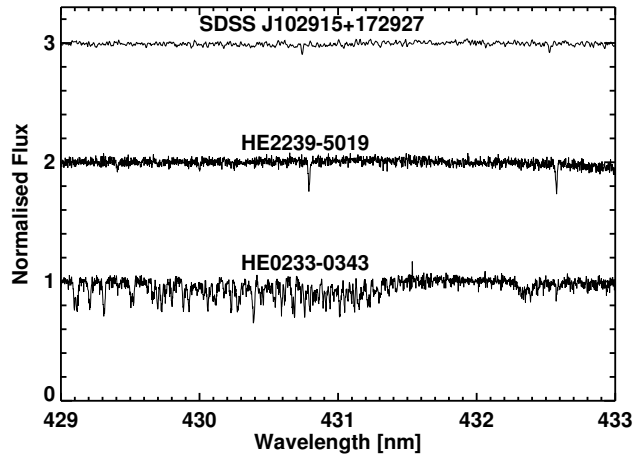
Figure 3.4: Spectral range including the CH G band in the spectra of SDSS J102915+172927 (top), HE 2239−5019 (middle), and HE 0233−0343 (bottom). The carbon lines are clearly seen in the spectrum of HE 0233−0343, but are absent in the other two spectra.

our four stars lie somewhat below the level predicted by the Galactic chemical evolution models of Nomoto et al. (2013). This may be due to NLTE effects. Gehren et al. (2004) report NLTE corrections of +0.5 dex for Al in a sample of metal-poor turn-off stars, while Bergemann & Gehren (2008) find corrections of up to +0.7 dex for Mn in their sample of metal-poor giant and dwarf stars. This would bring Al to the predicted level, whereas Mn would stay just below.

The middle and bottom panels of Figure 3.5 display the [Sr/Fe] and [Ba/Fe] abundance ratios, respectively, as functions of metallicity for our program stars and those of Yong et al. (2013). Both samples exhibit a large spread in the [Sr/Fe] and [Ba/Fe] ratios. The spread of abundances for these two elements was also discussed by Hansen et al. (2012, 2013) and Yong et al. (2013), all suggesting that more than one production site exists for Sr and Ba. The scatter in the Sr and Ba abundances of EMP stars has also been discussed by Aoki et al. (2013b), who studied the [Sr/Ba] ratios in a sample of 260 EMP stars. They detected no stars with [Sr/Fe] > 0.0 for [Fe/H] < −3.6 (note that their sample only includes four stars with [Fe/H] < −3.6). They proposed to explain the distribution in the observed [Sr/Ba] ratios with a truncated r-process taking place in a type II SN, as described by Boyd et al. (2012). Aoki et al. (2013b) also stated that neither the r process nor the truncated r process are expected to produce stars with [Sr/Ba] < −0.5. They find six stars in their sample with [Sr/Ba] < −0.5, but suspect these to be contaminated with s-process material.
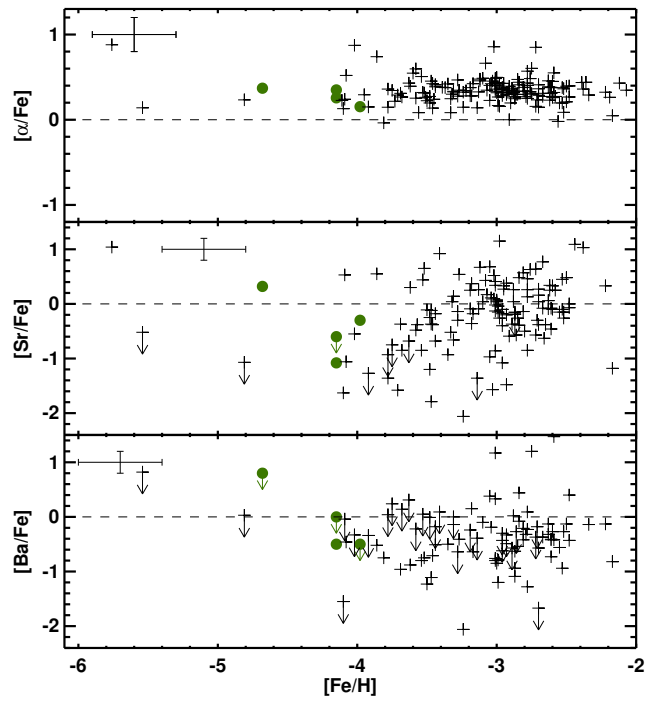
Figure 3.5: Mean [α/Fe] (top), [Sr/Fe] (middle), and [Ba/Fe] (bottom) abundances for our four UMP stars (green circles) and the sample of Yong et al. (2013) (black crosses). Upper limits are indicated by arrows; the dashed line is the solar value.

CHAPTER 4

An Elemental Assay of Very, Extremely, and Ultra Metal-Poor Stars

This chapter is taken from the paper "An Elemental Assay of Very, Extremely, and Ultra Metal-Poor Stars", describing the analysis and results of a sample of 23 metal-poor stars. The paper was published in The Astrophysical Journal, volume 807, page 173, with the following author list: T. Hansen, C. J. Hansen, N. Christlieb, T. C. Beers, D. Yong, M. S. Bessel, A. Frebel, A. E. Garcia Perez, V. M. Placco, J. E. Norris & M. Asplund. M. S. Bessell has derived spectrophotometric temperatures for the sample stars and C. J. Hansen has performed the abundance profile fits for the CEMP-s, $-r$ and r/s stars. The remaining analyses presented in this paper is work of the author of this thesis; all co-authors have commented on the manuscript.

4.1 Observations and data analyses

Our sample of 23 very metal-poor (VMP; [Fe/H] ≤ -2.0), extremely metal-poor (EMP; [Fe/H] ≤ -3.0), ultra metal-poor (UMP; [Fe/H] ≤ -4.0) stars presented here were originally selected from the Hamburg/ESO Survey (HES; Christlieb et al. 2008; Frebel et al. 2006), followed up with medium-resolution spectroscopy on a variety of 2-m to 4-m class telescopes (AAT 3.9m, CTIO 4m, CTIO 1.5m, ESO 3.6m, KPNO 4m, SOAR 4m, SSO 2.3m, and UKST 1.2m), and then observed at high spectral resolution with VLT/UVES (Dekker et al. 2000). Chapter 3 (Paper I) describes the observations and analysis of the four UMP stars in this sample.

The high-resolution spectroscopy of the stars in our sample was performed with UVES using the dichroic (DIC) beam splitter, allowing simultaneous observation with the blue and red arm, in order to cover a spectral range including a large number of chemical elements. Three different settings were used: DIC (blue central wavelength + red central wavelength),

covering the following wavelengths – DIC1 (390+580) blue: λ3260-4450 Å, red: λ4760-6840 Å, DIC2 (346+760) blue: λ3030-3880 Å, red: λ5650-9460 Å, and DIC2 (437+760) blue: λ3730-4990 Å, red: λ5650-9460 Å. The spectral resolving power varies with the choice of wavelength setting and slit width. The average resolving power of the spectra is R $\sim$ 45,000. Positions, observation dates, exposure times, and specific settings for the individual stars in the sample are listed in Table 4.1.

The spectra were reduced using the UVES reduction pipeline version 4.9.8. Radial-velocity shifts of the spectra were obtained using the IRAF[1] task FXCOR. Individual spectra were cross-correlated with a template spectrum obtained during the same observation run. For the 2005 run, HE 0134$-$1519 and HD 2796 were used as templates, for which we find $V_r = 244.0$ km s^{-1} and $V_r = -14.7$ km s^{-1}, respectively. For the 2006 run, HD 140283 was used, for which we find $V_r = -185.4$ km s^{-1}. For stars with multiple observations, the individual spectra were co-added with the IRAF SCOMBINE task. Finally the radial-velocity shifted (and combined) spectrum was normalized. Table 4.2 lists the derived radial velocities and signal-to-noise (S/N) ratios at specific wavelengths for the different spectra. When a wavelength region is covered by more than one setting, the one having the highest S/N ratio is listed. Note that, because the spectra were only obtained spanning at most a few nights, these data are not suitable for evaluation of the binary nature of our stars. However, the high accuracy of our derived radial velocities (typically better than 1 km s^{-1}) should prove useful for comparison with future binarity studies.

Three of the stars in our sample are re-discoveries and have radial velocities reported in the literature. These three stars are; HE 0054$-$2542 (CS 22942$-$019, CD-26:304), HE 0411$-$3558 (CS 22186$-$005) and HE 0945$-$1435. Preston & Sneden (2001) found HE 0054$-$2542 to be in a binary system with a period of 2800 days, while Norris et al. (1996) reports $V_r = 192.4$ km s^{-1} for HE 0411$-$3558, close to our value of $V_r = 196.2$ km s^{-1}, and Norris et al. (2013a) reports $V_r = 121.8.4$ km s^{-1} for HE 0945$-$1435, where we find $V_r = 144.8$ km s^{-1}, suggesting that it is a likely binary star.

4.2   Stellar parameters

The stellar atmospheric parameters were determined following most of the steps outlined in Yong et al. (2013) and in Chapter 3 (Paper I), so that the results of the abundance analyses of their sample and ours can be usefully combined.

The effective temperature ($T_{\rm eff}$) was, for the majority of the stars, determined by fitting spectrophotometric observations of the star with model-atmosphere fluxes (Bessell 2007; Norris et al. 2013a). For this step, medium-resolution spectra were obtained with the Wide Field Spectrograph (WiFeS; Dopita et al. 2007) on the Australian National University 2.3-m telescope at Siding Spring Observatory during 2012. This is a double-beam spectrograph using a dichroic mirror to separate the blue and red regions. The spectrograph covers the wavelength ranges 3000-6200 Å and 6000-9700 Å in the blue and red, respectively, with a resolution of 2 Å. The observations, data reduction, and analysis were performed as described in Section 4.1 of Norris et al. (2013a). The reduced spectra were cross-correlated against a

---

[1]IRAF is distributed by the National Astronomy Observatory, Inc., under cooperative agreement with the National Science Foundation.

Table 4.1: Observation log

Stellar ID	RA	Dec	Date	Exp.(s)	Slit (")^a	Setting^b
HE 0010−3422	00 13 08.9	-34 05 55	2005 Nov 18	3600	1.2/1.2	390/580
HE 0054−2542^{c,e}	00 57 18.0	-25 26 09	2005 Nov 19	1200	1.0/1.0	390/580
HE 0100−1622	01 02 58.5	-16 06 31	2005 Nov 18	3600	1.2/1.2	390/580
HE 0109−4510	01 12 08.1	-44 54 16	2005 Nov 18	3600	1.0/1.0	390/580
HE 0134−1519	01 37 05.4	-15 04 23	2005 Nov 17	3600	1.0/1.0	390/580
			2005 Nov 20	10800	0.8/0.8	346/760
HE 0233−0343	02 36 29.7	-03 30 06	2005 Nov 17	3600	0.8/0.8	390/580
			2005 Nov 18	7200	1.0/0.7	390/580
			2005 Nov 19	4940	0.8/0.7	346/760
			2005 Nov 20	3600	0.8/0.7	346/760
HE 0243−3044	02 45 16.4	-30 32 02	2005 Nov 18	5400	1.0/1.0	390/580
			2005 Nov 20	3600	0.8/0.7	437/760
HE 0411−3558^{d,e}	04 13 09.0	-35 50 39	2005 Nov 17	3600	0.4/0.3	390/580
HE 0440−1049^e	04 42 39.7	-10 43 24	2006 Apr 18	900	1.2/1.2	390/580
HE 0440−3426^e	04 42 08.1	-34 21 13	2006 Apr 17	900	1.2/1.2	390/580
HE 0448−4806^e	04 49 33.0	-48 01 08	2006 Apr 18	840	1.2/1.2	390/580
HE 0450−4902	04 51 43.3	-48 57 25	2006 Apr 17	3600	1.2/1.2	390/580
HE 0945−1435^f	09 47 50.7	-14 49 07	2006 Apr 17	3600	1.2/1.2	390/580
			2006 Apr 18	7200	0.8/0.7	437/760
HE 1029−0546	10 31 48.2	-06 01 44	2006 Apr 17	3950	1.2/1.2	390/580
			2006 Apr 18	7200	0.8/0.7	390/580
HE 1218−1828	12 21 19.3	-18 45 34	2006 Apr 21	6000	1.2/1.2	390/580
			2006 Apr 21	3000	0.8/0.7	390/580
HE 1241−2907	12 44 13.0	-29 23 47	2006 Apr 17	3600	1.2/1.2	390/580
HE 1310−0536	13 13 31.2	-05 52 13	2006 Apr 17	3600	1.2/1.2	390/580
			2006 Apr 18	7200	0.8/0.7	437/760
HE 1429−0347^e	14 32 26.1	-04 00 31	2006 Apr 17	1800	1.2/1.2	390/580
			2006 Apr 18	7200	0.8/0.7	437/760
HE 2159−0551^e	22 02 16.4	-05 36 48	2006 Apr 18	900	0.8/0.7	390/580
HE 2208−1239^e	22 10 53.3	-12 24 27	2006 Apr 18	600	0.8/0.7	390/580
HE 2238−4131	22 41 22.6	-41 15 57	2005 Nov 19	3600	1.2/1.2	390/580
HE 2239−5019	22 42 26.9	-50 04 01	2005 Nov 17	10800	1.0/0.8	390/580
HE 2331−7155	23 34 36.1	-71 38 51	2005 Nov 17	3600	0.8/0.8	390/580
			2005 Nov 20	7200	0.8/0.7	437/760

a Blue slit / red slit
b Spectrograph setting 390/580 = DIC1 (390+580), etc.
c CS 22942−019; CD−26:304.
d CS 22186−005.
e Frebel et al. (2006)
f Norris et al. (2013a)

Table 4.2: Radial velocities and signal-to-noise ratios

Stellar ID	V_r (km s^{-1})	$V_{r,\mathrm{err}}$ (kms^{-1})	S/N $\lambda 3400$ Å	S/N $\lambda 4300$ Å	S/N $\lambda 6700$ Å
HE 0010$-$3422	158.8	0.2	11	49	84
HE 0054$-$2542	$-$214.6	0.1	9	46	96
HE 0100$-$1622	28.6	0.3	3	17	39
HE 0109$-$4510	138.8	0.1	5	25	33
HE 0134$-$1519	244.0	1.0	14	54	75
HE 0233$-$0343	63.5	0.6	9	35	42
HE 0243$-$3044	39.8	0.3	9	14	32
HE 0411$-$3558	196.2	0.3	26	105	110
HE 0440$-$1049	158.9	3.0	16	65	86
HE 0440$-$3426	326.0	0.6	16	61	162
HE 0448$-$4806	133.5	0.7	10	44	68
HE 0450$-$4902	332.4	1.5	4	26	29
HE 0945$-$1435	144.8	0.4	12	44	80
HE 1029$-$0546	18.6	0.3	10	35	45
HE 1218$-$1828	147.1	0.5	4	19	33
HE 1241$-$2907	336.3	2.2	4	31	16
HE 1310$-$0536	113.2	1.7	1	39	65
HE 1429$-$0347	$-$143.3	0.4	3	71	129
HE 2159$-$0551	$-$131.3	0.8	2	50	72
HE 2208$-$1239	$-$43.1	0.6	5	55	102
HE 2238$-$4131	$-$42.0	0.3	2	13	32
HE 2239$-$5019	368.7	0.5	9	44	43
HE 2331$-$7155	210.6	0.8	6	51	120

grid of MARCS atmosphere models (Gustafsson et al. 2008) using the PHYTON program fitter, written by S.J. Murphy. The MARCS models have parameters ranging in T_{eff} from 2500 K to 8000 K, in steps of 100 K from 2500 K to 4000 K, and in steps of 250 K from 4000 K to 8000 K. Surface gravity ($\log g$) values for the grid were between -1.0 (cgs) and 5.5 (cgs) in steps of 0.5 dex, and metallicities between -5.0 and $+1.0$ in variable steps. As the stars in this sample all have very low metallicities, α-enhanced models were used, with $[\alpha/\text{Fe}] = +0.25$ for $-1.5 \leq [\text{Fe/H}] \leq -0.5$ and $[\alpha/\text{Fe}] = +0.4$ for $-5.0 \leq [\text{Fe/H}] < -1.5$.

For two stars in the sample (marked in Table 4.3) we did not have spectrophotometric observations. The effective temperatures for these stars were determined from broadband photometry, using the $V - K$ color index, as this is least affected by metallicity (Alonso et al. 1999). The V and K magnitudes for the stars are listed in Table 4.3. The 2MASS K magnitudes were converted to the Johnson photometric system using the filter conversion $K_{\text{Johnson}} = K_{\text{2MASS}} + 0.044$ (Bessell 2005). Reddening values, $E(B - V)$, are adopted from Schlegel et al. (1998); values exceeding 0.1 mag were corrected according to Bonifacio et al. (2000). These values were then converted to $E(V - K)$, using the relation from Alonso et al. (1996), $E(V - K) = 2.72\,E(B - V)$. The final de-reddened $V - K$ colors were thus found from the following equation: $V - K_{0,\text{Johnson}} = V_{\text{Johnson}} - K_{\text{2MASS}} + 0.044 - 2.72\,E(B - V)$.

To estimate the effective temperatures we used the calibration of Alonso et al. (1996), as this provides temperatures that are in good agreement with the scale used for the majority of our sample. We determined temperatures using this method for as many stars in the sample as possible, in order to estimate the offset between the two temperature scales. We found an average offset of $+30$ K between the two temperature scales, and have corrected the temperatures determined from the $V - K$ colors accordingly ($T_{\text{eff}} = T_{\text{eff},V-K} + 30$). The V and $B - V$ photometry listed for HE 0010$-$3422 in Table 4.3 is almost certainly in error, as it results in a temperature ~ 1500 K below what was found from the spectrophotometric observations. Due to this large difference, this star has been excluded from the determination of the offset between the two temperature scales.

Surface gravity ($\log g$) estimates for the stars were determined from the Y^2 isochrones (Demarque et al. 2004), assuming an age of 10 Gyr (Yong et al. 2013) and an α-element enhancement of $[\alpha/\text{Fe}] = +0.3$ (the isochrones exists with $[\alpha/\text{Fe}] = 0.0$, $[\alpha/\text{Fe}] = +0.3$ and $[\alpha/\text{Fe}] = +0.6$). The isochrones extend in metallicity down to $[\text{Fe/H}] = -3.5$, so for the six stars in the sample with metallicities in the range $-4.7 \leq [\text{Fe/H}] \leq -3.5$, a linear extrapolation down to $[\text{Fe/H}] = -4.7$ has been used to obtain the gravity estimate. The average difference between the listed surface gravities where the actual $[\text{Fe/H}]$ have been used and the surface gravity obtained using the $[\text{Fe/H}] = -3.5$ isochrone is small, on the order of 0.05 dex.

Figure 4.1 shows the T_{eff} vs. $\log g$ diagram for the program stars with isochrones for three different metallicities: $[\text{Fe/H}] = -1.9$, $[\text{Fe/H}] = -2.5$, and $[\text{Fe/H}] = -3.5$. All isochrones have $[\alpha/\text{Fe}] = +0.3$ and an age of 10 Gyr. The sample shows a mixture of dwarfs, sub-giants, and giants.

For five of the warmer stars in the sample, HE 0233$-$0343, HE 0411$-$3558, HE 0450$-$4209, HE 1241$-$2907, and HE 2239$-$5019, the isochrones returned two possible solutions for the gravity. For these five stars we have tried to derive spectroscopic gravities and/or checked the isochrone gravities by fitting profiles of gravity-sensitive lines. The gravity of stars can be determined spectroscopically by enforcing ionization equilibrium between lines formed
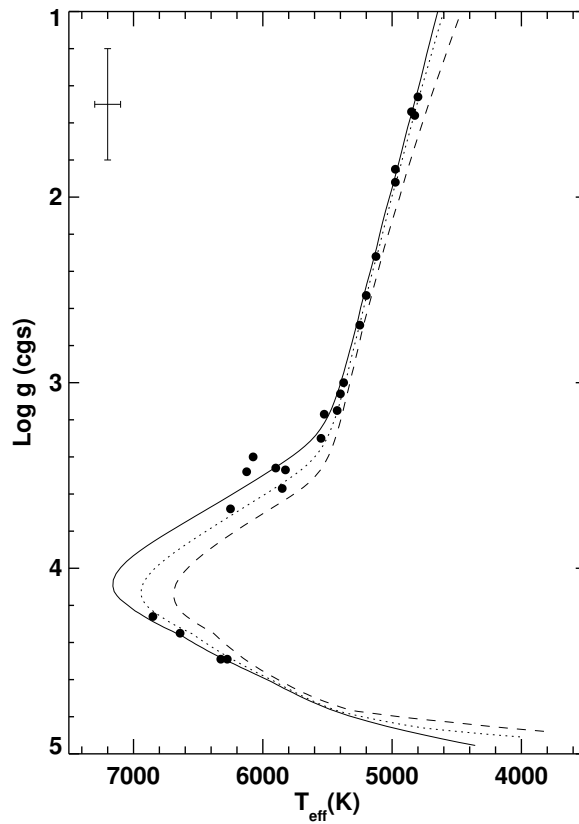
Figure 4.1: T_{eff} vs. $\log g$ diagram for the program stars, over-plotted with 10 Gyr isochrones for three different metallicities: [Fe/H] $= -3.5$ (solid line), [Fe/H] $= -2.5$ (dotted line) and [Fe/H] $= -1.9$ (dashed line). All of the isochrones have [α/Fe] $= +0.3$. A representative error bar on the derived parameters is shown in the upper left.

by neutral atoms and lines formed by ions, e.g., Fe I and Fe II or Ti I and Ti II, taking advantage of the fact that Fe I and Ti I lines are not significantly gravity sensitive, while the Fe II and Ti II lines are. We performed this analysis for the stars where both Fe I and Fe II or Ti I and Ti II lines were detected. A check of the gravity can also be performed by fitting the profiles of gravity-sensitive lines. Lines such as Mg I and the Ca II H and K lines exhibit strong pressure-broadened wings in cool stars. We performed spectral syntheses of these lines using model atmospheres with the two possible gravities, keeping all other parameters constant, in order to see which of the two possible gravities yields the best fit in the wings of these lines. The result of these tests yielded subgiant gravities for HE 0233−0343, HE 0411−3558 and HE 2239−5019 and dwarf gravities for HE 0450−4209 and HE 1241−2907 (see Table 4.3).

The microturbulent velocity (ξ) was computed in the usual way, by forcing the abundances from individual Fe I lines to show no trend with reduced equivalent width, $\log(W_\lambda/\lambda)$. For HE 0233−0343, too few Fe I line were present to determine the microturbulent velocity in this manner, so a fixed valued of $\xi = 2$ km s^{-1} was used for this star, following paper I.

Metallicities were determined from equivalent-width measurements of the Fe I lines. For a few stars we also detected a number of Fe II lines; for these stars there is good agreement between the abundance derived from the Fe II lines and that from the Fe I lines used for determining the temperature, gravity, and microturbulence.

The final stellar parameters and their estimated uncertainties are listed in Table 4.3.

4.3   Abundances

The elemental abundances were derived by synthesizing individual spectral lines and molecular bands. All abundances are derived under the assumption of 1D and Local Thermodynamic Equilibrium, and adopting the solar abundances from Asplund et al. (2009).

The 2011 version of MOOG (Sobeck et al. 2011; Sneden 1973) was used for the synthesis; this version of MOOG includes proper treatment of continuum scattering. For stars in the temperature range of our sample, the two main sources of opacity in stellar atmospheres are bound-free absorption from the negative hydrogen ion (H$^-$) and Rayleigh scattering from neutral atomic hydrogen. Their individual contributions to the total opacity depends on temperature and metallicity; at low temperature and low metallicity the contribution from Rayleigh scattering is almost equal to the contribution from bound-free absorption. So, when working with metal-poor stars it is especially important to model the scattering accurately to obtain the correct line intensities.

To perform the synthesis we used the α-enhanced NEWODF grid of ATLAS9 atmosphere models (Castelli & Kurucz 2003), interpolated with software developed by C. Allende Prieto, to obtain the models matching the parameters of the stars (e.g., Reddy et al. 2003; Allende Prieto et al. 2004). The α-enhanced ATLAS9 models cover a range in T_{eff}, from 3500 K to 50000 K, $\log g$, from 0.0 to 5.0 (cgs), for metallicities, [Fe/H], in the range -2.5 to $+0.5$ and [Fe/H] $= -4.0$. For the metallicity [Fe/H] $= -3.5$, models exists with temperatures in the range 3500 K to 6500 K, and surface gravities ranging from 0.0 to 5.0.

We used atomic data from the Gaia/ESO line list version 4 (Heiter et al., in prep.) for the analysis. This list covers the lines between 4750 Å to 6850 Å and 8500 Å to 8950 Å. For lines not covered by the Gaia/ESO line list, atomic data from the VALD database (Kupka

Table 4.3: Stellar photometry and stellar atmospheric parameters

Star	V	$B-V$	R[a]	$E(B-V)$	K[b]	$(V-K)_0$	$T_{\rm eff}$ (±100 K)	$\log g$ (±0.3 dex)	[Fe/H] (±0.2 dex)	ξ (±0.3 km s^{-1})
HE 0010−3422[c]	15.48	0.095	1	0.017	12.34	...	5400	3.1	−2.7	2.4
HE 0054−2542	12.69	0.880	2	0.040	10.65	1.89	5300	2.7	−2.5	1.3
HE 0100−1622	15.82	0.837	1	0.021	13.85	1.87	5400	3.0	−2.9	1.1
HE 0109−4510	16.01	0.523	1	0.011	14.18	1.75	5600	3.3	−3.0	1.1
HE 0134−1519	14.47	0.463	1	0.016	12.68	1.71	5500	3.2	−4.0	1.5
HE 0233−0343	15.43	0.437	1	0.025	14.06	1.26	6100	3.4	−4.7	2.0
HE 0243−3044	16.13	0.833	1	0.019	14.17	1.83	5400	3.2	−2.6	0.9
HE 0411−3558	12.96	0.382	1	0.011	11.58	1.31	6300	3.7	−2.8	3.4
HE 0440−1049	...	...	1	0.107	...	...	5800	3.5	−3.0	1.6
HE 0440−3426	11.44	1.440	3	0.013	8.97	2.39	4800	1.6	−2.2	1.9
HE 0448−4806	12.35	1.100	3	0.021	11.21	1.04	5900	3.6	−2.3	1.2
HE 0450−4902	...	...		0.009	...	...	6300	4.5	−3.1	1.2
HE 0945−1435	...	...	1	0.054	...	...	6300	4.5	−3.9	1.6
HE 1029−0546	15.63	0.355	1	0.043	14.37	1.10	6650[d]	4.3	−3.3	1.6
HE 1218−1828	16.34	0.493	1	0.043	14.70	1.48	5900[d]	3.5	−3.4	1.8
HE 1241−2907	...	...		0.071	...	...	6900	3.8	−3.0	1.8
HE 1310−0536	14.35	0.708	1	0.043	11.90	2.29	5000	1.9	−4.2	2.2
HE 1429−0347	13.69	0.687	1	0.110	11.41	1.94	5000	1.9	−2.7	1.5
HE 2159−0551	...	...		0.060	9.85	...	4800	1.5	−2.8	2.1
HE 2208−1239	...	...		0.041	...	...	5100	2.3	−2.9	2.0
HE 2238−4131	16.10	...		0.013	13.85	2.17	5200	2.5	−2.8	1.0
HE 2239−5019	15.85	0.393	1	0.009	14.28	1.50	6100	3.5	−4.2	1.8
HE 2331−7155	11.73	...		0.032	...	...	4900	1.5	−3.7	2.2

a Source of V and $B-V$ color; 1 = Beers et al. (2007a), 2 = Rossi et al. (2005), 3 = Høg et al. (2000).

b 2MASS Catalog (Skrutskie et al. 2006).

c The V and $B-V$ for this star reported by Beers et al. (2007a) is almost certainly in error.

d Photometric temperature.

et al. 2000) were adopted. A number of the elements analyzed exhibit hyperfine splitting (Sc, Mn, Co, Y, Zr, La, Pr, Nd and Eu). For those elements which only have lines in the region not covered by the Gaia/ESO line list, hyperfine splitting from Kurucz (1995) was used. The lines of Li, Ba, and Pb have both hyperfine splitting and isotopic shifts. The lines of Li and Ba are included in the Gaia/ESO line list, while Pb is not, so for this element data from Simons et al. (1989) was used.

Carbon and nitrogen abundances (or upper limits), and the isotopic ratios $^{12}C/^{13}C$, were obtained by synthesizing molecular bands, namely the 4300 Å CH G-band, the NH band at 3360 Å and the CN bands at 3890 Å and 4215 Å. All molecular information is taken from Masseron et al. (2014) and T. Masseron (priv. comm.). Dissociation energies of 3.47 eV, 3.42 eV, and 7.74 eV were used for the species CH, NH and CN, respectively.

When possible, N abundances were determined from synthesis of the CN bands using the C abundances computed from the CH band as fixed input. If no CN band was visible, the nitrogen abundance was derived from the NH band (which falls in a region of the spectra with substantially lower S/N). For stars where abundances could be derived from both bands the resultant N abundances, derived from the NH and CN bands respectively, are compared in Figure 4.2. For low N abundances, the results from the two bands agree well, while a discrepancy is seen at high N, with higher abundances being derived from the NH band compared to the CN band. The reason for this discrepancy is not clear, but the physical parameters, such as line positions and gf values, are less well-established for the NH band compared to the CN band, which could account, at least in part, for it.

The carbon abundance is coupled to the oxygen abundance through the CO molecule. Oxygen abundances or upper limits for the sample stars are derived from the 6300 Å line, but for the majority of our stars no reliable oxygen abundance could be obtained, so when deriving the carbon abundances we used a typical halo-star value of [O/Fe] = +0.4 for oxygen.

Molecular ^{13}CH features were identified for 11 of the stars in our sample. The $^{12}C/^{13}C$ isotopic ratios were determined from the analysis of ^{13}CH features in the wavelength range from 4210 Å to 4235 Å. Figure 4.3 shows the synthesis of the ^{13}CH line at 4230 Å in HE 2208−1239 for three different isotopic ratios.

The derived elemental abundances, along with propagated uncertainties arising from the effects of uncertainties of the stellar parameters, continuum placement, and line information, are listed in Table 4.4 for the "normal" metal-poor (hereafter, NMP) stars, Table 4.5 for the CEMP-no stars, Table 4.6 for the CEMP-s stars, and Table 4.7 for the CEMP-r and CEMP-r/s stars. The $^{12}C/^{13}C$ isotopic ratios, where available, are listed in Table 4.8.

4.4 Results

The abundance analysis yielded abundances or upper limits for 18 elements: Li, C, N, Na, Mg, Al, Si, Ca, Sc, Ti, Cr, Mn, Fe, Co, Ni, Sr, Ba and Eu, for all the stars in the sample, plus abundances or upper-limits of Y, Zr, La. Ce, Pr, Nd, Sm, Gd, Dy, Er and Pb, for the CEMP-s, CEMP-r and CEMP-r/s stars in the sample.

As many of our sample stars are carbon enhanced, resulting in blended lines, we have chosen to perform spectral synthesis to derive the abundances of individual elements, whereas abundances for the comparison sample of Yong et al. (2013) were derived mostly from
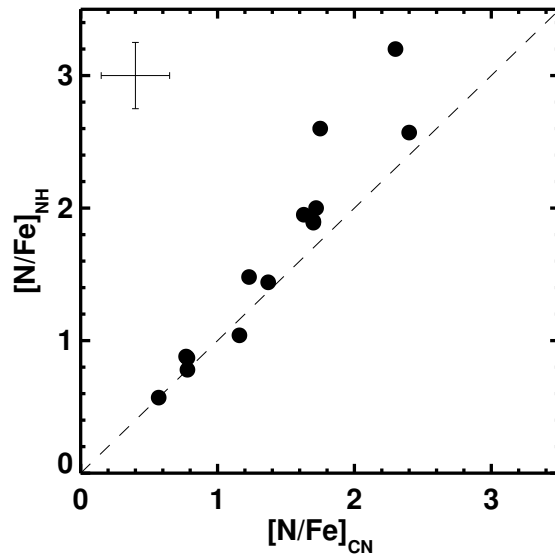
Figure 4.2: Comparison of nitrogen abundances estimated from the NH (3360 Å) and the CN (3890 Å) bands for stars where abundances could be derived from both bands. The dashed line is the one-to-one correlation. A representative error bar on the abundances ratios is shown in the upper left.
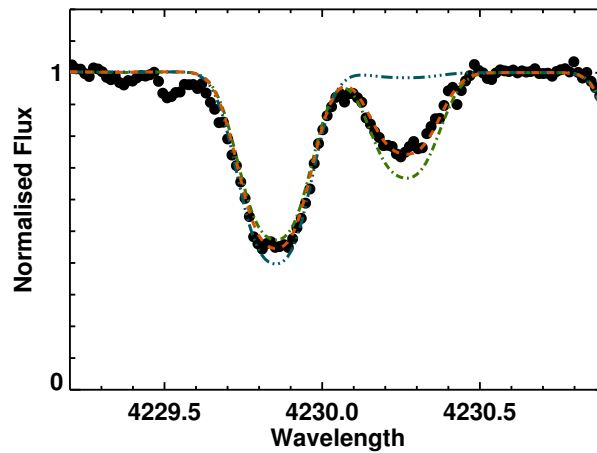
Figure 4.3: Synthesis of the ^{13}CH line at 4230 Å in HE 2208−1239 for three different isotopic ratios; 100% ^{12}CH (blue), ^{12}C/^{13}C = 79/21 (red) and ^{12}C/^{13}C = 70/30 (green).

Table 4.4: Derived abundances for "Normal" metal-poor (NMP) Stars

X/Fe	HE 0109−4510	HE 0411−3558	HE 0945−1435	HE 1218−1828	HE 1241−2907	HE 1429−0347	HE 2159−0551	HE 2239−5019
[Fe/H]	−2.96 (0.20)	−2.81 (0.20)	−3.87 (0.20)	−3.43 (0.20)	−3.00 (0.20)	−2.71 (0.20)	−2.81 (0.20)	−4.15 (0.20)
A(Li)	+1.46 (0.18)	< +1.44 ⋯	+1.88 (0.19)	+1.94 (0.17)	< +2.41 ⋯	+0.62 (0.16)	< +0.44 ⋯	+1.70 ⋯
[C/Fe]	+0.43 (0.26)	< +0.70 ⋯	< +2.00 ⋯	< +1.27	< +2.00 ⋯	+0.31 (0.23)	−0.24 (0.28)	< +1.70 ⋯
[N/Fe]	+0.57 (0.25)	< +1.30 ⋯	< +2.10 ⋯	< +1.70	< +2.60 ⋯	+1.89 (0.25)	+0.88 (0.29)	< +2.70 ⋯
[O/Fe]	< +2.30 ⋯	< +2.30 ⋯	< +4.00 ⋯	< +3.30	< +3.90 ⋯	+0.90 (0.15)	< +1.10 ⋯	< +4.00 ⋯
[Na/Fe]	−0.10 (0.19)	+0.02 (0.15)	< −0.30 ⋯	−0.33 (0.16)	+0.87 (0.18)	+1.00 (0.32)	−0.14 (0.30)	< −0.30 ⋯
[Mg/Fe]	+0.29 (0.19)	+0.24 (0.15)	+0.11 (0.14)	+0.32 (0.17)	+0.18 (0.19)	+0.28 (0.19)	+0.41 (0.24)	+0.45 (0.15)
[Al/Fe]	−0.91 (0.20)	−0.59 (0.20)	< −0.50 ⋯	−0.57 (0.22)	< −0.60 ⋯	+0.00 (0.17)	−0.82 (0.23)	−0.57 (0.21)
[Si/Fe]	+0.74 (0.20)	⋯ ⋯	+0.31 (0.16)	+0.06 (0.18)	+0.03 (0.20)	+0.66 (0.16)	+0.23 (0.22)	+0.06 (0.15)
[Ca/Fe]	+0.26 (0.18)	+0.22 (0.15)	+0.12 (0.18)	+0.60 (0.17)	+0.21 (0.19)	+0.49 (0.18)	+0.17 (0.23)	+0.23 (0.15)
[Sc/Fe]	+0.07 (0.22)	+0.38 (0.18)	< −0.10 ⋯	+0.12 (0.20)	+0.34 (0.22)	−0.08 (0.22)	−0.13 (0.27)	+0.32 (0.16)
[Ti/Fe]	+0.22 (0.23)	+0.59 (0.14)	−0.04 (0.18)	+0.25 (0.16)	+0.28 (0.18)	+0.30 (0.18)	+0.24 (0.23)	+0.37 (0.17)
[V/Fe]	< +0.80 ⋯	< +1.00 ⋯	< +1.80 ⋯	< +1.30	< +1.60 ⋯	+0.21 (0.17)	+0.17 (0.23)	< +2.00 ⋯
[Cr/Fe]	−0.47 (0.18)	−0.05 (0.17)	−0.17 (0.16)	−0.28 (0.19)	+0.04 (0.21)	−0.36 (0.18)	−0.40 (0.24)	+0.00 (0.17)
[Mn/Fe]	−1.02 (0.20)	−0.62 (0.20)	< −0.20 ⋯	−0.65 (0.22)	< +0.00 ⋯	−0.70 (0.20)	−0.45 (0.25)	< −0.10 ⋯
[Co/Fe]	+0.47 (0.21)	+0.16 (0.19)	< +1.00 ⋯	+0.38 (0.21)	< +1.00 ⋯	−0.11 (0.19)	−0.06 (0.25)	< +1.00 ⋯
[Ni/Fe]	+0.68 (0.21)	+0.10 (0.17)	+0.17 (0.14)	−0.06 (0.19)	+0.16 (0.21)	+0.00 (0.27)	−0.03 (0.30)	+0.24 (0.17)
[Zn/Fe]	< +0.80 ⋯	< +0.60 ⋯	< +1.80 ⋯	< +1.50	< +1.40 ⋯	+0.19 (0.15)	+0.36 (0.21)	< +2.00 ⋯
[Sr/Fe]	+1.00 (0.21)	−0.54 (0.19)	−0.90 ⋯	−0.51 (0.20)	−0.77 (0.22)	+0.10 (0.16)	+0.16 (0.22)	< −0.60 ⋯
[Ba/Fe]	−1.30 ⋯	−0.95 (0.14)	< 0.00 ⋯	< −0.52 ⋯	< −0.30 ⋯	−0.34 (0.17)	−1.58 (0.23)	< +0.00 ⋯
[Eu/Fe]	< +1.10 ⋯	< +1.50 ⋯	< +2.20 ⋯	< +2.00 ⋯	< +2.40 ⋯	+0.47 (0.20)	−0.20 (0.25)	< +2.50 ⋯

Table 4.5: Derived abundances for CEMP-no stars

[X/Fe]	HE 0100−1622	HE 0134−1519	HE 0233−0343	HE 0440−1049	HE 1310−0536	HE 2331−7155
[Fe/H]	−2.93 (0.20)	−3.98 (0.20)	−4.68 (0.20)	−3.02 (0.20)	−4.15 (0.20)	−3.68 (0.20)
A(Li)	< +1.12	⋯	+1.27 (0.19)	+1.77 (0.18)	+2.00 (0.14)	< +0.37
[C/Fe]	+2.75 (0.29)	+1.00 (0.26)	+3.48 (0.24)	+0.69 (0.25)	+2.36 (0.23)	+1.34 (0.26)
[N/Fe]	+1.90 (0.28)	< +1.00	< +2.80	+0.62	+3.20 (0.37)	+2.57 (0.28)
[O/Fe]	< +2.30	< +2.90	< +4.00	< +2.50	⋯	< +1.70
[Na/Fe]	> +1.00	−0.24 (0.15)	< +0.50	−0.04 (0.13)	+0.19 (0.14)	+0.46 (0.30)
[Mg/Fe]	+0.64 (0.23)	+0.25 (0.14)	+0.59 (0.15)	+0.79 (0.14)	+0.42 (0.16)	+1.20 (0.23)
[Al/Fe]	+0.46 (0.24)	−0.38 (0.20)	+0.03	−0.57 (0.20)	−0.39 (0.21)	−0.38 (0.21)
[Si/Fe]	⋯	+0.05 (0.16)	+0.37 (0.15)	+0.80 (0.15)	< +0.25	⋯
[Ca/Fe]	+0.49 (0.22)	+0.10 (0.13)	+0.34 (0.15)	+0.50 (0.14)	+0.00 (0.20)	+0.20 (0.22)
[Sc/Fe]	⋯	+0.00 (0.18)	< +0.70	−0.12 (0.18)	−0.07 (0.16)	+0.09 (0.25)
[Ti/Fe]	+0.71 (0.25)	+0.11 (0.21)	+0.18 (0.17)	+0.23 (0.14)	+0.35 (0.18)	+0.26 (0.22)
[V/Fe]	+0.67 (0.22)	< +1.20	< +2.50	< +0.80	< +0.90	+0.30 (0.21)
[Cr/Fe]	+0.08 (0.23)	−0.22 (0.18)	< +0.50	−0.14 (0.17)	−0.49 (0.26)	−0.45 (0.22)
[Mn/Fe]	−0.18 (0.24)	−0.65 (0.19)	< +0.20	−0.60 (0.22)	−0.79 (0.20)	−0.96 (0.24)
[Co/Fe]	+0.28 (0.25)	+0.20 (0.18)	< +1.60	+0.30 (0.19)	+0.28 (0.16)	+0.30 (0.23)
[Ni/Fe]	+0.37 (0.24)	+0.19 (0.19)	< +0.90	+0.18 (0.17)	−0.12 (0.20)	−0.04 (0.29)
[Zn/Fe]	< +0.90	< +1.20	< +2.60	< +0.80	< +1.30	< +0.70
[Sr/Fe]	+0.25 (0.25)	−0.30 (0.19)	+0.32 (0.19)	−0.30 (0.19)	−1.08 (0.14)	−0.85 (0.20)
[Ba/Fe]	< −1.80	< −0.50	< +0.80	−1.27 (0.15)	−0.50 (0.15)	−0.90 (0.21)
[Eu/Fe]	< +0.80	< +1.50	< +3.00	< +1.50	< +1.20	< +0.50

Table 4.6: Derived abundances for CEMP-*s* stars

[X/Fe]	HE 0054−2542	HE 0440−3426	HE 0450−4902	HE 1029−0546	HE 2238−4131
[Fe/H]	−2.48 (0.20)	−2.19 (0.20)	−3.07 (0.20)	−3.28 (0.20)	−2.75 (0.20)
A(Li)	< +0.57 ...	< +0.26 ...	< +1.98 ...	< +2.00 ...	< +0.30 ...
[C/Fe]	+2.13 (0.29)	+1.51 (0.25)	+2.03 (0.23)	+2.64 (0.20)	+2.63 (0.32)
[N/Fe]	+0.87 (0.27)	+0.78 (0.26)	+2.00 (0.29)	+2.90 (0.27)	+1.04 (0.33)
[O/Fe]	< +1.20 ...	+0.69 (0.17)	< +3.50 ...	< +3.70 ...	< +1.70 ...
[Na/Fe]	> +1.20 ...	+0.67 (0.30)	+0.23 (0.22)	... ...	> +1.60 ...
[Mg/Fe]	+0.78 (0.23)	+0.43 (0.21)	+0.53 (0.20)	−0.03 (0.17)	+0.87 (0.29)
[Al/Fe]	+0.10 (0.21)	... ...	−0.78 (0.26)	< −0.42 ...	+0.12 (0.28)
[Si/Fe]	... ...	... ...	+0.00 (0.21)	−0.03 (0.18)	... ...
[Ca/Fe]	+0.40 (0.22)	+0.23 (0.20)	+0.70 (0.23)	+0.16 (0.20)	+0.43 (0.28)
[Sc/Fe]	... ...	... ...	+0.12 (0.24)	+0.33 (0.21)	... ...
[Ti/Fe]	+0.42 (0.22)	+0.26 (0.20)	+0.58 (0.22)	+0.45 (0.20)	+0.44(0.28)
[V/Fe]	+0.28 (0.27)	+0.03 (0.19)	< +1.30 ...	< +1.20 ...	... ...
[Cr/Fe]	−0.03 (0.22)	−0.12 (0.20)	+0.03 (0.21)	−0.08 (0.18)	+0.00 (0.28)
[Mn/Fe]	−0.38 (0.24)	−0.63 (0.22)	−0.73 (0.26)	−0.14 (0.24)	−0.63 (0.30)
[Co/Fe]	−0.13 (0.25)	−0.54 (0.21)	< +0.60 ...	+0.90 (0.25)	−0.02 (0.29)
[Ni/Fe]	−0.10 (0.27)	+0.03 (0.28)	+0.00 (0.20)	+0.34 (0.17)	+0.00 (0.34)
[Zn/Fe]	< +0.08 ...	+0.06 (0.18)	< +1.40 ...	< +1.60 ...	< +0.70 ...
[Sr/Fe]	+1.65 (0.20)	+0.33 (0.18)	+0.64 (0.26)	+0.07 (0.24)	+1.75 (0.27)
[Y/Fe]	+1.99 (0.23)	+0.33 (0.19)	... ...	< +1.05 ...	+2.13 (0.28)
[Zr/Fe]	+2.26 (0.22)	+0.64 (0.20)	... ...	< +1.70 ...	+2.38 (0.29)
[Ba/Fe]	+1.52 (0.26)	+0.46 (0.19)	+1.21 (0.20)	+0.80 (0.17)	+1.80 (0.28)
[La/Fe]	+1.63 (0.24)	+1.18 (0.20)	... ...	... ...	+2.32 (0.28)
[Ce/Fe]	+1.50 (0.23)	+0.89 (0.18)	... ...	< +2.70 ...	+2.35 (0.27)
[Pr/Fe]	+1.60 (0.23)	+1.07 (0.20)	... ...	... ...	+2.26 (0.27)
[Nd/Fe]	+0.36 (0.23)	+0.30 (0.17)	... ...	< +2.46 ...	+1.05 (0.26)
[Sm/Fe]	+1.33 (0.21)	+1.01 (0.24)	... ...	... ...	+1.70 (0.31)
[Eu/Fe]	+0.78 (0.23)	< +0.62 ...	< +2.00 ...	< +2.50 ...	+1.10 (0.29)
[Gd/Fe]	+1.10 (0.24)	... ...	... ...	... ...	... ...
[Dy/Fe]	+1.20 (0.24)	+0.74 (0.21)	... ...	... ...	+1.70 (0.29)
[Er/Fe]	... ...	+1.14 (0.21)	... ...	... ...	> +2.00 ...
[Pb/Fe]	< +1.50 ...	+1.64 (0.23)	< +3.00 ...	+3.34 (0.23)	< +2.00 ...

Table 4.7: Derived abundances for CEMP-r and CEMP-r/s stars

	CEMP-r		CEMP-r/s	
[X/Fe]	HE 0010−3422	HE 0448−4806	HE 0243−3044	HE 2208−1239
[Fe/H]	−2.78 (0.20)	−2.26 (0.20)	−2.58 (0.20)	−2.88 (0.20)
A(Li)	< +1.11 . . .	< +1.49 . . .	< +0.97 . . .	< +0.77 . . .
[C/Fe]	+1.92 (0.31)	+2.24 (0.29)	+2.43 (0.27)	+1.30 (0.29)
[N/Fe]	+2.60 (0.27)	+1.44 (0.29)	+1.48 (0.28)	+1.95 (0.25)
[O/Fe]	< +2.02 . . .	< +1.90 . . .	< +1.90 . . .	< +1.40 . . .
[Na/Fe]	+1.00 (0.28)	> +0.70 . . .	> +1.00 . . .	. . . . . .
[Mg/Fe]	+0.34 (0.23)	+0.44 (0.20)	+1.08 (0.23)	+0.59 (0.20)
[Al/Fe]	−0.54 (0.21)	−0.23 (0.24)	+0.04 (0.22)	−0.32 (0.18)
[Si/Fe]	. . . . . .	. . . . . .	. . . . . .	. . . . . .
[Ca/Fe]	+0.26 (0.22)	+0.35 (0.20)	+0.12 (0.22)	+0.45 (0.19)
[Sc/Fe]	+0.45 (0.24)	+0.25 (0.23)	. . . . . .	+0.25 (0.19)
[Ti/Fe]	+0.59 (0.22)	+0.50 (0.20)	+0.43 (0.23)	+0.70 (0.19)
[V/Fe]	+0.73 (0.27)	+0.38 (0.21)	+0.73 (0.22)	+0.54 (0.25)
[Cr/Fe]	−0.23 (0.25)	−0.03 (0.22)	−0.07 (0.23)	−0.20 (0.22)
[Mn/Fe]	−0.71 (0.24)	−0.37 (0.26)	−0.47 (0.25)	−0.83 (0.22)
[Co/Fe]	+0.15 (0.25)	+0.04 (0.25)	+0.03 (0.24)	+0.10 (0.22)
[Ni/Fe]	+0.01 (0.27)	+0.14 (0.22)	+0.26 (0.30)	−0.10 (0.24)
[Zn/Fe]	+0.57 (0.21)	+0.33 (0.24)	< +0.50 . . .	+0.36 (0.18)
[Sr/Fe]	+0.85 (0.20)	+1.10 (0.23)	+0.97 (0.21)	+0.50 (0.17)
[Y/Fe]	+1.01 (0.23)	+0.93 (0.22)	+0.99 (0.22)	+0.37 (0.20)
[Zr/Fe]	+1.08 (0.22)	+1.10 (0.21)	+1.06 (0.23)	+0.84 (0.19)
[Ba/Fe]	+1.54 (0.26)	+1.78 (0.20)	+1.96 (0.22)	+1.68 (0.23)
[La/Fe]	+2.21 (0.24)	+2.33 (0.23)	+2.51 (0.23)	+1.96 (0.21)
[Ce/Fe]	+1.99 (0.23)	+2.20 (0.23)	+2.32 (0.21)	+1.80 (0.21)
[Pr/Fe]	+2.00 (0.20)	+2.24 (0.22)	+2.48 (0.22)	+1.77 (0.20)
[Nd/Fe]	+1.30 (0.23)	+1.46 (0.22)	+1.69 (0.20)	+1.06 (0.20)
[Sm/Fe]	+1.97 (0.21)	+2.09 (0.21)	+2.18 (0.26)	+1.76 (0.18)
[Eu/Fe]	+1.72 (0.23)	+1.87 (0.23)	+1.90 (0.24)	+1.52 (0.21)
[Gd/Fe]	. . . . . .	+1.92 (0.24)	+2.35 (0.23)	+1.61 (0.22)
[Dy/Fe]	. . . . . .	+1.89 (0.23)	+1.80 (0.24)	. . . . . .
[Er/Fe]	. . . . . .	+2.78 (0.22)	+2.64 (0.24)	+1.97 (0.20)
[Pb/Fe]	+2.62 (0.27)	+3.17 (0.29)	+3.07 (0.25)	+1.70 (0.36)

Table 4.8: ^{12}C/^{13}C isotopic ratios

Star	^{12}C/^{13}C	Type
HE 0010-3422	5	CEMP-r
HE 0054-2542	16	CEMP-s
HE 0100-1622	13	CEMP-no
HE 0134-1519	>4	CEMP-no
HE 0233-0343	>5	CEMP-no
HE 0243-3044	10	CEMP-r/s
HE 0440-3426	13	CEMP-s
HE 0448-4806	10	CEMP-r
HE 1029-0546	9	CEMP-s
HE 1310-0536	3	CEMP-no
HE 2208-1239	4	CEMP-r/s
HE 2238-4131	16	CEMP-s
HE 2331-7155	5	CEMP-no

equivalent-width measurements. All other aspects of the analysis are the same for the two samples, thus, by combining them we have a sample of over 200 homogeneously analyzed metal-poor stars. As a demonstration, we have derived abundances for HE 0146−1548 from the sample of Yong et al. (2013). These are listed in Table 4.9 along with the abundances listed in Yong et al. (2013). As can be seen, the two sets of abundances derived for this star agree very well.

The combined sample includes examples of all the different stellar abundance patterns that are commonly found at very low metallicity, for both carbon-enhanced stars (all four sub-classes are represented) and non carbon-enhanced stars. With this variety, and the fact that the combined sample includes some of the most metal-poor stars known, we are able to carry out a more detailed investigation of the signatures of our Galaxy's early chemical evolution than previous possible.

Yong et al. (2013) did not present Ba and Eu abundances for all the stars in their sample. However, abundances of these two elements are essential for the classification of CEMP stars (CEMP-no: [Ba/Fe] < 0, CEMP-s: [Ba/Fe] > +1, [Ba/Eu] > +0.5, CEMP-r: [Eu/Fe] > +1, CEMP-r/s: 0.0 < [Ba/Eu] < +0.5), thus we have searched the literature for Ba and Eu abundances for the full sample of CEMP stars from Yong et al. (2013); these additional abundances are listed in Table 4.10. The supplemental abundances are only used for classification of the CEMP stars, and not included in the plots, as they have not been derived in the same homogeneous manner as the abundances presented here. Table 4.10 also includes upper limits for Ba in HE 0107−5240, HE 0557−4840, and HE 1327−2326, as these all lie in the sparsely populated region with [Fe/H] < −4.0; we include them in our plots. The combined sample includes 143 NMP, 32 CEMP-no, 30 CEMP-s, 4 CEMP-r, and 4 CEMP-r/s stars.

Table 4.9: Abundances derived for HE 0145−1548

[X/Fe]	Yong et al. (2013)	This work
[C/Fe]	+0.84	+0.80
[Na/Fe]	+1.17	+1.15
[Mg/Fe]	+0.87	+0.86
[Al/Fe]	+0.14	+0.10
[Si/Fe]	+0.50	< +0.66
[Ca/Fe]	+0.22	+0.19
[Ti/Fe]	+0.17	+0.15
[Cr/Fe]	−0.38	−0.39
[Mn/Fe]	−0.59	−0.64
[Co/Fe]	+0.30	. . .
[Ni/Fe]	+0.05	+0.07
[Sr/Fe]	−0.38	−0.34
[Ba/Fe]	−0.71	−0.78

4.4.1   Carbon and nitrogen

Carbon and nitrogen are among the first elements to be synthesized in the universe following the Big Bang. Yet our understanding of the abundances of these two elements found in the most metal-poor stars of our Galaxy is still limited. It is recognized that the observed carbon and nitrogen abundances of a given star are subject to change as the star evolves past the main sequence and up the red giant branch. Material that has been C-depleted and N-enhanced in the lower layers of a stellar atmosphere is transported to the surface of the star via mixing, enhancing N at the expense of C at the surface of the star. Thus, if we require the abundances of these two elements at the time when the star was born, in order to better constrain its progenitor, we need to correct the abundances of C and N for these evolutionary effects.

Placco et al. (2014c) have developed a method for correcting the C abundances in metal-poor stars according to the evolutionary state of the star, based on the STARS stellar evolution code (Eggleton 1971; Stancliffe & Eldridge 2009c) and thermohaline mixing as described in Stancliffe et al. (2009b). We have corrected the C abundances for the giant stars in our sample using this method; for the Yong et al. (2013) sample we have used the corrections listed in Placco et al. (2014c), while corrections for our own sample can be seen in Table 4.11 (only including the non-zero corrections). For the remainder of this work we employ the corrected C abundances, unless stated otherwise. Note that no explicit correction is currently made for N.

[C/N] > 0 **vs.** [C/N] < 0 **stars**

Many of the carbon-enhanced stars are also found to be enhanced in nitrogen. However, the minority of VMP, EMP, and UMP stars have both elements detected, a deficiency that surely needs to be addressed in the near future. Only 79 of the 193 stars in the sample of Yong et al. (2013) have detections of both C and N. In our sample of 23 stars, we detect C

Table 4.10: Ba and Eu abundances from the literature

Star	[X/Fe]	Ref
	Ba	
BD-18:5550	-0.74	François et al. (2007)
CS 22880$-$074	$+1.31$	Aoki et al. (2002d)
CS 22892$-$052	$+0.99$	Sneden et al. (2003)
CS 22897$-$008	-1.00	François et al. (2007)
CS 29498$-$043	-0.45	Aoki et al. (2002c)
CS 29516$-$024	-0.90	François et al. (2007)
CS 30301$-$015	$+1.45$	Aoki et al. (2002d)
CS 31062$-$050	$+2.30$	Aoki et al. (2002d)
HD 196944	$+1.10$	Aoki et al. (2002b)
HE 0107$-$5240	$< +0.82$	Christlieb et al. (2004a)
HE 0557$-$4840	$< +0.03$	Norris et al. (2007)
HE 1300+0157	< -0.63	Cohen et al. (2008)
HE 1327$-$2326	$< +1.46$	Aoki et al. (2006)
	Eu	
CS 22880$-$074	$+0.50$	Aoki et al. (2002d)
CS 22892$-$052	$+1.64$	Sneden et al. (2003)
CS 22948$-$027	$+1.57$	Aoki et al. (2002d)
CS 29497$-$034	$+1.80$	Barbuy et al. (2005)
CS 29503$-$010	$+1.69$	Allen et al. (2012)
CS 30301$-$015	$+0.20$	Aoki et al. (2002d)
CS 31062$-$012	$+1.62$	Aoki et al. (2002d)
CS 31062$-$050	$+1.84$	Aoki et al. (2002d)
HD 196944	$+0.17$	Aoki et al. (2002d)
HE 0143$-$0441	$+1.46$	Cohen et al. (2006)
HE 0336+0113	$+1.18$	Cohen et al. (2013)
HE 1031$-$0020	$< +0.87$	Cohen et al. (2006)
HE 2158$-$0348	$+0.80$	Cohen et al. (2006)

Table 4.11: Carbon abundances corrected for stellar-evolution effects

Star	logg	[Fe/H]	[C/Fe]$_{original}$	[C/Fe]$_{corrected}$	[N/Fe]
HE 0054$-$2542	2.69	-2.48	$+2.13$	$+2.15$	$+0.87$
HE 0440$-$3426	1.56	-2.19	$+1.51$	$+1.64$	$+0.78$
HE 1310$-$0536	1.85	-4.15	$+2.36$	$+2.47$	$+3.20$
HE 1429$-$0347	1.92	-2.71	$+0.31$	$+0.45$	$+1.89$
HE 2159$-$0551	1.46	-2.81	-0.24	$+0.22$	$+0.88$
HE 2208$-$1239	2.32	-2.88	$+1.30$	$+1.31$	$+1.95$
HE 2238$-$4131	2.53	-2.75	$+2.63$	$+2.65$	$+1.04$
HE 2331$-$7155	1.54	-3.68	$+1.34$	$+1.69$	$+2.57$
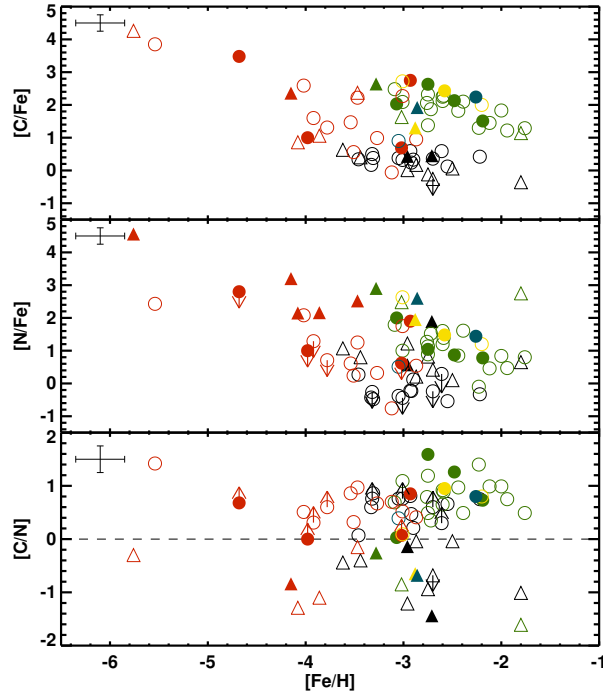
Figure 4.4: C and N abundances and [C/N] ratios for stars in this sample (filled symbols) and that of Yong et al. (2013) (unfilled symbols). Circles represent stars with [C/N] > 0; triangles are stars with [C/N] < 0. Symbols are color-coded according to black: "normal" metal-poor (NMP) stars, red: CEMP-no stars, green: CEMP-*s* stars, blue: CEMP-*r* stars, yellow: CEMP-*r/s* stars. An approximate error bar for the sample stars is shown in the upper left of each panel.

and N simultaneously for as many as 14 stars, increasing the number of stars with C and N detections in the combined sample by about 20%. In the combined sample we have 104 stars with both C and N detections, plus a few with a detection of either C or N and an upper limit on the other. Roughly equal numbers of these are NMP and CEMP stars.

Figure 4.4 shows the C and N abundances and the [C/N] ratios of our combined sample of stars as a function of metallicity. We have divided the stars into two groups – dots indicate stars where [C/N] > 0 ([C/Fe] > [N/Fe]) and triangles indicate stars where [C/N] < 0 ([C/Fe] < [N/Fe]). As we do not have the N abundance corrections corresponding to the C corrections mentioned above, this plot only includes dwarfs, subgiants, and early giants, for which the corrections in C and N will not alter the [C/N] > 0 or [C/N] < 0 status of the star. For the remainder of this paper we refer to this subsample as the "C/N stars".

Figure 4.5 shows the number of each type of metal-poor star with either [C/N] > 0 or [C/N] < 0. There are clearly more stars with [C/N] > 0 than with [C/N] < 0. For the
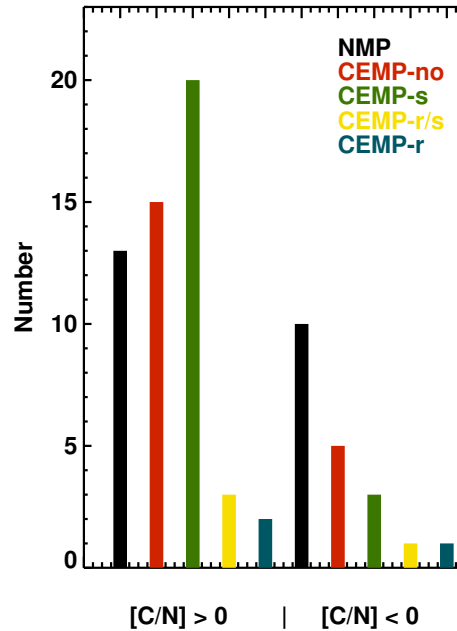
Figure 4.5: Number of stars with either [C/N] > 0 or [C/N] < 0 for the different types of metal-poor stars. Black: NMP stars, red: CEMP-no stars, green: CEMP-*s* stars, blue: CEMP-*r* stars, yellow: CEMP-*r/s* stars

NMP stars the numbers are roughly equal, while the CEMP-no and especially the CEMP-*s* stars are of the [C/N] > 0 variety. From inspection of the bottom panel of Figure 4.4, none of the CEMP-no stars with [C/N] < 0 are found with metallicities above [Fe/H] > −3.4; all CEMP-no stars with [C/N] < 0 are at the extremely low-metallicity end.

Examination of the abundance ratios for the remaining elements for these stars using this division between C- and N-dominated stars, plotted in Figure 4.6, Figure 4.7, Figure 4.8, and Figure 4.9, indicates that [Fe/H] = −3.4 also serves as a dividing line for the Na and Mg abundances in CEMP-no stars. Below this metallicity, stars with large over-abundances of these two elements appear, in contrast to the behavior above this metallicity. Two of the CEMP-no stars with [C/N] < 0, HE 1327−2326 and HE 2323−0256, show large enhancements in Na, Mg and Sr, while the other two stars, HE 1150−0428 and HE 1310−0536, both have [Mg/Fe] ∼ 0.4 and subsolar [Sr/Fe].

For the remainder of the elements we see the well-known abundance patterns found at low metallicity in these plots – moderate over-abundances of the α-elements and very low star-to-star scatter for both the α- and iron-peak elements, with a large scatter for the neutron-capture elements.
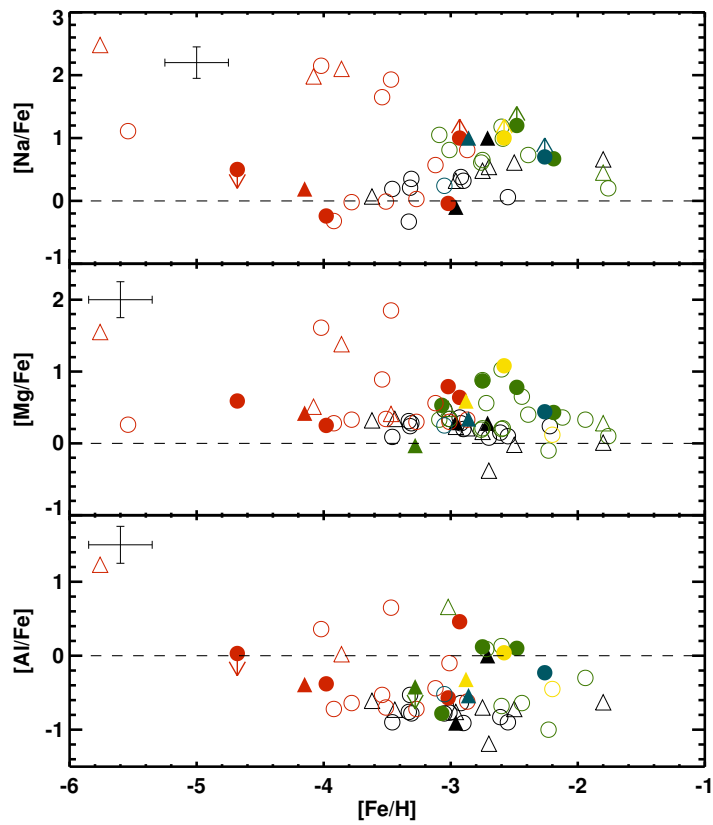
Figure 4.6: [Na/Fe], [Mg/Fe], and [Al/Fe] for the C/N stars. Color-coding of the stellar classes is as in Figure 4.4. An approximate error bar for the sample stars is shown in the upper left of each panel.
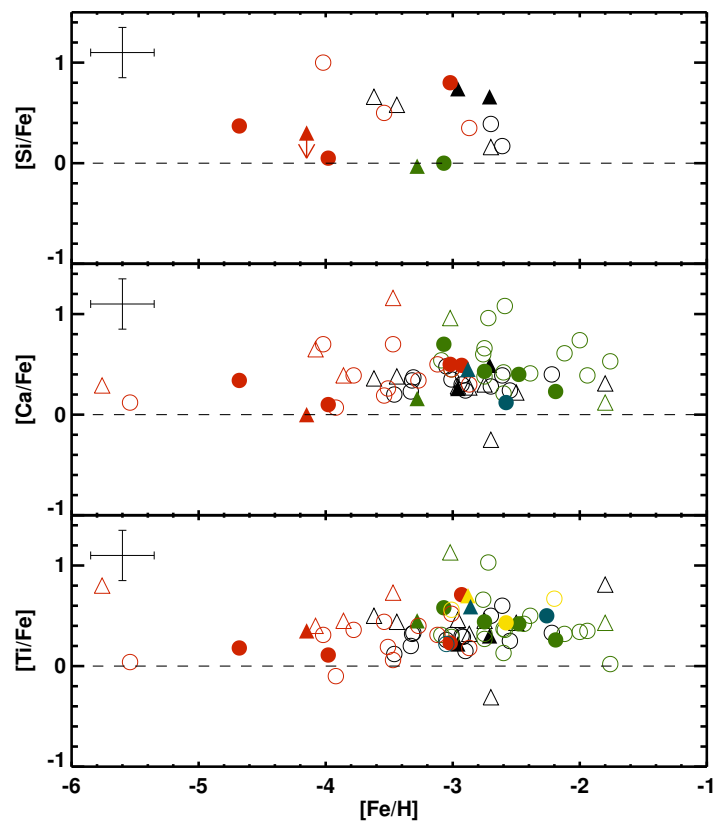
Figure 4.7: [Si/Fe], [Ca/Fe], and [Ti/Fe] for the C/N stars. Color-coding of the stellar classes is as in Figure 4.4. An approximate error bar for the sample stars is shown in the upper left of each panel.
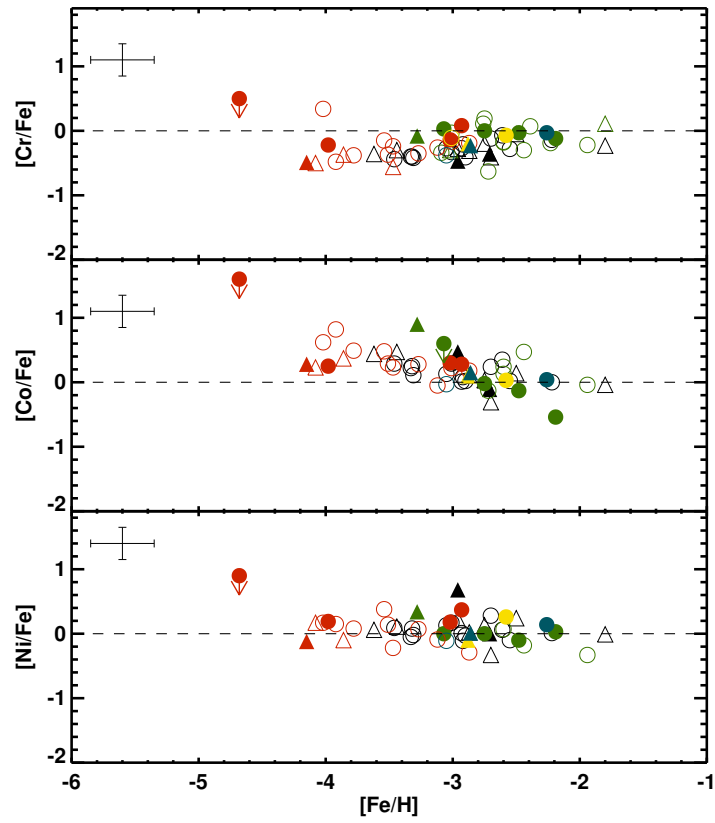
Figure 4.8: [Cr/Fe], [Co/Fe], and [Ni/Fe] for the C/N stars. Color-coding of the stellar classes is as in Figure 4.4. An approximate error bar for the sample stars is shown in the upper left of each panel.
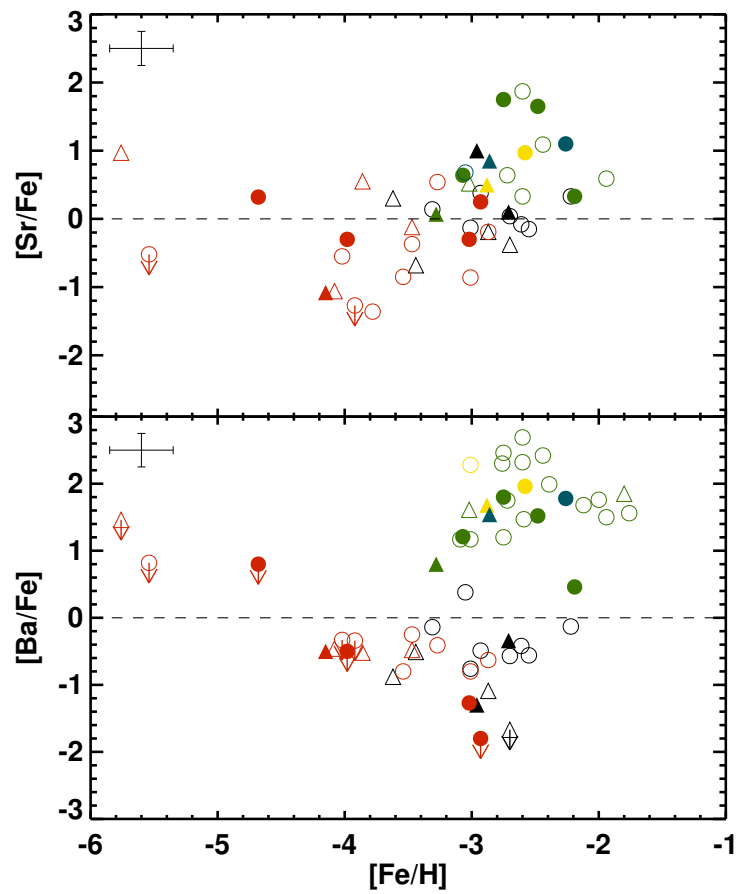
Figure 4.9: [Sr/Fe] and [Ba/Fe] for the C/N stars. Color-coding of the stellar classes is as in Figure 4.4. An approximate error bar for the sample stars is shown in the upper left of each panel.

An additional sub-class of metal-poor stars has been defined for stars with $[N/Fe] > +0.5$ and $[C/N] < -0.5$, the so-called nitrogen-enhanced metal-poor (NEMP) stars (Johnson et al. 2007). These stars are expected to be the result of mass transfer from an intermediate-mass AGB star that has undergone hot bottom burning, and thereby produced large amounts of nitrogen. Very few of these stars are known to exist, so here we consider the six stars in our sample with $[C/N] < 0$ to see if they are possible NEMP stars. Two of the stars, HE $1310-0536$ and HE $2331-7155$, are CEMP-no stars, and two, HE $1429-0347$ and HE $2159-0551$, are NMP stars. None of these exhibits excesses of neutron-capture elements, as would be expected for the NEMP stars, thus they can be excluded from this class. This leaves HE $0010-3422$ (a CEMP-r star) and HE $2208-1239$ (a CEMP-r/s star) as NEMP candidates. The binary status of these two stars is not known, but future radial-velocity monitoring should be able to clarify if they are consistent with an NEMP classification.

The carbon plateau(s)

Spite et al. (2013) suggested the presence of two separate plateaus or "bands" in the distribution of C abundances, as a function of [Fe/H], for VMP and EMP stars. The C abundances for stars with metallicities $[Fe/H] > -3$ appeared to cluster around the solar carbon abundance ($A(C) \sim 8.5$[2]), while those with $[Fe/H] < -3$ (including the lowest metallicity stars known) cluster around a lower C abundance, $A(C) \sim 6.5$. These authors proposed that the two bands could be associated with differing astrophysical production sites for the C in these stars – those in the higher band being the result of mass transfer of C from an asymptotic giant-branch (AGB) companion (i.e., extrinsic enrichment), whereas those in the lower band being the result of C that is intrinsic to the star (that is, the C was already present in the ISM from which the star was born). It is useful to note that Spite et al. (2013) only used dwarfs and turnoff stars in their study, stars where the C abundances are not expected to be altered due to evolutionary effects. The recent paper by Bonifacio et al. (2015) confirms the existence of the two carbon bands for a larger sample, including the stars from Yong et al. (2013).

We consider this question again with our new sample. Figure 4.10 shows the absolute carbon abundances, $A(C)$, for the stars in our new sample (dots) along with those of Yong et al. (2013) (plusses), as a function of [Fe/H]. The top panel shows only the CEMP stars, while the bottom panel shows both the CEMP and NMP stars. There does indeed appear to exist a difference in the C abundances for the lower metallicity and higher metallicity CEMP stars, as suggested by Spite et al. (2013). Our larger dataset exhibits a smoother transition between the two bands in the metallicity region $[Fe/H] \sim -3.4$ to $[Fe/H] \sim -3.2$. Bonifacio et al. (2015) identify four CEMP-no stars with C abundances on the high carbon band. In Figure 4.10 it can be seen that our sample includes three CEMP-no stars with C abundances on the high band. These three stars – HE $0100-1622$ ($[Ba/Fe] < -1.80$), HE $2202-4831$ ($[Ba/Fe] = -1.28$) and HE $2356-0410$ ($[Ba/Fe] = -0.80$) are all confirmed CEMP-no stars, hence they challenge the interpretation of the two bands as being solely due to extrinsic and intrinsic processes. We note that the binary status of this handful of stars is not presently known, and would clearly be of great interest to constrain. If the CEMP-no stars found on the high carbon band are indeed the result of mass transfer in a

---

[2]Here we employ the standard notation that $A(X) = \log \epsilon(X) + 12.0$.
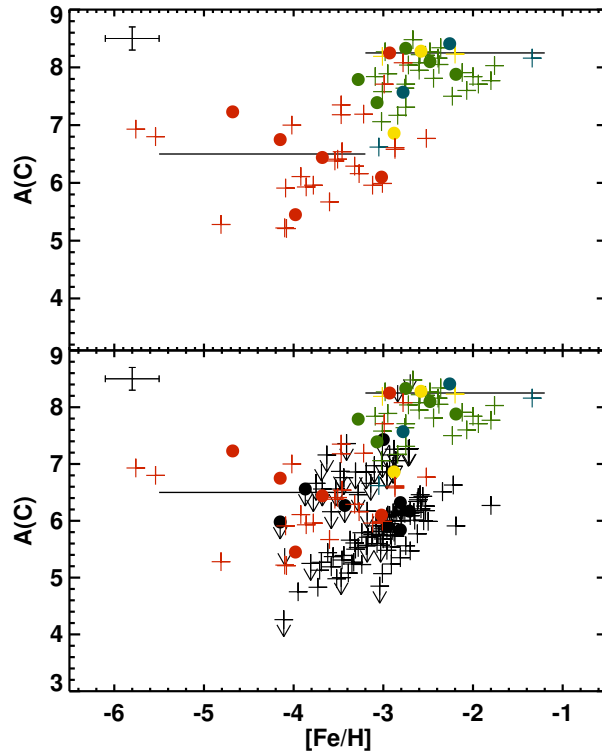
Figure 4.10: A(C) abundances for sample stars (dots) and stars from Yong et al. (2013) (plusses). The top panel shows only CEMP stars, while all stars (including non carbon-enhanced stars) are shown in the bottom panel. The two carbon bands are indicated by solid lines, and upper limits on individual C abundances are indicated by arrows. Symbols are color-coded according to black: "normal" metal-poor (NMP) stars, red: CEMP-no stars, green: CEMP-s stars, blue: CEMP-r stars, yellow: CEMP-r/s stars. An approximate error bar for the sample stars is shown in the upper left of each panel.

binary system, it will be difficult to explain how large amounts of carbon but no or very small amounts of s-process elements have been transferred from their AGB companion.

We also see that CEMP-r and CEMP-r/s stars are found at both the high and the low levels of C enhancement. It would be interesting to examine larger samples of these stars, in order to search for the possible dominance of either high or low carbon-abundance stars for either of these CEMP sub-classes.

The large carbon enhancements found in the lowest metallicity stars is expected to be related to the formation of low-mass stars in the early universe. It has been demonstrated that low-mass stars can form as a result of cooling of gas clouds via fine-structure lines of carbon and oxygen (Bromm & Loeb 2003; Frebel et al. 2007b). Hence, the large C abundances found at the lowest metallicities in our sample support the formation of low-mass stars via this channel.
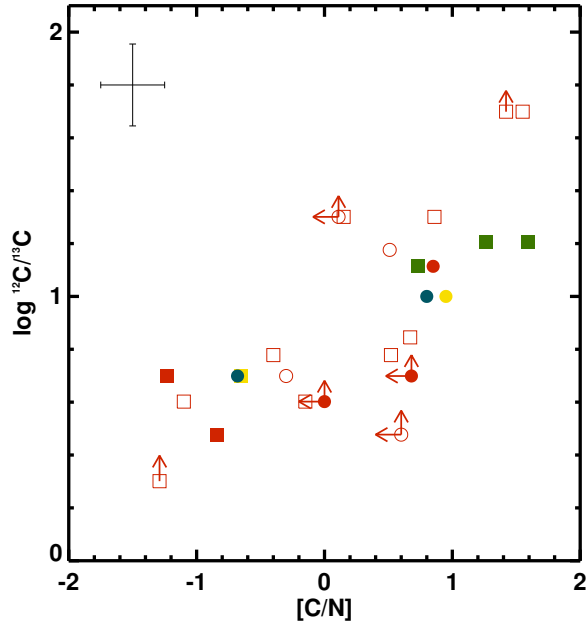
Figure 4.11: ^{12}C/^{13}C isotopic ratios, as a function of [C/N], for CEMP stars in the combined sample and from Norris et al. (2013b). The squares represent stars with log $g > 3.0$; dots represent stars with log $g < 3.0$. Filled symbols are from the combined sample; open symbols are from Norris et al. (2013b). The color-coding of the symbols is as in Figure 4.4. An approximate error bar for the sample stars is shown in the upper left of the panel.

4.4.2 ^{12}C/^{13}C isotopic ratios

When internal mixing occurs in stars, whether that mixing is due to convection driven by rapid rotation ("spinstars," see Meynet et al. 2006; Hirschi 2007; Maeder et al. 2015a) or convection in AGB stars during their evolution (Herwig 2005), the carbon is transported from the core (spinstars) or from the surface (AGB stars) to the H-burning shell where the CNO cycle is active, the carbon is transformed into ^{13}C and ^{14}N. These signatures should be detectable in the ^{12}C/^{13}C isotopic ratio of a star. High ^{12}C/^{13}C and [C/N] ratios indicate only partial hydrogen burning by the CNO cycle, while low ^{12}C/^{13}C and [C/N] ratios are a signature of more complete burning by the CNO cycle (Maeder et al. 2015a).

Chiappini et al. (2008) calculated the predicted ^{12}C/^{13}C isotopic ratio in the primordial ISM from which the first low-mass stars formed, if the first-generation stars were dominated by spinstars. They predict the ^{12}C/^{13}C isotopic ratio to be between 30-300, whereas if the first stars were not dominated by spinstars, the ratio would be ~ 4500 at [Fe/H] $= -3.5$ and as much as ~ 31000 at [Fe/H] $= -5.0$. Models of mixing and fallback SNe events (Umeda & Nomoto 2003; Nomoto et al. 2013), suggested to occur in the early universe, also predicts low ^{12}C/^{13}C isotopic ratios, due to the mixing in the pre-supernova evolution stage between the He convective shell and H-rich envelope Iwamoto et al. (2005). However, Maeder et al. (2015a) predict differences in the ratio due to the different physical conditions and timescales for the production of ^{13}C during the stellar evolution of spinstars or in the

SN explosion of the mixing and fallback models.

We have derived the ^{12}C/^{13}C isotopic ratios for 11 of our stars, and lower limits for an additional two stars. Norris et al. (2013b) also investigated ^{12}C/^{13}C isotopic ratios in their sample of CEMP-no stars (which, except for BD+44°493 and Segue 1-7, all belong to the Yong et al. (2013) sample), but they were able to derive isotopic ratios for only 5 of their 15 stars; for the remaining they provided lower limits. Figure 4.11 plots the ^{12}C/^{13}C isotopic ratios, as a function of [C/N] (uncorrected C abundances), for the CEMP stars in our sample and those of Norris et al. (2013b). In this plot, dots represent stars with $\log g < 3.0$ in which some internal CNO cycle processing might have changed the initial ^{12}C/^{13}C isotopic ratios, and squares represent stars with $\log g > 3.0$ stars, which should have preserved their initial ^{12}C/^{13}C isotopic ratios.

We find low (~ 5) ^{12}C/^{13}C isotopic ratios for all of our CEMP-no stars, consistent with the equilibrium value for CNO-cycle processed material. This shows that the material from which these stars formed has undergone mixing, whether in spinstars or in some pre-supernova evolution. The ^{12}C/^{13}C isotopic ratios found in the CEMP-s stars of our sample are generally higher (~ 13). This value is low enough to be a signature of H-burning via the CNO cycle, which is also expected if the carbon excess found in CEMP-s stars are transferred from an AGB companion, where multiple dredge up events mix the material in the star. However, according to Bisterzo et al. (2012), current AGB models do not include sufficient mixing to replicate the low ^{12}C/^{13}C isotopic ratios found in CEMP-s stars.

4.4.3   Lithium

Chapter 3 (Paper I) explored the lithium abundances detected in the UMP CEMP-no stars presented there, showing that all of these have Li abundances below the plateau found for non carbon-enhanced metal-poor dwarfs at A(Li) $= 2.05$, the so-called Spite plateau (Spite & Spite 1982). This result supplements a similar finding by Masseron et al. (2012), and is consistent with the possible depletion of Li by the progenitors of CEMP-no stars suggested by Piau et al. (2006). In this model, the first, presumably massive, stars that formed in the universe are believed to have destroyed all of their Li. The observed Li abundances of the EMP and UMP stars are expected to be the result of the mixing of the Li-free material ejected from the first stars with the unprocessed ISM having a Li abundance generated by Big Bang Nucleosynthesis. In this sense the lithium abundances of metal-poor main-sequence and subgiant stars can also be used to estimate the degree to which the material from the source star has been diluted.[3]

In this paper we present three additional CEMP-no stars, HE 0100−1622 with A(Li) < 1.12, HE 0440−1049 with A(Li) $= 2.00$, and HE 2331−7155 with A(Li) < 0.37. The latter star is a giant with $\log g = 1.5$, so this star has most likely internally depleted its initial lithium. The one star, HE 0440−1049, with a higher Li abundance, close to the Spite plateau value also has the lowest carbon-abundance ratio among these stars ([C/Fe] $= +0.69$).

We have also examined the Li abundances for the CEMP-s, CEMP-r and CEMP-r/s

---

[3]We note that, although it is presented without attribution, the scenario proposed by Bonifacio et al. (2015) to account for the "meltdown" of the Spite Li plateau at low metallicities and the possible resolution of the so-called cosmological Li problem (their Sec. 5.2) is essentially the same as that proposed by Piau et al. (2006), as acknowledged by P. Bonifacio (private comm. to TCB).
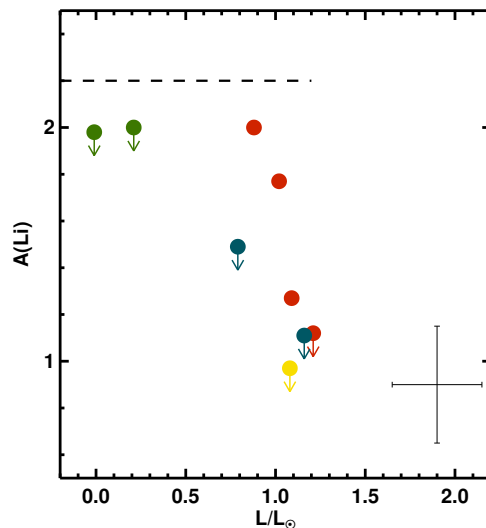
Figure 4.12: Absolute Li abundances, $A(Li)$ and upper limits, indicated by arrows, as a function of luminosity, for the dwarf and subgiant CEMP stars in our sample. The Spite plateau lithium abundance ($A(\text{Li}) = 2.2$) is indicated with a dashed line. The color-coding of the symbols is as in Figure 4.4. An approximate error bar for the sample stars is shown in the lower right of the panel.

stars in our new sample, but only upper limits could be derived for these. Figure 4.12 shows the Li abundances and upper limits detected for all the dwarf and subgiants in our sample, including those presented in Chapter 3 (Paper I), as function of luminosity (Yong et al. 2013 did not present Li abundances for their stars). The additional CEMP-no stars follow the result from Chapter 3 (Paper I) and Masseron et al. (2012) that all CEMP-no stars exhibit some level of Li depletion with respect to the Spite plateau.

4.4.4 Strontium and barium

The strontium and barium abundances for VMP stars have received a great deal of attention over the past few years, in part because these two species are often the only neutron-capture elements for which abundances can be measured in the most metal-poor stars, making these two elements our only clue to the nature of neutron-capture processes at the earliest times in our Galaxy (Aoki et al. 2013a; Hansen et al. 2013; Roederer et al. 2014a).

We have obtained detections or strong upper limits for Sr and Ba for all the stars in our sample, listed in Table 4.4, Table 4.5, Table 4.6 and Table 4.7. Figure 4.13 and Figure 4.14 shows the absolute Sr and Ba abundances as a function of [Fe/H]. Figure 4.13 shows only the CEMP stars, while Figure 4.14 shows all of the stars in our combined sample.

Inspection of Figure 4.13 and Figure 4.14 indicates a clear grouping of the different classes of stars considered in our study. Recall that [Ba/Fe] is used to differentiate the CEMP-no stars from the CEMP-s and CEMP-r/s stars. The NMP (non carbon-enhanced stars) exhibit a wide range of Ba abundances, from $A(\text{Ba}) \sim -4.0$ to $A(\text{Ba}) \sim 0.0$, while
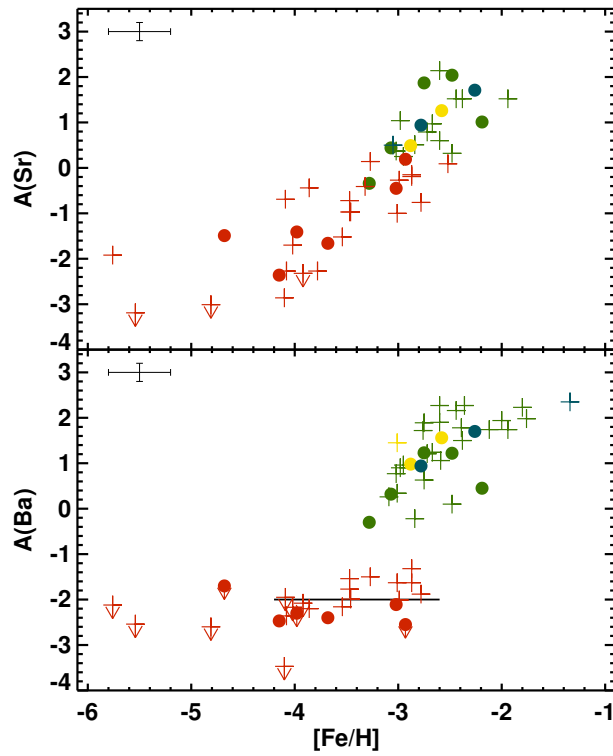
Figure 4.13: Absolute abundances of Sr and Ba, as a function of [Fe/H], for the CEMP stars. The suggested A(Ba) floor is indicated by the solid line. The symbols and color-coding are as in Figure 4.10. An approximate error bar for the sample stars is shown in the upper left of each panel.
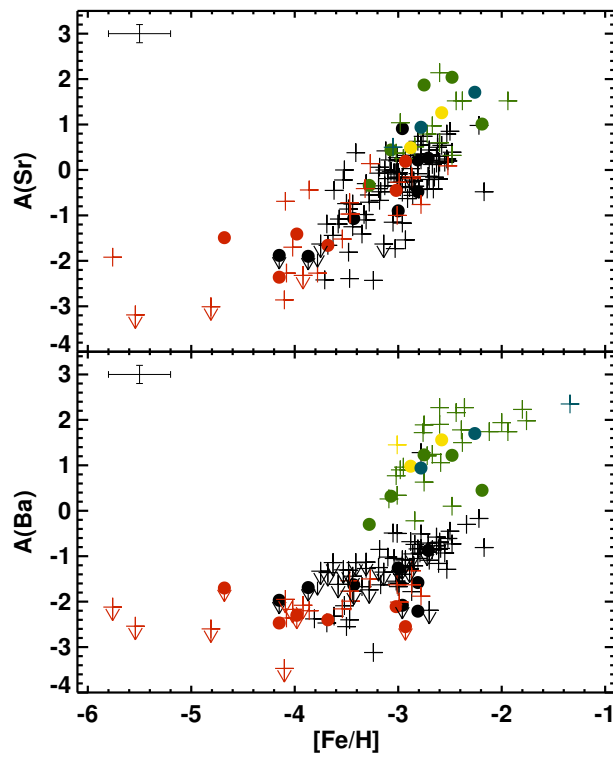
Figure 4.14: Absolute abundances of Sr and Ba, as function of [Fe/H], for all of the stars in our combined sample. The symbols and color-coding are as in Figure 4.10. An approximate error bar for the sample stars is shown in the upper left of each panel.

all the CEMP-no stars for which we have Ba detections exhibit Ba abundances of $A(\text{Ba}) \sim -2.0$, independent of metallicity (most clearly seen when plotting only the CEMP stars, Figure 4.13). In contrast, the behavior of the Sr abundances for stars in our sample is substantially different. The individual classes of the stars in our sample are mixed together in a band showing decreasing $A(\text{Sr})$ with decreasing [Fe/H], but with a possible change in the trend at the lowest metallicity (around [Fe/H] ~ -4.2). We emphasize that the area below [Fe/H] $= -4$ is only sparsely populated, with most stars only having an upper limit on Sr and Ba. The current data certainly suggest the presence of a floor in Ba at extremely low metallicity, but not for Sr; more detections of both species are strongly desired.

In the universe today, Ba is primarily produced by the main s-process in lower-mass AGB stars (Busso et al. 1999), but as this process was not operating in the early universe, the Ba found in the CEMP-no stars must have some alternative origin. It was shown by Frischknecht et al. (2010) that spinstars can produce some amount of slow neutron-capture elements such as Sr and Ba via the "weak" s-process, provided some Fe seeds are available. It is possible that these elements can also be produced by the mixing and fallback models, by ejection of a tiny fraction of the heavy elements created in the explosion (Takahashi et al. 2014). Recently, Roederer et al. (2014a) found four CEMP-no stars with clear r-process-element abundance patterns, confirming the early onset of the rapid neutron-capture process in the Galaxy. These authors also stress the need for Fe seeds for the weak s-process to operate efficiently in spinstars, meaning it will not occur in a completely metal-free star.

4.4.5 Abundance profiles

The peculiar abundance patterns of the CEMP-s stars, showing large enhancements in carbon, nitrogen, and slow neutron-capture elements, are believed to be the result of mass transfer from an AGB companion in a binary system with the presently-observed low-mass metal-poor star. Indeed, radial-velocity monitoring of CEMP-s stars are consistent with essentially all of these stars belonging to binary systems (Lucatello et al. 2005). Thus, the abundances observed in CEMP-s stars offer us a unique opportunity to constrain the properties of very metal-poor AGB stars.

In the above division of stars into those with either [C/N] > 0 or [C/N] < 0, we see that the great majority of the CEMP-s stars have [C/N] > 0. To further investigate the properties of the AGB stars that created the elemental over-abundances detected in CEMP-s stars, Figure 4.15 shows the observed elemental-abundance patterns of two CEMP-s stars – one having [C/N] > 0 and one with [C/N] < 0 – along with the predicted yields from metal-poor ($Z = 0.0001$) AGB models of three different masses ($1.3\text{M}_\odot$, $1.5\text{M}_\odot$, and $2.0\text{M}_\odot$), taken from the F.R.U.I.T.Y database (Cristallo et al. 2011, 2009).

None of the models reproduce the large amounts of carbon and nitrogen detected in these stars, and none of the models have [C/N] < 0. The heavy neutron-capture elements for the CEMP-s star with [C/N] > 0 (HE 0054$-$2542) are well-fit by the M=$1.5\text{M}_\odot$ model, but none of the models produce sufficient amounts of the light neutron-capture elements (Sr,Y, and Zr) to match this star. The star with [C/N] < 0 (HE 1029$-$0546) is also not well-fit by any of the models, but it does exhibit a general lower enhancement in s-process elements than the [C/N] > 0 star, pointing toward a lower mass AGB star as the progenitor of HE 1029$-$0546.
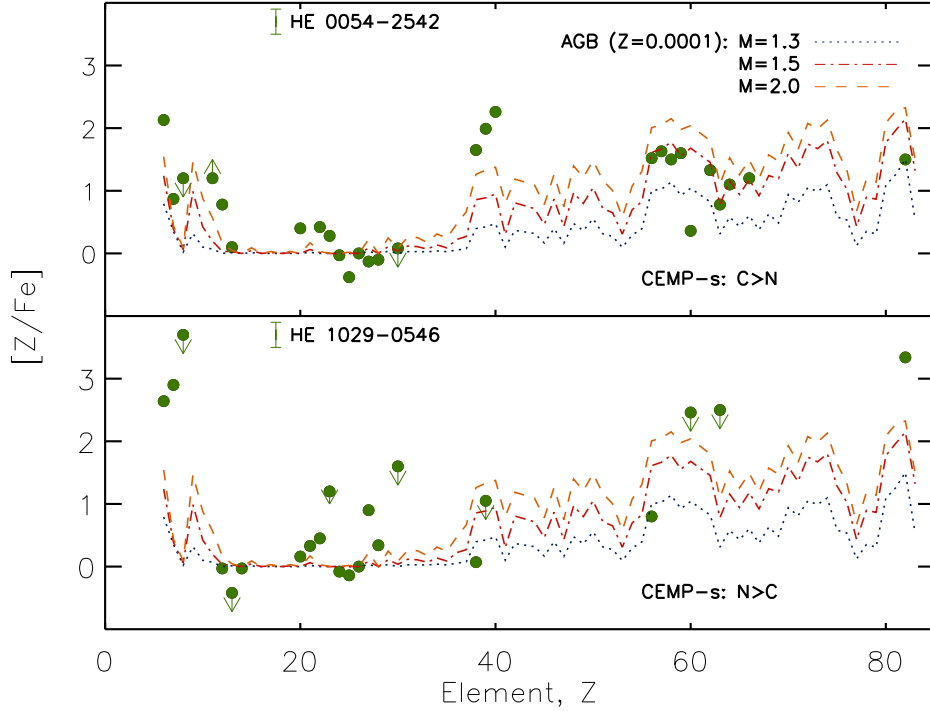
Figure 4.15: Observed elemental-abundance patterns for two CEMP-*s* stars, along with predicted yields for metal-poor AGB models of three different masses, 1.3M$_\odot$, 1.5M$_\odot$, and 2.0M$_\odot$. A representative error bar on the derived abundances is shown next to the star name in each panel.

Figure 4.16 shows the observed elemental-abundance patterns of the two CEMP-*r* and CEMP-*r/s* stars in our sample along with yields from the same metal-poor AGB stars. For the CEMP-*r* stars (left panels) none of the AGB models reproduce the observed C and N abundances, and while the most massive AGB model does reproduce some of the observed abundances for the n-capture elements in HE 0010−3422, none of the models are a good fit for the abundances observed in HE 0448−4806. Considering the CEMP-*r/s* stars (right panels), the two most massive AGB models fit the observed C abundance for HE 2208−1239 and also some of the n-capture element abundances observed in this star. For the other CEMP-*r/s* star, only the abundances for Sr, Y, and Zr can be reproduced by an AGB model.

It should also be noted that the material transferred from the AGB star and onto the presently-observed CEMP star is expected to be mixed with the original stellar material via thermohaline mixing (Stancliffe et al. 2007; Stancliffe & Glebbeek 2008). The amount of dilution for the transferred material is not presently well-constrained, hence we have not included it in the comparison between observed abundances and AGB yields.
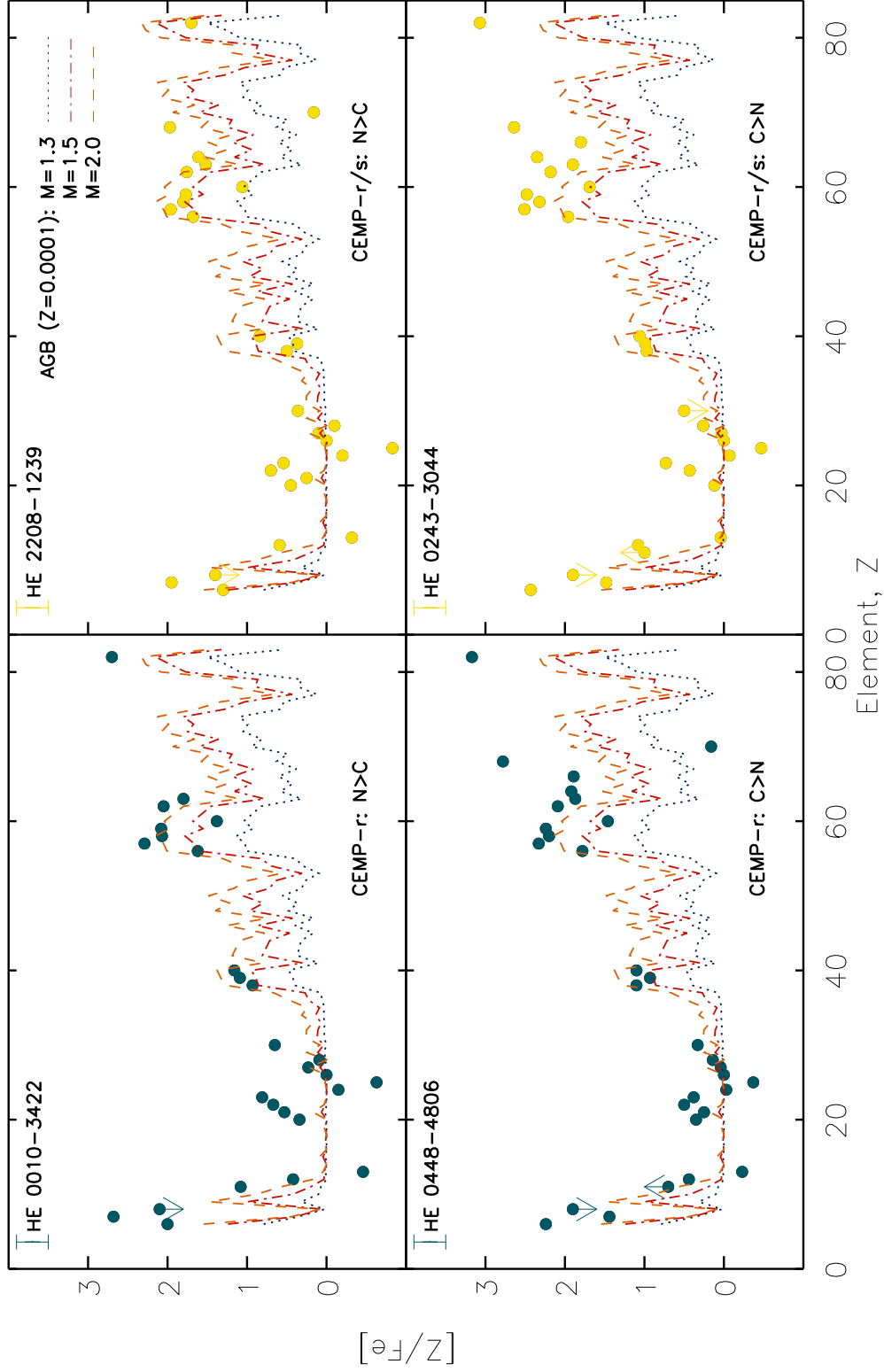
Figure 4.16: Observed elemental-abundance patterns for the two CEMP-r stars (left panels) and the two CEMP-r/s stars (right panels) in our sample, along with predicted yields for metal-poor AGB stars of three different masses, 1.3M$_\odot$, 1.5M$_\odot$, and 2.0M$_\odot$. A representative error bar on the derived abundances is shown next to the star name in each panel.

Radial velocity monitoring of r-process enhanced stars

This chapter is taken from the paper "The role of binaries in the enrichment of the early Galactic halo, I. The r-process-enhanced metal-poor stars", describing the radial-velocity monitoring of a sample of 17 r-process enhanced stars. The paper is accepted for publication in Astronomy & Astrophysics, with the following author list: T. Hansen, J. Andersen, B. Nordström, T. C. Beers, J. Yoon, and L. A. Buchhave. J. Andersen has calculated Roche-lobe radii for the stars. The remaining analyses presented here is work of the author of this thesis; all co-authors have commented on the manuscript.

5.1 Sample stars

The sample stars are listed in Table 5.1, including their V magnitudes and $B-V$ colours, and reported [Fe/H] and [Eu/Fe] abundances. The last column of this table indicates whether a given star is considered to be a member of the moderately r-process-enhanced class (r-I; $+0.3 \leq$ [r/Fe] $\leq +1.0$) or the highly r-process-enhanced class (r-II; [r/Fe] $> +1.0$), according to the definitions of Beers & Christlieb (2005).

All but two of our sample stars were selected from the HK survey of Beers and colleagues (Beers et al. 1985, 1992) and the Hamburg/ESO survey of Christlieb and collaborators (Christlieb et al. 2008). The sample includes a number of the canonical examples of the r-process-element enhancement phenomenon; CS 22892−052, the first EMP star with detected Th (McWilliam et al. 1995; Sneden et al. 2000), CS 31082−001, the first EMP star with detected U (Hill et al. 2002; Cayrel et al. 2004), and HE 1523−0901, the most extremely r-process enhanced giant known (Frebel et al. 2007a). All except HE 1523−0901 were analyzed in the Hamburg/ESO R-process Enhanced Star (HERES) survey (Christlieb et al. 2004b; Barklem et al. 2005). Accordingly, most of our programme stars are in the Southern Hemisphere (but north of declination $\delta \sim -25°$) and have $V \lesssim 16$, which is the practical limit for 1-hour integrations with the NOT.

Table 5.1: r-I and r-II stars monitored for radial-velocity variation

Stellar ID	RA (J2000)	Dec (J2000)	V	B − V	[Fe/H]	[Eu/Fe]	Class
HD 20	00:05:15	−27:16:18	9.24	0.54	−1.58	+0.80	r-I
CS 29497−004	00:28:07	−26:03:03	14.03	0.70	−2.81	+1.62	r-II
CS 31082−001	01:29:31	−16:00:48	11.67	0.77	−2.78	+1.66	r-II
HE 0432−0923	04:34:26	−09:16:50	15.17	0.73	−3.19	+1.25	r-II
HE 0442−1234	04:44:52	−12:28:46	12.91	1.08	−2.41	+0.52	r-I
HE 0524−2055	05:27:04	−20:52:42	14.01	0.88	−2.58	+0.49	r-I
HE 1044−2509	10:47:16	−25:25:17	14.35	0.67	−2.89	+0.94	r-I
HE 1105+0027	11:07:49	+00:11:38	15.65	0.39	−2.42	+1.81	r-II
HE 1127−1143	11:29:51	−12:00:13	15.89	0.68	−2.73	+1.08	r-II
HE 1219−0312	12:21:34	−03:28:40	15.94	0.64	−2.81	+1.41	r-II
HE 1430+0053	14:33:17	+00:40:49	13.69	0.59	−3.03	+0.72	r-I
HE 1523−0901	15:26:01	−09:11:38	11.13	1.06	−2.95	+1.82	r-II
CS 22892−052	22:17:01	−16:39:26	13.21	0.80	−2.95	+1.54	r-II
HE 2224+0143	22:27:23	+01:58:33	13.68	0.71	−2.58	+1.05	r-I
HE 2244−1503	22:47:26	−14:47:30	15.35	0.66	−2.88	+0.95	r-I
HD 221170	23:29:29	+30:25:57	7.71	1.02	−2.14	+0.85	r-I
CS 30315−029	23:34:27	−26:42:19	13.66	0.92	−3.33	+0.72	r-I

V and $B - V$ are from Beers et al. (2007a), except for HD 221170, which is taken from
Christlieb et al. (2004b), and HE 1127−1143, which is from Henden et al. (2015).
[Fe/H] and [Eu/Fe] are from Barklem et al. (2005), except for HE 1523−0901,
where values from Frebel et al. (2007a) are listed.

5.2 Observations

Spectra for our radial-velocity monitoring programme were obtained with the NOT, in service mode, using the FIES spectrograph[1], which has been used successfully for exo-planet research (Buchhave et al. 2012). The spectra cover the wavelength range 3640 Å − 7360 Å in 78 orders, at a resolving power of R ∼46,000. The SNR of the spectra is ∼10 on average, but ranges from ∼2 to ∼20. A SNR of ∼10 is obtained in ∼20 min for a star of $V = 14.5$, so a typical clear night yielded ∼10-15 spectra of the stars in Table 5.1. Integrations of 900 s or longer were split into three exposures, in order to enable effective cosmic ray rejection.

The observing strategy was based on the assumed analogy with the Ba II and CH binaries found by McClure (1984) and McClure et al. (1980) to have periods of order ∼ 300-3000 days and amplitudes of ∼ 3-10 km s^{-1}. Accordingly, spectra have been obtained at roughly monthly intervals since June 2007, and reduced immediately, so that follow-up of any variable objects could be planned efficiently. As we demonstrate, this strategy has worked well.

5.3 Reduction and analysis

The observations were reduced with pipeline software originally developed by Lars Buchhave to deliver high-precision radial velocities of exo-planet host stars from echelle spectrographs, in particular the FIES instrument (Buchhave 2010).

This reduction procedure includes all the normal steps, such as bias subtraction, division by a flat-field exposure, cosmic ray removal, 2-D order extraction, etc. Sky background is only significant for the faintest stars if observed close to the full Moon, which was avoided in the nightly planning. Moreover, even substantial amounts of scattered moonlight are harmless if the two cross-correlation peaks are well separated, which is virtually always the case for our high-velocity programme stars.

For the wavelength calibration, a separate wavelength solution is created for each target spectrum, using Th-Ar calibration spectra taken just before each science frame. This procedure has been found to yield adequate velocity stability, as we demonstrate below.

5.3.1 Multi-order cross-correlation

With the reduced spectra in hand, multi-order cross-correlation against an optimized template spectrum is then performed, using software also developed by L. Buchhave (Buchhave 2010). The radial velocity from each individual order is determined by a Gaussian fit to the peak of the cross-correlation function (CCF); their mean value, weighted by the total photon count in each order, is taken as the final radial velocity from the observation.

Performing the cross-correlation order-by-order enables us to hand-pick the spectral regions to be used in the correlation, including regions with strong absorption lines and excluding regions with only few and/or weak lines, which is a significant advantage when dealing with spectra of stars of such peculiar chemical compositions. Filtering is also applied to the spectrum before the cross-correlation to remove unwanted frequencies. The filters are

---

[1]http://www.not.iac.es/instruments/fies/

Table 5.2: Results for the observed radial-velocity standard stars

Stellar ID	RA (J2000)	Dec (J2000)	B	V	RV mean (km s^{-1})	σ (km s^{-1})	Nobs	ΔT (days)
HD 3765	00:40:49	+40:11:14	8.30	7.36	−63.35	0.033	60	2672
HD 38230	05:46:02	+37:17:05	8.19	7.36	−29.14	0.035	46	2771
HD 79210	09:14:23	+52:41:12	9.07	7.63	+10.45	0.048	29	2746
HD 115404	13:16:51	+17:01:02	7.46	6.52	+7.67	0.036	34	2891
HD 151541	16:42:39	+68:11:18	8.32	7.56	+9.44	0.028	30	2857
HD 182488	19:23:34	+33:13:19	7.15	6.36	−21.65	0.035	61	2072
HD 197076	20:40:45	+19:56:08	7.06	6.44	−35.37	0.052	26	2857

carefully optimized for each star to remove noise while retaining even the narrowest stellar absorption lines.

5.3.2 Optimization of the template spectra

The choice of the template spectrum for the cross-correlation is crucial for the accuracy of the resulting radial velocities, especially in these spectra where the usual iron-peak elements only show weak lines, but strong lines exist from the normally rare neutron-capture elements.

Four different recipes have been used to construct the template spectra, depending on the quality of the target spectra: Strongest, Co-add, CS 31082−001 and Delta. The "Strongest" template is the spectrum of a given star with the maximum signal level for that star. The advantage of using a spectrum of the same star as a template is the perfect match to the observed spectrum; the disadvantage is that a template with relatively low SNR will introduce noise into the correlation. The "Co-add" template is constructed by shifting a selection of the best spectra of the star to a common radial velocity and co-adding them. This results in a template with high SNR (which is also a perfect match for the target spectra), and will generally allow more orders to be included in the correlation, compared to a correlation with the strongest single spectrum as template. However, when creating the "Co-add" template, an initial correlation with the strongest spectrum as template is used to determine the shift of the other spectra. Any small residual shift will then broaden the spectral lines in the "Co-add" template spectrum and yield less precise results in the final correlation.

For the fainter stars, the "Strongest" template may introduce too much noise into the correlation, and a good "Co-add" template cannot then be constructed. Instead, a "Co-add" template from a bright star with a very similar spectrum may then be used as template; for these stars we have used CS 31082−001 in this manner. The final template option, used here for the faintest stars, is the "Delta" template, a synthetic spectrum consisting of δ functions at the (solar) wavelengths of selected lines. Sample spectra of the faint stars have been inspected for strong lines to be included in the "Delta" template spectrum. Correlation with this template yields velocities on an absolute scale, and has thus also been used to determine the absolute velocity of the other templates and to convert all velocities to an absolute scale.

5.3.3 Standard stars

A few well-established radial-velocity standard stars from Table 2 of Udry et al. (1999) were observed on every usable observing night in order to monitor any zero-point variations in the velocities. These are listed in Table 5.2, along with our mean (heliocentric) velocities and dispersions for these stars. The mean difference of our velocities from the standard values is 73 m s^{-1}, with a standard deviation of 69 m s^{-1}. This demonstrates that our results for the target stars are on a system consistent with that of Udry et al. (1999), and that the accuracy of our results is not limited by the stability of the spectrograph.

5.3.4 Error estimates

The internal error of the mean velocity from each spectrum is calculated as the standard deviation of the velocities from the individual orders used in the correlation. It is listed along with each observed velocity in Appendix A, and is used to plot the error bars of the data in the orbital plots shown in Fig. 5.2. For each star, the average internal error for the velocities is computed as the mean of these internal standard deviations, and is used to assess the quality of the correlation and the order selection.

The *external* standard deviation, σ, of the radial-velocity observations for each star, given in Table 5.2 for the radial-velocity standards and in Table 5.3 for the programme stars, is computed as:

$$\sigma = \sqrt{\frac{1}{N-1}\sum_{j-0}^{N-1}(v_j - \bar{v})^2}. \tag{5.1}$$

Imperfect guiding and centering of the star on the fibre end along with imperfect cancellation of changes in ambient temperature and atmospheric pressure, etc., contributes to small variations in the derived radial velocities, which are reflected in the standard deviations of the constant programme and radial-velocity standard stars.

For the three detected binaries in our sample, the above value for σ is inflated due to the orbital motion, and the relevant uncertainty estimate is the σ from the orbital solutions given in Table 5.4.

5.4 Results

The results of our radial-velocity monitoring of the sample stars are summarized in Table 5.3, which lists the star name, the number of observations (Nobs), the template used for each star, the mean (heliocentric) radial velocity and standard deviation over the observed time span (ΔT), and the binary status for each star. The individual observed heliocentric radial velocities are listed in Appendix A, together with the Julian dates of the observations and their internal errors.

As can be seen from a glance at Table 5.3, fourteen of our stars exhibit no variation in their radial velocities at the level of a few hundred meters per second over the eight years of monitoring. For the brighter targets, the standard deviations of the observed velocities

Table 5.3: Mean Heliocentric Radial-Velocities, Standard Deviations, and Time-Span Covered for the Programme Stars

Stellar ID	Nobs	Template	RV mean (km s^{-1})	σ (km s^{-1})	ΔT (days)	Binary
HD 20	14	Strongest	-57.914	0.041	2603	No
CS 29497$-$004	12	Co-add	$+105.008$	0.366	2583	No
CS 31082$-$001	24	Co-add	$+139.068$	0.105	2642	No
HE 0432$-$0923	18	Delta	-64.800	0.988	2737	No
HE 0442$-$1234	28	Co-add	$+237.805$	8.294	2618	Yes
HE 0524$-$2055	13	CS 31082$-$001	$+255.425$	0.195	2338	No
HE 1044$-$2509	14	Delta	$+365.789$	17.110	1887	Yes
HE 1105$+$0027	9	Delta	$+76.197$	0.496	1573	No
HE 1127$-$1143	7	Delta	$+229.157$	0.454	1998	No
HE 1219$-$0312	5	Delta	$+162.416$	1.094	2171	No
HE 1430$+$0053	20	Co-add	-107.749	0.426	2493	No
HE 1523$-$0901	34	Co-add	-163.271	0.284	2594	Yes
CS 22892$-$052	19	Co-add	$+13.549$	0.164	2174	No
HE 2224$+$0143	24	Co-add	-113.085	0.190	2420	No
HE 2244$-$1503	14	Delta	$+147.928$	0.246	2207	No
HD 221170	30	Strongest	-121.201	0.105	2174	No
CS 30315$-$029	14	Co-add	-169.346	0.352	2672	No

are $\sim$100 m s^{-1} (dominated by centering and guiding errors), rising to $\sim$ 1 km s^{-1} for the fainter targets, due to the lower SNR of their spectra. Moreover, least-squares fits of the velocities vs. time reveal no net trends over the observing period.

5.4.1   Comparison with literature data

Table B.1 in appendix B lists mean radial velocities (based on high-resolution spectroscopy) from the literature for the single stars in our sample, along with the complete time span covered by the combined data (including our own measurements). Most of the stars have only been observed (once) earlier by Barklem et al. (2005), for which they estimate an error of a few km s^{-1}, and we find excellent agreement between their results and ours. For HD 20 and HD 221170, radial velocities were also reported by Carney et al. (2003), who list 13 observations for HD 20 and 18 for HD 221170, spanning 4641 and 5145 days, with (external) standard deviations of 0.41 and 0.61 km s^{-1}, respectively. Their mean radial velocities of -57.18 km s^{-1} and -121.77 km s^{-1} are consistent with our results, given the slight offset of the CfA velocities from the system of Udry et al. (1999).

For the faint star HE 1219$-$0312, our five measurements with the 2.5-m NOT span 2171 days from 2007, while the five epochs of the earlier Hayek et al. (2009) VLT/UVES observations span $\sim$ 400 days. The standard deviations ($\sim$1 km s^{-1}) and their mean radial velocity (163.1 km s^{-1}) are similar to ours, and consistent with our own conclusion that this star is single.

From inspection of Table B.1 it is clear that, while the coverage of the listed spans

for most of the single stars is rather sparse, the spans themselves are from two to five times longer than those obtained during the course of our own radial-velocity monitoring programme. The lack of observed variations beyond what can be accounted for by the expected errors across multiple spectrograph/telescope combinations strengthens our claim that the stars we classify as single are indeed so.

5.4.2 Binary orbits

Three of our stars are spectroscopic binaries, as first reported by Hansen et al. (2011). HE 0442−1234 was found already by P. Bonifacio et al. (private comm.) to be a long-period binary, while HE 1044−2509 and HE 1523−0901 are new discoveries from our programme. All three orbits have now been fully completed, with particular attention being paid to assessing the reality of the very low-amplitude velocity variations of HE 1523−0901. After rejecting early observations made under poor conditions (strong moonlight, poor seeing), and with now almost nine orbital revolutions completed, we have satisfied ourselves that this nearly face-on orbit is real and the orbital parameters are reliable (see below).

In contrast to this result, our own (far more accurate) velocity data clearly disprove the putative orbit suggested by Preston & Sneden (2001) for CS 22892-052, with $P \sim 128$ days and $K \sim 1.0$ km s^{-1}. Both this star and CS 31082−001 are clearly single stars, as can be seen from Table 5.3 and Figure 5.1, where the derived radial velocities for the two stars are plotted as a function of time. Our results for stars observed with similar time spans and accuracies in parallel parts of our overall programme show that binaries with orbital periods of 20-30 years are detected with certainty even after the first couple of years with ∼monthly observations.

The observed $K \sim 350$ m s^{-1} of HE 1523−0901 is the smallest measured with certainty in our programme, highlighting the null result for the other, single stars. The corresponding tiny mass function implies either a companion of mass in the brown-dwarf range (for $i \sim 90°$), or a very low orbital inclination, or a combination of both. Assuming $i \lesssim 2.5°$ leads to a secondary mass in the late M-dwarf range, 0.25 M$_\odot$ – still plausible within the statistics for a single case in a sample of several tens of potential (southern) r-I and r-II targets.

Long-period envelope pulsations are a potential alternative origin of radial-velocity variations for this and other cool giant stars, and we have also found some strongly carbon-enhanced VMP and EMP stars showing similar low-level radial-velocity fluctuations. The frequency of real spectroscopic binaries with very low inclinations is far too low to ascribe all such low-amplitude velocity variations to binary orbital motion, and most marginal variations are, in the end, found not to be strictly periodic. Thus, it may be that low-level pulsations, rather than velocity accuracy, may set the ultimate limit to the length of the binary periods that can be reliably detected by the radial-velocity technique, as is the case for exo-planet orbits.

Our current knowledge of the pulsational characteristics of late-type evolved stars is derived from the systematic microlensing surveys for MACHOs towards the Magellanic Clouds (Wood 2000; Riebel et al. 2010). The late-type pulsators with periods of 200-1000 days are typically C-type AGB stars or Mira variables, but stars below the tip of the red-giant branch have shorter periods, and the cause of their light variation is not known. Precise light and colour curves for field VMP/EMP stars with equally well-determined distances,
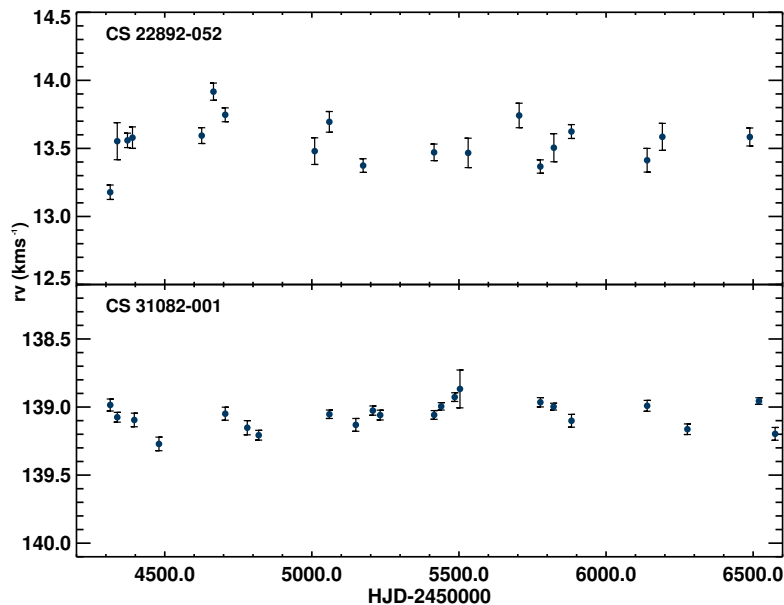
Figure 5.1: Heliocentric radial velocities derived for CS 22892−052 (top) and CS 31082−001 (bottom), as a function of time.

or at least log q, periods or pseudo-periods of order a year, and phasing consistent with pulsations would be needed to settle the issue definitively. However, obtaining them with sufficient accuracy is not an easy task, and none has been reported for HE 1523−0901.

The final orbital elements for the three binary systems among our programme stars are listed in Table 5.4, and velocity curves with all available observations are shown in Figure 5.2.

5.4.3   Frequency and properties of *r*-I and *r*-II binaries

The distribution of periods and eccentricities of our three binaries is also fully as expected for binary systems with normal giant primary stars. This is illustrated most simply in Figure 5.3, which shows a period – eccentricity diagram constructed from the orbital data for 141 giant binary members of (Population I) Galactic open clusters by Mermilliod et al. (2007) and Mathieu et al. (1990), plotted as dots, while our three binaries are shown as red plus symbols. As seen, their orbital eccentricities are completely normal for giant binaries, which are typically tidally circularized for periods up to ∼ 150 days, depending on age and stellar mass, and show no sign of tidal or other processes that could be connected to their outstanding chemical peculiarity. In contrast, the transition between circular and eccentric orbits seems to occur at periods of ∼ 4−800 days for binaries with former AGB companions.

Further information on the presently unseen companions can be derived by considering the volume available to them during their evolution; i.e. their Roche-lobe radii, which can be computed from the observed orbital separation (assuming no exchange or loss of mass
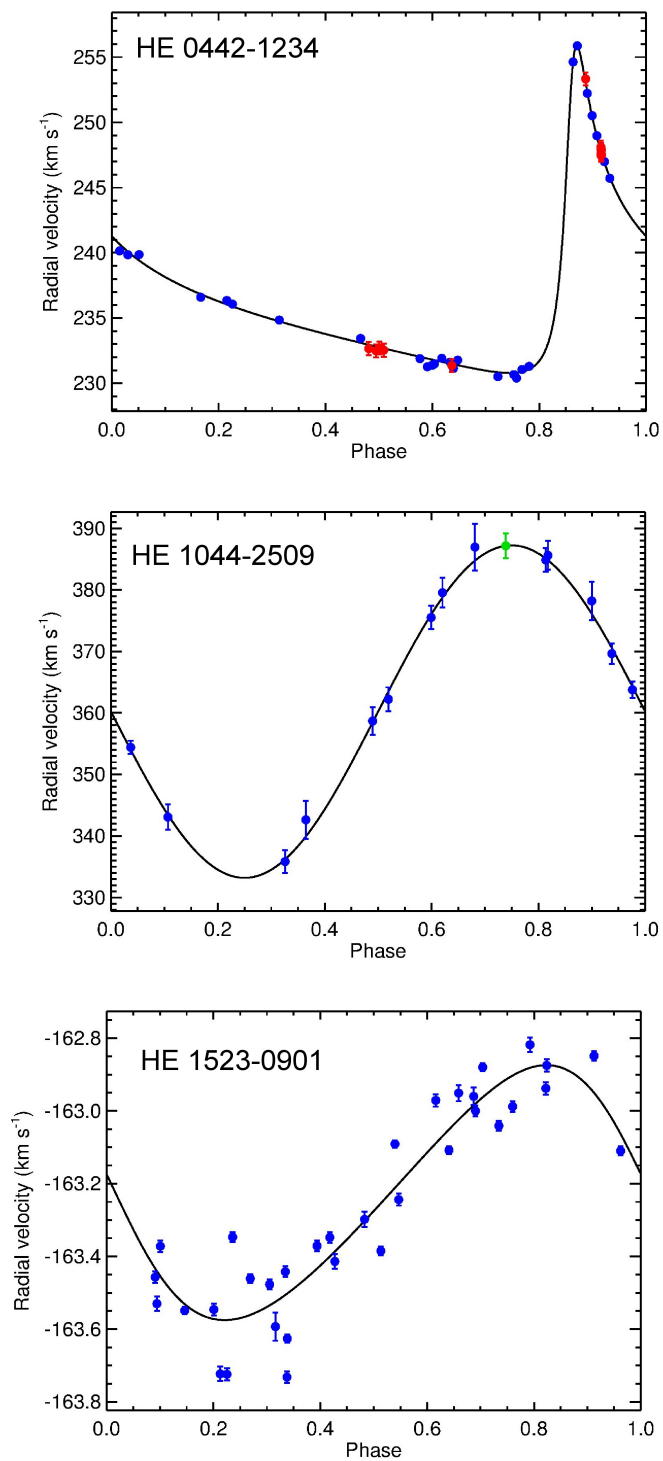
Figure 5.2: Orbital solutions for the three binary systems found in our programme. Top: HE 0442−1234 (blue this work, red P. Bonifacio private comm.), middle: HE 1044−2509 (blue this work, green Barklem et al. (2005)) and bottom: HE 1523−0901.

Table 5.4: Orbital parameters of the binary systems in the sample

Parameter	HE 0442−1234	HE 1044−2509	HE 1523−0901
Period (days)	2515.2±5.5	36.561±0.009	303.05±0.25
T_0 (BJD)	2457918.3±1.0	2455737.1±0.1	2455068.0±4.1
K (km s^{-1})	12.541±0.016	27.024±0.96	0.350±0.003
γ (km s^{-1})	236.35±0.01	360.22±0.57	-163.23±0.003
e	0.767±0.001	0.000^a	0.163±0.010
ω °	316.6±0.1	90.00	81.7±4.7
$a\sin i$ (R$_\odot$)	400.2±1.2	19.6±0.7	2.07±0.02
f(m) (M$_\odot$)	0.136±0.001	0.075±0.009	1.3E-5±4E-8
σ (km s^{-1})	0.28	1.88	0.11
R_{Roche} (R$_\odot$, M$_1$ = 0.8 M$_\odot$, M$_2$ = 0.6 M$_\odot$)	59	13	53
R_{Roche} (R$_\odot$, M$_1$ = 0.8 M$_\odot$, M$_2$ = 1.4 M$_\odot$)	770	46	220

a) Eccentricity for HE1044-2509 fixed to zero.
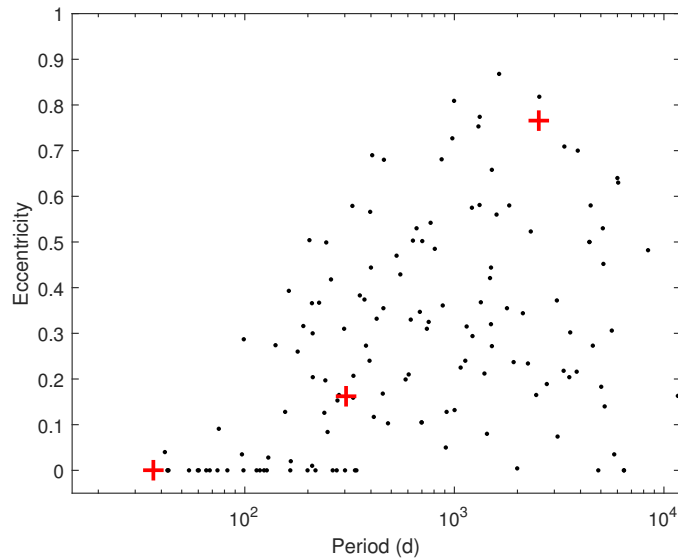
Figure 5.3: Period – eccentricity diagram for giant binaries. Dots: 141 members of Galactic open clusters (Mermilliod et al. 2007; Mathieu et al. 1990); red plus signs: The three r-I and r-II binaries discussed in this paper.

and angular momentum) and a range of assumed stellar masses. We first adopt a common mass of 0.8 $M_\odot$ for the observed EMP giants and assume that the companion is a (sub)dwarf (i.e., unevolved) star of mass 0.6 $M_\odot$, at least three magnitudes fainter than the star we do see. The present radius of the latter can be estimated from the adopted mass and a typical log $g \sim 1.5$ dex, i.e. R $\sim$ 30 $R_\odot$.

With the observed orbital elements, notably $a_1 \sin i$ and the mass function, we then adjust i until the computed M_2 reaches 0.6 $M_\odot$, and calculate the corresponding Roche-lobe radii, which are given in Table 5.4. For HE 0442−1234, the minimum secondary mass is 0.67 $M_\odot$ already for $i = 90°$; for HE 1044−2509 and HE 1523−0901, we find $i = 62°$ and 1.3°, respectively, for a secondary mass of 0.6 $M_\odot$.

However, we might alternatively assume that the companions were initially *more* massive than 0.8 $M_\odot$, i.e., in the range of 1-8 $M_\odot$, where they would have gone through the AGB phase and likely have evolved into now-invisible white dwarfs (WDs) with typical masses of 0.6 $M_\odot$, and thus identical R_{Roche} to the ones found above. It is possible that the WD might also have the maximum WD mass of 1.4 $M_\odot$, in which case the entire system would be much larger and the Roche-lobe radius of the companion a larger share of that again. Nominal Roche-lobe radii for this case are also given in Table 5.4, and illustrate the dramatic change in the space available to the star during its evolution, depending on its assumed mass.

For HE 1044−2509, even this R_{Roche} is still too small to accommodate a typical AGB star of $\sim$200 $R_\odot$. In any case, the observed absence of any s-process signatures indicates that mass transfer from a putative AGB companion did not happen in any of these systems, while a supernova explosion of a putative, even more massive companion would likely have disrupted the binary system (Tauris & Takens 1998).

In summary, binary systems seem to occur as a normal part of the formation of r-process-enhanced metal-poor stars, and are unrelated to the process by which they acquired their outstanding chemical anomalies.

CHAPTER 6

Radial-velocity monitoring of CEMP-no stars

This chapter is taken from the paper "The role of binaries in the enrichment of the early Galactic halo, II. Carbon enhanced extremely metal-poor stars - the CEMP-no stars", describing the radial-velocity monitoring of a sample of 24 CEMP-no stars. The paper is submitted to Astronomy & Astrophysics, with the following author list: T. Hansen, J. Andersen, B. Nordström, T. C. Beers, V. M. Placco, J. Yoon, and L. A. Buchhave. V. M. Placco has perfomed the abundance syntthehsis and J. Andersen has calculated Roche-lobe radii for the stars. The remaining analyses presented here is work of the author of this thesis; all co-authors have commented on the manuscript.

6.1 Sample selection, observation, and analysis

6.1.1 Sample selection

Our initial observing list, established in 2006, comprised a total of 23 CEMP stars with pedigrees of widely different quality, plus 17 r-process enhanced stars, drawn from the from the HK surveys of Beers, Preston, & Shectman (Beers et al. 1985, 1992) and the Hamburg/ESO survey of Christlieb and collaborators (Christlieb et al. 2008). The initial sample of CEMP stars also included one of the most metal-poor stars known to date, HE 1327−2326 (Aoki et al. 2006; Frebel et al. 2006).

By 2010, the overall conclusion of the r-process programme had already become clear (Hansen et al. 2011), while the significance of the different spatial distributions of the CEMP-s and CEMP-no subclasses, and the potentially different binary frequencies and origins of their C excess, had assumed greater importance. At the same time, our observing technique had been refined and amply tested. From 2011, the r-process programme was therefore limited to sparsely sampled long-term monitoring, while 25 likely new CEMP-no stars were selected from the same sources and added to the regular programme. We also

Table 6.1: The sample of CEMP-no stars monitored for radial-velocity variation

Stellar ID	RA (J2000)	Dec (J2000)	V	$B-V$	Ref	[Fe/H]	[C/Fe]	[Ba/Fe]	Ref
HE 0020−1741	00:22:44	−17:24:28	12.89	0.94	a	−4.11	+1.36	< −0.67	1
CS 29527−015	00:29:11	−19:10:07	14.26	0.40	d	−3.55	+1.18	< +0.10	10
CS 22166−016	00:58:24	−14:47:07	12.75	0.65	b	−2.40	+1.02	−0.37	4
HE 0219−1739	02:21:41	−17:25:37	14.73	1.52	b	−3.09	+1.90	< −1.39	1
BD+44°493	02:26:50	+44:57:47	9.22	0.67	a	−3.83	+1.35	−0.60	2
HE 0405−0526	04:07:47	−05:18:11	10.72	0.71	a	−2.18	+0.92	−0.22	1
HE 1012−1540	10:14:53	−15:55:53	14.04	0.66	a	−3.51	+2.22	+0.19	6
HE 1133−0555	11:36:12	+06:11:43	15.43	0.64	b	−2.40	+2.20	−0.58	1
HE 1150−0428	11:53:07	−04:45:03	15.01	0.76	a	−3.21	+2.28	−0.44	6
HE 1201−1512	12:03:37	−15:29:33	13.79	0.55	a	−3.92	+1.60	< −0.34	3
HE 1300+0157	13:02:56	+01:41:52	14.06	0.48	b	−3.49	+1.31	−0.74	6
BS 16929−005	13:03:30	+33:51:09	13.61	0.62	b	−3.27	+0.99	−0.41	3
HE 1300−0641	13:03:34	−06:57:21	14.80	0.62	b	−3.14	+1.29	−0.77	8
HE 1302−0954	13:04:58	−10:10:11	13.96	0.79	a	−2.25	+1.17	< −0.53	1
CS 22877−001	13:13:55	−12:11:42	12.16	0.77	b	−2.71	+1.00	−0.49	5
HE 1327−2326	13:30:06	−23:41:54	13.53	0.44	b	−5.76	+4.26	< +1.46	3
HE 1410+0213	14:13:06	+01:59:21	13.05	1.14	b	−2.14	+1.71	−0.26	6
HE 1506−0113	15:09:14	−01:24:57	14.44	0.64	a	−3.54	+1.65	−0.80	3
CS 22878−027	16:37:36	+10:22:08	14.41	0.44	c	−2.52	+0.86	< −0.75	3
CS 29498−043	21:03:52	−29:42:50	13.63	1.12	b	−3.75	+1.90	−0.45	7
CS 29502−092	22:22:36	−01:38:24	11.87	0.77	b	−2.99	+0.96	−1.20	3
HE 2318−1621	23:21:22	−16:05:06	12.73	0.68	a	−3.67	+1.04	−1.61	9
CS 22949−037	23:26:30	−02:39:58	14.36	0.79	b	−3.93	+1.01	−0.77	6
CS 22957−027	23:59:13	−03:53:49	13.62	0.80	b	−3.06	+2.13	−0.96	6

Photometry:(a) Henden et al. (2015); (b) Beers et al. (2007a); (c) Preston et al. (1991); (d) Norris et al. (1999)
Abundances: (1) This work; (2) Ito et al. (2013); (3) Yong et al. (2013); (4) Giridhar et al. (2001);
(5) Aoki et al. (2002a); (6) Cohen et al. (2013); (7) Aoki et al. (2002c); (8) Barklem et al. (2005);
(9) Placco et al. (2014a); (10) Bonifacio et al. (2009) and M. Spite (priv. communication).

Table 6.2: Templates, mean heliocentric radial velocities and standard deviations, and observed time spans for the sample stars.

Stellar ID	Nobs	Template	RV mean (km s^{-1})	σ (km s^{-1})	ΔT (Days)	Binary
HE 0020$-$1741	8	Co-add	+92.976	0.213	1033	No
CS 29527$-$015	5	BD+44°493	+47.077	0.478	702	No
CS 22166$-$016	8	Co-add	$-$210.504	0.803	1033	No
HE 0219$-$1739	15	Co-add	+106.689	5.090	2207	Yes
BD+44°493	18	Co-add	$-$150.084	0.051	1298	No
HE 0405$-$0526	13	Co-add	+165.657	0.039	904	No
HE 1012$-$1540	8	Delta	+226.362	0.740	802	No
HE 1133$-$0055	9	Co-add	+270.302	0.316	2217	No
HE 1150$-$0428	13	Strongest	+48.042	8.350	2220	Yes
HE 1201$-$1512	5	Delta	+239.450	1.854	420	No
HE 1300+0157	5	BD+44°493	+74.536	0.692	411	No
BS 16929$-$005	7	Delta	$-$50.735	0.600	884	No
HE 1300$-$0641	2	Delta	+68.822	0.090	386	No
HE 1302$-$0954	3	BD+44°493	+32.538	0.039	386	No
CS 22877$-$001	15	Co-add	+166.297	0.111	2923	No
HE 1327$-$2326	9	Delta	+64.344	1.170	2577	No
HE 1410+0213	23	Co-add	+81.140	0.180	3005	No
HE 1506$-$0113	10	Delta	$-$81.467	2.772	492	Yes
CS 22878$-$027	7	Delta	$-$91.294	1.102	1034	No
CS 29498$-$043	15	Delta	$-$32.488	0.701	2603	No
CS 29502$-$092	20	Co-add	$-$67.215	0.093	2603	No
HE 2318$-$1621	7	BD+44°493	$-$41.698	0.279	1034	No
CS 22949$-$037	7	BD+44°493	$-$125.560	0.269	765	No
CS 22957$-$027	18	Co-add	$-$67.305	5.736	1568	Yes

included the bright CEMP-no star BD+44°493 in the programme, the abundance pattern of which has been studied extensively (Ito et al. 2013; Placco et al. 2014b). Ultimately, two of the candidate CEMP-no stars were shown not to be sufficiently carbon enhanced to be considered CEMP stars, and dropped from our programme. One of our candidate CEMP-s stars, discussed in Paper III, turned out to be a CEMP-no star, and hence was moved to the sample discussed here.

Our final sample of 24 CEMP-no programme stars is given in Table 6.1, which lists their V magnitudes, $B - V$ colours, and reported [Fe/H], [C/Fe] and [Ba/Fe] abundances (either from the literature or determined as described below).

6.1.2   Abundance information

Five of the stars in our sample had no Ba abundance measurement in the published literature, and one star (HE 0405$-$0526)lacked published estimates for [Fe/H] and [C/Fe] as well. For HE 0405$-$0526, we therefore derived estimates of [Fe/H] and [C/Fe] from

a medium-resolution ($R \sim 2000$) spectrum obtained with the SOAR Telescope (program SO2011B-002), using the n-SSPP software pipeline described in detail by Beers et al. (2014). For this star, as well as for the remaining stars with initiallly missing Ba abundances, we have used the high-resolution spectra obtained for the radial-velocity monitoring. These have been co-added to produce a higher signal-to-noise ratio (SNR) spectrum, following the description in Paper I for co-add templates, but including only the orders containing the Ba lines at $\lambda = 4554$ Å and $\lambda = 4934$ Å.

Ba abundances or upper limits were then obtained from spectral synthesis of these spectra using the 2014 version of MOOG and the line list retrieved from the VALD database (Kupka et al. 1999), including hyperfine splitting and isotopic shifts. The co-added spectra may have slightly broadened lines, due to the initial correlation when creating this spectrum, as described in Paper I, which could influence the abundances derived from these and result in a higher abundance being derived. We have taken this into account when estimating the error on the derived abundances.

For three of the stars we considered, only an upper limit on the Ba abundance could be derived; however, all of these firmly classify the stars as CEMP-no stars. For HE 0405−0526 and HE 1133−0555, we derive Ba abundances of [Ba/Fe] $= -0.22$ and [Ba/Fe] $= -0.58$ respectively, with an estimated error of 0.3 dex, also classifying them as CEMP-no stars.

CS 29527−015, HE 1012−1540, and HE 1327−2326 have derived Ba abundances or upper limits that do not qualify them as CEMP-no stars based on the formal definition ([Ba/Fe] < 0), [Ba/Fe] $< +0.10$, [Ba/Fe] $= +0.19$, and [Ba/Fe] $< +1.46$, respectively. However, the light-element signatures found for HE 1012−1540 and HE 1327−2326 – [N/Fe] $= +1.25$, [O/Fe] $= +2.14$, [Na/Fe] $= +1.02$ and [Mg/Fe] $= +1.38$ for HE 1012−1540 (Cohen et al. 2013), and [N/Fe] $= +4.53$, [O/Fe] $= +3.68$, [Na/Fe] $= +2.17$ and [Mg/Fe] $= +1.67$ for HE 1327−2326 (Frebel et al. 2008), clearly indicate their association with the CEMP-no sub-class. For CS 29527−015 an absolute carbon abundance of $A(\mathrm{C})$ [1] $= 6.06$ was found by Bonifacio et al. (2009), pointing to a CEMP-no classification for this star, but further observations are needed to confirm this.

6.1.3 Observations and data reduction

The observations, data reduction, and analysis procedures follow those described in Paper I of this series, to which we refer the interested reader for details; here we just provide a short summary. Our programme stars were observed at roughly monthly intervals with the FIES spectrograph at the 2.5-m Nordic Optical Telescope on La Palma, Spain. The spectra cover a wavelength range of 3640 Å to 7360 Å at a resolving power of $R \sim 46,000$, and have an average SNR of 10. For obvious reasons, the stars added to the programme in 2010 were observed for shorter spans and, coupled with persistently adverse spring weather conditions later, less intensively than the stars from the initial sample.

Reductions and multi-order cross-correlation with a template spectrum were performed with software developed by L. Buchhave. The template spectrum used for a given star was either: The spectrum with maximum SNR ("strongest"); a co-added spectrum constructed from all the best spectra for the star ("Co-add"); a synthetic spectrum consisting of delta

---

[1] $A(\mathrm{X}) = \log \epsilon\,(\mathrm{X}) + 12.00$.

functions ("Delta"); or finally a co-added spectrum of the bright CEMP-no star BD+44°493. The template used for each star is identified in Table 6.2.

Our error definitions and error analysis are also described in Paper I. Note especially that the standard deviations given in Tables 6.2 and 6.3 are the standard deviation of the radial velocity observations for each star, not standard errors of the mean.

The standard stars observed on this programme, along with their derived mean heliocentric radial velocities (RV) and standard deviations (σ), are listed in Table 2 of Paper I in this series. The mean difference of our velocities from the standard values is 73 m s^{-1}, with a standard deviation of 69 m s^{-1}, demonstrating that our results are not limited by the stability of the FIES spectrograph.

6.2 Results

The results of our radial-velocity observations for our CEMP-no stars are summarised in Table 6.2, which lists the number of observations (Nobs), the cross-correlation templates employed, mean heliocentric radial velocity (RV mean) and standard deviation (σ) over the observed time span (ΔT), and the binary status of each programme star. The individual observed heliocentric radial velocities are listed in Appendix A, together with the Julian dates of the observations and the corresponding internal errors.

It is immediately apparent from inspection of Table 6.2 that the great majority of the stars (20 out of 24) exhibit no significant radial-velocity variation over the monitoring periods specified for each star in Table 6.2. As for the r-process-element enhanced stars discussed in Paper I, the standard deviation of the observed velocities vary from $\sim$ 100 m s^{-1} for the bright targets, dominated by centering and guiding errors, to $\sim$ 1 km s^{-1} for the fainter targets with low-SNR spectra.

6.2.1 Comparison with published radial velocities for the constant stars

Radial-velocity observations for 15 of our programme stars have been published previously and help to extend the time spans of the data and strengthen the conclusion on their (non-) binary nature. We have checked the literature for velocities of the non-binary stars in our sample, based on moderate to high-resolution spectra by authors who claim estimated velocity errors of $\sim$2 km s^{-1} or better. Table B.3 in Appendix B summarizes the results of this exercise. Note that these data are typically based on a single observation (or the mean of several closely spaced observations). In each case, the total time span given includes the oldest measurement that we consider reliable.

It is remarkable that *no* velocity in this comparison sample deviates from our own mean radial velocity by more than can be accounted for by the published errors, especially since the data was obtained with different spectrographs and were reduced and measured independently. As seen from the table, the observed time span for many of our programme stars now cover on the order of a decade or more. Clearly, if any of stars we consider to be single are in fact members of a binary system, they are likely to have extremely long periods (but see discussion below).

An illustrative case is the bright star BD+44°493, which was also observed by Starkenburg et al. (2014). As seen from Table 6.2 and B.3, the radial velocities derived by Starken-
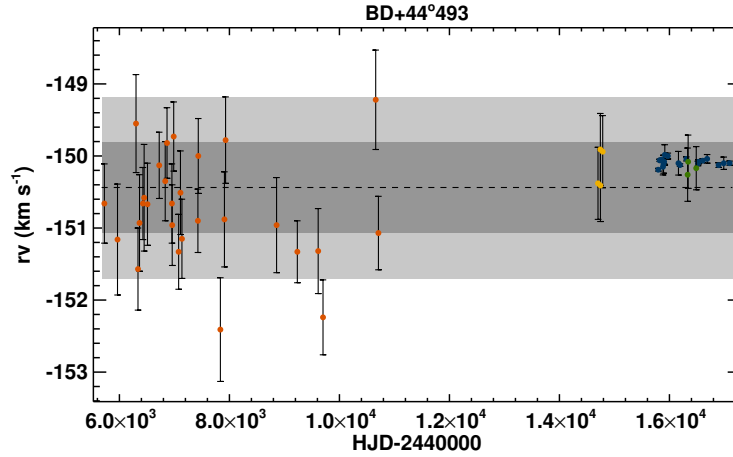
Figure 6.1: Radial-velocity history of BD+44°493 vs. time. *Blue* : This work, *green* : Carney et al. (2003), *yellow* : Ito et al. (2013), and *red* : Starkenburg et al. (2014). Dashed line: Global mean radial velocity; grey shaded areas: 1 and 2σ regions around the global mean.

burg et al. (2014) are in excellent agreement with our derived velocities for both this and other constant stars (all except CS 29502-092 are within the stated 1-σ error bars; and CS 29502-092 agrees within 2σ). Radial velocities for BD+44°493 were also reported by Carney et al. (2003) and Ito et al. (2013), whose measured mean velocities of -150.64 km s^{-1} and -150.15 km s^{-1}, respectively, are both in excellent agreement with our result. The Carney et al. data are particularly valuable, since they enlarge the three-year time span of our own data by 13 years (1984 to 1997). Together, these four data sets contain 53 measurements spanning a total of 11368 days ($\sim$ 31 years) with a standard deviation of 0.63 km s^{-1}. Figure 6.1 show all the radial velocity data for BD+44°493 as function of time. Clearly, this star is single.

6.2.2 Binaries in the sample of CEMP-no stars
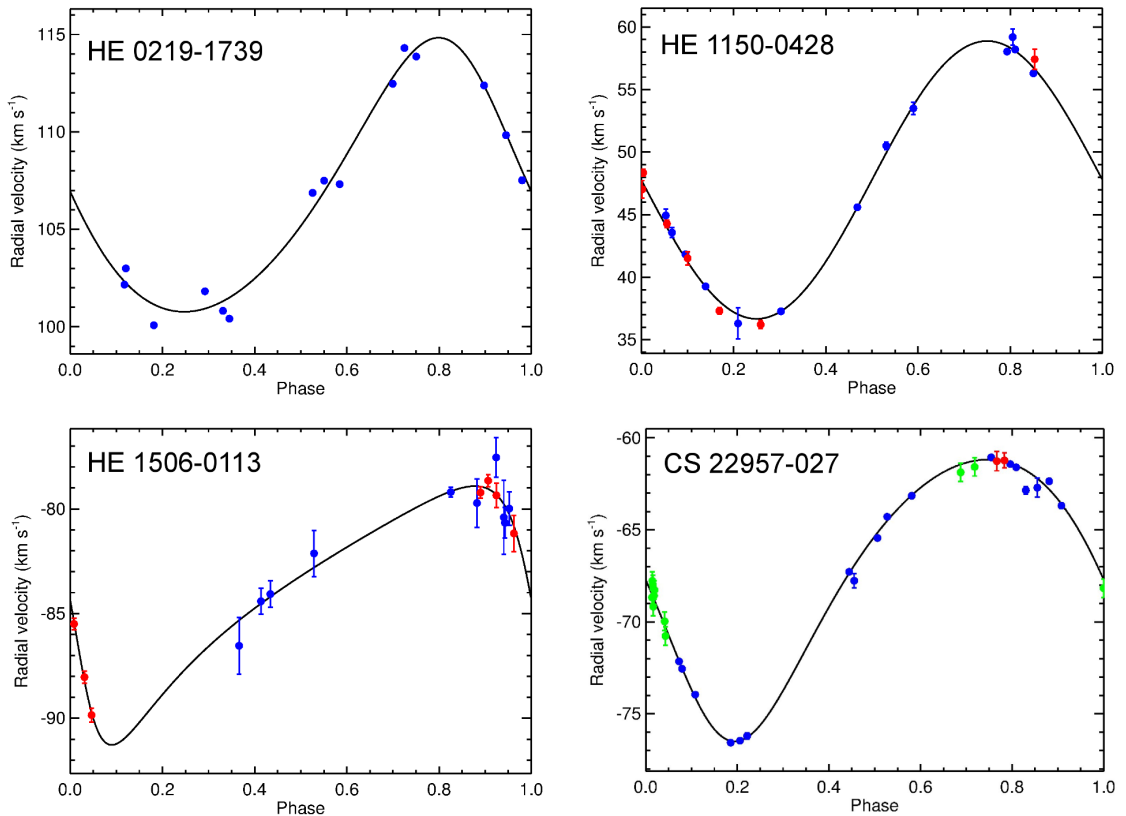
Figure 6.2: Orbit solutions for the four binaries found among our programme stars. Top left: HE 0219−1739, top right: HE 1150−0428, bottom left: HE 1506−0113, and bottom right: CS 22957−027. Blue: This work; red: Starkenburg et al. (2014); green: Preston & Sneden (2001).

Four stars in our sample exhibit clear and systematic variations in their radial velocities over the monitoring period: HE 0219−1739, HE 1150−0428, HE 1506−0113, and CS 22957−027, and we have been able to determine orbits for all of them, combining our radial velocities with earlier, published data. The final orbital parameters for these systems are listed in Table 6.3, and the radial-velocity curves are shown in Figure 6.2, including the literature data and toytal time spans as noted below. For the Starkenburg et al. (2014) data (red points in Figure 6.2), we find an offset of only ~ 450 m s^{-1} between our data and theirs, based on three constant stars in common. For the data from Preston & Sneden (2001) (green points in Figure 6.2), we have applied a correction of ~ 1.84 km s^{-1} to achieve consistency with our velocities.

Table 6.3 also lists the calculated Roche-lobe radii for the present secondaries in the four binary systems, calculated following the procedure described in Paper I and assuming present primary masses of 0.8 M$_\odot$ and secondary masses of 0.4 and 1.4 M$_\odot$ – the lower and

Table 6.3: Orbital parameters of the binary systems identified in the sample

Parameter	HE 0219−1739	HE 1150−0428	HE 1506−0113	CS 22957−027
Period (days)	1802.5±5.0	289.7±0.1	841.0±19.2	1080.0±0.8
T_0 (HJD)	2455981.4±1.7	2455759.3±0.3	2456448.7±3.5	2455660.0±1.6
K (km s^{-1})	7.032±0.022	11.102±0.043	6.179±0.624	7.661±0.039
γ (km s^{-1})	+106.809±0.016	+47.779±0.035	−83.997±0.327	−67.500±0.026
e	0.162±0.004	0.000±0.000	0.495±0.044	0.193±0.007
ω °	29.8±1.0	0.0±0.0	111.0±11.5	155.2±1.6
$a\sin i$ (R$_\odot$)	247.2±1.0	63.56±0.09	89.3±9.5	160.5±0.4
f(m) (M$_\odot$)	0.062±0.004	0.041±0.002	0.013±0.001	0.048±0.003
σ (km s^{-1})	0.867	0.670	0.853	0.454
ΔT/P (total)	1.2	7.7	1.1	4.7
R_{Roche} (R$_\odot$, M$_1$ = 0.8 M$_\odot$, M$_2$ = 0.4 M$_\odot$)	121	29	56	73
R_{Roche} (R$_\odot$, M$_1$ = 0.8 M$_\odot$, M$_2$ = 1.4 M$_\odot$)	442	131	268	310

upper limits to the mass of a white dwarf (WD), which would be the likely remnant if the CEMP-no star were polluted by an initially more massive AGB star. As can be seen from Table 6.3, for the maximum WD mass (1.4M$_\odot$), all the systems could have accommodated an AGB star (R ∼200R$_\odot$), while for the lowest WD masses, the majority of the Roche-lobes would be too small.

Notes on individual stars:

CS 22957−027: Both Preston & Sneden (2001) and Starkenburg et al. (2014) found significant variations in the velocity of CS 22957−027, but neither was able to determine a period. Our own data cover the orbit securely, with the earlier data improving the period determination. Starkenburg et al. (2014) also reported large velocity variations in HE 1150−0428 and HE 1506−0113, but the data were too sparse to determine the orbital period. Our own data for HE 1150−0428, obtained over a longer time span, determine the orbit securely, while the data by Starkenburg et al. (2014) are fully consistent with it. In contrast, the early Starkenburg et al. (2014) data for HE 1506−0113 (red points in Figure 6.2) were crucial in covering the orbit and determining its period. Additional observations will be useful in refining the orbital elements, but the essentials are in hand.

HE 1410+0213 presented a special difficulty, despite the large number of good observations (Table 6.2). The fairly large dispersion of the velocities and apparently systematic trends during individual years led us to suspect that it was a nearly face-on spectroscopic binary, and we were able to derive a plausible circular orbit with a period of ∼330 days and a velocity amplitude of ∼280 m s^{-1}. This, however, required an inclination of less than 1°, very unlikely in such a small sample of stars. Moreover, a later observation did not fit the putative orbit. We were faced with a similar situation for a CEMP-*s* star, which will be discussed in Paper III.

After much experimentation, we concluded that HE 1410+0213 is most probably single, but exhibits low-amplitude pulsations of the kind described by Riebel et al. (2010) for C-rich variables in the LMC. Mattsson (2015) describes how a combination of a strong stellar wind with such pulsations might enhance the mass loss from such an intrinsically bright EMP giant or AGB star. This could explain why the absolute C abundance of HE 1410+0213, places it in the "high-C band" of Spite et al. (2013), discussed further below.

CS 29527−015 was suggested to be a double-lined spectroscopic binary by Bonifacio et al. (2009), due to asymmetries in the absorption lines detected in their high-resolution, high(er)-SNR UVES spectra. We find no evidence for this – nor for any velocity variations – in our observations of the star, but additional high-resolution spectra may be required to firmly determine the binary nature of this star.

Our sample of CEMP-no stars comprises 4 binaries and 20 single stars, We thus derive a binary frequency of 17%±5%, identical to that found for the *r*-process-enhanced stars in Paper I of this series (18%±6%), and to the 16% ±4% binary frequency found by Carney et al. (2003) in their study of 91 metal-poor ([Fe/H] ≤ −1.4) field red giants.

6.2.3 Binary parameters

The four binary systems in our sample exhibit a similar combination of periods and eccentricities to those found by Carney et al. (2003) for metal-poor field red giants and dwarfs (see their Figure 5), for Population I cluster giants by Mermilliod et al. (2007), and by us for the *r*-process enhanced VMP and EMP stars discussed in Paper I. Figure 6.3 shows the period - eccentricity distribution for our binary stars (red plus signs), compared to the literature data from Mermilliod et al. (2007) and Mathieu et al. (1990) (black dots). Our binary stars are completely indistinguishable from those of chemically normal population I and II giants, with HE 1150−0428 defining a cutoff period for circular orbits of > 300 days.
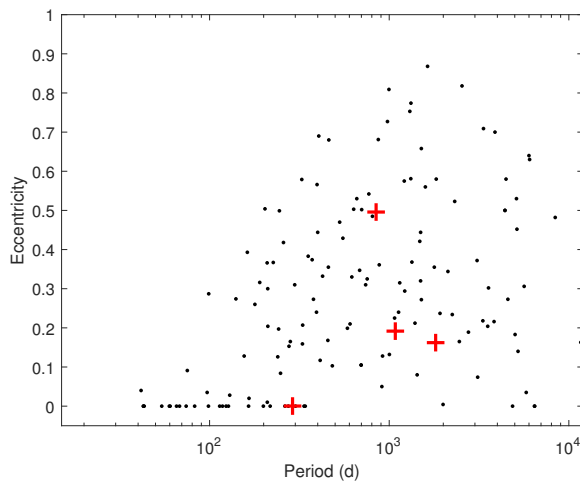
Figure 6.3: Period - eccentricity distribution for the binary systems in our sample (red plus signs), compared to literature data (black dots; Mermilliod et al. 2007; Mathieu et al. 1990).

Radial-velocity monitoring of CEMP-s stars

This chapter is taken from the paper "The role of binaries in the enrichment of the early Galactic halo, II. Carbon enhanced extremely metal-poor stars - the CEMP-s stars", describing the radial-velocity monitoring of a sample of 18 CEMP-s and four CEMP-r/s stars. The paper will be submitted to Astronomy & Astrophysics, with the following author list: T. Hansen, J. Andersen, B. Nordström, T. C. Beers, V. M. Placco, J. Yoon, and L. A. Buchhave. V. M. Placco has performed the abundance synthesis and J. Andersen has calculated Roche-lobe radii for the stars. The remaining analyses presented here is work of the author of this thesis; all co-authors have commented on the manuscript.

7.1   Sample stars, observations and analysis

The sample stars are presented in Table 7.1, which lists their V and $B - V$ colours, and reported [Fe/H], [C/Fe] and [Ba/Fe] abundances, either from the literature or derived as described below. The majority of the stars are selected from the Hamburg/ESO survey of Christlieb and collaborators (Christlieb et al. 2008).

A number of stars in our programme had no abundance estimate (or upper limit) for barium available in the literature; Ba which is required in order to make a confident assignment of a stars into the CEMP-s sub-class. For these we have derived Ba abundances (or upper limits) from the co-added high resolution NOT spectra following the procedure described in chapter 6 (Paper II). This exercise firmly confirms the classification of all of these stars as CEMP-s stars.

The four stars listed in the lower section of Table 7.1; HE 0039− 2635, HE 1031−0020, CS 30301−015, and LP 625−44, have been suggested to be CEMP-r/s stars; carbon stars showing enhancement in both the r- and s-process elements ($0.0 < $ [Ba/Eu] $< +0.5$, Beers & Christlieb 2005). The following values have been found for the Eu abundances in these three stars – HE 0039−2635: [Eu/Fe] $= +1.80$ (Barbuy et al. 2005); HE 1031−0020: [Eu/Fe] $<$

Table 7.1: The sample of CEMP-s and CEMP-r/s stars monitored for radial-velocity variation

Stellar ID	RA (J2000)	Dec (J2000)	V	B − V	ref	[Fe/H]	[C/Fe]	[Ba/Fe]	ref
			CEMP-s						
HE 0002−1037	00:05:23	−10:20:23	13.70	0.48	a	−3.75	+3.19	+1.67	1
HE 0017+0055	00:20:22	+01:12:07	11.46	1.53	b	−2.80	+1.99	< +1.62	1
HE 0111−1346	01:13:47	−13:30:50	12.48	1.31	b	−1.91	+1.70	< +2.32	1,2
HE 0151−0341	01:53:43	−03:27:14	13.36	1.14	b	−2.46	+2.46	+1.22	1,2
HE 0206−1916	02:09:20	−19:01:55	14.00	1.13	b	−2.09	+2.10	+1.97	3
HE 0319−0215	03:21:46	−02:04:34	13.79	1.39	b	−2.30	+2.00	+0.52	1
HE 0430−1609	04:32:51	−16:03:39	13.17	1.25	b	−3.00	+1.14	+1.62	1
HE 0441−0652	04:43:30	−06:46:54	14.23	1.02	b	−2.47	+1.38	+1.11	3
HE 0507−1430	05:09:17	−16:50:05	14.49	1.54	b	−2.40	+2.60	+1.30	4
HE 0507−1653	05:10:08	−14:26:32	12.51	1.13	b	−1.38	+1.29	+1.89	3
HE 0854+0151	08:57:30	+01:39:50	14.98	0.92	b	−1.80	+1.60	+0.82	1
HE 0959−1424	10:02:04	−14:39:22	13.37	0.60	b	−1.42	+2.30	+1.24	1
HE 1045+0226	10:48:03	+02:10:47	14.10	1.01	a	−2.20	+0.97	+1.24	5
HE 1046−1352	10:48:30	−14:08:12	14.71	0.68	b	−2.76	+3.30	+1.38	1
HE 1523−1155	15:26:41	−12:05:43	13.23	1.35	b	−2.15	+1.86	+1.72	3
HE 2201−0345	22:03:58	−03:30:54	14.31	1.18	b	−2.80	+2.30	+0.62	1
HE 2312−0758	23:14:55	−07:42:32	14.32	1.02	a	−3.47	+1.86	+1.99	1
HE 2330−0555	23:32:55	−05:38:50	14.56	0.85	b	−2.78	+2.09	+1.22	3
			CEMP-r/s						
HE 0039−2635*	00:41:40	−26:18:54	12.22	1.12	b	−2.90	+2.63	+2.03	6
CS 30301−015	15:08:57	+02:30:19	13.04	1.00	b	−2.64	+1.60	+1.45	7
HE 1031−0020	10:34:24	−00:36:09	11.87	0.74	a	−2.81	+1.58	+1.55	8
LP 624−44	16:43:14	−01:55:30	11.68	1.16	a	−2.72	+2.25	+2.83	9

* CS 29497−034

Photometry: (a) Henden et al. (2015), (b) Beers et al. (2007a).

Abundances: (1) this work, (2) Kennedy et al. (2011), (3) Aoki et al. (2007), (4) Beers et al. (2007b),

(5) Cohen et al. (2013), (6) Barbuy et al. (2005), (7) Aoki et al. (2002b),

(8) Cohen et al. (2013), (9) Aoki et al. (2002c)

+0.82 (Cohen et al. 2013); CS 30301−015: [Eu/Fe] = +0.20 (Aoki et al. 2002b); LP 625−44: [Eu/Fe] = +1.72 (Aoki et al. 2002c). Using the [Ba/Fe] listed in Table 7.1 (from the same literature sources), we obtain the following [Ba/Eu] ratios: +0.23, > +1.27, +1.25 and +1.11 for HE 0039−2635, HE 1031−0020, CS 30301−015, and LP 625−44, respectively. Only HE 0039−2635 formally qualifies as a CEMP-r/s star; newer-the-less, Eu is detected in three of these stars, and this should be accounted for in any formation scenario of such stars.

Observations, reductions, and analysis procedures follow those of chapter 5 (Paper I of this series), to which the interested reader is referred for details; here only a short summary is given. The stars were observed with the FIES spectrograph at the Nordic Optical Telescope. The spectra cover a wavelength range of 3640 Å to 7360 Å, with a spectral resolving power $R \sim 46,000$, and average signal-to-noise ratio (SNR) of 10. Reductions and multi-order cross-correlation was performed with software developed by L. Buchhave. The template spectra used for this sample are: Spectrum for a given star with maximum signal ("strongest"), Co-added spectrum of the best spectra of a given star ("Co-add"), Synthetic spectrum consisting of delta functions ("Delta"), and co-add of bright star with a spectrum similar to the object (HE 0507−1653).

The spectra of the CEMP-s (and CEMP-r/s) stars are different than those of the r-process-enhanced stars and the CEMP-no stars presented in chapters 5 and 6 (Paper I and Paper II of this series), in that they have multiple neutron-capture-element absorption lines, which facilitated a more precise correlation including more spectral orders. As a consequence, the majority of these stare were correlated with either the strongest or co-add template.

The standard stars observed on this programme, along with their derived mean RV and standard deviations are listed in Table 2 of paper I of this series. The mean difference of our velocities from the standard values is 73m s^{-1} with standard deviation of 69m s^{-1}, demonstrating that our results are not limited by the stability of the spectrograph.

7.2   Results

The results of the radial velocity monitoring of the sample of CEMP-s stars are summarized in Table 7.2, listing number of observations (Nobs), cross-correlation template, mean radial velocity and standard deviation (σ) over the observed time span (ΔT), along with the binary status, for each sample star. The individual observed heliocentric radial velocities are listed in Appendix A, together with the Julian dates of the observations and the corresponding internal errors.

From inspection of Table 7.2 it can be seen that the majority (18 of 22) of the sample stars exhibit significant radial-velocity variation over the eight year period of monitoring.

A few of the stars in our sample have reported radial-velocity measurements in the literature. For the four stars exhibiting no radial-velocity variations (which might be considered either single stars or stars with extremely long periods) the literature measurements are listed in Table B.4, which also lists the combined time spans for the observation of these stars. For the binary stars, the literature data is reviewed below, and included in the orbital solution when possible.

Table 7.2: Templates, mean heliocentric radial velocities and standard deviations, and observed time spans for the sample stars

Stellar ID	Nobs	Template	RV mean (km-s^{-1})	σ (km-s^{-1})	ΔT (Days)	Binary
			CEMP-s			
HE 0002−1037	9	Co-add	−32.135	5.660	1033	Yes
HE 0017+0055	27	Strongest	−80.175	1.167	2673	Yes
HE 0111−1346	8	Strongest	+42.727	6.864	704	Yes
HE 0151−0341	11	Co-add	−35.685	9.136	1011	Yes
HE 0206−1916	8	Co-add	−199.509	0.109	805	No
HE 0319−0215	16	Co-add	−225.782	2.357	2207	Yes
HE 0430−1609	14	Co-add	+231.095	1.574	901	Yes
HE 0441−0652	16	Co-add	−30.647	2.655	2371	Yes
HE 0507−1430	11	Strongest	+44.802	7.920	1064	Yes
HE 0507−1653	15	Co-add	+348.280	4.859	2124	Yes
HE 0854+0151	15	Co-add	+138.297	7.798	1757	Yes
HE 0959−1424	18	HE 0507−1653	+343.615	0.660	2736	Yes
HE 1045+0226	6	HE 0507−1653	+131.498	0.280	803	No
HE 1046−1352	12	Strongest	+79.471	21.250	1812	Yes
HE 1523−1155	8	Co-add	−43.156	3.597	334	Yes
HE 2201−0345	25	Co-add	−55.778	3.452	2642	Yes
HE 2312−0758	10	Co-add	+33.321	3.196	1034	Yes
HE 2330−0555	19	Co-add	−235.124	0.251	2573	No
			CEMP-r/s			
HE 0039−2635	2	Strongest	−47.739	6.136	278	Yes
CS 30301−015	18	Co-add	+86.607	0.077	2233	No
HE 1031−0020	22	Co-add	+68.660	1.157	2924	Yes
LP 625−44	28	Co-add	+35.036	3.348	2667	Yes
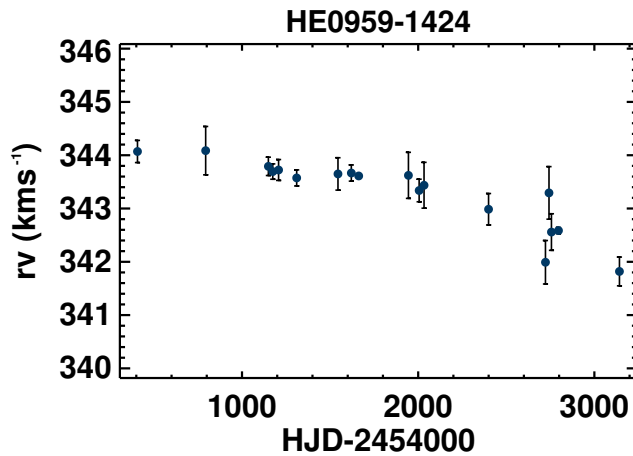
Figure 7.1: Radial velocities measured for HE 0959−1424 as function of time. The measured velocities exhibit a clear decline over the monitoring period.

HE $0039-2635$ was also included in the sample of Lucatello et al. (2005), with one measurement from 2002. Barbuy et al. (2005) reports 11 measurements, over a period of $\sim$3000 days between 1995 and 2004, for this star, with an rms of 3.4 km s^{-1}. Barbuy et al. (2005) also reports an orbital solution for this system, with P = 4130 days and $e = 0.2$. We have combined our data for this star with the literature data, and find a shorter but more eccentric orbit, with P = 3419 and $e = 0.536$; see Figure 7.6 and Table 7.7

For LP $625-44$ there are literature measurements reported by Norris et al. (1997): Five measurements in the period from 1988 to 1996; Aoki et al. (2000): Two measurements from 1998 and 2000; and Lucatello et al. (2005): Three measurements between 2000 and 2002. None of the authors listed above had sufficient data for this star to compute an orbital solution. However, by combining the literature data with our extensive data for this star, covering a total time span of 9582 days, we compute an orbit with a period of P = 4863 days and $e = 0.351$; see Figure 7.6 and Table 7.7. We find the following offsets between our and the literature data – Norris et al. -0.14 m s^{-1}; Aoki et al. $+451.96$ m s^{-1}; and Lucatello et al. $+155.87$ m s^{-1}.

Aoki et al. (2007) have reported radial velocities for HE $0507-1653$ (353.0 km s^{-1}) and HE $1523-1155$ (-45.0 km s^{-1}), for the former this point fits well with our derived orbital solution (red point in Figure 7.4). For the latter star, we have not been able to fit an orbit including the measurement from Aoki et al., indicating that the orbit we show in Figure 7.4 is likely not the final orbit for this star, and more measurements are needed.

The final orbital parameters for 17 of the binary systems in our sample are listed in Tables 7.3, 7.4, 7.5, and 7.6; radial-velocity curves are shown in Figures 7.2 to 7.6. Tables 7.3, 7.4, 7.5, and 7.6 also list the calculated Roche-lobe radii of the secondary in the systems, assuming a primary mass of $0.8 M_{\odot}$ and secondary masses of $0.4 M_{\odot}$ and $1.4 M_{\odot}$ respectively. The procedure for calculating the Roche-lobe radii is described in Paper I.

For HE $0959-1424$ we have not been able to compute an orbital solution, but Figure 7.1 shows the measured radial velocities as a function of time. A slow but clear decline over the 2736 day time span of RV-monitoring is seen in the measured velocities for this star. We conclude that this star is a binary with a very long period, possibly on the order of 10000 days or more.
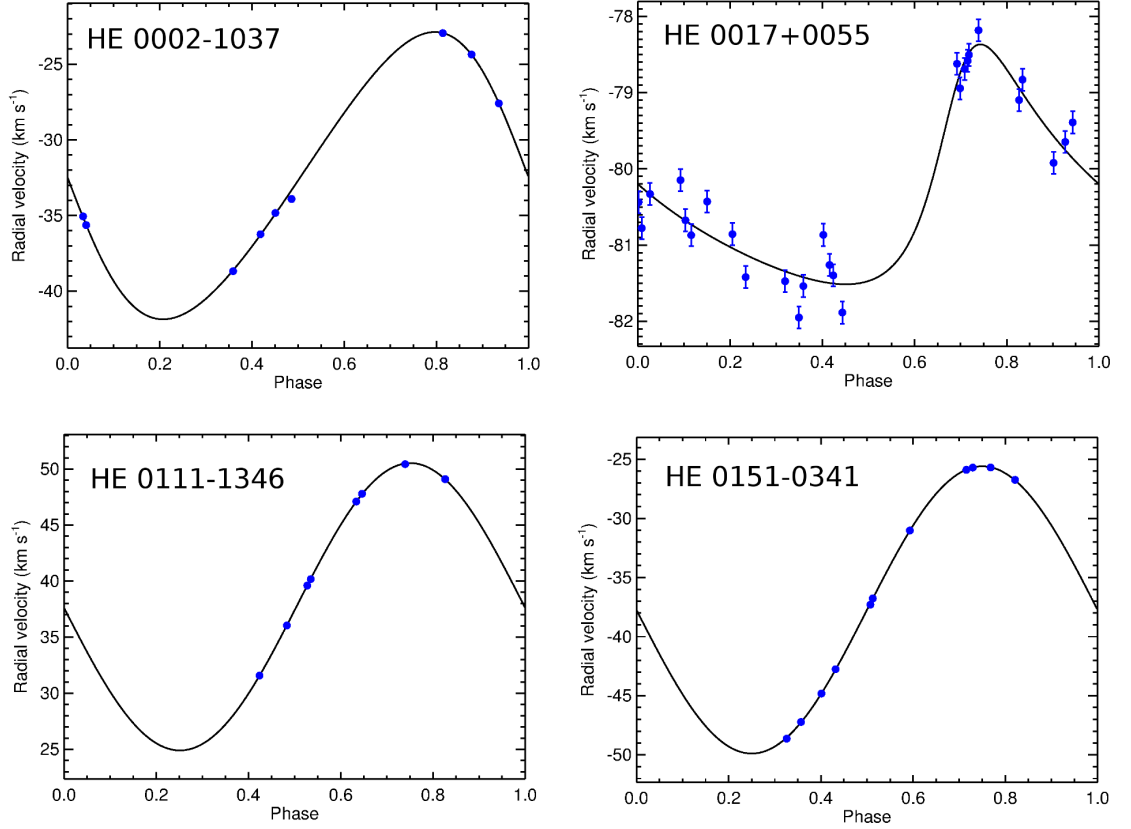
Figure 7.2: Orbit of HE 0002−1037 (top left), HE 0017+0055 (top right), HE 0111−1346 (bottom left) and HE 0151−0341 (bottom right)

Table 7.3: Orbital parameters of recognized binary stars in our sample displayed in Figure 7.2

Parameter	HE 0002−1037	HE 0017+0055	HE 0111−1345	HE 0151−0341
Period (days)	741.1±1.1	3558	403.7±0.2	358.9±0.2
T_0 (HJD)	2456622.3±0.7	2455143.9±10.3	2456318.7±0.3	2455314.1±0.8
K (km s^{-1})	9.497±0.081	1.615±0.045	12.811±0.037	12.128±0.033
γ (km s^{-1})	−32.271±0.049	−80.257±0.028	+37.608±0.025	−37.497±0.036
e	0.141±0.006	0.432	0.008±0.002	0.000±0.000
ω °	84.3±2.7	0.0±0.0	0.0±0.0	0.0±0.0
$a\sin i$ (R$_\odot$)	138.0±0.5	102.4±19.3	103.0±0.1	86.2±0.2
f(m) (M$_\odot$)	0.064±0.003	0.001±0.020	0.090±0.0002	0.067±0.0004
σ (km s^{-1})	0.34	0.11	0.57	0.50
R_{Roche} (R$_\odot$, M$_1$ = 0.8 M$_\odot$, M$_2$ = 0.4 M$_\odot$)	67.1	61.6	56.	42.2
R_{Roche} (R$_\odot$, M$_1$ = 0.8 M$_\odot$, M$_2$ = 1.4 M$_\odot$)	242.2	154.7	161.9	146.3
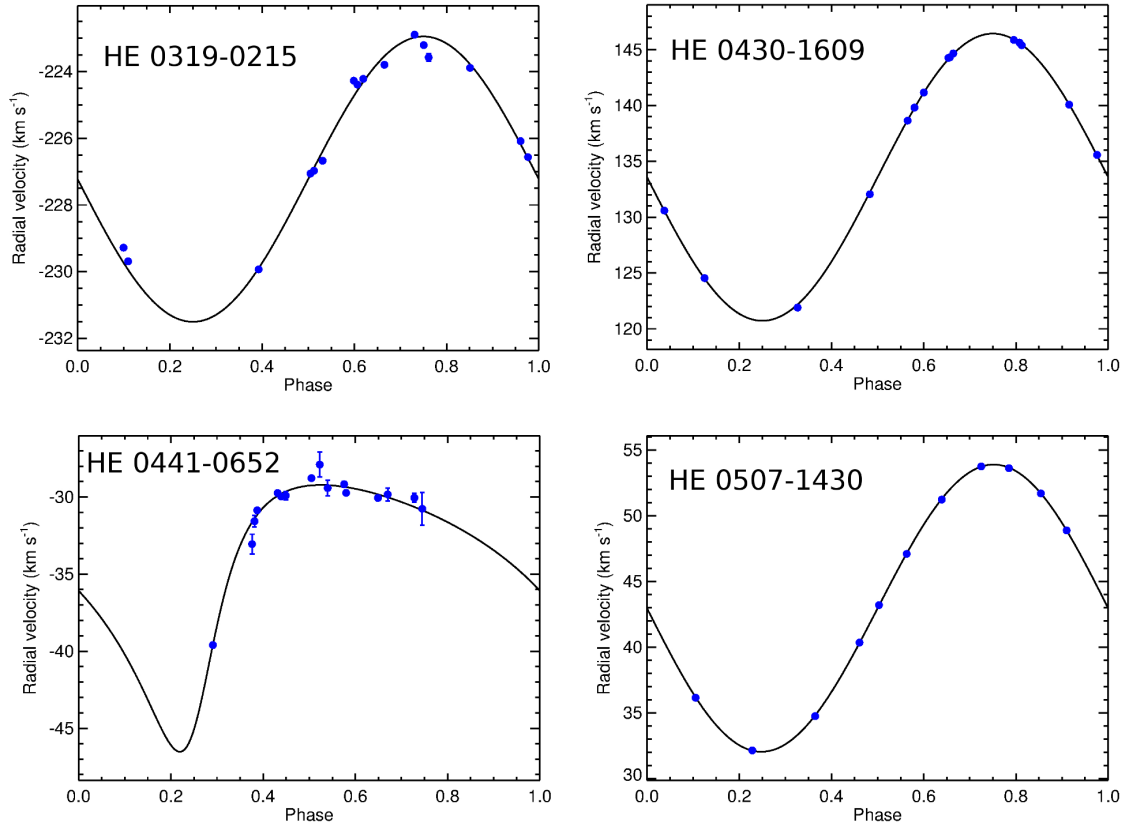
Figure 7.3: Orbit of HE 0319−0215 (top left), HE 0430−1906 (top right), HE 0441−0652 (bottom left) and HE 0507−1430 (bottom right)

Table 7.4: Orbital parameters of recognized binary stars in our sample displayed in Figure 7.3

Parameter	HE 0319−0215	HE 0430−1609	HE 0441−0652	HE 0507−1430
Period (days)	3078.0±24.7	1155.2±110.0	5222.3±628.2	447.0±0.2
T_0 (HJD)	2453572.3±18.5	2457280.9±80.0	2458407.9±308.4	2455272.7±0.2
K (km s^{-1})	4.278±0.048	2.379±0.092	8.651±3.250	10.927±0.011
γ (km s^{-1})	−227.226±0.051	+230.739±0.129	−34.577±1.949	+42.957±0.009
e	0.000±0.000	0.456±0.052	0.476±0.037	0.006± 0.002
ω °	0.0±0.0	96.9±3.3	217.4±0.04	84.2±10.5
$a \sin i$ (R$_\odot$)	260.3±3.2	48.1±4.3	702.0 ±164.0	96.5±0.1
f(m) (M$_\odot$)	0.025±0.005	0.001±0.003	0.180±0.310	0.060±0.001
σ (km s^{-1})	0.33	0.12	0.96	0.48
R_{Roche} (R$_\odot$, M$_1$ = 0.8 M$_\odot$, M$_2$ = 0.4 M$_\odot$)	142.0	74.5	470.4.5	46.6
R_{Roche} (R$_\odot$, M$_1$ = 0.8 M$_\odot$, M$_2$ = 1.4 M$_\odot$)	634.4	305.7	874.1	169.1
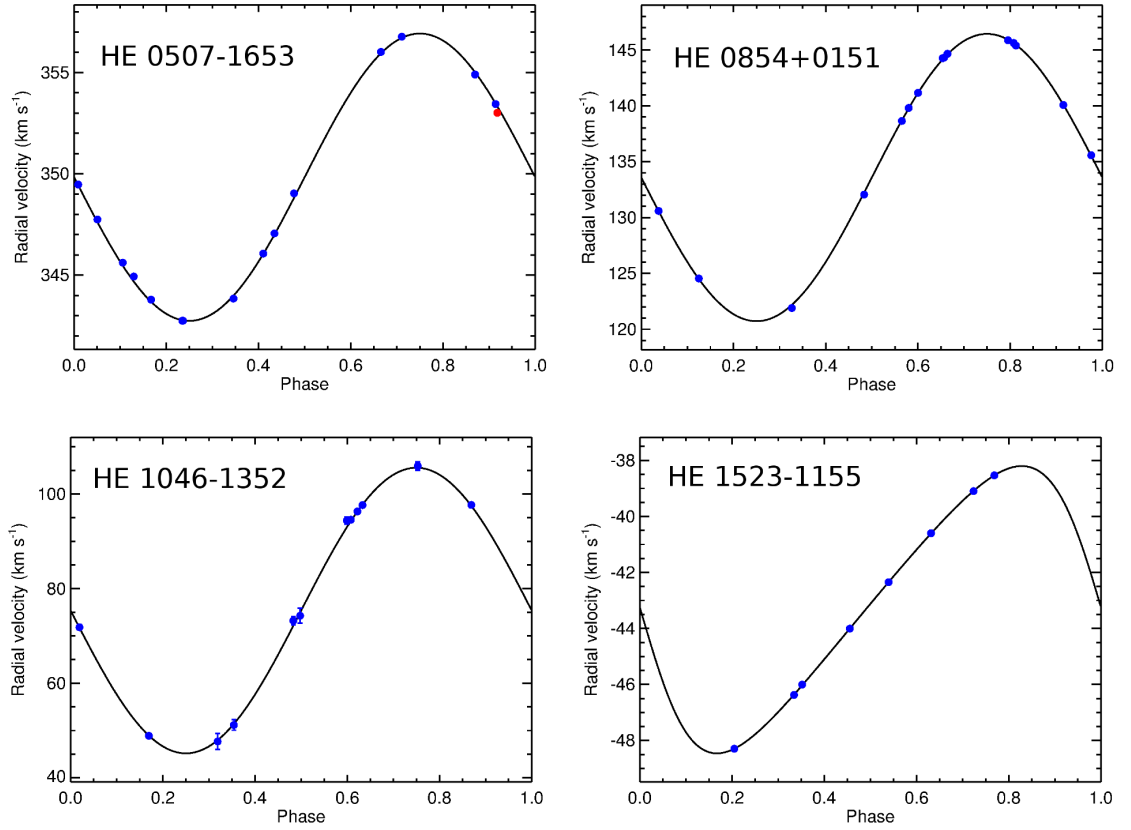
Figure 7.4: Orbit of HE 0507−1653 (top right), HE 0845+0151 (top right), HE 1046−1352 (bottom left) and HE 1523−1155 (bottom right), blue this work, red Aoki et al. (2007)

Table 7.5: Orbital parameters of recognized binary stars in our sample displayed in Figure 7.4

Parameter	HE 0507−1653	HE 0854+0151	HE 1046−1352	HE 1523−1155
Period (days)	404.0±0.1	389.9±0.1	20.2±0.001	308.0±1.6
T_0 (HJD)	2455840.1±0.1	2455305.6±0.1	2455199.9±0.03	2457004.4±28.9
K (km s^{-1})	7.091±0.080	12.859±0.029	30.186±0.297	5.414±1.280
γ (km s^{-1})	+349.842±0.060	+133.578±0.020	+75.370±0.155	−42.820±1.681
e	0.000±0.000	0.000±0.000	0.000±0.000	0.287±0.141
ω °	0.0±0.0	0.0±0.0	0.0±0.0	90.5±11.0
$a\sin i$ (R$_\odot$)	56.63±0.03	99.09±0.07	12.03±0.10	30.2±0.4
f(m) (M$_\odot$)	0.015±0.002	0.086±0.003	0.057±0.008	0.004±0.0001
σ (km s^{-1})	4.45	0.56	0.47	0.02
R_{Roche} (R$_\odot$, M$_1$ = 0.8 M$_\odot$, M$_2$ = 0.4 M$_\odot$)	36.1	52.0	8.7	
R_{Roche} (R$_\odot$, M$_1$ = 0.8 M$_\odot$, M$_2$ = 1.4 M$_\odot$)	155.7	155.4	22.0	
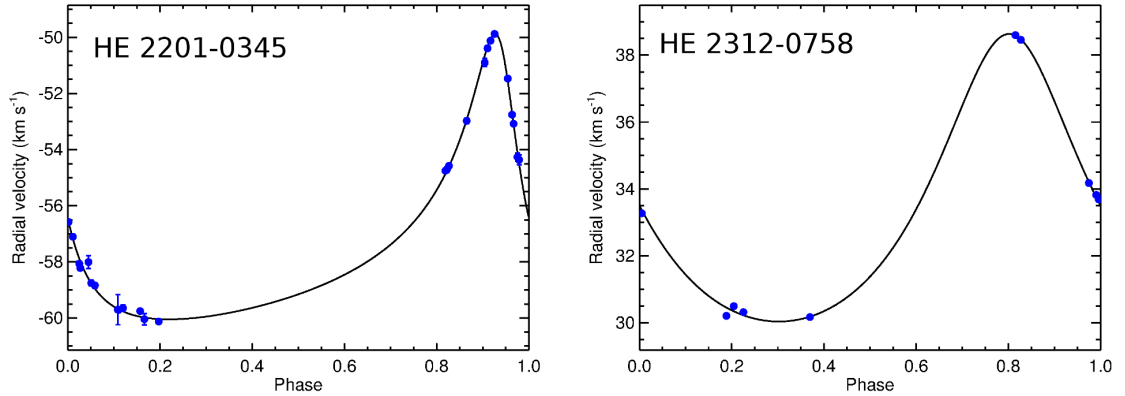
Figure 7.5: Orbit of HE 2201−0345 (left) and HE 2312−0758 (right)

Table 7.6: Orbital parameters of recognized binary stars in our sample displayed in Figure 7.5

Parameter	HE 2201−0345	HE 2312−0758
Period (days)	7576.8±93.6	1610.9±121.1
T_0 (HJD)	2455690.8±5.5	2456484.2±23.1
K (km s^{-1})	5.047±0.025	4.326±0.216
γ (km s^{-1})	−57.845±0.042	+34.341±0.411
e	0.600	0.082±0.055
ω °	28.0±0.0	0.0±0.0
$a\sin i$ (R$_\odot$)	611.6±7.7	153.0±5.7
f(m) (M$_\odot$)	0.053±0.0002	0.014±0.006
σ (km s^{-1})	0.60	0.26
R_{Roche} (R$_\odot$, M$_1$ = 0.8 M$_\odot$, M$_2$ = 0.4 M$_\odot$)	277.2	92.9
R_{Roche} (R$_\odot$, M$_1$ = 0.8 M$_\odot$, M$_2$ = 1.4 M$_\odot$)	1148.2	414.1
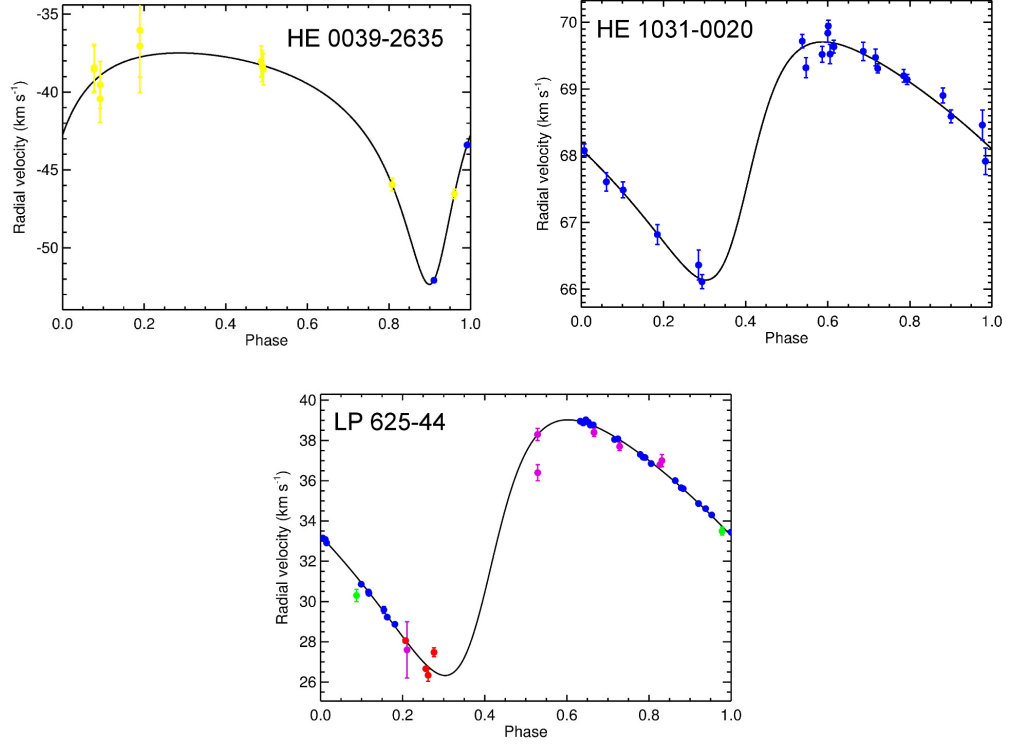
Figure 7.6: Orbit of HE 0039−2635 (top), HE 1031−0020 (middle) and LP 625−44 (bottom), Blue: this work, purple: Norris et al. (1997), red: Lucatello et al. (2005), green: Aoki et al. (2000), yellow: Barbuy et al. (2005).

Table 7.7: Orbital parameters of recognized binary stars in our sample displayed in Figure 7.6

Parameter	HE 0039−2635	HE 1031+0020	LP 625−44
Period (days)	3418.6±495.8	3867.3±174.9	4863.3±
T_0 (HJD)	2456547.7±418.7	2456006.1±53.6	2456006.6±
K (km s^{-1})	7.425±3.040	1.785±0.069	6.350±0.044
γ (km s^{-1})	−41.102±12.487	+68.218±0.061	+33.632±0.065
e	0.536±0.215	0.379	0.352±0.000
ω $^\circ$	16.5±47.5	244.0	244.4±0.0
$a\sin i$ (R$_\odot$)	424.0±139	126.5±27.7	571.4±17.8
f(m) (M$_\odot$)	0.09±0.53	0.002±0.036	0.106±0.013
σ (km s^{-1})	1.11	0.17	0.42
R_{Roche} (R$_\odot$, M$_1$ = 0.8 M$_\odot$, M$_2$ = 0.4 M$_\odot$)	273.1	284.1	403.2
R_{Roche} (R$_\odot$, M$_1$ = 0.8 M$_\odot$, M$_2$ = 1.4 M$_\odot$)	358.5	727.8	800.5
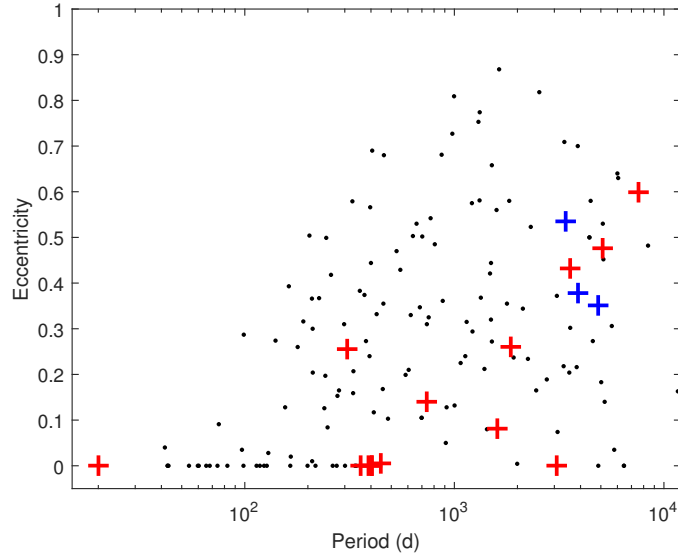
Figure 7.7: Period - eccentricity distribution for CEMP-s (red) and CEMP-r/s (blue) binary systems in the sample, compared to literature data (black dots; Mermilliod et al. 2007; Mathieu et al. 1990).

7.3 Binary stars

18 binary systems was detected in our sample. The systems have periods range from 20 days to $\sim$30 years, and mostly circular orbits. Figure 7.7 shows the distribution of periods and eccentricities for the binary systems in our sample; red crossed are CEMP-s stars and blue are CEMP-r/s. As cut-of of $\sim$300 days is found for the systems. The three stars with Eu detection (HE 0039$-$2635, HE 1031$-$0020 and LP 625$-$44) have similar long period eccentric orbits. These stars are among the systems found with the longest periods, see Table 7.6.

7.4 Mass transfer in binary systems

To form a CEMP-s star, mass transfer needs to have occurred in the binary system, from the AGB star and onto the low mass star we observe today as a CEMP-s star. Mass can be transferred from one star to the other in a binary system in three more or less efficient ways; Roche-lobe over flow (RLOF), wind transfer or wind Roche-lobe over flow (WRLOF).

Roche-lobe overflow happens when one of the stars in a binary system expands beyond its Roche-lobe radii (ex. during the AGB phase), mass can then be transferred to the companion via the inner Lagrange point (L1). This is the most efficient way to transfer mass in a binary system, but for the RLOF to be most efficient, the separation of the two stars in the system has to be relatively small. If the stars are to far apart none of them will ever fill their Roche-lobes, on the other hand if the stars are two close they will enter a common envelope evolution where mass transfer is also inefficient. If a binary system

undergo RLOF this will have a strong effect on circularizing the orbit and even more so if they enter a common envelope phase. In Tables 7.3, 7.4, 7.5, 7.6, and 7.7 we list the Roche-lobe radii of the secondary of mass of 0.4 and 1.4 $M_\odot$ for our binary systems.

Another method for mass transfer in a binary system is wind transfer. Here the low mass star moves through the wind of the AGB star and thereby accrete mass Bondi & Hoyle (1944). This type of mass transfer works when the wind velocity is much higher than the orbital velocity of the accreting star. That is not always the case for wide binary systems, if $P \sim 10^4$ days the orbital velocity is $\sim$10 km s^{-1} and the wind from AGB stars can have velocities of 5-30 km s^{-1} (Abate et al. 2013)

Boffin & Jorissen (1988) explored the possibility of creating Ba stars (higher metalicity equivalent of CEMP-*s* stars) via wind transfer in a detached binary system, using the Bondi-Hoyle wind accretion scenario. They find that the Ba stars could have been formed this way. This type of mass transfer allows for the orbits to stay long and do not circularize the orbits as would happen with Roche-lobe overflow.

A third option is the wind Roche-lobe mass transfer, which can happen in systems where the wind of the donor star is gravitationally confined to the Roche-lobe of the star. The wind can then be focused towards the orbital plane of the binary system and transferred to the secondary via L1, this type of transfer can be 100 time more efficient than normal wind transfer (Mohamed & Podsiadlowski 2007). The pulsations of the AGB star push the matter outwards til it reach temperatures where dust can form, typically at a few stellar radii, the radiation pressure then accelerates the dust to escape velocities. For the WRLOF to be efficient, the region where the wind is accelerated beyond the escaping point (wind acceleration radii), needs to be larger than the Roche-lobe of the star or a significant fraction (Mohamed & Podsiadlowski 2007). The WRLOF mechanism facilitates mass transfer in binary systems that are to wide for mass transfer via traditional RLOF. The majority of the material which is not accreted by the secondary is lost via the outer Lagrange points (L2 and L3) and thus carry away angular momentum from the system, shrinking the orbits (Abate et al. 2013).

7.4.1 Known CEMP-*s* binary systems

A number of CEMP-*s* stars not included in our sample have been found to be part of binary systems and have determined orbital parameters. Abate et al. (2015) modeled the mass transfer of 15 CEMP-*s* binary systems with known periods and abundance patterns. The majority of these systems are best reproduced with an enhanced Bondi-Hoyle-Lyttleton wind accretion efficiency; a model the authors doubt is realistic, but it emphasizes the need for very efficient mass transfer to create the abundance patterns observed in the CEMP-*s* stars. Their model with WRLOF and spherically symmetric wind, widen the orbits as the mass is transferred, i.e., small initial periods are found and consequently small secondary masses as these would otherwise over flow their Roche-lobes. Some of the stars in the sample of Abate et al. (2015) have also evolved past the main sequence and hence need even more mass transferred to account for the dilution happening in the first dredge up episode. In some of the systems also a common envelope phase is needed to shrink the orbits to the current size. Especially for binary system found by Lucatello et al. (2003) with a period of 3.33 days. The binary system they try to model have periods ranging between 3.33 and
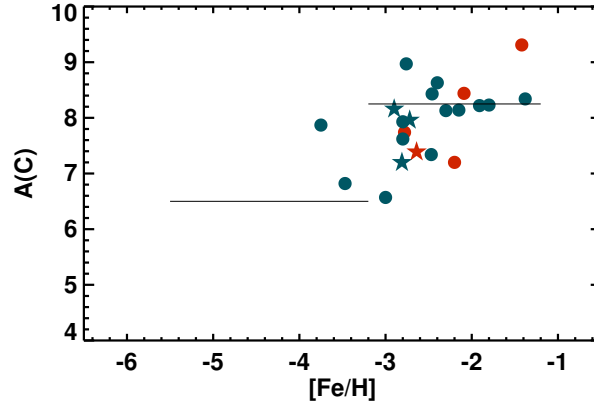
Figure 7.8: Absolute C abundances for the sample stars, dots represent CEMP-*s* stars and stars CEMP-*r/s* stars, red are single stars and blue are binaries. The two C-bands of Spite et al. (2013) are indicated by horizontal lines.

4280 days, and they find initial periods of 1170 to 130000 days for these systems. They conclude it is generally necessary for the systems to efficiently lose angular momentum and transfer mass with high accretion efficiency.

Another uncertainty of this formation scenario for the CEMP-*s* stars, when modeling the mass transfer in these system to match the abundance pattern in the CEMP-*s* star, is the degree to which the transferred material is diluted when reaching the CEMP-*s* stars via thermohaline mixing, which is very poorly constrained (Stancliffe et al. 2007; Stancliffe & Glebbeek 2008). This dilution is independent of any dredge up episodes happening during the evolution of the low-mass CEMP-*s* stars.

7.5   Single stars

Our sample includes four stars which exhibit no variation in their radial-velocities over the period of monitoring, HE 0206−1916, HE 1045+0226, HE 2330−0555 and CS 30301−015. The latter being one of the stars with detected Eu. It is very unlikely that the binary mass transfer scenario is the explanation for the excess of C and *s*-process elements seen in these stars. Hence a different formation channel have to be invoked. To explore this, we have plotted the abundance information in-common for all of the stars, namely the C, Fe and Ba abundances. This is shown in Figure 7.8 and 7.9, as can be seen, the single stars show no different abundance signature for these elements, than the binary stars. More detailed abundances analysis of all the stars may reveal differences in the abundance patterns of the single stars compared to those found in binary systems, which can help constrain the formation scenario of these stars.
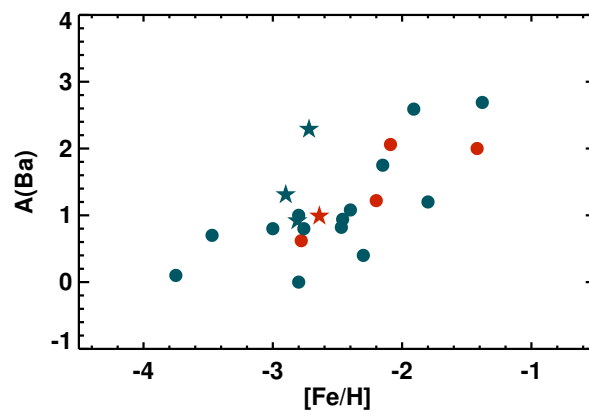
Figure 7.9: Absolute Ba abundances for the sample stars, dots represent CEMP-s stars and stars CEMP-r/s stars, red are single stars and blue are binaries.

CHAPTER 8

Discussion

Below I will summarize and discuss the abundance signatures and the binary nature found for the stars in the various samples, and what can be learned about the different progenitors that are currently suggested to account for the stars. However, one result which is consistently found in all abundance analyses of very metal-poor stars, both carbon-enhanced and non-carbon-enhanced (see Cayrel et al. 2004; Yong et al. 2013), and which is confirmed in the work presented here, is the small over-abundance detected for the α-elements ($< [\mathrm{Ca, Ti/Fe}] > \sim +0.35$) and the very low star-to-star scatter for both the α-elements (~ 0.15 dex), and the iron-peak elements (~ 0.20 dex).

8.1   CEMP-no stars

A lot of this work has been focused on the CEMP-no stars to try and constrain the progenitors of these stars via their abundances pattern and binary properties. The discussions below is divided into different element groups detected in the CEMP-no stars, and the question of the binary nature for these stars.

8.1.1   Lithium

The lithium abundances in carbon-enhanced stars are a relatively unexplored chapter in the history of Galactic chemical evolution. Theoretical efforts include Stancliffe (2009a). Lithium is detected for only a few CEMP stars, and even fewer of these are CEMP-no stars, though the samples of CEMP-no stars are increasing quickly, in particular, from dedicated searches for CEMP stars (e.g., Placco et al. 2010, 2011, 2013, 2014a).

Li is detected for three of the six CEMP-no stars in this sample, and the derived Li abundances for these indicate a Li depletion in the stars relative to the Spite Li plateau. These detections highlight the need for progenitors of CEMP-no stars that produce large amounts of carbon, but only small amounts of neutron-capture elements, while to some extent depleting the lithium.

The possible progenitors of the CEMP-no stars listed in section 1.3.2 will result in different Li abundances, measured for the stars. If CEMP-no stars are the result of mass transfer from an AGB companion, then the Li abundances in CEMP-no stars will reflect a combination of (1) Galactic chemical evolution and (2) Li production/destruction in the AGB companion. Masseron et al. (2012) test how mass transfer from an AGB companion will affect the Li abundance of CEMP stars. They examined a set of different AGB models and different depletion factors for the transferred material, but found that none of the models could explain the observed spread in Li abundances of the CEMP-no stars of their sample. It should be mentioned, however, that the amount of the Li that is depleted after a possible mass transfer via mixing and rotation of the CEMP star itself is very uncertain (Talon & Charbonnel 2005; Stancliffe et al. 2007).

If on the other hand massive stars are the progenitors, the Li abundances of CEMP-no stars should lie below the level found in non-carbon-enhanced stars, as Li should be depleted (or totally destroyed) in such objects. Hence, when the gas from these mixes with the ISM in their surroundings (and forms the CEMP-no stars), the overall Li abundance will be lowered (Meynet et al. 2010). In fact, as suggested by Piau et al. (2006), this process might be responsible for the lowering of the primordial Li abundance from the level predicted from Big Bang Nucleosynthesis calculations, the lack of scatter among stars on the plateau at metallicities $-2.5 < $ [Fe/H] $ < -1.5$, due to complete mixing (e.g., Ryan et al. 1999), the downturn and increase of scatter in the Li abundances for stars with [Fe/H] $ < -2.5$, due to incomplete local mixing (Sbordone et al. 2010), and the very low (or absent) Li among the lowest metallicity stars (e.g., Frebel et al. 2005; Keller et al. 2014).

In this view, the fact that Li abundances for CEMP-no stars are always *below* the level of the Spite Li plateau (see e.g., Masseron et al. 2012) can be understood as the result of various degrees of local mixing between Li-astrated material ejected from first-generation stars and the surrounding gas having the primordial level of Li.

8.1.2 Carbon and nitrogen

The carbon enhancement, detected for three of the four UMP stars described in chapter 3, is consistent with the picture of carbon enhancement in the early universe found by other authors (e.g., Carollo et al. 2012; Norris et al. 2013b). An enrichment of carbon in the early universe also supports one of the proposed formation scenarios for low-mass stars, that gas clouds can fragment as a result of cooling via fine-structure lines of carbon and oxygen (Frebel et al. 2007b).

The data presented here also supports the claim of Spite et al. (2013) and Bonifacio et al. (2015) for the presence of two carbon "bands" that comprise the distribution of the absolute carbon abundances for CEMP stars, although with a smoother transition between the bands than was found by these authors. The majority of the CEMP-no stars have carbon abundances falling on the lower band ($A(C) \sim 6.5$), but a few with metalicities above [Fe/H] > -3.0 have carbon abundances in the higher band ($A(C) \sim 8.5$), indicating a different origin for the carbon found in these three stars as opposed to those with carbon abundances in the lower band.

The different progenitors suggested for CEMP-no stars all involve some degree of mixing and processing, which can be seen in the C and N abundances of the un-evolved CEMP-no

stars (see section 1.4.2).

In the spinstar scenario, a star that exhibits [C/N] > 0 is the result of incomplete hydrogen burning via the CNO cycle, followed by mild mixing, whereas a star with [C/N] < 0 is the sign of more complete hydrogen burning (Maeder et al. 2015a). Other abundance signatures detected in some CEMP-no stars, such as low $^{12}C/^{13}C$ isotopic ratios, which is found in all the CEMP-no stars presented here where this ratio could be measured, can also be explained, according to Maeder et al. (2015a), as the result of more mixing and processing of material in the spinstar. Also the high Na, Mg and Al abundances, as detected in two of the CEMP-no stars with [C/N] < 0, can also be explained, this way. In fact Maeder & Meynet (2015b) has suggested a classification system for CEMP-no stars based on the mixing and processing that has happened in the spinstar to produce the element pattern seen in the CEMP-no star. However signatures such as low $^{12}C/^{13}C$ isotope ratios are also predicted from the the mixing and fallback models. So far, no values for expected $^{12}C/^{13}C$ ratios has been published for the SNe models, making a comparison difficult.

In the combined sample of 30 CEMP-no stars, stars with [C/N] > 0 as well as stars with [C/N] < 0 are found, but the latter are only found at extremely low metallicity, [Fe/H] < −3.4. The CEMP-no stars with large enhancements in Na, Mg and Al are also only found below this metallicity; above this metallicity the abundance spread is smaller. This indicates that the large degrees of internal mixing and processing required to produce the abundance pattern seen in stars such as HE 1327−2326 (Frebel et al. 2006) and HE 2323−0256 (Yong et al. 2013) was only operating at the very earliest times.

8.1.3 Neutron-capture elements

The origin of neutron-capture elements in low-metallicity stars is not yet well-understood. A large spread is seen in the abundances of the neutron-capture elements Sr and Ba for CEMP-no stars (indistinguishable from that of non-carbon-rich metal-poor stars).

Figure 8.1 shows the derived [Sr/Ba] ratios of the three UMP, CEMP-no stars in my sample (described in detail in Chapter 3), together with the ratios for stars from the Yong et al. (2013) sample that have detections of both Sr and Ba. The dashed red line indicates [Sr/Ba] = −0.4, used as an upper limit for the main s-process signature of AGB stars. It should be noted that large spread is seen in the efficiency of the main s-process element production of the AGB stars (Bisterzo et al. 2011). However, low [Sr/Ba] ratios are observed for s-process elements produced in AGB stars. The value of [Sr/Ba] < −0.4 is taken from Spite et al. (2013), while [Sr/Ba] = −0.5 was used by Aoki et al. (2013b). At Solar metallicity, Sr is a tracer of the weak s-process, in massive stars (Heil et al. 2009; Pignatari et al. 2010), while Ba is a tracer of the main s-process taking place in AGB stars (Busso et al. 1999; Käppeler et al. 2011). At low metallicity, where the main s-process was not yet active, the picture is different.

To assess the origin of the Sr and Ba detected in these three CEMP-no stars, the [Sr/Ba] ratio can be compared to that for classical main s-process-enhanced metal-poor stars, and in strongly r-process-enhanced metal-poor stars. Lucatello et al. (2003) reported on the abundances analysis of HE 0024−2523, a classical main s-process-enhanced star with carbon enhancement. This star was also found to be in a binary system, and the authors argued that the carbon and s-process-element enhancement is the result of mass transfer from an AGB
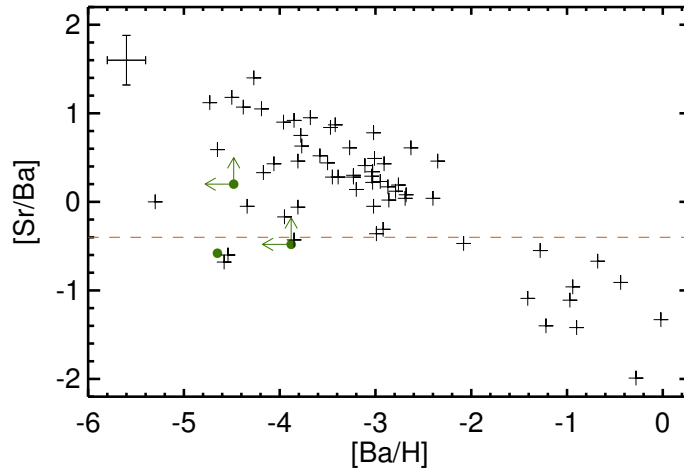
Figure 8.1: [Sr/Ba] ratios plotted against Ba abundances, [Ba/H], for our three CEMP-no stars (green circles) and the sample of Yong et al. (2013) (black crosses). Arrows indicate upper limits; the dashed red line indicates [Sr/Ba] = −0.4. Ratios above this line indicate production of Sr and Ba by the weak *s* process in massive stars or by the *r* process, while those below indicate production by the main *s* process in AGB stars.

companion. The [Sr/Ba] ratio in this star is [Sr/Ba] = −1.12, a very low value, due to its high Ba abundance. For the three CEMP-no stars, the following [Sr/Ba] ratios was found: [Sr/Ba] > +0.20 (HE 0134−1519), [Sr/Ba] > −0.48 (HE 0233−0343), and [Sr/Ba] = −0.58 (HE 1310−0536). The ratios found in HE 0233−0343 and HE 1310−0536 could indicate production by the main *s* process. However, these stars are CEMP-no stars, i.e., their individual abundance ratios of Ba relative to iron are low ([Ba/Fe] < 0), and they are also UMP stars ([Fe/H] < −4.0). At such low metallicity, Ba is more likely produced in the main *r*-process from SNe, and Sr in the weak *s*-process in massive stars. The following [Sr/Ba] ratios have been found in strongly *r*-process-enhanced metal-poor stars: [Sr/Ba] = −0.52 in CS 31082-001 (Hill et al. 2002); [Sr/Ba] = −0.41 for CS 22892−052 (Sneden et al. 2003); and [Sr/Ba] = −0.46 for CS 29497−004 (Christlieb et al. 2004b). These ratios are very similar to those found in HE 0233−0343 and HE 1310−0536. The ratio found in HE 0134−1519 indicates that the Sr and Ba in this star could have been produced in the weak *s*-process in spinstars.

Cescutti et al. (2013) proposed that the spread in Sr and Ba abundances detected in CEMP-no stars could be explained by spinstar progenitors. Their model includes a standard *r*-process (presumably in the natal clouds), plus a contribution from the weak *s*-process occurring in spinstars. With this combination, they can model the spread seen in the abundances of Sr and Ba in metal-poor stars, including the CEMP-no stars, while also reproducing the low scatter in α-elements. They do, however, state that their models cannot reproduce the [C/O] and [N/O] ratios in the same CEMP-no stars, but point to the scenario of Meynet et al. (2010), where low-mass stars belonging to the forming stellar

cluster of a spinstar are enriched in carbon via stellar winds from the spinstar.

The abundance data, analysed in this thesis, show a "floor" in the absolute Ba abundances of CEMP-no stars, at an abundance level $A(\text{Ba}) \sim -2$; see Figure 4.13 and 4.14, on page 71 and 72 respectively. This plateau only exists for the CEMP-no stars, and must be an unique signature for the progenitors of these stars. Both the spinstar and the mixing and fallback models can produce some amount of neutron-capture elements (see introduction). For the mixing and fallback models however no yields have yet been published. Also the spinstars require Fe seeds, hence some prior SNe pollution is needed for these to produce neutron-capture elements.

Roederer (2013) asked the question if *any* stars, no matter at what low metallicity, completely lack neutron-capture elements. The CEMP-no stars are thought to be among the first low-mass stars to have formed, and although not in all of these, neutron-capture elements have been detected, the discovery of a floor for the absolute Ba abundance of CEMP-no stars at extremely low metallicity supports the interpretation that some mechanism producing neutron-capture elements was present very early in the Galaxy.

8.1.4 Binarity

From the radial-velocity sample of CEMP-no stars, a binary frequency of 17%±5% (4 out of 24) is derived, which is similar to that found for the r-process-enhanced stars in Chapter 3 (18%±6%), and to the 16% ±4% binary frequency found by Carney et al. (2003) in their study of 91 metal-poor ([Fe/H] ≤ -1.4) field red giants.

Figure 8.2 shows the absolute carbon abundances of the stars in the sample as a function of metalicity; blue dots represent the detected binary stars and red dots represent the single stars. As can be seen from inspection of this figure, three of the CEMP-no stars (HE 0219−1739, HE 1133−0555, and HE 1410+0213) have carbon abundances corresponding to the high-C band. HE 0219−1739 is a binary with ample space to accommodate a companion at the AGB stage in its Roche-lobe for the assumed minimum and maximum masses (0.4 M$_\odot$ and 1.4 M$_\odot$) of the white dwarf remnant (see Table 6.3 on page 96). HE 1410+0213 and HE 1133−0555 are both most likely single, but HE 1410+0213 is pulsating (see section 6.2.2), which could enhance any mass loss by a strong stellar wind.

Two of the more metal-poor binary stars have carbon abundances that lie in the transition area between the two bands around [Fe/H] ~ -3.0, where both CEMP-no and CEMP-s stars can be found. These two stars are HE 1150−0428 and CS 22957−027, the former having a circular orbit with a period of P = 290 days, and the latter having a slightly eccentric orbit with a period of P = 1080 days (see Figure 6.2 on page 6.2). Only one of the stars with an absolute carbon abundance clearly on the low band is found to be in a binary system, HE 1506−0113, having an eccentric orbit with a period of P = 841 days (see Figure 6.2 on page6.2). This star also exhibits high abundance ratios of Na and Mg ([Na/Fe] = +1.65 and [Mg/Fe] = +0.89; Yong et al. 2013), signatures that are also found for many other CEMP-no stars (Norris et al. 2013b). It is worth noting that HE 1150−0428 also exhibits a high Na abundance [Na/Fe] = +1.31, but normal Mg abundance [Mg/Fe] = +0.36 (Cohen et al. 2013). For CS 22957−027, Cohen et al. (2013) report a high Na abundance ratio ([Na/Fe] = +0.80), but a low Mg ratio ([Mg/Fe] = +0.11), while Aoki et al. (2002c) report a higher Mg ratio ([Mg/Fe] = +0.69).
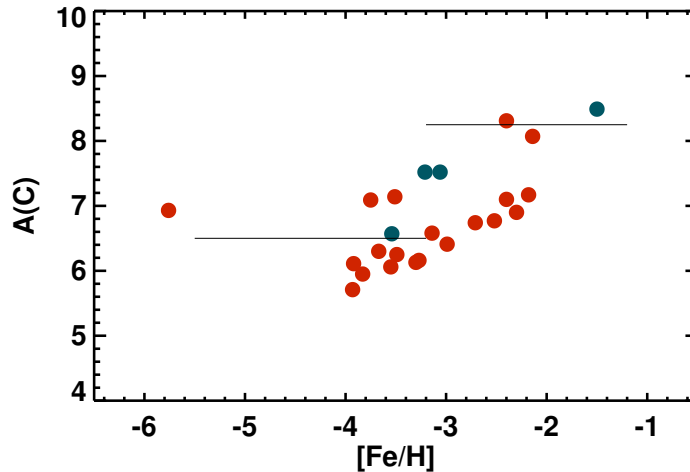
Figure 8.2: Absolute carbon abundances of the programme stars, as a function of metallicity. Blue dots represent recognized binaries in the sample; red dots represent non-binaries. The high-C and low-C bands of Spite et al. (2013) are indicated by the horizontal lines.

It is clearly highly desirable to obtain further information on the possible binary nature of the other six CEMP-no stars with carbon abundances found on the high-C band, based on this and previous work (Bonifacio et al. 2015), and expand the sample of such stars. Should the majority turn out to be members of binary systems (rather unlikely in view of the present results), and in particular if there are signs that mass transfer has occurred, this would lend support to the existence of AGB stars that produce very little if any s-process elements, opening the possibility that a new nucleosynthesis process might need to be invoked, or that our understanding of the operation of the s-process at low metallicity is incomplete. If these stars are also found to be single, another distant production site must be invoked.

8.1.5 Progenitors

The results of the radial velocity monitoring of CEMP-no stars exclude the binary mass transfer formation scenario for the vast majority of these stars. The two remaining suggested progenitors are the massive, fast-rotating stars (Meynet et al. 2006; Hirschi 2007; Maeder et al. 2015a) and the proposed mixing and fallback supernovae (Umeda & Nomoto 2003; Nomoto et al. 2013), or possibly contributions from both. Both models explain well the observed large over-abundances of carbon and nitrogen found in CEMP-no stars.

Tominaga et al. (2014) have used "profile fitting" to show that the yields from mixing and fallback SNe well-fit the observed abundance patterns of CEMP-no stars. With a range of explosion energies and mass cuts, and by including mixing in some of the models, the authors fit the abundance profiles of 12 CEMP-no stars. Tominaga et al. (2014) also point out that the mixing and fallback SN model fits all the observed elements up to atomic number $\mathcal{Z} = 30$, including the α-elements and the iron-peak elements, while the spinstar

models require a complementary SN contribution to create these elements in the appropriate proportion. However, as seen above, recent result of Maeder et al. (2015a) show that spinstar yields also well explain the abundances found in CEMP-no stars.

Norris et al. (2013b) suggested that, in order to distinguish between spinstars and the mixing and fallback SNe for CEMP-no stars, one needs to investigate the abundances in these stars for elements that are produced in the deeper layers of the progenitor stars, such as Si and Ca. For this sample, the Ca abundances follow the general α-element trends of VMP halo stars, and only a few of the stars have detections of Si. More predicted elemental yields, over the full range of elements – both light and heavy, along with predicted ^{12}C/^{13}C ratios for both sets of progenitor models, and additional CEMP-no stars with measured Si abundances, are required to resolve this issue.

8.1.6 Second generation stars

The fact that CEMP-no stars do not require mass transfer from a binary companion to account for their distinctive elemental-abundance patterns, is strong evidence that they may indeed be bona-fide second-generation stars, formed from an ISM polluted by a previous (possibly first-generation) population of stars. However, this is not the only evidence for this association. Below a brief summary is given of observational signatures that point to these stars being real second generation stars.

- **The increased frequency of CEMP stars at low metallicity**: It has been recognized for over a decade that the relative numbers of CEMP stars (compared to C-normal stars) increases dramatically as [Fe/H] declines from [Fe/H] = −2.0 to the most Fe-poor star known (SMSS J0313-6708, with [Fe/H] $\lesssim$ −7.8; Keller et al. 2014; Bessell et al. 2015). Recent large samples of VMP and EMP stars from SDSS/SEGUE, e.g., Lee et al. (2013), have reinforced this result based on the thousands of CEMP stars found in this survey. It has also been shown that, at the lowest metalicities, the CEMP-no stars are the dominant sub-class of CEMP stars (Aoki et al. 2007; Norris et al. 2013b). Indeed, when limited to the sample of recognized or likely CEMP-no stars, the derived frequencies increase by 5-10% relative to CEMP stars when considered as a single class (Placco et al. 2014c).

- **The dominance of CEMP-no stars at the lowest metallicity**: Seven of the eight stars known with [Fe/H] < −4.5: SMSS J0313−6708 ([Fe/H] $\leq$ −7.8, Keller et al. 2014; Bessell et al. 2015); HE 1327−2326 ([Fe/H] = −5.7, Frebel et al. 2006; Aoki et al. 2006), HE 0107−5240 ([Fe/H] = −5.4, Christlieb et al. 2004a), SDSS J1313−0019 ([Fe/H] = −5.0, Allende Prieto et al. 2015; Frebel et al. 2015), HE 0557−4840 ([Fe/H] = −4.8, Norris et al. 2007), SDSS J1742+2531 ([Fe/H] = −4.8, Bonifacio et al. 2015), SDSS J1029+1729 ([Fe/H] = −4.7, Caffau et al. 2011), HE 0233−0343 ([Fe/H] = −4.7, Hansen et al. 2014) are CEMP-no stars. The star SDSS J035+0641 may be added to this list in the near future (Bonifacio et al. 2015 report [Ca/H] = −5.0). The lone exception is SDSS J1029+1729, for which Caffau et al. (2011) report [C/Fe] $\leq$ +0.9, but higher SNR data is required in order to be certain of its status.

- **The bimodal distribution of $A(C)$ for CEMP stars**: As discussed above, the recent recognition that the absolute carbon abundance of CEMP stars is apparently bimodal clearly indicates that a source of carbon production other than that associated with AGB stars is required in the early Universe.

- **The Li abundances of CEMP-no stars**: As discussed by Hansen et al. (2014) and references therein, the observed abundances of lithium for CEMP-no stars are *all* below the Spite Li plateau. While many of these stars may have had their Li depleted due to internal mixing during giant-branch evolution, this does not apply to all cases (HE 1327−2326, for example, is a warm sub-giant with very low Li; several other such stars are listed in Masseron et al. 2012). This provides support for the suggestion by Piau et al. (2006) that Li astration by the progenitors associated with the production of carbon in the CEMP-no stars, followed by mixing with primordial gas, may well be involved.

- **The observed Be and B abundance limits for BD+44°493**: The elements Be and B are thought to form in the early Universe exclusively by spallation reactions involving high-energy cosmic rays (Prantzos 2012), which implies that the abundances of these elements in CEMP-no stars should be uniformly low if they are indeed second-generation stars (due to the lack of a significant background cosmic-ray flux at these early times). Placco et al. (2014b) indeed reported very low upper limits for the abundances of Be and B in BD+44°493 ($\log \epsilon$ (Be) < -2.3 and $\log \epsilon$ (B) < -0.7). A low upper limit for Be ($\log \epsilon$ (Be) < -1.8) was also previously found by Ito et al. (2013) for this star. Although future such observations (from the ground for Be, from space for B) are required for additional CEMP-no stars, the results for BD+44°493 are already compelling.

- **The association of CEMP-no stars with the outer-halo population of the Galaxy**: Carollo et al. (2012) confirmed the early suggestion by Frebel et al. (2006; see also Beers et al., in prep.) that the fraction of CEMP stars increases with distance from the Galactic plane. The Carollo et al. study also showed a significant contrast in the frequency of CEMP stars between the inner- and outer-halo components of the Milky Way, with the outer halo having roughly twice the fraction of CEMP stars as the inner halo. They interpreted this as an indication that the progenitor population(s) of the outer halo likely had additional astrophysical sources of carbon production, beyond the AGB sources that may dominate for inner-halo stars. Subsequently, Carollo et al. (2014) offered evidence that the CEMP-*s* stars are preferentially associated with the inner-halo population, while the CEMP-no stars appear more strongly associated with the outer-halo population. This result suggests that the dominant progenitors of CEMP stars in the two halo components were different; massive stars for the outer halo, and intermediate-mass stars in the case of the inner halo.

- **The discovery of damped Ly-alpha systems with enhanced carbon**: Cooke et al. (2011, 2012) have reported on recently discovered high-redshift carbon-enhanced damped Ly-alpha systems that exhibit elemental-abundance patterns which resemble those from that expected from massive, carbon-producing first stars, and speculated that these progenitors are the same as those responsible for the abundance patterns associated with CEMP-no stars in the Galaxy. To our knowledge, this is one of the first cases, if not *the* first, of evidence for a direct linkage between the observed abundances in cosmologically distant objects with local extremely metal-poor stars. It also underscores our main conclusion that the excess carbon was not provided by a binary companion, but was produced elsewhere and transported interstellar distances through the early ISM.

8.2 CEMP-s stars

The largest sub-class of CEMP stars are the CEMP-s. Five new CEMP-s stars have been discovered in this work. The origin of the CEMP-s stars has for some time been ascribed to mass transfer in a binary system from a now extinct AGB star (Ryan et al. 2005; Lucatello et al. 2005). However, there are still abundance signatures found in CEMP-s stars which the AGB models have difficulties in explaining. Also CEMP-s stars exists for which no variation in their radial-velocities are detected (Lucatello et al. 2005)

8.2.1 Abundances

For the 32 CEMP-s stars in the combined sample, I find that the great majority exhibit larger C-enhancements than N-enhancements, i.e., [C/N] > 0. However, a few CEMP-s stars with [C/N] < 0 are found, suggesting that a higher degree of H-burning via the CNO cycle has occurred in the AGB companion in these cases. I also find higher ^{12}C/^{13}C isotopic ratios for the CEMP-s stars in this sample than found for the CEMP-no stars. However, the observed ratios are sufficiently low to require extensive mixing, which is also expected in an AGB star. Nevertheless, the observed ^{12}C/^{13}C ratios for CEMP-s stars are not reproduced by the AGB models (Bisterzo et al. 2012).

The CEMP-s stars in the sample have carbon abundances that place them on the higher of the two carbon bands of Spite et al. (2013), shown in Figure 4.10 on page 67. Thus, there appears to be a maximum carbon abundance attained for the CEMP-s stars, which provides a constraint on the efficiency of the mass transfer and/or the production of C in AGB stars at very low metallicity.

Figure 4.15 on page 4.15 showed derived abundance patterns for four of the newly discovered CEMP-s stars along with AGB stellar yields from the F.R.U.I.T.Y database (Cristallo et al. 2011, 2009). None of the models was able to fit both the light (C and N) and heavy (neutron-capture) elements. Bisterzo et al. (2012) fitted the abundance patterns of a large number of individual CEMP-s and CEMP-r/s stars with the yields from AGB star models. The outcome of this exercise showed that the models have problems reproducing the C and N abundances and the ^{12}C/^{13}C ratios detected in the CEMP stars. Carbon is generally over produced in their models. This combined with detections of low ^{12}C/^{13}C ratios points to a large degree of mixing not included in their models. Also the s-process

problems pose a problem. The AGB models of Bisterzo et al. (2012) predict roughly (within 0.3 dex) similar abundances of the first (Sr, Y, Zr) and second (Ba, La, Ce, Pr and Nd) peak elements, while spectroscopic data for CEMP-*s* stars show an internal spread in these elements of more the 0.5 dex; Ba is often found to be more enhanced than the other second peak elements.

8.2.2 Binarity

15 binary systems were confidently detected among the the 18 CEMP-*s* stars monitored for radial-velocity variations. Confirming the connection between the binary nature of these stars and their excess of carbon and *s*-process elements. The calculation of Roche-lobe radii for the stars also show, that for the majority of the systems there is room for an AGB companion with-in the Roche-lobe. However, as discussed in section 7.4.1 the modeling of mass transfer in these systems still face problems, when having to account for the short periods of some of these systems and the abundance patterns detected in the CEMP-*s* stars.

Three of the CEMP-*s* stars exhibited no variation in their radial velocity over period of monitoring. Thus these three stars may not be the result of mass transfer from an AGB companion. Figure 7.8 and 7.9 on page 111 and 112 explore the C, Fe, and Ba abundances in the three presumably single stars. This reveal no specific signature for these stars compared to the binary stars for these elements.

8.3 CEMP-*r* stars

The first CEMP-*r* star to be found was CS 22892-052 (McWilliam et al. 1995; Sneden et al. 2003). This star is both classified as an *r*-II star[1], and a CEMP-*r* star. It has an abundance pattern for the heavy *r*-process elements that well-fits the scaled Solar system *r*-process abundance pattern. Two new CEMP-*r* stars have been detected in this work, almost doubling the number of known CEMP-*r* stars.

8.3.1 Abundances

Three CEMP-*r* stars was known prior to this work (Roederer et al. 2014c). These three stars were all detected from their enhanced *r*-process element signature and then later turned out to also be C-rich. The two CEMP-*r* detected in this sample were first identified as CEMP stars and then classified as CEMP-*r* based on their Ba and Eu abundances. Hence it still remains to be tested if the two stars, added to the CEMP-*r* stars sample in this work, also show the classical scaled Solar system *r*-process abundances pattern, which is seen in other *r*-process enhanced stars.

The general abundance patterns, for the α and iron-peak elements, detected in the two CEMP-*r* stars in this sample follow those of the other CEMP end EMP stars. However, the C abundances of the stars places one on the high, and one on the low carbon-abundance band respectively (see Figure 4.10 on page 67, blue points). Also the $^{12}C/^{13}C$ isotopic ratios found in these stars match both what is found for the CEMP-*s* stars and for the CEMP-no stars.

---

[1] $[Eu/Fe] > +1.0$ and $[Ba/Eu] < 0.0$ (Beers & Christlieb 2005)

One of the CEMP-r stars may be classified as a NEMP star (see section 1.3.3), however the confirmation of its binary-pollution origin awaits future radial-velocity monitoring.

8.3.2 Binarity

It is not known with certainty what astrophysical site produces the carbon over-abundances for CEMP-r stars. Radial-velocity monitoring of CS 22892-052 shows that this star is unlikely to be in a binary system (see Figure 5.1 on page 84), suggesting that the carbon enhancements seen for CEMP-r stars are not the result of mass transfer in a binary system. More likely (as in the case of the CEMP-no stars), the CEMP-r stars were born from an ISM that was previously polluted with carbon. Future radial velocity monitoring of larger samples of these stars is needed to determine if the binary frequency among these stars resemble that of the CEMP-no stars.

8.4 CEMP-r/s stars

This work has also identified two new stars of the CEMP-r/s sub-class, which exhibit contributions from both the r- and s-process. It has been proposed that the CEMP-r/s stars were born with their r-process-element abundances, and then gained their carbon and s-process-element abundances via mass transfer in a binary system (Qian & Wasserburg 2003). More recently, it has also been suggested by (Bertolli et al. 2013) that these stars could be the result of the i-process, a neutron-capture process that is intermediate between the r- and the s-process, and thought to occur in high-mass "super-AGB" stars.

8.4.1 Abundances

The general abundance patterns, for the α and iron-peak elements, detected in the two CEMP-r/s stars in this sample, follow those of the other CEMP and EMP stars. As was also the case for the two CEMP-r stars, one CEMP-r/s star is found on each of the two carbon-abundance bands (see Figure 4.10 on page 67, yellow points). Additionally the $^{12}C/^{13}C$ isotopic ratios found in these stars also match both what is found for the CEMP-s stars and for the CEMP-no stars.

Masseron et al. (2010) found the ratio of Pb to heavy s-process elements ([Pb/hs]) in CEMP-r/s stars correlate with the N abundances. This is a signature of a convective driven s-process in thermal pulses in AGB stars, with $^{22}Ne(\alpha,n)^{25}Mg$ as the neutron source (Goriely & Siess 2005). During a pulse, the ^{14}N is burned to ^{22}Ne, giving way to the neutron flux. This gives a very high neutron density, which results in an r/s signature of the elements produced. Based on Ba and Eu abundances for the stars, it was also argued by Lugaro et al. (2012) that the abundances patterns found for CEMP-s and CEMP-r/s stars can not come form the same AGB star source.

Finally, one of the CEMP-r/s stars may be classified as a NEMP star (see section 1.3.3), however as was the case for the CEMP-r star, the confirmation of the binary-pollution origin awaits future radial-velocity monitoring.

8.4.2 Binarity

Four CEMP-r/s stars were included in the radial-velocity monitoring program. Three of these exhibited significant variations in their radial velocities over the period of monitoring. All three have long period (>3000 days) with ample space inside their Roche-lobes for an AGB companion, both for a minimum (0.4 $M_\odot$) and maximum (1.4 $M_\odot$) white dwarf mass (see Figure 7.6 and Table 7.7 on page 108). Barbuy et al. (2005) analysed two CEMP-r/s stars CS 22948−027 ([Ba/Eu] = 0.38) and HE 0039−2635 ([Ba/Eu] = 0.23). The latter was also included in our binary program. Both of these stars turn out to be in binary systems. This result in a total of five CEMP-r/s stars found to be in binary systems. This result could suggest a binary formation scenario for these stars. However, it must be emphasized this result is based on very small numbers. Future radial velocity monitoring of larger samples of these stars will reveal if the binary frequency for these stars is similar to what is found for the CEMP-s stars.

8.5 r-process enhanced stars

8.5.1 Binary frequency

The result of the radial velocity monitoring of the r-process enhanced stars is, that only 3 of the 17 programme stars are binaries, while 14 are confirmed to be single stars, yielding a binary frequency of $\sim 18\%$.

This sample is relatively small, since HERES stars south of the NOT limit could not be observed (only stars north of declination $\sim 25°$ can be observed with the NOT), but only two other r-process-enhanced stars, the r-II star HE 2327−5642 and the r-I star CS 22183−031, have been reported in the literature to show variable radial velocities. HE 2327−5642 was discovered by Mashonkina et al. (2010); their data cover a range of ~ 4.3 years, during which the radial velocity of the star varied by ~ 20 km s^{-1}. The other star, CS 22183−031, is included in the sample of Roederer et al. (2014c), who reported on the identification of nine new r-process-enhanced stars. The radial-velocity data for neither of these stars is sufficient to derive an orbital solution for the systems.

The bright r-I star HD 115444 (Westin et al. 2000) was not observed in this programme, but literature data confirms that it, with variations of no more than 1 km s^{-1} over a sparsely-sampled range of 24 years; see Table B.2, is very likely also a single star. This is also the case for its r-process-*poor* counterpart HD 122563, with variations of no more than 1.5 km s^{-1} over a sparsely-sampled range of 59 years; see Table B.2.

The binary frequency of 18% found here for the r-I and r-II stars is completely consistent with the 16±4% of binaries with periods up to 6,000 days found by Carney et al. (2003) in their survey of 91 metal-poor field giants, and the $\sim 22\%$ binaries with periods up to $\sim 15,000$ days found by Mermilliod et al. (2008) in their sample of $\sim 1,300$ Population I giants in Galactic open clusters. A binary frequency of 100% for this class of VMP and EMP stars is clearly ruled out, a conclusion that would only be reinforced if HE 1523−0901 would eventually be proved to be a single pulsating star rather, than a binary with a nearly face-on orbit.

Overall, it can thus be concluded that the observed dramatic excess of r-process elements

in this sample of stars is not just a surface effect produced locally by a binary companion, but rather was produced by a remote source and imprinted on the parent clouds across interstellar distances. It also seems hard to imagine how the local binary scenario could produce stars like HD 122653, with a *deficit* of *r*-process elements relative to the standard abundance pattern.

8.5.2   The origin of *r*-I and *r*-II stars

The separation of *r*-process-enhanced stars into the *r*-I and *r*-II classes was originally a matter of convenience, since the heavy-element abundance patterns of the most enhanced stars could be more easily observed due to their relatively stronger lines at low metallicity. As the sample of such stars has grown, it has become clear that these classes also exhibit rather different behavior with metallicity; the *r*-II stars are found in a relatively narrow range of metallicity near [Fe/H] ~ -3.0, while the *r*-I stars cover a larger range of metallicity, $-3.5 <$ [Fe/H] < -1.5 (Beers 2013). It remains unclear whether this constraint implies that different classes of astrophysical progenitors might be responsible for the *r*-I and *r*-II stars, or whether the initial *r*-process content in the natal clouds of the *r*-I stars has simply been diluted by the elemental mix of standard chemical evolution.

All of the programme stars are giants. However, it is important to note that Aoki et al. (2010) have shown that the star SDSS J2357$-$0052 is a cool ($T_{\rm eff}$ $\sim$5000 K) main-sequence dwarf with [Fe/H] $= -3.4$, and [Eu/Fe] $= +2.0$, making it simultaneously the lowest metallicity, and most Eu-enriched *r*-II star yet found. This star is of particular interest, as all previous *r*-process-enhanced stars identified to date have been in more evolved stages of evolution. Since dwarfs with the temperature of SDSS J2357$-$0052 do not have convective atmospheres, it can be reasonably concluded that the *r*-process-enhancement phenomenon is not due to some chemical peculiarity arising from the presence of a convective envelope in such stars. Unfortunately, although this star is sufficiently bright (V $\sim$15.6) for the programme described above, it was discovered too late to be included in our target list, but the results of radial-velocity monitoring over about a year by Aoki et al. did not reveal any evidence for significant variation.

The nine newly-recognized *r*-process-enhanced stars (based on high-resolution spectroscopic follow-up of HK survey stars) by Roederer et al. (2014c) include subgiants and the field equivalents of red horizontal-branch stars, reaffirming that *r*-process enhancement is not an evolutionary effect in the stars. Roederer et al. (2014c) also compare the abundance pattern of the light elements in their *r*-process-enhanced stars with that of *non r*-process-enhanced stars with similar stellar parameters. No evidence was found to indicate that the *r*-process-enhanced stars have different abundance patterns for the light elements than for the comparison sample, leading the authors to conclude that the event(s) producing the high levels of *r*-process material seen in these stars do not produce a distinct light-element abundance pattern. Neither does the large *r*-process enhancement seem to be coupled to the carbon and nitrogen abundances in the stars, although a few of the *r*-II stars are found to also be enhanced in carbon, the most well-known example being CS 22892$-$052 (Sneden et al. 2000).

Mashonkina et al. (2010) explored the Sr, Ba and Eu abundances for a number of *r*-I and *r*-II stars. They found very similar [Ba/Eu] abundance ratios for the two groups

([Ba/Eu] $\sim$ +0.60), but the mean [Sr/Eu] ratio differed by 0.36 dex between the two groups, with the r-II stars having the lowest ratio, [Sr/Eu] = -0.93. The authors argued that elements from the first and second r-process peak are of common origin in the r-II stars, whereas for the r-I stars the picture is less clear.

Competing scenarios for the origin of the r-I and r-II stars invoke non-spherical, jet-producing supernova explosions, or neutrino winds from merging neutron star binaries. Detailed observations of the abundance patterns predicted from the two competing scenarios may be the best guide to identifying the production site(s), but the frequency of these stars ($\sim$ 3% among VMP and EMP stars; Roederer et al. 2014c) provides another clue; any jets in such scenarios must be highly collimated in order to selectively enrich only a small fraction of molecular clouds in the early ISM.

One circumstance is also worthy of note, although its interpretation is currently unclear: Of the two r-II stars with secure detections of uranium, CS 31082$-$001 exhibits the so-called "actinide boost" (Hill et al. 2002), and has now been shown to be a single star, while the detailed r-process abundance pattern of the newly-identified binary HE 1523$-$0901 does not. While this may just be a result of small-number statistics on these very rare objects, it should be kept in mind as the sample grows; the details of their chemical-abundance patterns would appear to offer our most reliable clue to the origin of this difference.

CHAPTER 9

Outlook

The field of Galactic archaeology has seen great advances in the recent years with more metal-poor stars being discovered and analysed, pushing the detections to lower and lower metalicity. The work has revealed several sub-groups of stars with abundance patterns that vary from the bulk of metal-poor stars analysed. However, there are still a number of unanswered questions concerning the formation of these stars, the nature of their progenitors and of nucleosynthesis processes in the early Universe.

This thesis has presented high-resolution elemental-abundance analyses for a sample of 23 metal-poor stars and the results of radial-velocity monitoring of 17 r-process enhanced stars (r-I and r-II stars), 24 CEMP-no stars, 18 CEMP-s, and four CEMP-r/s stars.

The radial-velocity monitoring for the samples of 24 CEMP-no stars, 18 CEMP-s, and four CEMP-r/s stars span of up to eight years. In this time four binary systems have been identified among the CEMP-no stars and 18 among the CEMP-s and $-r/s$ stars. Concluding that the C excess seen in CEMP-no stars is not coupled to the binary nature of the stars, while this is the case for the majority of the CEMP-s stars. However, there are still large challenges for the mass transfer models of these systems. The majority of the detected CEMP-no binary stars have C abundances either in the (transition) area between the two C-bands of Spite et al. (2013), an area populated by both CEMP-no and CEMP-s stars, or on the high-C band. For the binary and single CEMP-s and -r/s stars there are no clear separation in the C abundances. Clearly there is a need for additional RV monitoring observations of CEMP-no and CEMP-s stars, as well as detailed abundance analyses of these stars. From which more stars with high/low carbon-band association can be identified, in order to better understand the astrophysical implications of these bands. More RV monitoring observations are also needed to enlarge the sample of binary systems with known orbital parameters, which will help constrain the mass transfer models. The ongoing survey by Placco et al. to detect bright CEMP stars among the RAVE stars with [Fe/H] < -2 (Kordopatis et al. 2013) will be an ideal source of candidates for radial-velocity monitoring, once these have been confirmed as CEMP-no or CEMP-s stars. Of the 17 r-process enhanced stars monitored over eight years, 14 exhibit no radial-velocity

variations during this period, and are thus presumably single, while three are binaries with normal orbital periods and eccentricities. Hence, there is no evidence that the r-process enhancement seen in the r-I and r-II stars is causally linked to the binary nature of these stars. Thus the moderate-to-high r-process-element abundances derived for these stars must be an imprint of the clouds from which the stars were formed. Future abundance analyses for larger samples of these stars, will help to constrain the nature of the objects and the chain of events that polluted the natal clouds of these stars. More precise and new measurements of the nuclear reactions at up-coming facilities such as FAIR[1], will also provide important information for the modeling of the r-process.

Six new CEMP-no stars were identified in this work. The discussion in section 8.1.6 shows that there is now compelling evidence that the CEMP-no stars are among the first low-mass stars to form in the early Universe, and, as such, contain the chemical imprints of the very first stars. However, thus far, no clear distinction between the abundance patterns of the prime candidates for production of large amounts of carbon in the early Universe has been found, either in the models or in the derived abundances of the CEMP-no stars. Furthermore, at present none of the suggested progenitors (faint SN with mixing or fallback and spinstars) can explain the full range of elements for which abundances are derived for CEMP-no stars – from the light-elements, the α-elements, the iron-peak elements, and to the neutron-capture elements. Hence, as suggested by Takahashi et al. (2014), the observed abundance patterns of CEMP-no stars (perhaps in particular those in the transition area between the low- and high-C bands) could arise from a combination of the two suggested progenitors, or another primordial source that has yet to be identified.

Five new CEMP-s stars, two new CEMP-r stars, and two new CEMP-r/s stars were also identified in this work. The radial-velocity monitoring have proven that the majority of CEMP-s stars are the result of mass transfer in a binary system, however, the yields from AGB models still do not fit the full abundance pattern seen in the CEMP-s stars. There is some evidence of CEMP-r/s stars might also be the result of mass transfer in a binary system (three out of four CEMP-r/s stars exhibited radial-velocity variations), but very little is known about the possible companion star. For the CEMP-r stars there is no evidence of a binary formation scenario, but only one of the five CEMP-r stars known have been monitored for radial-velocity variations.

The detection of three CEMP-s stars and one CEMP-r/s which exhibit no variation in their radial velocities over the eight years of monitoring, indicates the need of alternative formation channels for these stars. No specific signature of their C, Fe, and Ba abundances could be derived, but comparison of the detailed abundance patterns of binary stars to that of single stars, will help to explore this option further.

The general request, to make further progress in this field, is larger samples of the variety of low-metallicity stars presented here. To distinguish between the abundance patterns of stars representing the general trends and those that are just peculiar outliers. Recent years have seen an increase in the High-resolution spectroscopic follow-up of stars from several large surveys, such as; SkyMapper (Keller et al. 2007, 2014; Jacobson et al. 2015), TOPoS (Caffau et al. 2013b), based on stars selected by SDSS/SEGUE (Yanny et al. 2009; Aoki et al. 2013b), the CEMP-star searches from the HK survey, the HES, and the RAVE

---

[1]http://www.fair-center.eu/

survey (Steinmetz et al. 2006) described by Placco et al. (2010, 2011, 2013, 2014a, and in preparation), and the LAMOST survey (Deng et al. 2012; Li et al. 2015). These samples need to be expanded even further. These surveys will soon provide more examples of CEMP-r and CEMP-r/s stars, of which our current samples have very limited numbers. They will also enlarge the numbers of known CEMP-s and CEMP-no stars. With detailed and homogeneous analyses of these stars, we can look forward to detecting the elemental abundance signatures that constrain the nature and sites of the nucleosynthesis events that first enriched the Milky Way.

The issue of a homogeneous analysis of these stars is also an important step. Even small differences in the methods applied to derive stellar parameters of a star can result in large variations in the derived abundances for the star. An example is the influence of temperature on the abundances derived from molecular bands. Such inhomogeneities may conceal subtle differences in the abundance patterns of the stars, which are important for constraining the nature of the progenitors of the stars. In this aspect the Gaia[2] mission will help by measuring parallaxes of a great number of stars, for which stellar parameters can then be derived from first principles. This will help calibrate relations used to derive stellar parameters for stars where no parallaxes exists, such as the color temperature relations used in this work.

Another important way to improve the derived abundances is even more precise line list information, especially for the molecular bands. Although recent work in this area has improved the results greatly (Masseron et al. 2014), inconsistencies still exists for abundances derived from different molecular bands of the same element. An example is the N abundances derived from the NH band and the CN bands, as shown in Figure 4.2 on page 4.2. In the spectra of the CEMP stars, where many of the lines are blended with the strong CH and CN bands, more precise line information is also immensely important to derive precise abundances for other elements.

The most metal-poor stars in the halo may be be accreted from smaller systems orbiting the Galaxy such as dwarf galaxies. In recent years a number of metal-poor stars have been detected in dwarf galaxies (Frebel et al. 2015). These galaxies are old and small systems which have presumable seen a more simple star formation history, compared to larger galaxies like the Milky Way. Expansion of the sample of metal-poor stars from dwarf galaxies will allow us to study the metal-poor stars in the environment in which they formed, and reconstruct the early chemical evolution of these systems. However, these systems are vary faint and on the limit of what we can observe with current facilities, but upcoming facilities such as the E-ELT[3] and the TMT[4] predict a bright future for this field.

---

[2]http://sci.esa.int/gaia/
[3]http://www.eso.org/sci/facilities/eelt/
[4]http://www.tmt.org/

Individual heliocentric radial velocities measured

A.1 Individual heliocentric radial velocities measured for the r-process enhanced stars

Table A.1: HD 20

HJD	RV (km s^{-1})	RV$_{err}$ (km s^{-1})
2454314.661653	-57.892	0.033
2454338.615723	-57.891	0.022
2454373.612652	-57.900	0.024
2454819.293270	-57.983	0.030
2455126.580295	-57.946	0.041
2455175.394755	-57.978	0.023
2455503.480513	-57.855	0.070
2455776.652777	-57.940	0.022
2455796.657395	-57.927	0.025
2455859.514789	-57.862	0.034
2456139.703103	-57.863	0.027
2456241.446457	-57.899	0.064
2456529.679820	-57.934	0.023
2456917.579578	-57.924	0.027

Table A.2: CS 29497−004

HJD	RV (km s^{-1})	RV$_{err}$ (km s^{-1})
2454373.642892	+104.329	0.116
2454705.631179	+104.873	0.065
2454780.500993	+105.409	0.292
2454819.320354	+105.561	0.084
2455175.419215	+105.010	0.063
2455415.686599	+104.941	0.061
2455439.606743	+105.124	0.060
2455796.671082	+105.434	0.077
2455858.545060	+105.060	0.060
2456191.589163	+105.050	0.045
2456530.687786	+104.829	0.054
2456956.535485	+104.471	0.094

Table A.3: CS 31082−001

HJD	RV (km s^{-1})	RV$_{err}$ (km s^{-1})
2454314.681742	+138.985	0.044
2454338.656269	+139.075	0.036
2454396.548819	+139.095	0.050
2454480.372487	+139.271	0.050
2454705.645953	+139.049	0.048
2454780.529216	+139.152	0.052
2454819.336946	+139.207	0.036
2455059.684154	+139.053	0.031
2455149.486943	+139.131	0.047
2455207.337039	+139.026	0.034
2455232.321077	+139.059	0.036
2455415.734837	+139.058	0.032
2455439.622078	+138.995	0.027
2455485.577689	+138.927	0.032
2455503.470979	+138.867	0.139
2455776.741087	+138.965	0.034
2455821.588602	+138.997	0.025
2455882.542281	+139.101	0.047
2456139.725335	+138.991	0.040
2456276.485443	+139.163	0.039
2456519.736731	+138.956	0.024
2456574.672228	+139.197	0.047
2456956.570319	+139.252	0.078

Table A.4: HE 0432−0923

HJD	RV	RV_{err}
	$(km\ s^{-1})$	$(km\ s^{-1})$
2454338.702068	−64.948	0.983
2454373.722874	−64.876	1.097
2454396.715153	−66.294	1.602
2454406.637662	−64.942	1.710
2454459.590478	−62.264	2.232
2454480.431485	−65.026	1.202
2454516.372208	−64.832	0.592
2454780.591463	−64.462	1.896
2454819.450079	−64.460	1.351
2455075.713863	−65.352	1.544
2455176.552628	−64.543	0.684
2455232.419859	−65.290	1.106
2455531.609740	−64.654	1.303
2455620.393797	−63.236	2.281
2455944.449119	−66.678	2.308
2456191.699846	−64.856	1.104
2456545.689792	−64.892	1.340

Table A.5: HE 0442−1234

HJD	RV	RV_{err}
	(km s^{-1})	(km s^{-1})
2454338.746568	+231.895	0.043
2454373.755033	+231.272	0.022
2454396.675349	+231.387	0.045
2454406.673221	+231.488	0.047
2454480.469787	+231.625	0.037
2454496.400729	+231.149	0.135
2454516.413321	+231.777	0.020
2454705.704003	+230.516	0.030
2454780.549248	+230.670	0.046
2454793.526401	+230.398	0.173
2454819.485376	+231.059	0.041
2454852.550506	+231.299	0.045
2455059.709842	+254.627	0.039
2455079.721105	+255.868	0.030
2455126.674591	+252.221	0.032
2455149.614597	+250.514	0.037
2455171.540400	+248.975	0.021
2455207.416924	+246.988	0.029
2455232.382885	+245.710	0.030
2455439.745696	+240.146	0.032
2455478.744628	+239.853	0.067
2455531.646433	+239.862	0.033
2455821.705466	+236.600	0.024
2455944.486938	+236.352	0.046
2455971.360048	+236.071	0.040
2456191.737737	+234.847	0.023
2456574.706961	+233.444	0.020
2456956.723997	+231.920	0.055

Table A.6: HE 0524−2055

HJD	RV	RV$_{err}$
	(km s^{-1})	(km s^{-1})
2454396.640800	+255.070	0.185
2454406.717056	+255.306	0.110
2454480.496860	+255.712	0.098
2454820.481773	+255.614	0.142
2455149.688274	+255.624	0.084
2455207.491478	+255.546	0.104
2455503.608363	+255.614	0.551
2455531.544536	+255.478	0.171
2455882.598085	+255.358	0.108
2456005.376504	+255.236	0.360
2456207.754219	+255.340	0.082
2456603.661353	+255.443	0.088
2456956.750015	+255.185	0.196

Table A.7: HE 1044−2509

HJD	RV	RV$_{err}$
	(km s^{-1})	(km s^{-1})
2454909.489857	+342.628	3.089
2454930.426948	+369.639	1.671
2455174.767340	+379.567	2.399
2455207.625989	+362.229	1.939
2455620.563564	+384.868	1.939
2455704.385256	+343.075	2.077
2455712.405032	+335.836	1.872
2455718.397062	+358.699	2.243
2455722.397011	+375.517	1.896
2455725.396840	+386.965	3.807
2455730.395197	+385.629	2.338
2455733.391004	+378.210	3.132
2455738.401973	+354.412	1.072
2456796.438819	+363.768	1.346

Table A.8: HE 1105+0027

HJD	RV	RV$_{err}$
	(km s^{-1})	(km s^{-1})
2454459.682587	+76.353	1.799
2454464.668667	+76.746	1.762
2454516.585694	+75.947	1.514
2454909.650314	+75.405	0.794
2455232.610390	+76.608	0.991
2455344.429621	+76.620	1.860
2455531.735132	+76.372	1.831
2455662.477811	+76.280	1.239
2456033.449115	+75.442	1.403

Table A.9: HE 1127−1143

HJD	RV	RV$_{err}$
	(km s^{-1})	(km s^{-1})
2454459.748479	+229.676	2.402
2454481.662602	+229.183	1.172
2454964.473253	+228.850	1.277
2455232.656932	+228.583	1.005
2455620.602643	+229.334	1.314
2455662.541359	+228.736	1.308
2456458.454152	+229.734	0.725

Table A.10: HE 1219−0319

HJD	RV	RV$_{err}$
	(km s^{-1})	(km s^{-1})
2454481.728699	+163.210	3.750
2454625.460187	+162.919	1.680
2455620.657226	+163.474	2.343
2456090.413526	+161.166	2.464
2456652.702430	+161.310	2.342

Table A.11: HE 1430+0053

HJD	RV	RV_{err}
	(km s^{-1})	(km s^{-1})
2454219.667720	-107.225	0.276
2454314.443374	-108.199	0.203
2454459.780220	-107.456	0.161
2454464.791534	-107.738	0.217
2454480.776288	-107.848	0.177
2454625.420967	-107.371	0.217
2454930.698058	-107.699	0.173
2454951.700884	-107.748	0.256
2454987.473997	-107.662	0.181
2455232.782505	-107.709	0.145
2455344.579755	-107.138	0.179
2455620.687317	-107.719	0.243
2455662.702207	-107.560	0.173
2455704.614991	-107.359	0.157
2455738.545590	-108.383	0.218
2455776.455326	-108.773	0.204
2456005.755704	-108.120	0.622
2456033.623529	-108.201	0.206
2456078.504562	-107.171	0.187
2456712.726996	-107.900	0.651

Table A.12: HE 1523−0901

HJD	RV	RV$_{err}$
	(km s^{-1})	(km s^{-1})
2454219.705449	−163.546	0.016
2454254.642226	−163.593	0.039
2454285.507316	−163.348	0.015
2454314.462351	−163.385	0.012
2454625.508366	−163.091	0.010
2454930.677427	−163.244	0.016
2454951.718880	−162.971	0.017
2454964.675531	−162.951	0.022
2454987.509060	−163.041	0.014
2455344.542474	−162.849	0.013
2455415.386096	−163.549	0.010
2455439.363821	−163.724	0.016
2455620.738975	−162.875	0.017
2455662.681656	−163.110	0.012
2455704.633870	−163.372	0.016
2455738.564258	−163.723	0.020
2455776.438140	−163.732	0.016
2456005.728789	−163.530	0.020
2456078.539561	−163.442	0.015
2456307.786409	−163.457	0.016
2456351.717323	−163.347	0.014
2456372.687769	−163.477	0.014
2456399.619896	−163.371	0.015
2456426.543882	−163.298	0.021
2456474.451216	−163.108	0.011
2456488.426825	−162.960	0.024
2456489.500440	−163.000	0.015
2456520.424407	−162.818	0.020
2456529.377789	−162.938	0.017
2456664.770980	−163.461	0.012
2456685.790500	−163.626	0.011
2456712.759468	−163.414	0.020
2456796.646910	−162.880	0.011
2456813.610868	−162.988	0.015

Table A.13: CS 22892−052

HJD	RV	RV$_{err}$
	(km s^{-1})	(km s^{-1})
2454314.576915	+13.178	0.053
2454338.541838	+13.553	0.136
2454373.414188	+13.559	0.053
2454390.364640	+13.579	0.079
2454625.684458	+13.594	0.058
2454665.611641	+13.917	0.063
2454705.568239	+13.747	0.051
2455009.693164	+13.480	0.098
2455059.511399	+13.695	0.076
2455174.314885	+13.374	0.050
2455415.522393	+13.471	0.061
2455531.326532	+13.467	0.108
2455704.706380	+13.742	0.090
2455776.612557	+13.367	0.049
2455822.600538	+13.505	0.103
2455882.349889	+13.624	0.051
2456139.644767	+13.413	0.087
2456191.399426	+13.585	0.099
2456488.673600	+13.584	0.066

Table A.14: HE 2224+0143

HJD	RV	RV$_{err}$
	(km s^{-1})	(km s^{-1})
2454314.626987	-113.002	0.070
2454338.455766	-113.041	0.061
2454373.470335	-113.043	0.113
2454625.646394	-112.867	0.147
2454665.630399	-112.981	0.118
2454705.522460	-113.104	0.115
2455009.711530	-113.138	0.099
2455059.529868	-113.020	0.056
2455070.548978	-112.989	0.159
2455175.444551	-113.221	0.079
2455344.685686	-112.945	0.119
2455415.497735	-112.930	0.102
2455439.426753	-112.968	0.103
2455503.356818	-113.402	0.352
2455531.410900	-113.220	0.136
2455704.677515	-113.216	0.095
2455776.507942	-112.924	0.093
2455796.580352	-112.817	0.094
2455882.328613	-113.245	0.106
2456078.720195	-113.064	0.081
2456140.610920	-113.674	0.186
2456191.379978	-113.152	0.059
2456488.693610	-113.205	0.084
2456956.553882	-112.876	0.303

Table A.15: HE 2244$-$1503

HJD	RV	RV_{err}
	(km s^{-1})	(km s^{-1})
2454338.580931	+147.980	1.346
2454373.501898	+148.051	1.007
2454390.393739	+148.275	1.573
2454665.675576	+147.791	1.192
2455059.563356	+147.724	1.446
2455149.413670	+148.224	1.470
2455415.573319	+148.194	1.123
2455439.540189	+147.532	1.306
2455478.531528	+147.567	0.899
2455738.686456	+147.855	0.872
2455776.556273	+147.947	1.562
2455822.637317	+148.094	1.569
2456191.476165	+148.111	0.922
2456545.578750	+147.649	1.362

Table A.16: HD 221170

HJD	RV	RV$_{err}$
	(km s^{-1})	(km s^{-1})
2454314.636048	-121.161	0.010
2454338.524441	-121.179	0.009
2454373.528280	-121.107	0.009
2454390.345759	-121.253	0.010
2454406.586097	-121.114	0.011
2454480.397616	-121.164	0.013
2454625.656022	-121.267	0.012
2454705.500584	-121.138	0.017
2454780.452621	-121.111	0.012
2454793.471559	-121.182	0.011
2454820.348668	-121.321	0.014
2455009.719853	-121.078	0.011
2455059.695625	-121.185	0.009
2455071.639351	-121.199	0.017
2455171.399245	-121.340	0.008
2455344.693948	-121.230	0.011
2455415.506520	-121.259	0.012
2455439.446714	-121.227	0.008
2455503.346059	-121.358	0.014
2455531.470241	-121.412	0.011
2455704.717098	-121.256	0.009
2455738.710786	-121.253	0.018
2455776.728437	-121.333	0.012
2455796.566301	-121.342	0.011
2455859.532089	-121.249	0.009
2455892.424873	-121.011	0.029
2455915.320942	-121.166	0.077
2456140.740348	-121.075	0.010
2456241.340390	-121.056	0.013
2456488.721460	-121.000	0.010

Table A.17: CS 30315$-$029

HJD	RV (km s^{-1})	RV$_{err}$ (km s^{-1})
2454314.742671	-168.937	0.074
2454373.581743	-169.408	0.066
2454705.601838	-169.668	0.074
2455059.649134	-169.963	0.071
2455175.377253	-168.867	0.130
2455415.665073	-169.830	0.078
2455776.636347	-169.582	0.071
2455796.640879	-169.184	0.055
2455821.555408	-169.165	0.065
2455859.497621	-169.214	0.092
2455882.472080	-169.087	0.100
2456139.682491	-169.008	0.242
2456530.669987	-169.196	0.120
2456987.357305	-169.738	0.077

A.2   Individual heliocentric radial velocities measured for the CEMP-no stars

Table A.18: HE 0020−1741

HJD	RV	RV$_{err}$
	km s^{-1}	km s^{-1}
2456191.553850	+92.725	0.057
2456277.325704	+92.619	0.090
2456530.727938	+93.201	0.058
2456545.641765	+93.085	0.057
2456603.431706	+92.945	0.067
2456893.629396	+93.192	0.064
2456986.461205	+93.099	0.070
2457225.690882	+92.944	0.118

Table A.19: CS 29527−015

HJD	RV	RV$_{err}$
	km s^{-1}	km s^{-1}
2456193.657074	+47.016	1.931
2456214.489204	+46.936	0.586
2456531.626981	+47.137	0.101
2456603.479383	+46.486	1.844
2456895.609724	+47.811	1.426

Table A.20: CS 22166−016

HJD	RV	RV_{err}
	km s^{-1}	km s^{-1}
2456191.570891	−210.289	0.220
2456300.388000	−210.344	0.242
2456531.654302	−210.477	0.161
2456579.603014	−210.404	0.183
2456652.456871	−209.670	0.903
2456895.638248	−210.397	0.036
2456956.601783	−212.384	1.018
2457225.706367	−210.071	0.269

Table A.21: HE 0219−1739

HJD	RV	RV_{err}
	km s^{-1}	km s^{-1}
2454396.611647	+102.993	0.064
2454705.669847	+101.817	0.056
2455126.606616	+106.873	0.057
2455171.488102	+107.500	0.056
2455232.347099	+107.317	0.051
2455439.645440	+112.468	0.041
2455485.610217	+114.309	0.046
2455531.495382	+113.868	0.063
2455796.705307	+112.387	0.037
2455882.508124	+109.832	0.065
2455945.426690	+107.516	0.151
2456193.705723	+102.161	0.052
2456308.451562	+100.074	0.087
2456578.607672	+100.814	0.052
2456603.608463	+100.413	0.082

Table A.22: BD+44°493

HJD	RV	RV_{err}
	km s^{-1}	km s^{-1}
2455796.731150	-150.191	0.019
2455821.602481	-150.061	0.016
2455859.544117	-150.050	0.017
2455882.390816	-150.150	0.113
2455892.414452	-150.114	0.125
2455903.488584	-150.080	0.032
2455915.503192	-149.985	0.141
2455971.385310	-150.001	0.041
2456163.698695	-150.101	0.164
2456191.605915	-150.126	0.018
2456307.434407	-150.041	0.028
2456518.689701	-150.104	0.031
2456528.699713	-150.081	0.028
2456603.638647	-150.066	0.025
2456685.418052	-150.040	0.060
2456893.598206	-150.127	0.032
2456987.491755	-150.101	0.086
2457094.349390	-150.100	0.029

Table A.23: HE 0405−0526

HJD	RV	RV$_{err}$
	km s^{-1}	km s^{-1}
2456190.761992	+165.656	0.014
2456209.746333	+165.593	0.057
2456213.772353	+165.684	0.032
2456241.709356	+165.674	0.057
2456340.434828	+165.568	0.110
2456528.683688	+165.668	0.029
2456603.556421	+165.639	0.017
2456685.438636	+165.676	0.019
2456686.360900	+165.708	0.021
2456726.353768	+165.667	0.071
2456986.480120	+165.662	0.024
2457018.579283	+165.700	0.034
2457094.366572	+165.641	0.023

Table A.24: HE 1012−1540

HJD	RV	RV$_{err}$
	km s^{-1}	km s^{-1}
2456340.537113	+225.399	1.158
2456426.386869	+226.508	1.046
2456458.405646	+225.820	1.976
2456752.448580	+227.622	1.786
2456796.400824	+226.276	0.719
2456987.772426	+227.167	0.966
2457076.586146	+225.772	0.906
2457142.415352	+226.330	1.094

Table A.25: HE 1133−0555

| HJD | RV | RV$_{err}$ |
	km s^{-1}	km s^{-1}
2454951.480644	+270.590	0.297
2455207.661330	+269.969	0.391
2455738.452327	+270.772	0.224
2456005.578838	+270.609	0.429
2456033.538287	+269.883	0.571
2456307.743507	+270.264	0.468
2456426.426846	+270.612	0.316
2456796.484997	+269.945	0.510
2457168.502711	+270.264	0.504

Table A.26: HE 1150−0428

| HJD | RV | RV$_{err}$ |
	km s^{-1}	km s^{-1}
2454254.469526	+59.198	0.631
2454464.774604	+50.506	0.305
2454481.794575	+53.500	0.493
2454909.540207	+43.574	0.403
2454930.649908	+39.265	0.104
2455207.697467	+41.831	0.220
2455704.477220	+58.205	0.053
2456005.672746	+56.305	0.094
2456064.445022	+44.939	0.506
2456278.762138	+58.039	0.192
2456399.466063	+36.305	1.247
2456426.466103	+37.280	0.053
2456474.416329	+45.598	0.078

Table A.27: HE 1201−1512

HJD	RV	RV$_{err}$
	km s^{-1}	km s^{-1}
2456722.550471	+242.676	2.665
2456756.503043	+238.280	2.525
2456814.436159	+238.593	1.086
2457110.570965	+238.337	. . .
2457142.522877	+239.365	0.705

Table A.28: HE 1300+0157

HJD	RV	RV$_{err}$
	km s^{-1}	km s^{-1}
2456756.542595	+75.397	0.531
2456796.569354	+74.182	0.418
2456840.398240	+75.141	0.321
2457142.604191	+73.800	0.284
2457168.543909	+74.159	0.146

Table A.29: BS 16929−005

HJD	RV	RV$_{err}$
	km s^{-1}	km s^{-1}
2456340.583325	−50.188	2.672
2456426.503527	−51.478	0.973
2456652.666926	−50.625	1.020
2456722.615544	−50.970	1.810
2456756.432118	−49.880	1.415
2457096.737115	−50.575	0.166
2457225.402088	−51.430	0.814

Table A.30: HE 1300−0641

HJD	RV	RV$_{err}$
	km s^{-1}	km s^{-1}
2456756.628997	+68.759	1.104
2457142.577242	+68.885	0.646

Table A.31: HE 1302−0954

HJD	RV	RV$_{err}$
	km s^{-1}	km s^{-1}
2456756.590880	+32.494	0.268
2457111.063422	+32.549	0.229
2457142.552710	+32.570	0.124

Table A.32: CS 22877−001

HJD	RV	RV_{err}
	km s^{-1}	km s^{-1}
2454219.526768	+166.288	0.071
2454254.500103	+166.360	0.075
2454909.559431	+166.422	0.087
2454951.514264	+166.194	0.070
2454964.525457	+166.332	0.082
2455207.715279	+166.330	0.074
2455344.525470	+166.207	0.064
2455554.795730	+166.266	0.044
2455620.725908	+166.220	0.058
2455704.535965	+166.112	0.045
2456005.692575	+166.283	0.087
2456033.654814	+166.519	0.091
2456033.711811	+166.402	0.247
2456722.657147	+166.376	0.152
2457142.537184	+166.147	0.082

Table A.33: HE 1327−2326

HJD	RV	RV_{err}
	km s^{-1}	km s^{-1}
2454219.542926	+65.578	. . .
2454930.612715	+64.974	. . .
2455232.754648	+62.764	. . .
2455344.464871	+63.630	. . .
2455620.712669	+65.347	. . .
2455704.502164	+64.463	0.935
2455945.751608	+62.329	. . .
2456006.750000	+65.188	. . .
2456796.598655	+64.818	0.159

Only the spectral order containing
the Mg triplet could be used for
the correlation for the majority
of the spectra of this star, thus
an internal error could not be
calculated for these spectra.

Table A.34: HE 1410+0213

HJD	RV	RV$_{err}$
	km s^{-1}	km s^{-1}
2454219.643865	+80.983	0.024
2454314.427327	+81.213	0.028
2454516.758372	+81.111	0.159
2454909.570456	+81.069	0.046
2454930.734724	+81.026	0.036
2454951.686449	+80.874	0.028
2455232.768813	+81.025	0.020
2455262.603235	+80.918	0.056
2455344.565415	+81.068	0.028
2455555.796783	+81.291	0.178
2455620.765457	+80.837	0.030
2455662.717240	+80.960	0.021
2455704.599755	+81.183	0.021
2455776.420181	+81.414	0.016
2456005.703435	+81.143	0.042
2456033.595529	+81.330	0.043
2456078.490141	+81.348	0.032
2456722.586745	+81.417	0.173
2457079.771538	+81.389	0.055
2457096.777330	+81.357	0.050
2457110.655228	+81.202	0.103
2457142.633878	+81.069	0.031
2457225.423528	+80.984	0.037

Table A.35: HE 1506−0113

HJD	RV	RV$_{err}$
	km s^{-1}	km s^{-1}
2456756.666987	−85.865	1.202
2456796.621783	−85.830	0.153
2456813.637005	−83.626	0.952
2456893.378926	−83.223	0.594
2457142.677901	−81.052	0.524
2457190.528825	−79.152	0.449
2457225.469049	−77.545	0.943
2457239.418486	−80.405	1.765
2457241.405630	−80.661	0.736
2457249.435833	−79.985	0.798

Table A.36: CS 22878−027

HJD	RV	RV$_{err}$
	km s^{-1}	km s^{-1}
2456191.343802	−91.097	0.810
2456756.724060	−89.769	0.331
2456796.698016	−90.696	1.839
2456887.392049	−90.533	1.495
2457142.721805	−91.674	0.768
2457168.690235	−92.330	1.021
2457225.500502	−92.956	0.078

Table A.37: CS 29498−043

HJD	RV	RV$_{err}$
	km s^{-1}	km s^{-1}
2454314.535743	−32.557	1.583
2454338.491418	−32.080	0.964
2454373.380034	−32.911	1.247
2454665.594229	−32.885	1.988
2454705.541235	−33.060	0.421
2455059.460229	−32.215	1.468
2455070.509288	−33.641	2.553
2455149.322697	−31.798	1.008
2455415.540797	−32.527	1.318
2455439.469033	−32.242	1.385
2455738.656324	−31.819	1.760
2455776.589351	−32.193	0.682
2456033.722001	−31.172	0.865
2456458.700787	−32.383	1.420
2456917.501102	−33.836	1.839

Table A.38: CS 29502−092

HJD	RV	RV$_{err}$
	km s^{-1}	km s^{-1}
2454314.615516	−67.045	0.061
2454373.458720	−67.215	0.051
2454625.669705	−67.200	0.061
2454665.647386	−67.284	0.060
2454705.583752	−67.143	0.054
2454964.724327	−67.152	0.071
2455059.495880	−67.266	0.065
2455126.513232	−67.213	0.088
2455174.330130	−67.225	0.055
2455344.673757	−67.116	0.068
2455415.485690	−67.193	0.066
2455439.439882	−67.216	0.051
2455503.319269	−67.452	0.088
2455531.397775	−67.351	0.105
2455704.690065	−67.173	0.082
2455776.526490	−67.174	0.055
2456139.661574	−67.368	0.066
2456191.367411	−67.157	0.073
2456458.712569	−67.180	0.068
2456917.518394	−67.175	0.100

Table A.39: HE 2318−1621

HJD	RV	RV$_{err}$
	km s^{-1}	km s^{-1}
2456191.508735	−41.724	0.136
2456458.678220	−41.780	0.085
2456512.729591	−41.299	0.228
2456574.601390	−42.136	0.210
2456888.556884	−41.612	0.299
2456956.516288	−41.446	0.270
2457225.639412	−41.891	0.112

Table A.40: CS 22949−037

HJD	RV	RV$_{err}$
	km s^{-1}	km s^{-1}
2456191.418846	−125.488	0.490
2456213.439688	−125.619	0.423
2456518.588656	−125.438	1.300
2456574.639061	−126.021	1.465
2456881.545231	−125.238	1.834
2456886.533402	−125.775	1.247
2456956.499023	−125.341	1.153

Table A.41: CS 22957−027

| HJD | RV | RV$_{err}$ |
	km s^{-1}	km s^{-1}
2454314.650763	−61.056	0.053
2454373.602779	−61.598	0.071
2454396.522335	−62.847	0.209
2454480.353018	−63.679	0.119
2454665.720088	−72.551	0.112
2454780.480070	−76.573	0.109
2454819.304024	−76.207	0.170
2455059.670725	−67.280	0.056
2455071.664734	−67.767	0.388
2455126.567510	−65.441	0.085
2455149.455854	−64.285	0.130
2455207.320651	−63.146	0.131
2455439.578111	−61.418	0.084
2455503.374442	−62.705	0.525
2455531.350698	−62.359	0.139
2455738.721957	−72.151	0.063
2455776.669030	−73.957	0.105
2455882.450486	−76.464	0.111

A.3   Individual heliocentric radial velocities measured for the CEMP-s stars

Table A.42: HE 0002$-$1037

HJD	RV	RV$_{err}$
	km s^{-1}	km s^{-1}
2456191.526147	-36.232	0.043
2456241.458147	-33.904	0.170
2456530.708942	-24.357	0.035
2456574.575672	-27.586	0.043
2456647.456005	-35.054	0.075
2456652.377850	-35.631	0.052
2456888.574694	-38.674	0.062
2456956.435645	-34.828	0.069
2457225.656989	-22.946	0.068

Table A.43: HE 0017+0055

HJD	RV	RV$_{err}$
	km s^{-1}	km s^{-1}
2454314.670183	-78.622	0.007
2454338.641932	-78.944	0.007
2454373.622398	-78.691	0.009
2454396.537062	-78.583	0.007
2454406.596620	-78.505	0.012
2454480.386805	-78.183	0.012
2454793.484623	-79.098	0.018
2454820.338620	-78.830	0.017
2455059.736462	-79.922	0.008
2455149.473028	-79.647	0.010
2455207.349798	-79.391	0.015
2455415.608056	-80.439	0.009
2455439.591411	-80.778	0.010
2455503.408603	-80.330	0.023
2455738.734358	-80.148	0.008
2455776.682146	-80.675	0.008
2455821.576587	-80.870	0.009
2455944.325305	-80.429	0.011
2456139.712932	-80.857	0.010
2456241.391015	-81.420	0.018
2456545.626650	-81.474	0.011
2456652.417968	-81.951	0.015
2456686.320885	-81.538	0.015
2456840.718234	-80.866	0.028
2456888.542073	-81.261	0.013
2456917.598109	-81.398	0.014
2456987.381314	-81.885	0.009

Table A.44: HE 0111−1346

HJD	RV	RV$_{err}$
	km s^{-1}	km s^{-1}
2456213.659444	+50.431	0.022
2456531.674512	+39.604	0.015
2456534.728230	+40.177	0.024
2456574.621608	+47.100	0.015
2456579.622577	+47.786	0.020
2456652.402653	+49.094	0.021
2456893.652457	+31.577	0.018
2456917.616733	+36.046	0.019

Table A.45: HE 0151−0341

HJD	RV	RV$_{err}$
	km s^{-1}	km s^{-1}
2456213.703823	−37.298	0.070
2456307.328144	−25.696	0.064
2456518.734619	−47.217	0.041
2456545.658288	−42.753	0.047
2456574.656858	−36.767	0.030
2456603.509903	−31.030	0.042
2456647.482111	−25.892	0.065
2456652.476148	−25.703	0.072
2456685.393398	−26.739	0.065
2456893.720328	−44.812	0.051
2457225.720998	−48.629	0.065

Table A.46: HE 0206−1916

HJD	RV	RV$_{err}$
	km s^{-1}	km s^{-1}
2456213.681263	−199.498	0.048
2456307.375085	−199.397	0.053
2456529.696685	−199.370	0.024
2456546.732984	−199.683	0.061
2456603.534709	−199.600	0.038
2456893.674974	−199.419	0.043
2456987.436076	−199.550	0.061
2457018.497295	−199.555	0.067

Table A.47: HE 0319−0215

HJD	RV	RV$_{err}$
	km s^{-1}	km s^{-1}
2454780.643689	−229.933	0.029
2455126.644034	−227.058	0.024
2455149.512004	−226.974	0.030
2455207.385991	−226.673	0.017
2455415.709630	−224.274	0.023
2455439.679575	−224.389	0.019
2455478.610560	−224.219	0.022
2455620.348376	−223.797	0.026
2455821.650158	−222.893	0.012
2455882.567658	−223.207	0.020
2455915.541295	−223.575	0.117
2456191.633081	−223.890	0.017
2456528.727595	−226.084	0.028
2456578.646920	−226.565	0.018
2456956.694772	−229.280	0.085
2456987.520739	−229.692	0.063

Table A.48: HE 0430−1609

HJD	RV	RV$_{err}$
	km s^{-1}	km s^{-1}
2456209.690592	+228.371	0.040
2456214.654241	+228.334	0.022
2456529.716263	+229.881	0.038
2456545.730320	+229.969	0.021
2456574.684591	+230.133	0.018
2456685.460615	+230.756	0.030
2456722.361986	+230.964	0.048
2456893.697354	+231.838	0.053
2456917.637467	+231.930	0.038
2456956.768407	+232.277	0.121
2456986.656563	+232.347	0.022
2457076.358109	+232.758	0.083
2457092.346379	+232.852	0.024
2457110.358267	+232.918	0.061

Table A.49: HE 0441−0652

HJD	RV	RV$_{err}$
	km s^{-1}	km s^{-1}
2454705.735103	−39.600	0.154
2455149.581199	−33.053	0.639
2455176.496757	−31.568	0.372
2455207.533051	−30.860	0.149
2455439.705451	−29.741	0.163
2455478.647456	−29.967	0.081
2455531.570190	−29.901	0.271
2455821.679132	−28.773	0.130
2455915.581695	−27.892	0.810
2456005.349692	−29.417	0.507
2456191.662290	−29.167	0.183
2456214.674794	−29.727	0.170
2456574.733031	−30.053	0.135
2456685.488846	−29.826	0.417
2456987.465562	−30.047	0.298
2457076.433918	−30.762	1.056

Table A.50: HE 0507−1430

HJD	RV	RV$_{err}$
	km s^{-1}	km s^{-1}
2455149.651408	+53.744	0.017
2455176.599630	+53.614	0.027
2455207.454782	+51.698	0.016
2455232.476681	+48.880	0.016
2455478.681570	+40.340	0.029
2455821.736708	+32.139	0.018
2455882.665281	+34.746	0.032
2455944.524311	+43.196	0.044
2455971.413617	+47.094	0.037
2456005.413409	+51.227	0.077
2456213.733744	+36.148	0.030

Table A.51: HE 0507−1653

HJD	RV	RV$_{err}$
	km s^{-1}	km s^{-1}
2454793.550003	+346.064	0.053
2454820.459438	+349.034	0.025
2455126.697287	+342.750	0.015
2455171.570518	+343.843	0.014
2455207.512910	+347.058	0.018
2455439.724022	+349.472	0.014
2455478.722314	+345.614	0.052
2455503.570082	+343.789	0.046
2455531.523350	+342.751	0.030
2455860.691905	+347.747	0.015
2455892.557389	+344.930	0.117
2456191.757342	+354.904	0.012
2456209.721195	+353.449	0.021
2456531.711978	+356.770	0.018
2456917.659643	+356.020	0.025

Table A.52: HE 0854+0151

| HJD | RV | RV$_{err}$ |
	km s^{-1}	km s^{-1}
2454516.507427	+135.575	0.033
2454780.704703	+144.261	0.072
2454930.383320	+130.585	0.034
2454964.394295	+124.541	0.054
2455149.732651	+141.161	0.032
2455171.717504	+144.308	0.024
2455174.671458	+144.662	0.041
2455232.528285	+145.394	0.025
2455531.690232	+139.809	0.040
2455620.456709	+145.626	0.041
2455662.423714	+140.074	0.028
2455822.744791	+121.901	0.112
2455915.759905	+138.642	0.129
2456005.485413	+145.867	0.061
2456273.714222	+132.054	0.062

Table A.53: HE 0959−1424

HJD	RV	RV_{err}
	km s^{-1}	km s^{-1}
2454406.772763	+344.070	0.208
2454793.711499	+344.086	0.454
2455149.763136	+343.791	0.172
2455174.722187	+343.693	0.144
2455207.588494	+343.723	0.196
2455310.370417	+343.574	0.151
2455544.723641	+343.649	0.304
2455620.544214	+343.666	0.152
2455662.388325	+343.611	0.030
2455944.564130	+343.622	0.432
2456005.518489	+343.338	0.212
2456033.367572	+343.436	0.430
2456399.385005	+342.986	0.295
2456722.521472	+341.991	0.408
2456742.419581	+343.293	0.493
2456756.387624	+342.558	0.343
2456796.374127	+342.586	0.058
2457142.385004	+341.819	0.270

Table A.54: HE 1045+0226

HJD	RV	RV_{err}
	km s^{-1}	km s^{-1}
2456307.696978	+131.672	0.228
2456399.434205	+131.652	0.099
2456652.617506	+131.564	0.104
2456712.675310	+131.685	0.364
2457076.619316	+131.460	0.399
2457110.443693	+130.954	0.178

Table A.55: HE 1046−1352

HJD	RV	RV$_{err}$
	km s^{-1}	km s^{-1}
2454909.613891	+94.395	0.795
2454930.455633	+97.658	0.147
2454964.434686	+47.693	1.670
2455174.742203	+105.913	0.851
2455232.573342	+96.330	0.147
2455310.392709	+73.223	0.859
2455344.391658	+48.887	0.278
2455554.780134	+94.567	0.543
2455620.516046	+97.700	0.553
2456006.503646	+71.838	0.545
2456033.412298	+51.174	1.102
2456721.611888	+74.268	1.555

Table A.56: HE 1523−1155

HJD	RV	RV$_{err}$
	km s^{-1}	km s^{-1}
2456756.697691	−48.291	0.032
2456796.675081	−46.371	0.052
2456888.383899	−40.602	0.040
2457110.726222	−46.003	0.069
2457142.655990	−44.005	0.038
2457168.614095	−42.346	0.034
2457225.447813	−39.096	0.042
2457239.393065	−38.533	0.023

Table A.57: HE 2201−0345

HJD	RV	RV$_{err}$
	km s^{-1}	km s^{-1}
2454314.594364	−54.753	0.055
2454338.512406	−54.716	0.097
2454373.446484	−54.580	0.083
2454665.706516	−52.975	0.095
2454964.707046	−50.901	0.142
2455009.671319	−50.392	0.095
2455059.482102	−50.122	0.066
2455126.498797	−49.879	0.072
2455344.661261	−51.469	0.052
2455415.473509	−52.756	0.061
2455439.410671	−53.080	0.045
2455503.332209	−54.265	0.142
2455531.365776	−54.366	0.182
2455704.662309	−56.579	0.037
2455776.493497	−57.104	0.086
2455882.302609	−58.067	0.089
2455898.303887	−58.217	0.093
2456033.738562	−58.005	0.225
2456078.704130	−58.752	0.096
2456139.621388	−58.840	0.094
2456518.504268	−59.702	0.536
2456530.614563	−59.711	0.068
2456603.447061	−59.645	0.117
2456886.518078	−59.754	0.090
2456956.461286	−60.042	0.202
2457192.706827	−60.125	0.057

Table A.58: HE 2312−0758

HJD	RV	RV$_{err}$
	km s^{-1}	km s^{-1}
2456191.438029	+38.599	0.049
2456213.456368	+38.456	0.052
2456488.710179	+34.178	0.042
2456518.677073	+33.821	0.044
2456528.667747	+33.688	0.059
2456545.611904	+33.273	0.047
2456887.520966	+30.209	0.068
2456917.535781	+30.497	0.068
2456956.480121	+30.319	0.065
2457225.622918	+30.172	0.056

Table A.59: HE 2330−0555

HJD	RV	RV_{err}
	km s^{-1}	km s^{-1}
2454314.711836	−235.085	0.083
2454373.550888	−235.018	0.074
2454396.574802	−234.617	0.279
2455059.605701	−235.294	0.093
2455080.608758	−235.058	0.110
2455126.539073	−235.143	0.060
2455176.414354	−235.146	0.160
2455415.633807	−235.227	0.144
2455439.497335	−235.098	0.161
2455478.573649	−234.834	0.046
2455503.444799	−235.796	0.913
2455531.439197	−235.040	0.118
2455776.707594	−235.430	0.109
2455796.607358	−235.283	0.069
2455882.421279	−235.136	0.099
2456141.696801	−234.980	0.132
2456241.363645	−234.795	0.359
2456530.642253	−235.081	0.108
2456887.546840	−235.298	0.172

A.4   Individual heliocentric radial velocities measured for the CEMP-r/s stars

Table A.60: HE 0039−2635

HJD	RV	RV$_{err}$
	km s^{-1}	km s^{-1}
2456241.416689	−52.078	0.023
2456518.712541	−43.400	0.023

Table A.61: CS 30301−015

HJD	RV	RV$_{err}$
	km s^{-1}	km s^{-1}
2454254.625789	+86.747	0.094
2454314.478888	+86.510	0.081
2454480.790009	+86.638	0.054
2454625.524112	+86.607	0.049
2454909.593179	+86.585	0.078
2454930.718391	+86.636	0.066
2454951.734288	+86.674	0.094
2454987.490752	+86.577	0.048
2455059.374819	+86.462	0.055
2455344.594361	+86.562	0.048
2455415.401156	+86.663	0.058
2455439.379581	+86.510	0.056
2455704.560699	+86.620	0.065
2455776.469383	+86.611	0.064
2456005.713875	+86.564	0.134
2456033.638821	+86.633	0.058
2456078.519452	+86.566	0.061
2456488.399886	+86.763	0.044

Table A.62: HE 1031$-$0020

HJD	RV	RV$_{err}$
	km s^{-1}	km s^{-1}
2454219.429377	+69.718	0.103
2454254.441079	+69.319	0.152
2454406.740957	+69.519	0.119
2454459.641462	+69.839	0.141
2454464.634459	+69.944	0.086
2454481.612353	+69.524	0.145
2454516.553324	+69.634	0.096
2454793.768709	+69.565	0.136
2454909.516560	+69.473	0.124
2454930.530754	+69.308	0.067
2455174.702644	+69.198	0.095
2455207.606295	+69.142	0.075
2455544.740474	+68.903	0.114
2455620.492360	+68.592	0.096
2455915.795124	+68.460	0.222
2455944.582812	+67.917	0.197
2456033.386404	+68.077	0.098
2456241.744801	+67.609	0.138
2456399.406592	+67.486	0.120
2456722.489396	+66.819	0.149
2457110.393432	+66.361	0.227
2457142.442704	+66.111	0.106

Table A.63: LP 625−44

HJD	RV	RV$_{err}$
	km s^{-1}	km s^{-1}
2454219.722357	+38.955	0.039
2454254.658776	+38.870	0.111
2454285.562859	+39.027	0.060
2454314.494240	+38.911	0.041
2454338.417197	+38.770	0.047
2454373.357383	+38.773	0.051
2454625.629361	+38.051	0.038
2454665.570945	+38.081	0.093
2454930.746220	+37.306	0.046
2454964.698450	+37.168	0.059
2454987.526901	+37.153	0.036
2455059.430199	+36.853	0.075
2455344.604713	+36.007	0.060
2455415.373780	+35.652	0.057
2455439.392197	+35.608	0.057
2455620.750793	+34.869	0.059
2455704.580366	+34.615	0.062
2455776.413597	+34.301	0.048
2456005.740590	+33.446	0.086
2456033.681847	+33.154	0.106
2456062.714848	+33.086	0.091
2456078.557492	+32.913	0.069
2456488.412914	+30.863	0.052
2456574.332167	+30.479	0.037
2456579.325817	+30.406	0.081
2456756.743360	+29.588	0.167
2456796.713489	+29.225	0.068
2456887.379911	+28.872	0.056

Literature data for radial velocities

B.1 Literature data for the single r-process enhanced stars

Table B.1: Mean heliocentric radial velocities from the literature and total time-span covered for the single stars

Star ID	ΔT Total (days)	$\bar{RV}$ (this work) (km s^{-1})	$\bar{RV}$ (lit) (km s^{-1})	N	Ref
HD 20	10011	−57.914	−57.4	3	Carney & Latham (1986)
			−57.2	13	Carney et al. (2003)
			−57.5	1	Barklem et al. (2005)
CS 29497−004	4742	+105.008	+105.1	1	Barklem et al. (2005)
CS 31082−001	5193	+139.068	+139.1	8	Hill et al. (2002)
			+138.9	2	Aoki et al. (2003)
			+138.2	1	Tsangarides et al. (2003)
			+138.9	1	Honda et al. (2004)
			+139.4	1	Barklem et al. (2005)
			+139.0	1	Carrera et al. (2013)
			+138.4	1	Kordopatis et al. (2013)
			+138.9	1	Roederer et al. (2014a)
HE 0432−0923	3582	−64.800	−66.6	1	Barklem et al. (2005)
HE 0524−2055	4032	+255.425	+255.3	1	Barklem et al. (2005)
HE 1105+0027	3267	+76.197	+77.0	1	Barklem et al. (2005)
HE 1127−1143	3785	+229.157	+228.5	1	Barklem et al. (2005)
HE 1219−0312	3885	+162.416	+163.6	1	Barklem et al. (2005)
			+163.1	5	Hayek et al. (2009)
HE 1430+0053	3942	−107.749	−107.4	1	Barklem et al. (2005)
CS 22892−052	8788	+13.549	+13.1	10	McWilliam et al. (1995)
			+13.6	1	Norris et al. (1996)
			+12.5	15	Preston & Sneden (2001)
			+13.2	1	Aoki et al. (2003)
			+12.7	1	Honda et al. (2004)
			+14.5	1	Barklem et al. (2005)
			+13.3	1	Bonifacio et al. (2009)
			+13.0	2	Roederer et al. (2014a)
HE 2224+0143	3968	−113.085	−112.3	1	Barklem et al. (2005)
HE 2244−1503	3960	+147.928	+148.1	1	Barklem et al. (2005)
HD 221170	10921	−121.201	−119.0	4	Wilson (1953)
			−123.7	3	Wallerstein et al. (1963)
			−121.8	18	Carney et al. (2003)
			−120.7	1	Barklem et al. (2005)
			−121.7	1	Carney et al. (2008)
			−121.8	1	Soubiran et al. (2008)
CS 30315−029	4741	−169.346	−169.2	1	Barklem et al. (2005)

Table B.2: Mean heliocentric radial velocities for single r-process stars not included in the programme

Star ID	ΔT Total (days)	$\bar{RV}$ (km s^{-1})	N	Ref
HD 115444	8812	-27.6	3	Griffin et al. (1982)
		-26.2	2	Bartkevicius et al. (1992)
		-27.1	2	Aoki et al. (2003)
		-27.2	1	Famaey et al. (2005)
HD 122563	21575	-26.1	3	Wilson & Joy (1950)
		-26.5	6	Wallerstein et al. (1963)
		-24.9	6	Woolley & Harding (1965)
		-26.0	1	Bond (1980)
		-26.0	1	Roederer et al. (2008)
		-26.4	1	Bonifacio et al. (2009)
		-25.6	2	Hollek et al. (2011)
		-26.1	3	Roederer et al. (2014a)

B.2   Literature data for the single CEMP-no stars

Table B.3: Mean heliocentric radial velocities from the literature and total time-span covered for the single CEMP-no stars

Stellar ID	ΔT Total (days)	mean RV (this work) (km s^{-1})	mean RV (km s^{-1})	N	Ref
HE 0020−1741	3333	+93.018	+93.02	1	Kordopatis et al. (2013)
CS 29527−015	7745	+47.077	+45.7	1	Norris et al. (1996)
			+48	1	Aoki et al. (2013a)
CS 22166−016	3727	−209.769	−210	1	Roederer et al. (2014b)
BD+44°493	11368	−150.084	−151.3	6	Carney & Latham (1986)
			−150.6	28	Carney et al. (2003)
			−150.3	4	Ito et al. (2013)
			−150.0	2	Roederer et al. (2014b)
			−150.1	4	Starkenburg et al. (2014)
HE 1012−1540	4646	+226.362	+225.6	2	Cohen et al. (2008)
			+226.3	2	Cohen et al. (2013)
			+225.6	2	Roederer et al. (2014b)
HE 1201−1512	2524	+239.450	+238.0	4	Norris et al. (2013a)
HE 1300+0157	4338	+74.536	+74.3	3	Barklem et al. (2005)
			+73.4	1	Cohen et al. (2008)
			+74.5	6	Starkenburg et al. (2014)
BS 16929−005	5157	+50.619	−51.2	1	Honda et al. (2004)
			−54.0	1	Lai et al. (2004)
			+50.4		Aoki et al. (2007)
			−51.7	1	Lai et al. (2008)
			−50.5	5	Starkenburg et al. (2014)
HE 1300−0641	4329	+68.822	+67.9	2	Barklem et al. (2005)
CS 228877−001	6228	+166.297	+166.1	1	Aoki et al. (2002a)
HE 1327−2326	3660	+64.344	+63.9	1	Aoki et al. (2006)
CS 22878−027	4355	−91.016	−91.3	2	Lai et al. (2008)
			−91.2	2	Roederer et al. (2014b)
			−91.5	6	Starkenburg et al. (2014)
CS 29498−043	4800	−32.488	−32.5	1	Aoki et al. (2002b)
			−32.6	1	Aoki et al. (2002c)
			−32.9	3	Aoki et al. (2004)
			−32.6	2	Roederer et al. (2014b)
CS 29502−092	4782	−67.215	−67.7	1	Tsangarides et al. (2003)
			−67.0	1	Lai et al. (2004)
			−65.2	1	Ruchti et al. (2011)
			−67.0	1	Sakari et al. (2013)
			−66.6	1	Roederer et al. (2014b)
			−66.8	3	Starkenburg et al. (2014)
CS 22949−037	5129	−125.560	−126.4	1	McWilliam et al. (1995)
			−125.7	1	Norris et al. (2001)
			−125.6	4	Depagne et al. (2002)
			−125.6	1	Bonifacio et al. (2009)
			−125.4	2	Roederer et al. (2014b)
			−125.9	2	Starkenburg et al. (2014)

Note that no additional radial-velocity measurements was found for HE 1133−0555.

B.3   Literature data for the single CEMP-s and CEMP-r/s stars

Table B.4: Mean heliocentric radial velocities from the literature and total time-span covered for the single CEMP-s and CEMP-r/s stars

Stellar ID	ΔT Total (days)	mean RV (this work) (km s^{-1})	mean RV (km s^{-1})	N	Ref
HE 0206$-$1916		-199.509	-200.0	1	Aoki et al. (2007)
HE 1045+0226		$+131.498$	$+131.2$	1	Cohen et al. (2013)
HE 2330$-$0555		-235.124	-235.0	1	Aoki et al. (2007)
CS 30301$-$015		$+86.61$	$+85.5$	1	Tsangarides et al. (2003)
			$+86.5$	1	Aoki et al. (2002b)
			$+85.5$	2	Lucatello et al. (2005)

Bibliography

Abate, C., Pols, O. R., Izzard, R. G., Mohamed, S. S., & de Mink, S. E. 2013, Astronomy & Astrophysics, 552, A26

Abate, C., Pols, O. R., Karakas, A. I., & Izzard, R. G. 2015, Astronomy & Astrophysics, 576, A118

Allen, D. M., Ryan, S. G., Rossi, S., Beers, T. C., & Tsangarides, S. A. 2012, Astronomy & Astrophysics, 548, A34

Allende Prieto, C., Barklem, P. S., Lambert, D. L., & Cunha, K. 2004, Astronomy & Astrophysics, 420, 183

Allende Prieto, C., Fernández-Alvar, E., Aguado, D. S., et al. 2015, Astronomy & Astrophysics, 579, A98

Alonso, A., Arribas, S., & Martinez-Roger, C. 1996, Astronomy & Astrophysics, 313, 873

Alonso, A., Arribas, S., & Martínez-Roger, C. 1999, Astronomy & Astrophysicss, 140, 261

Aoki, W., Ando, H., Honda, S., et al. 2002b, Publications of the Astronomical Society of Japan, 54, 427

Aoki, W., Beers, T. C., Christlieb, N., et al. 2007, The Astrophysical Journal, 655, 492

Aoki, W., Beers, T. C., Honda, S., & Carollo, D. 2010, The Astrophysical Journal Letters, 723, L201

Aoki, W., Beers, T. C., Lee, Y. S., et al. 2013a, The Astronomical Journal, 145, 13

Aoki, W., Frebel, A., Christlieb, N., et al. 2006, The Astrophysical Journal, 639, 897

Aoki, W., Honda, S., Beers, T. C., & Sneden, C. 2003, The Astrophysical Journal, 586, 506

Aoki, W., Norris, J. E., Ryan, S. G., Beers, T. C., & Ando, H. 2000, The Astrophysical Journal Letters, 536, L97

Aoki, W., Norris, J. E., Ryan, S. G., Beers, T. C., & Ando, H. 2002a, The Astrophysical Journal, 567, 1166

Aoki, W., Norris, J. E., Ryan, S. G., Beers, T. C., & Ando, H. 2002c, The Astrophysical Journal Letters, 576, L141

Aoki, W., Norris, J. E., Ryan, S. G., et al. 2004, The Astrophysical Journal, 608, 971

Aoki, W., Ryan, S. G., Norris, J. E., et al. 2002d, The Astrophysical Journal, 580, 1149

Aoki, W., Suda, T., Boyd, R. N., Kajino, T., & Famiano, M. A. 2013b, The Astrophysical Journal Letters, 766, L13

Arcones, A. & Montes, F. 2011, The Astrophysical Journal, 731, 5

Arnett, W. D., Bahcall, J. N., Kirshner, R. P., & Woosley, S. E. 1989, Annual Review of Astronomy & Astrophysics, 27, 629

Asplund, M. 2005, Annual Review of Astronomy & Astrophysics, 43, 481

Asplund, M., Grevesse, N., Sauval, A. J., & Scott, P. 2009, Annual Review of Astronomy & Astrophysics, 47, 481

Asplund, M., Lambert, D. L., Nissen, P. E., Primas, F., & Smith, V. V. 2006, The Astrophysical Journal, 644, 229

Barbuy, B., Spite, M., Spite, F., et al. 2005, Astronomy & Astrophysics, 429, 1031

Barklem, P. S., Christlieb, N., Beers, T. C., et al. 2005, Astronomy & Astrophysics, 439, 129

Bartkevicius, A., Sperauskas, J., Rastorguev, A. S., & Tokovinin, A. A. 1992, Baltic Astronomy, 1, 47

Beers, T. 2013, Nuclei in the Cosmos XII, Proceedings of Science, PoS (NIC-XII), 56

Beers, T. C., Carollo, D., Ivezić, Ž., et al. 2012, The Astrophysical Journal, 746, 34

Beers, T. C. & Christlieb, N. 2005, Annual Review of Astronomy & Astrophysics, 43, 531

Beers, T. C., Flynn, C., Rossi, S., et al. 2007a, The Astrophysical Journals, 168, 128

Beers, T. C., Norris, J. E., Placco, V. M., et al. 2014, The Astrophysical Journal, 794, 58

Beers, T. C., Preston, G. W., & Shectman, S. A. 1985, The Astronomical Journal, 90, 2089

Beers, T. C., Preston, G. W., & Shectman, S. A. 1992, The Astronomical Journal, 103, 1987

Beers, T. C., Rossi, S., Norris, J. E., et al. 1998, Space Science Reviews, 84, 139

Beers, T. C., Sivarani, T., Marsteller, B., et al. 2007b, The Astronomical Journal, 133, 1193

Bergemann, M. & Cescutti, G. 2010b, Astronomy & Astrophysics, 522, A9

Bergemann, M. & Gehren, T. 2008, Astronomy & Astrophysics, 492, 823

Bergemann, M., Lind, K., Collet, R., Magic, Z., & Asplund, M. 2012, Monthly Notices of the Royal Astronomical Society, 427, 27

Bergemann, M., Pickering, J. C., & Gehren, T. 2010a, Monthly Notices of the Royal Astronomical Society, 401, 1334

Bertolli, M. G., Herwig, F., Pignatari, M., & Kawano, T. 2013, ArXiv:1310.4578

Bessell, M. S. 2005, Annual Review of Astronomy & Astrophysics, 43, 293

Bessell, M. S. 2007, The Publications of the Astronomical Society of the Pacific, 119, 605

Bessell, M. S., Collet, R., Keller, S. C., et al. 2015, The Astrophysical Journal Letters, 806, L16

Bisterzo, S., Gallino, R., Straniero, O., Cristallo, S., & Käppeler, F. 2010, Monthly Notices of the Royal Astronomical Society, 404, 1529

Bisterzo, S., Gallino, R., Straniero, O., Cristallo, S., & Käppeler, F. 2011, Monthly Notices of the Royal Astronomical Society, 418, 284

Bisterzo, S., Gallino, R., Straniero, O., Cristallo, S., & Käppeler, F. 2012, Monthly Notices of the Royal Astronomical Society, 422, 849

Boffin, H. M. J. & Jorissen, A. 1988, Astronomy & Astrophysics, 205, 155

Bond, H. E. 1980, Astrophysical Journal Supplement, 44, 517

Bondi, H. & Hoyle, F. 1944, Monthly Notices of the Royal Astronomical Society, 104, 273

Bonifacio, P., Caffau, E., Spite, M., et al. 2015, Astronomy & Astrophysics, 579, A28

Bonifacio, P., Monai, S., & Beers, T. C. 2000, The Astronomical Journal, 120, 2065

Bonifacio, P., Spite, M., Cayrel, R., et al. 2009, Astronomy & Astrophysics, 501, 519

Boyd, R. N., Famiano, M. A., Meyer, B. S., et al. 2012, The Astrophysical Journall, 744, L14

Bromm, V. & Loeb, A. 2003, Nature, 425, 812

Buchhave, L. A. 2010, Unv. of Copenhagen

Buchhave, L. A., Latham, D. W., Johansen, A., et al. 2012, Nature, 486, 375

Burbidge, E. M., Burbidge, G. R., Fowler, W. A., & Hoyle, F. 1957, Reviews of Modern Physics, 29, 547

Busso, M., Gallino, R., & Wasserburg, G. J. 1999, Annual Review of Astronomy & Astrophysics, 37, 239

Caffau, E., Bonifacio, P., François, P., et al. 2011, Nature, 477, 67

Caffau, E., Bonifacio, P., François, P., et al. 2013a, Astronomy & Astrophysics, 560, A15

Caffau, E., Bonifacio, P., Sbordone, L., et al. 2013b, Astronomy & Astrophysics, 560, A71

Carney, B. W., Gray, D. F., Yong, D., et al. 2008, The Astronomical Journal, 135, 892

Carney, B. W. & Latham, D. W. 1986, The Astronomical Journal, 92, 60

Carney, B. W., Latham, D. W., Stefanik, R. P., Laird, J. B., & Morse, J. A. 2003, The Astronomical Journal, 125, 293

Carollo, D., Beers, T. C., Bovy, J., et al. 2012, The Astrophysical Journal, 744, 195

Carollo, D., Beers, T. C., Chiba, M., et al. 2010, The Astrophysical Journal, 712, 692

Carollo, D., Beers, T. C., Lee, Y. S., et al. 2007, Nature, 450, 1020

Carollo, D., Freeman, K., Beers, T. C., et al. 2014, The Astrophysical Journal, 788, 180

Carrera, R., Pancino, E., Gallart, C., & del Pino, A. 2013, Monthly Notices of the Royal Astronomical Society, 434, 1681

Castelli, F. & Kurucz, R. L. 2003, in IAU Symposium, Vol. 210, Modelling of Stellar Atmospheres, ed. N. Piskunov, W. W. Weiss, & D. F. Gray, 20P

Cayrel, R., Depagne, E., Spite, M., et al. 2004, Astronomy & Astrophysics, 416, 1117

Cescutti, G., Chiappini, C., Hirschi, R., Meynet, G., & Frischknecht, U. 2013, Astronomy & Astrophysics, 553, A51

Chiappini, C., Ekström, S., Meynet, G., et al. 2008, Astronomy & Astrophysics, 479, L9

Christlieb, N., Beers, T. C., Barklem, P. S., et al. 2004b, Astronomy & Astrophysics, 428, 1027

Christlieb, N., Bessell, M. S., Beers, T. C., et al. 2002, Nature, 419, 904

Christlieb, N., Gustafsson, B., Korn, A. J., et al. 2004a, The Astrophysical Journal, 603, 708

Christlieb, N., Schörck, T., Frebel, A., et al. 2008, Astronomy & Astrophysics, 484, 721

Coc, A., Uzan, J.-P., & Vangioni, E. 2013, ArXiv:1307.6955

Cohen, J. G., Christlieb, N., McWilliam, A., et al. 2008, The Astrophysical Journal, 672, 320

Cohen, J. G., Christlieb, N., Thompson, I., et al. 2013, The Astrophysical Journal, 778, 56

Cohen, J. G., McWilliam, A., Shectman, S., et al. 2006, The Astronomical Journal, 132, 137

Cohen, J. G., Shectman, S., Thompson, I., et al. 2005, The Astrophysical Journal Letters, 633, L109

Collaboration, P. 2013, arXiv:1203.5076

Collet, R., Asplund, M., & Trampedach, R. 2006, The Astrophysical Journall, 644, L121

Collet, R., Asplund, M., & Trampedach, R. 2007, Astronomy & Astrophysics, 469, 687

Cooke, R., Pettini, M., & Murphy, M. T. 2012, Monthly Notices of the Royal Astronomical Society, 425, 347

Cooke, R., Pettini, M., Steidel, C. C., Rudie, G. C., & Jorgenson, R. A. 2011, Monthly Notices of the Royal Astronomical Society, 412, 1047

Couchman, H. M. P. & Rees, M. J. 1986, Monthly Notices of the Royal Astronomical Society, 221, 53

Cowan, J. J. & Sneden, C. 2006, Nature, 440, 1151

Cristallo, S., Piersanti, L., Straniero, O., et al. 2011, The Astrophysical Journals, 197, 17

Cristallo, S., Straniero, O., Gallino, R., et al. 2009, The Astrophysical Journal, 696, 797

Dekker, H., D'Odorico, S., Kaufer, A., Delabre, B., & Kotzlowski, H. 2000, in Society of Photo-Optical Instrumentation Engineers (SPIE) Conference Series, Vol. 4008, Optical and IR Telescope Instrumentation and Detectors, ed. M. Iye & A. F. Moorwood, 534–545

Demarque, P., Woo, J.-H., Kim, Y.-C., & Yi, S. K. 2004, The Astrophysical Journals, 155, 667

Deng, L.-C., Newberg, H. J., Liu, C., et al. 2012, Research in Astronomy & Astrophysics, 12, 735

Depagne, E., Hill, V., Spite, M., et al. 2002, Astronomy & Astrophysics, 390, 187

Dopita, M., Hart, J., McGregor, P., et al. 2007, Astrophysics and Space Science, 310, 255

Drake, J. J., Smith, V. V., & Suntzeff, N. B. 1992, The Astrophysical Journal Letters, 395, L95

Ebisuzaki, T., Shigeyama, T., & Nomoto, K. 1989, The Astrophysical Journal Letters, 344, L65

Eggleton, P. P. 1971, Monthly Notices of the Royal Astronomical Society, 151, 351

Famaey, B., Jorissen, A., Luri, X., et al. 2005, Astronomy & Astrophysics, 430, 165

François, P., Depagne, E., Hill, V., et al. 2007, Astronomy & Astrophysics, 476, 935

Frebel, A., Aoki, W., Christlieb, N., et al. 2005, Nature, 434, 871

Frebel, A., Chiti, A., Ji, A. P., Jacobson, H. R., & Placco, V. M. 2015, ArXiv:1507.01973

Frebel, A., Christlieb, N., Norris, J. E., Aoki, W., & Asplund, M. 2006, The Astrophysical Journal Letters, 638, L17

Frebel, A., Christlieb, N., Norris, J. E., et al. 2007a, Astrophysical Journal Letters, 660, L117

Frebel, A., Collet, R., Eriksson, K., Christlieb, N., & Aoki, W. 2008, The Astrophysical Journal, 684, 588

Frebel, A., Johnson, J. L., & Bromm, V. 2007b, Monthly Notices of the Royal Astronomical Society, 380, L40

Frebel, A. & Norris, J. E. 2015, ArXiv:1501.06921

Freiburghaus, C., Rosswog, S., & Thielemann, F.-K. 1999, The Astrophysical Journall, 525, L121

Frischknecht, U., Hirschi, R., Meynet, G., et al. 2010, Astronomy & Astrophysics, 522, A39

Frischknecht, U., Hirschi, R., & Thielemann, F.-K. 2012, Astronomy & Astrophysics, 538, L2

Gallino, R., Bisterzo, S., Straniero, O., Ivans, I. I., & Käppeler, F. 2006, Memorie della Società Astronomica Italiana, 77, 786

Gehren, T., Liang, Y. C., Shi, J. R., Zhang, H. W., & Zhao, G. 2004, Astronomy & Astrophysics, 413, 1045

Giridhar, S., Lambert, D. L., Gonzalez, G., & Pandey, G. 2001, The Publications of the Astronomical Society of the Pacific, 113, 519

Goriely, S., Bauswein, A., & Janka, H.-T. 2011, Astrophysical Journal Letters, 738, L32+

Goriely, S. & Siess, L. 2005, in IAU Symposium, Vol. 228, From Lithium to Uranium: Elemental Tracers of Early Cosmic Evolution, ed. V. Hill, P. Francois, & F. Primas, 451–460

Gratton, R., Sneden, C., & Carretta, E. 2004, Annual Review of Astronomy & Astrophysics, 42, 385

Griffin, R., Gustafsson, B., Vieira, T., & Griffin, R. 1982, Monthly Notices of the Royal Astronomical Society, 198

Gustafsson, B., Edvardsson, B., Eriksson, K., et al. 2008, Astronomy & Astrophysics, 486, 951

Hansen, C. J., Bergemann, M., Cescutti, G., et al. 2013, Astronomy & Astrophysics, 551, A57

Hansen, C. J. & Primas, F. 2011, Astronomy & Astrophysics, 525, L5+

Hansen, C. J., Primas, F., Hartman, H., et al. 2012, Astronomy & Astrophysics, 545, A31

Hansen, T., Andersen, J., Nordström, B., Buchhave, L. A., & Beers, T. C. 2011, The Astrophysical Journall, 743, L1

Hansen, T., Hansen, C. J., Christlieb, N., et al. 2014, The Astrophysical Journal, 787, 162

Hayek, W., Wiesendahl, U., Christlieb, N., et al. 2009, Astronomy & Astrophysics, 504, 511

Heger, A. & Woosley, S. E. 2010, The Astrophysical Journal, 724, 341

Heil, M., Juseviciute, A., Käppeler, F., et al. 2009, Publications of the Astronomical Society of Australia, 26, 243

Henden, A. A., Levine, S., Terrell, D., & Welch, D. L. 2015, in American Astronomical Society Meeting Abstracts, Vol. 225, American Astronomical Society Meeting Abstracts, 336.16

Herwig, F. 2005, Annual Review of Astronomy & Astrophysics, 43, 435

Hilditch, R. W. 2001, An Introducion To Close Binary Stars, 1st edn. (Cambridge University Press)

Hill, V., Plez, B., Cayrel, R., et al. 2002, Astronomy & Astrophysics, 387, 560

Hinshaw, G., Larson, D., Komatsu, E., et al. 2013, The Astrophysical Journals, 208, 19

Hirschi, R. 2007, Astronomy & Astrophysics, 461, 571

Hirschi, R. & et al. 2006, in Reviews in Modern Astronomy, Vol. 19, Reviews in Modern Astronomy, ed. S. Roeser, 101

Høg, E., Fabricius, C., Makarov, V. V., et al. 2000, Astronomy & Astrophysics, 355, L27

Hollek, J. K., Frebel, A., Roederer, I. U., et al. 2011, The Astrophysical Journal, 742, 54

Honda, S., Aoki, W., Ando, H., et al. 2004, The Astrophysical Journal Supplement Series, 152, 113

Ito, H., Aoki, W., Beers, T. C., et al. 2013, The Astrophysical Journal, 773, 33

Ito, H., Aoki, W., Honda, S., & Beers, T. C. 2009, The Astrophysical Journall, 698, L37

Ivans, I. I., Kraft, R. P., Sneden, C., et al. 2001, The Astronomical Journal, 122, 1438

Iwamoto, N., Umeda, H., Tominaga, N., Nomoto, K., & Maeda, K. 2005, Science, 309, 451

Jacobson, H. R., Keller, S., Frebel, A., et al. 2015, The Astrophysical Journal, 807, 171

Johnson, J. A., Herwig, F., Beers, T. C., & Christlieb, N. 2007, The Astrophysical Journal, 658, 1203

Jonsell, K., Barklem, P. S., Gustafsson, B., et al. 2006, Astronomy & Astrophysics, 451, 651

Käppeler, F., Gallino, R., Bisterzo, S., & Aoki, W. 2011, Reviews of Modern Physics, 83, 157

Keller, S. C., Bessell, M. S., Frebel, A., et al. 2014, Nature, 506, 463

Keller, S. C., Schmidt, B. P., Bessell, M. S., et al. 2007, Publications of the Astronomical Society of Australia, 24, 1

Kennedy, C. R., Sivarani, T., Beers, T. C., et al. 2011, The Astronomical Journal, 141, 102

Kifonidis, K., Plewa, T., Janka, H.-T., & Müller, E. 2000, The Astrophysical Journal Letters, 531, L123

Kirby, E. N., Simon, J. D., Geha, M., Guhathakurta, P., & Frebel, A. 2008, The Astrophysical Journall, 685, L43

Klessen, R. S., Glover, S. C. O., & Clark, P. C. 2012, Monthly Notices of the Royal Astronomical Society, 421, 3217

Kordopatis, G., Gilmore, G., Steinmetz, M., et al. 2013, The Astronomical Journal, 146, 134

Kraft, R. P. 1994, Astronomical Society of the Pacific, 106, 553

Kraft, R. P., Sneden, C., Smith, G. H., et al. 1997, The Astronomical Journal, 113, 279

Kupka, F., Piskunov, N., Ryabchikova, T. A., Stempels, H. C., & Weiss, W. W. 1999, Astronomy & Astrophysics Supplement, 138, 119

Kupka, F. G., Ryabchikova, T. A., Piskunov, N. E., Stempels, H. C., & Weiss, W. W. 2000, Baltic Astronomy, 9, 590

Kurucz, R. L. 1995, in Astronomical Society of the Pacific Conference Series, Vol. 78, Astrophysical Applications of Powerful New Databases, ed. S. J. Adelman & W. L. Wiese, 205

Lai, D. K., Bolte, M., Johnson, J. A., & Lucatello, S. 2004, The Astronomical Journal, 128, 2402

Lai, D. K., Bolte, M., Johnson, J. A., et al. 2008, The Astrophysical Journal, 681, 1524

Lawler, J. E., Bonvallet, G., & Sneden, C. 2001, The Astrophysical Journal, 556, 452

Lee, Y. S., Beers, T. C., Masseron, T., et al. 2013, The Astronomical Journal, 146, 132

Li, H.-N., Zhao, G., Christlieb, N., et al. 2015, The Astrophysical Journal, 798, 110

Lind, K., Bergemann, M., & Asplund, M. 2012, Monthly Notices of the Royal Astronomical Society, 427, 50

Lucatello, S., Beers, T. C., Christlieb, N., et al. 2006, The Astrophysical Journall, 652, L37

Lucatello, S., Gratton, R., Cohen, J. G., et al. 2003, The Astronomical Journal, 125, 875

Lucatello, S., Tsangarides, S., Beers, T. C., et al. 2005, The Astrophysical Journal, 625, 825

Lugaro, M., Karakas, A. I., Stancliffe, R. J., & Rijs, C. 2012, The Astrophysical Journal, 747, 2

Maeder, A. & Meynet, G. 2001, Astronomy & Astrophysics, 373, 555

Maeder, A. & Meynet, G. 2015b, Astronomy & Astrophysics, 580, A32

Maeder, A., Meynet, G., & Chiappini, C. 2015a, Astronomy & Astrophysics, 576, A56

Marsteller, B. E., Beers, T. C., Sivarani, T., et al. 2005, in Bulletin of the American Astronomical Society, Vol. 37, American Astronomical Society Meeting Abstracts, 131.03

Mashonkina, L., Christlieb, N., Barklem, P. S., et al. 2010, Astronomy & Astrophysics, 516, A46+

Mashonkina, L., Korn, A. J., & Przybilla, N. 2007, Astronomy & Astrophysics, 461, 261

Masseron, T., Johnson, J. A., Lucatello, S., et al. 2012, The Astrophysical Journal, 751, 14

Masseron, T., Johnson, J. A., Plez, B., et al. 2010, Astronomy & Astrophysics, 509, A93

Masseron, T., Plez, B., Van Eck, S., et al. 2014, Astronomy & Astrophysics, 571, A47

Mathieu, R. D., Latham, D. W., & Griffin, R. F. 1990, The Astronomical Journal, 100, 1859

Mattsson, L. 2015, ArXiv:1505.04758

McClure, R. D. 1984, The Astrophysical Journall, 280, L31

McClure, R. D., Fletcher, J. M., & Nemec, J. M. 1980, The Astrophysical Journall, 238, L35

McWilliam, A. 1998, The Astronomical Journal, 115, 1640

McWilliam, A., Preston, G. W., Sneden, C., & Searle, L. 1995, The Astronomical Journal, 109, 2757

Mermilliod, J.-C., Andersen, J., Latham, D. W., & Mayor, M. 2007, Astronomy & Astrophysics, 473, 829

Mermilliod, J. C., Mayor, M., & Udry, S. 2008, Astronomy & Astrophysics, 485, 303

Meyer, B. S., Mathews, G. J., Howard, W. M., Woosley, S. E., & Hoffman, R. D. 1992, The Astrophysical Journal, 399, 656

Meynet, G., Ekström, S., & Maeder, A. 2006, Astronomy & Astrophysics, 447, 623

Meynet, G., Hirschi, R., Ekstrom, S., et al. 2010, Astronomy & Astrophysics, 521, A30

Mohamed, S. & Podsiadlowski, P. 2007, in Astronomical Society of the Pacific Conference Series, Vol. 372, 15th European Workshop on White Dwarfs, ed. R. Napiwotzki & M. R. Burleigh, 397

Montes, F., Beers, T. C., Cowan, J., et al. 2007, The Astrophysical Journal, 671, 1685

Mucciarelli, A., Salaris, M., Bonifacio, P., Monaco, L., & Villanova, S. 2014, Monthly Notices of the Royal Astronomical Society, 444, 1812

Nissen, P. E. & Schuster, W. J. 2010, Astronomy & Astrophysics, 511, L10

Nomoto, K., Kobayashi, C., & Tominaga, N. 2013, Annual Review of Astronomy & Astrophysics, 51, 457

Norris, J. E., Bessell, M. S., Yong, D., et al. 2013a, The Astrophysical Journal, 762, 25

Norris, J. E., Christlieb, N., Korn, A. J., et al. 2007, The Astrophysical Journal, 670, 774

Norris, J. E., Ryan, S. G., & Beers, T. C. 1996, The Astrophysical Journal Supplement Series, 107, 391

Norris, J. E., Ryan, S. G., & Beers, T. C. 1997, The Astrophysical Journal, 488, 350

Norris, J. E., Ryan, S. G., & Beers, T. C. 1999, The Astrophysical Journal Supplement Series, 123, 639

Norris, J. E., Ryan, S. G., & Beers, T. C. 2001, The Astrophysical Journal, 561, 1034

Norris, J. E., Yong, D., Bessell, M. S., et al. 2013b, The Astrophysical Journal, 762, 28

Piau, L., Beers, T. C., Balsara, D. S., et al. 2006, The Astrophysical Journal, 653, 300

Pignatari, M., Gallino, R., Heil, M., et al. 2010, The Astrophysical Journal, 710, 1557

Pignatari, M., Gallino, R., Meynet, G., et al. 2008, The Astrophysical Journall, 687, L95

Pilachowski, C. A. 1989, in The Abundance Spread within Globular Clusters: Spectroscopy of Individual Stars, ed. G. Cayrel de Strobel, 1–7

Placco, V. M., Beers, T. C., Roederer, I. U., et al. 2014b, The Astrophysical Journal, 790, 34

Placco, V. M., Frebel, A., Beers, T. C., et al. 2014a, The Astrophysical Journal, 781, 40

Placco, V. M., Frebel, A., Beers, T. C., et al. 2013, The Astrophysical Journal, 770, 104

Placco, V. M., Frebel, A., Beers, T. C., & Stancliffe, R. J. 2014c, The Astrophysical Journal, 797, 21

Placco, V. M., Kennedy, C. R., Beers, T. C., et al. 2011, The Astronomical Journal, 142, 188

Placco, V. M., Kennedy, C. R., Rossi, S., et al. 2010, The Astronomical Journal, 139, 1051

Prantzos, N. 2012, Astronomy & Astrophysics, 542, A67

Preston, G. W., Shectman, S. A., & Beers, T. C. 1991, The Astrophysical Journal Supplement Series, 76, 1001

Preston, G. W. & Sneden, C. 2001, The Astronomical Journal, 122, 1545

Qian, Y.-Z. & Wasserburg, G. J. 2001, The Astrophysical Journall, 552, L55

Qian, Y.-Z. & Wasserburg, G. J. 2003, The Astrophysical Journal, 588, 1099

R.D., M. & A.W., W. 1990, The Astrophysical Journal, 352, 709

Reddy, B. E., Tomkin, J., Lambert, D. L., & Allende Prieto, C. 2003, Monthly Notice of the Royal Astronomical Society, 340, 304

Reifarth, R., Lederer, C., & Käppeler, F. 2014, Journal of Physics G Nuclear Physics, 41, 053101

Riebel, D., Meixner, M., Fraser, O., et al. 2010, The Astrophysical Journal, 723, 1195

Roederer, I. U. 2013, The Astronomical Journal, 145, 26

Roederer, I. U., Cowan, J. J., Preston, G. W., et al. 2014c, Monthly Notices of the Royal Astronomical Society, 445, 2970

Roederer, I. U., Lawler, J. E., Sneden, C., et al. 2008, The Astrophysical Journal, 675, 723

Roederer, I. U., Preston, G. W., Thompson, I. B., Shectman, S. A., & Sneden, C. 2014a, The Astrophysical Journal, 784, 158

Roederer, I. U., Preston, G. W., Thompson, I. B., et al. 2014b, The Astronomical Journal, 147, 136

Rossi, S., Beers, T. C., Sneden, C., et al. 2005, The Astronomical Journal, 130, 2804

Ruchti, G. R., Fulbright, J. P., Wyse, R. F. G., et al. 2011, The Astrophysical Journal, 737, 9

Ryan, S. G., Aoki, W., Norris, J. E., & Beers, T. C. 2005, The Astrophysical Journal, 635, 349

Ryan, S. G., Norris, J. E., & Beers, T. C. 1999, The Astrophysical Journal, 523, 654

Sackmann, I.-J. & Boothroyd, A. I. 1992, The Astrophysical Journall, 392, L71

Sakari, C. M., Shetrone, M., Venn, K., McWilliam, A., & Dotter, A. 2013, Monthly Notices of the Royal Astronomical Society, 434, 358

Sbordone, L., Bonifacio, P., Caffau, E., et al. 2010, Astronomy & Astrophysics, 522, A26

Schlegel, D. J., Finkbeiner, D. P., & Davis, M. 1998, The Astrophysical Journal, 500, 525

Simons, J. W., Palmer, B. A., Hof, D. E., & Oldenborg, R. C. 1989, Journal of the Optical Society of America B Optical Physics, 6, 1097

Sivarani, T., Beers, T. C., Bonifacio, P., et al. 2006, Astronomy & Astrophysics, 459, 125

Skrutskie, M. F., Cutri, R. M., Stiening, R., et al. 2006, The Astronomical Journal, 131, 1163

Smith, G. H. 1987, Astronomical Society of the Pacific, 99, 67

Sneden, C. 1973, The Astrophysical Journal, 184, 839

Sneden, C., Cowan, J., & Gallino, R. 2008, Annual Review of Astronomy & Astrophysics, 46, 241

Sneden, C., Cowan, J., Lawler, J. E., et al. 2003, The Astrophysical Journal, 591, 936

Sneden, C., Cowan, J. J., Ivans, I. I., et al. 2000, The Astrophysical Journal, 533, L139

Sneden, C., McWilliam, A., Preston, G. W., et al. 1996, The Astrophysical Journal, 467, 819

Sobeck, J. S., Kraft, R. P., Sneden, C., et al. 2011, The Astronomical Journal, 141, 175

Soubiran, C., Bienaymé, O., Mishenina, T. V., & Kovtyukh, V. V. 2008, Astronomy & Astrophysics, 480, 91

Spergel, D. N., Bean, R., Doré, O., et al. 2007, The Astrophysical Journal Supplement Series, 170, 377

Spite, F. & Spite, M. 1982, Astronomy & Astrophysics, 115, 357

Spite, M., Caffau, E., Bonifacio, P., et al. 2013, Astronomy & Astrophysics, 552, A107

Spite, M., Cayrel, R., Plez, B., et al. 2005, Astronomy & Astrophysics, 430, 655

Stancliffe, R. J. 2009a, Monthly Notices of the Royal Astronomical Society, 394, 1051

Stancliffe, R. J., Church, R. P., Angelou, G. C., & Lattanzio, J. C. 2009b, Monthly Notices of the Royal Astronomical Society, 396, 2313

Stancliffe, R. J. & Eldridge, J. J. 2009c, Monthly Notices of the Royal Astronomical Society, 396, 1699

Stancliffe, R. J. & Glebbeek, E. 2008, Monthly Notices of the Royal Astronomical Society, 389, 1828

Stancliffe, R. J., Glebbeek, E., Izzard, R. G., & Pols, O. R. 2007, Astronomy & Astrophysics, 464, L57

Starkenburg, E., Shetrone, M. D., McConnachie, A. W., & Venn, K. A. 2014, Monthly Notices of the Royal Astronomical Society, 441, 1217

Steinmetz, M., Zwitter, T., Siebert, A., et al. 2006, The Astronomical Journal, 132, 1645

Suda, T., Aikawa, M., Machida, M. N., Fujimoto, M. Y., & Iben, Jr., I. 2004, The Astrophysical Journal, 611, 476

Takahashi, K., Umeda, H., & Yoshida, T. 2014, The Astrophysical Journal, 794, 40

Talon, S. & Charbonnel, C. 2005, Astronomy & Astrophysics, 440, 981

Tauris, T. M. & Takens, R. J. 1998, Astronomy & Astrophysics, 330, 1047

Tinsley, B. M. 1979, The Astrophysical Journal, 229, 1046

Tolstoy, E., Hill, V., & Tosi, M. 2009, Annual Review of Astronomy & Astrophysics, 47, 371

Tominaga, N., Iwamoto, N., & Nomoto, K. 2014, The Astrophysical Journal, 785, 98

Tominaga, N., Umeda, H., & Nomoto, K. 2007, The Astrophysical Journal, 660, 516

Travaglio, C., Gallino, R., Arnone, E., et al. 2004, The Astrophysical Journal, 601, 864

Tsangarides, S. A., Ryan, S. G., & Beers, T. C. 2003, in Astronomical Society of the Pacific Conference Series, Vol. 304, CNO in the Universe, ed. C. Charbonnel, D. Schaerer, & G. Meynet, 133

Udry, S., Mayor, M., & Queloz, D. 1999, in Astronomical Society of the Pacific Conference Series, Vol. 185, IAU Colloq. 170: Precise Stellar Radial Velocities, ed. J. B. Hearnshaw & C. D. Scarfe, 367

Umeda, H. & Nomoto, K. 2002, The Astrophysical Journal, 565, 385

Umeda, H. & Nomoto, K. 2003, Nature, 422, 871

Umeda, H. & Nomoto, K. 2005, The Astrophysical Journal, 619, 427

Wallerstein, G., Greenstein, J. L., Parker, R., Helfer, H. L., & Aller, L. H. 1963, The Astrophysical Journal, 137, 280

Westin, J., Sneden, C., Gustafsson, B., & Cowan, J. J. 2000, The Astrophysical Journal, 530, 783

White, S. D. M. & Rees, M. J. 1978, Monthly Notices of the Royal Astronomical Society, 183

Wilson, R. E. 1953, Carnegie Institute Washington D.C. Publication, 0

Wilson, R. E. & Joy, A. H. 1950, The Astrophysical Journal, 111, 221

Winteler, C., Käppeli, R., Perego, A., et al. 2012, The Astrophysical Journall, 750, L22

Wood, P. R. 2000, Publications of the Astronomical Society of Australia, 17, 18

Woolley, R. v. d. R. & Harding, G. A. 1965, Royal Greenwich Observatory Bulletins, 93, 363

Woosley, S. E., Wilson, J. R., Mathews, G. J., Hoffman, R. D., & Meyer, B. S. 1994, The Astrophysical Journal, 433, 229

Yanny, B., Rockosi, C., Newberg, H. J., et al. 2009, The Astronomical Journal, 137, 4377

Yong, D., Norris, J. E., Bessell, M. S., et al. 2013, The Astrophysical Journal, 762, 26